Dynamic Atomic Force Microscopy and applications in biomolecular imaging

Sergio Santos Hernandez

Submitted in accordance with the requirements for the degree of Doctor of Philosophy

The University of Leeds
School of Physics and Astronomy
& Faculty of Biological Sciences

April 2011

The candidate confirms that the work submitted is his/her own, except where work which has formed part of jointly-authored publications has been included. The contribution of the candidate and the other authors to this work has been explicitly indicated below. The candidate confirms that appropriate credit has been given within the thesis where reference has been made to the work of others.

Chapter 3 is based on:

1) Santos, S., Barcons, V., Font, J. & Thomson, N. H. Cantilever dynamics in amplitude modulation AFM: continuous and discontinuous transitions. *J. Phys. D: Appl. Phys.* 43, 275401-275407 (2010).

2) Santos, S., Barcons, V., Font, J. & Thomson, N. H. Bi-stability of amplitude modulation AFM in air: deterministic and stochastic outcomes for imaging biomolecular systems. *Nanotechnology* 21, 225710-225720 (2010).

3) Santos, S. & Thomson, N. H. *High resolution imaging of Immunoglobulin G (IgG) antibodies and other biomolecules using amplitude modulation atomic force microscopy in air*. (Humana Press, 2011).

where the candidate has devised the experiments with the help of the supervisors, written the first drafts of the publications, produced the experimental data, developed the models and, with the help and in collaboration with Victor Barcons and Josep Font, implemented the model for simulation and produced and edited the figures.

Chapter 4 is based on:

4) Barcons, V., Santos, S., Bonass, W. A., Font, J. & Thomson, N. H. Monostability of sharp-tip impact oscillators interacting with surface hydration layers. *Euro Physics Letters,* Submitted (2011).

where the candidate has devised the experiments with the help of the co-authors, written the first draft, produced the experimental data, developed the model, implemented the model in Matlab and produced and edited the figures except for those produced in the C programming language which have been implemented by Victor Barcons under the supervision of Josep Font.

Chapter 5 is based on:

5) Santos, S., Barcons, V., Christenson, H. K., Thomson, N. H. & Font, J. The intrinsic resolution limit in the atomic force microscope: implications for heights of nano-scale features. *PLoS ONE*, Submitted (2011).

where the candidate has devised the experiments with the help of Neil H Thomson, written the first drafts of the publications, produced the experimental data with DNA samples, developed the models with the help of Hugo K Christenson, implemented the model with the help and in collaboration with Victor Barcons and Josep Font and produced and processed the data. Neil H Thomson has devised the experiments and produced the experimental data with antibodies samples.

Chapter 6 is based on:

6) Santos, S. & Thomson, N. H. Energy dissipation in a dynamic nanoscale contact. *Applied Physics Letters* 98, 013101-013103 (2011).

7) Barcons, V., Santos, S., Thomson, N. H. & Font, J. Dynamics of nano-mechanical junctions under the influence of adsorbed water layers. *Physical Review Letters*, Submitted (2010).

where the candidate has devised the experiments with the help of Neil H Thomson, written the first drafts, produced the experimental data, developed the models, implemented the model in Matlab and produced and edited the figures except for those produced in the C programming language which have been implemented by Victor Barcons under the supervision of Josep Font.

All publications have been completed with the help and expertise of Neil H Thomson and decisions on submission have been made jointly. All the experiments have been devised jointly with the supervisors. DNA samples have been kindly provided by Daniel J. Billingsley under the supervision of William A Bonass.

I would like to thank my supervisors Dr Neil Thomson and Dr William Bonass for their guidance and support. I would also like to thank Tony Fischer (Fischer-Cripps laboratories), Hugo K Christenson, Daniel Billingsley (University of Leeds), Antonio Vazquez (Universidad de la Coruña), Victor Barcons and Josep Font (Universitat Politècnica de Catalunya). This work was sponsored by BBSRC and Asylum Research Corporation.

Abstract

The Atomic Force Microscope (AFM) is a key member of the Scanning Probe Microscope (SPM) family. Its versatility allows it to image and manipulate nanoscale features with high precision, making it one of the main instruments in nanotechnology for surface characterization. The aim of this thesis is to improve robustness, reproducibility, resolution and data interpretation in ambient conditions for dynamic AFM of heterogeneous samples.

The AFM is particularly notorious for lack of reproducibility with apparent height and width being the two main measured parameters where accuracy is sought. Here i) the origins of reproducibility, or lack thereof, have been investigated experimentally via a systematic approach to imaging for the whole range of parameter space and relative humidity, ii) smooth and step-like transitions have been investigated both experimentally and with simulations, iii) a method to mechanically stabilise the tip radius and calculate the effective area of interaction in the dynamic mode has been developed and used to predict the number of eV dissipated per atom per cycle, iv) a method to predict the tip radius *in situ* has been developed, v) three types of dynamic behaviour have been categorised and distinguished (Type I, II and III) allowing to both predict the tip radius and noise patterns, vi) a general interpretation of a mechanism behind height reconstruction and vii) a novel high resolution and low wear imaging technique (SASS) have been developed, modelled, implemented and interpreted with the help of simulations.

The most general outcome of this work is that the tip radius has to be well characterised since it plays a major role in any AFM experiment. The investigation is general for nano-mechanical forced oscillators in ambient conditions and the calculations will lead to mapping of local chemistry and mechanics at higher resolution.

Table of contents

List of Figures

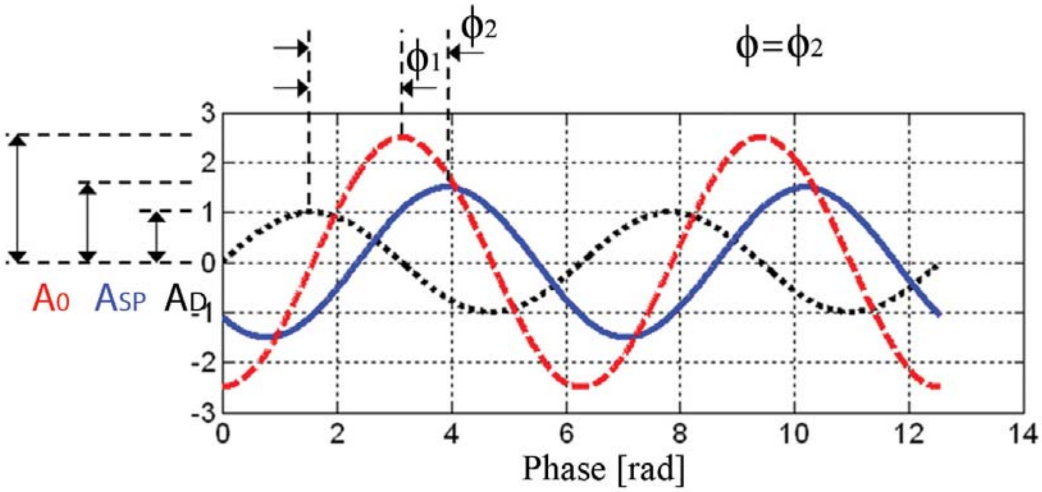

Figure I

Scheme of the common signals used in AM AFM. The amplitude of the unperturbed cantilever for a given drive frequency and drive force is A_0 (dashed red line). The amplitude of the cantilever when interacting with the surface is the amplitude set-point A_{sp} (continuous blue line) and it is shown to lag the drive amplitude A_D (dotted black line) by an angle Φ (the phase shift). The latter is used in AM AFM to obtain phase contrast images. In the scheme, the amplitude set-point lag is larger than the free amplitude lag, thus the cantilever is in the attractive force regime in this case; the initial phase shift prior to engaging is $\phi=\phi_1=90$ degrees. On engaging $\phi=\phi_2>90$ degrees. Phase contrast is obtained with $\phi=\phi_2$. As with the phase, i.e. ϕ_1 and ϕ_2, note that both the free amplitude and the amplitude-set point signal cannot actually coexist at a given time since this is the physical amplitude of the end of the cantilever for the free cantilever (A_0) and for the cantilever when interacting with the surface (A_{sp}) respectively. Thus, measurements are always relative. The scales of both axis are arbitrary here since there are not required for the discussion.

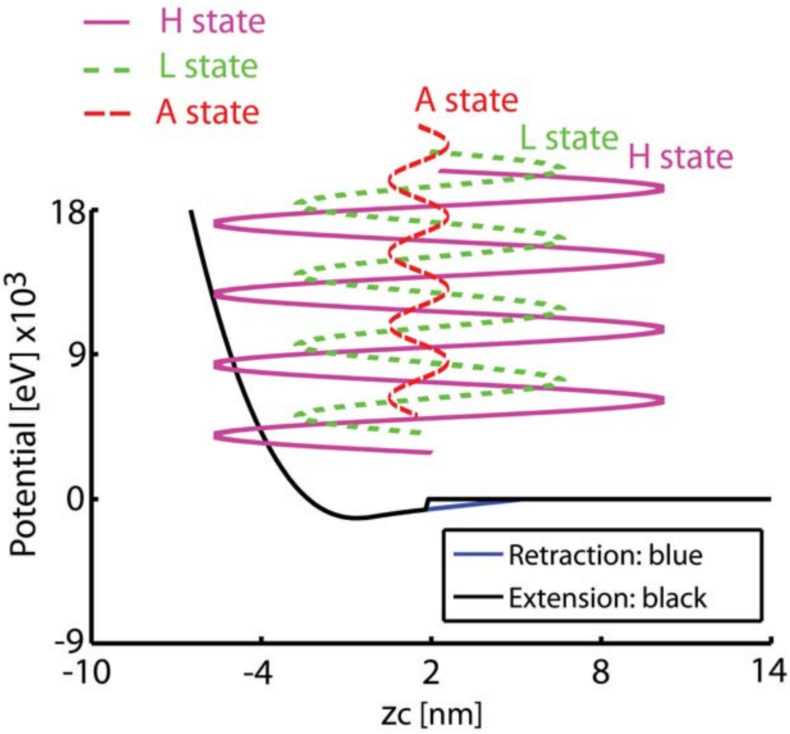

Figure II

Scheme of the tip-surface potential where the vertical axis expresses the energy of the interaction in eV and the horizontal axis expresses the tip-sample separation z_c. The black continuous line in the potential represents the extension of the tip and the continuous blue line the retraction for which some hysteresis is observed. This hysteresis is a consequence of adding the capillary tip-surface force. The scheme has been obtained for a tip of 20 nm in radius, a water layer of h=0.6 nm and an effective, an effective elastic modulus of E^*=10 GPa and a surface energy of 20 mJ. The actual separation here is z_c=2 nm implying that any z amplitude larger than 2nm is already mechanically contacting the surface. At this separation, the three possible oscillation states are represented. The H-state is represented with a continuous purple line, the L-state with a dashed green line and the A-state with a dashed red line. Here it is easy to observe that while the A-state is purely attractive in the sense that the amplitude of oscillation is much smaller than the separation z_c, the L and H-states might be net attractive or net repulsive. That is, while intermittent contact with the surface might or might not occur during an oscillation in the L and H-states, the attractive and repulsive regimes are defined by the net force per cycle as defined in Eqn. I.1 below and not by whether intermittent contact occurs.

$$< F_{ts} >= \frac{1}{T}\int_a^{a+T} F_{ts}\,dt \qquad \text{(I.1)}$$

Definition of the net or average force regimes.

List of acronyms

a: contact radius in the region where mechanical contact occur

A: amplitude of oscillation when the tip is interacting with the surface and the feedback is off (Fig. I)

A_0: free amplitude of oscillation for the unperturbed cantilever (Fig. I)

A_c: critical oscillation amplitude

AD (PD): Amplitude (Phase) Distance curve (Figs. III and IV)

AFM: Atomic Force Microscopy

AM AFM: Amplitude Modulation Atomic Force Microscopy

APD: Amplitude and Phase Distance curve (Figs. III and IV)

A_{sp}: amplitude of oscillation, or amplitude set-point, when the tip is interacting with the surface and the feedback is on (Fig. I)

A-state: Attractive amplitude branch or state (Fig. II)

d: tip-surface or tip-sample distance

d^*: effective tip-surface or tip-sample distance when there are water layers on the tip and the surface ($d^*=d-2h$)

d_{on}: distance for which the capillary force forms on extension or approach

d_{off}: distance for which the capillary force ruptures on retraction

dAFM: dynamic Atomic Force Microscopy

DMT: Derjaguin-Muller-Toporov model of contact mechanics

dsDNA: double stranded Deoxyribonucleic acid

E^*: effective value of elastic modulus in the tip-surface contact

E: elastic modulus of the surface

E_s: elastic modulus of the sample. This accounts for the elastic modulus of a surface feature on the plane

E_t: elastic modulus of the tip

f: drive frequency

F_0 : maximum drive or force amplitude

f_0: drive frequency in Hz

F_D : driving force

FM AFM: Frequency Modulation Atomic Force Microscopy

F_{ts}: tip-sample and/or tip-surface force or interaction

H: Hamaker constant for the tip-surface pair

h: height of the water layers on the surfaces

H_s: Hamaker constant for the tip-sample pair. The sample is a surface feature with which the tip interacts with apart from the infinite surface
H-state: High amplitude branch or state (Fig. II)

k: spring constant of the cantilever

L-state: Low amplitude branch or state (Fig. II)

N region: Negative slope region

P: radius of an end on cylinder

P_m: mean pressure in the contact
Q: quality factor

ϕ: also termed $\Delta\phi$ or phase for phase contrast imaging (Fig. I)

ϕ_0: drive phase

R: the tip here is modelled as a sphere and the radius of curvature is termed R

R_2: sample's radius for a spherical sample

RH: Relative Humidity

SASS: Small Amplitude Small Set Point (Figs. III and IV)

Type I APD curves: APD curves displaying the SASS and N regions but not the A-state
Type II APD curves: APD curves displaying characteristics of both Type I APD

curves and Type III APD curves. These are transition APD cruves

Type III APD curves: APD curves displaying the A-state and no SASS region for small values of free amplitude
vdW: long range and zero frequency van der Waals interactions

V_{men}: volume of the water meniscus

z: instantaneous tip position relative to z_c (Fig. 3.1)

z_c/A_0: normalised equilibrium tip-surface separation for the unperturbed cantilever

z_c**:** tip-surface separation or equilibrium position of the tip for the unperturbed cantilever (Fig. 3.1)
β (ω/ω_r): normalised drive frequency

γ: surface energy

γ_{H_2O}: surface energy of water

δ: sample deformation or indentation. This accounts for the deformation under compression for a two body pair such as a sphere-sphere pair or a sphere-surface pair
ΔA: variation in amplitude when the tip is interacting with the surface relative to A_0 when the feedback is disabled
ΔA_{sp}: variation in amplitude when the tip is interacting with the surface relative to A_0

Δz_c: z or z-piezo signal (topographic imaging)

ω: angular drive frequency, i.e. $2\pi f_0$

ω_0: natural frequency of the cantilever

ω_r: angular resonant frequency of the free cantilever

Terminology

This section provides definitions of some of the basic parameters used in this work. In dynamic AFM (dAFM) a vibrating cantilever is excited by a sinusoidal force, the **driving force** F_D (Eqn. (I.2) and Fig. I). While in air, and before contact, the maximum amplitude of cantilever oscillation is termed the **free amplitude** A_0 (Fig. I). Here, the **amplitude of oscillation** when the tip is interacting with the surface is termed A or A_{sp} (Fig. I) according to whether feedback is disabled or enabled respectively. The value of A_0 depends on F_D and the (angular) **drive frequency** ω. We write

$$F_D = F_0 \cos(\omega t + \phi_0) \qquad \text{(I.2)}$$

where F_0 is the **maximum drive or force amplitude** and ϕ_0 is the **drive phase** (Fig. I). Furthermore, we write the (angular) **resonant frequency** of the free cantilever as ω_r and the **natural frequency** as ω_0. Two different values for z are to be distinguished here; z for **instantaneous tip position** relative to the equilibrium position of the tip for the unperturbed cantilever or z_c or **tip-surface separation** (Fig. 3.1). Furthermore, the variation of two main parameters are monitored in Amplitude Modulation (AM) AFM and these are the z or z-piezo Δz_c signal (**topographic imaging**) and the phase $\Delta\phi$, or simply ϕ (**phase contrast imaging**, Fig. I). This is the phase shift of A or A_{sp} relative to F_D. Note that in the dAFM convention the sign of the phase is inverted relative to the standard theory of vibrations. Hence, for the free cantilever in air, when simple harmonic motion occurs, the value of ϕ is defined to be 90 degrees (Fig. I).[1]

The variation in amplitude when the tip is interacting with the surface is written ΔA or ΔA_{sp} according to whether feedback is disabled or enabled respectively. The **normalised drive frequency** is written β (ω/ω_r) and the **normalised separation** z_c/A_0. These normalised parameters are sometimes useful to present data and/or discuss general behaviour. Care needs to be taken when discussing AM and FM since A_0 is commonly used in AM to refer to the free amplitude and in FM to the oscillation amplitude. This is partly because A, or equivalently A_{sp} in AM AFM, is the set oscillation amplitude in FM but also the free oscillation amplitude A_0. The **tip-sample** and/or **tip-surface** force or interaction is written as F_{ts}.

The tip here is modelled as a sphere and the radius is termed R when interacting with an infinite surface. For the interaction between a spherical sample and the tip, the sample's radius is R_2. For example, the “sample” could be a single molecule or nanoparticle. For the long range interaction's the van der Waals forces are modelled using Hamaker's approach.[2] The **Hamaker constant** is termed H (as opposed to the typical A). This is customary in AFM because A is typically reserved for the amplitude. The values of Hamaker given here stand for the Hamaker (H_s) of the tip-sample pair and (H) that of the tip-surface pair. That is, even though we refer to the Hamaker of the sample and surface we imply tip-sample and tip-surface respectively. The letter E^* is reserved for the effective value of elastic modulus in the tip-surface contact unless otherwise stated. Ambiguity of the meaning of E can arise due to this being currently used in the literature to refer to either elastic modulus or energy dissipation and/or stored energy. However, when its meaning can lead to confusion, the definition is given in each section. A brief discussion on the physical meaning of some concepts in the thesis is given below.

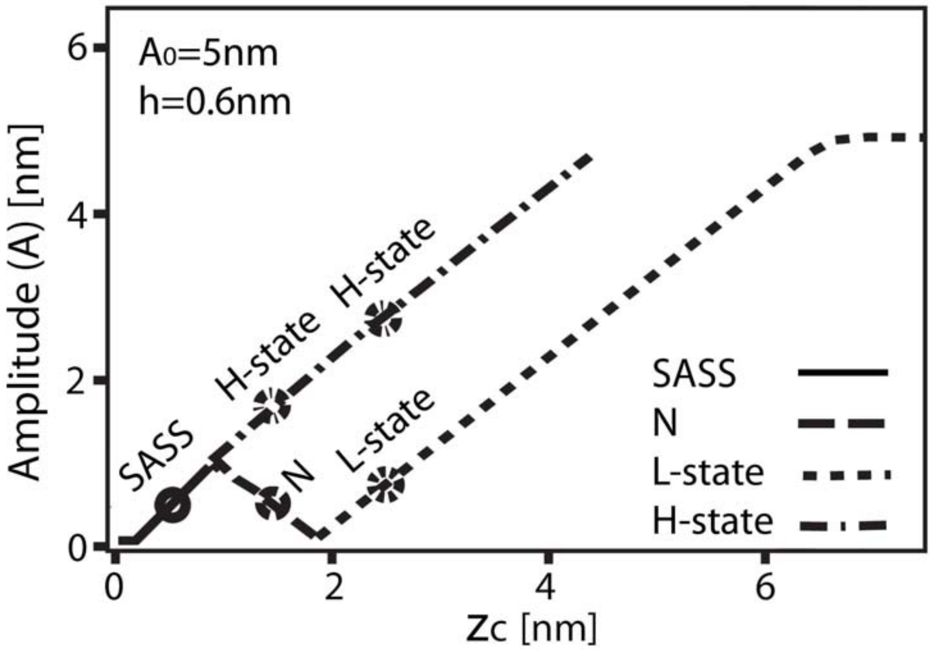

Figure III

Simulated AD curve where the L (small dashed lines) and H (dash-dotted lines) states and the N (large dashed lines) and SASS (continuous line) regions are observed. A water layer of height h=0.6 nm has been included in the simulation to observe the N and SASS regions. For large values of z_c/A_0 (i.e. large relative $z_c/A_0\sim1$) the L and H-states dominate whereas for smaller (i.e. $z_c/A_0<<1$) values the N and SASS regions appear. The markers indicate a value of z_c ($z_c\sim2.5$nm) for which the H and L sates coexist, another ($z_c\sim1.5$nm) for which the N region and the H-state coexist and a final one ($z_c\sim0.5$nm) for which only the SASS region exists. Thus all regions except the SASS are bistable whereas the SASS is a monostable region; a switch between two states can take place wherever there are two solutions for a given z_c. The parameters are: $f=f_0$=312 kHz, k=40 N/m, R=2.5 nm, Q=500, γ=40 mJ, E=10 GPa, E_t=120 GPa, h=0.6 nm and A_0=5 nm.

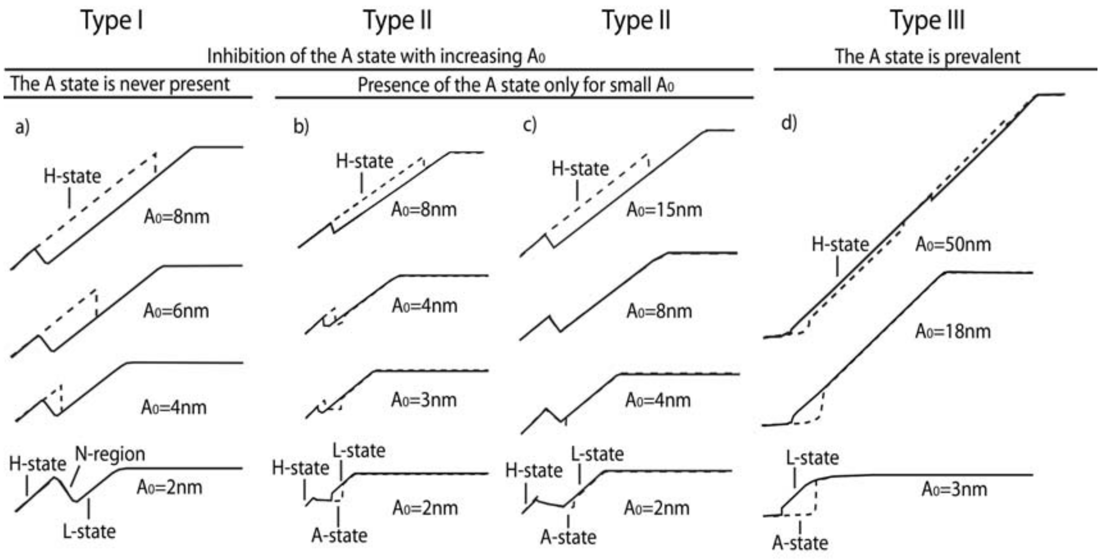

Figure IV

Experimental AD curves obtained on a mica surface at resonance with k~40 N/m. Type a) I, b) II and c) III curves are shown. The y-axis is the amplitude in nm and the z-axis the z_c separation. Nevertheless since it is the shape of the curves with increasing free amplitude which allows differentiation of curves, only the shape and the free amplitude corresponding to each curve is shown. From bottom to top the free amplitude has been increased discretely to allow observation of the several characteristics of the type of curve. The A, L and H-states are pointed for each type. Notice that the A-state is only prevalent with increasing free amplitude for Type III curves.

APD: Amplitude-Phase-Distance curves. In APD curves the tip-surface separation is slowly decreased and then increased while monitoring the behaviour of the amplitude A (AD curves) phase (AP curves) or both (APD curves). In simulations, other distances curves such as force and contact time distance curves can be acquired. Example of AD curves are given in Figs. III andIV above. A full description of APD curves is given in Chapter 3.3.2.

Attractive regime: the attractive regime or attractive force regime is defined as a net attractive average force per cycle where, during one cycle, repulsive forces might or might not be present. It is convention however to define the attractive force regime as that for which the phase is larger than 90 degrees. While this convention typically agrees with the above more physically significant definition, there are cases for which it might not (Fig. I). A full description of the attractive regime is given in Chapters 3.3.3 and 3.3.4.

Repulsive regime: the repulsive regime or repulsive force regime is defined as a net repulsive average force per cycle where, during one cycle, attractive forces might or might not be present. It is convention however to define the repulsive force regime as that for which the phase is less than 90 degrees. While this convention typically agrees with the above more physically significant definition, there are cases for which it might not (Fig. II). A full description of the repulsive regime is given in Chapters 3.3.3 and 3.3.4.

L and H-states: the L (H) state or L (H) oscillation branch or mode is an oscillation branch that typically coexists (Fig. III) with the H (L) branch for a given set of operational parameters. The physical significance of the two branches only makes sense where both coexist for a given separation z_c. In such cases, for a given z_c the amplitude in the L-state is significantly less than that in the H-state implying that the cantilever oscillates higher above the surface in the L-state than in the H-state. This is the physical significance behind the typical equivalence between the attractive and repulsive regimes and the L and H-states respectively (Fig. II). A brief description of the L and H-states is given in Chapter 3.3.1 and a detailed description in Chapter 3.3.4.

SASS region: monostable parameter-space region where the cantilever oscillates with angstroms of oscillation amplitude and where the tip-surface separation is numerically very similar to it, i.e. A_{sp}/z_c~1 and z_c<1 nm. Monostability here refers to a single oscillation branch, i.e. the SASS branch, being observed (Fig. III). The SASS region is described in detail in Chapter 4.2.

N region: the N region is a region of the parameter space occurring for separations z_c directly above the SASS region (Fig. III) and where the amplitude increases with decreasing z_c. Strictly speaking the N region has to be observed for relatively small values of free amplitude A_0, i.e. A_0<5 nm, and has to occur in between the L and H branches connecting them. The N region is described in detail in Chapter 4.2.

A-state: the A-state is branch in dAFM in ambient conditions which appears at several angstroms above the surface for Type II and III systems (see below). The branch might or might not be an oscillation branch implying that the amplitude might actually be zero (Figs. II and IVd). The A-state is described in detail in Chapter 6.2.

Type I APD curves: APD curves displaying the SASS and N regions and where the A-state is not observed. In Type I APD curves, and for sufficiently small values of free amplitude (Fig. IVa) the trajectory on extension is always L, N and SASS and on retraction SASS, N and L. As the free amplitude is increased the trajectory on extension is always L, N and SASS and on retraction SASS, H and L. Type I, II and II curves are described in detail in Chapter 6.2.2.

Type II APD curves: transition APD curves displaying characteristics of both Type I and III curves (Figs. IVb and IVc). Type I, II and II curves are described in detail in Chapter 6.2.2.

Type III APD curves: for small free amplitudes, i.e. A_0<5 nm, the A-state typically dominates on retraction, presents a large hysteresis and the amplitude might tend to zero, i.e. might not be an oscillation solution. Type III APD curves for larger free amplitudes are characterised by the persistence of the A-state and hysteresis and the inhibition of the H-state (or repulsive regime) for even relatively large values of free amplitude. In Type III APD curves, and for sufficiently small values of free amplitude (Fig. IVd) the trajectory on extension is always L, A and on retraction A and L where major hysteresis is observed. As the free amplitude is sufficiently increased the H-state might be reached (Fig. IVd). Type I, II and II curves are described in detail in Chapter 6.2.2.

Type I systems: systems displaying Type I APD curves. These are typically cantilever-surface pairs for which the tip is ultra-sharp (i.e. R<5 nm) and the cantilever relatively stiff (i.e. k>1-10 N/m).

Type III systems: cantilever-surface pairs displaying characteristics of both Type I and III APD curves.

Type III systems: systems displaying Type III APD curves. These are typically cantilever-surface pairs for which the tip is not ultra-sharp (i.e. R>5 nm), the cantilever is not sufficiently stiff (i.e. k<1-10 N/m) or a combination of both. The effect of the cantilever stiffness can be readily demonstrated experimentally.

Chapter 1

1. Introduction

1.1 Overview of the thesis

This thesis studies the dynamics of the cantilever in dynamic AFM (dAFM) and its applications in biomolecular imaging under ambient conditions. Robustness, reproducibility and straight forward interpretation of the acquired data are expected characteristics of a high resolution microscope. The two main parameters that the AFM routinely characterizes are the width and the height of the surface features with chemical mapping being a long standing goal. Here, double stranded DNA (dsDNA) on mica is used as a model system to find out how apparent width and height depend on the system characteristics and the cantilever dynamics. This biologically relevant system has been chosen for simplicity and because it well characterised.

The relevance and importance of developing the appropriate instrumentation to visualize nanoscale processes and interpret and validate models was recognized since the beginning of nanotechnology.[3-4] In this respect, the present analysis relies on experimentation carried out with an AFM in the dynamic mode which permits, amongst others, obtaining experimental data on the behaviour of nano-mechanical forced oscillators in ambient conditions. Even though the cantilever has micro-scale dimensions, the model is based on the behaviour of a nanometre sized sphere interacting with a surface. Furthermore, in air, and with higher quality factor (Q) levers, it has been shown[5] the cantilever approximates very well to a mass on a spring where higher modes can be neglected. Thus, the analysis presented here is general and represents a unified theory of nano-mechanical forced oscillators in ambient conditions. Understanding dynamic nanoscale interactions between nano and micro-objects and/or surfaces is essential in nanotechnology since it has applications for Nano-Electro-Mechanical-Systems (NEMS) and Micro-Electro-Mechanical-Systems (MEMS), nanoscale mechanical actuators, wetting, protein-membrane interactions, nanoparticle interactions, powders and granular materials in general and, in particular, to biological processes where the role of water films is relevant.[6-11]

In Chapter 1, a brief introduction to the different AFM modes of operation is given. The fundamentals of dsDNA molecular structure are also briefly discussed with a view to providing the necessary understanding of the secondary structure and its properties and to briefly introduce structural molecular biology. Chapter 2 discusses the history of biomolecular imaging with the AFM and the relevance of ambient imaging. The core results of this thesis are presented in Chapters 3-6. In Chapter 3, the fundamental Amplitude Modulation (AM) AFM theory is presented and a systematic experimental analysis is carried out and compared with theoretical predictions. The relevance of peak forces is also discussed. In Chapter 4, a new phenomenon, i.e. the monostability of the system a few angstroms above the surface is discussed and shown to be related to the water layer present on surfaces in ambient conditions; this phenomenon leads to increased resolution and greatly improved stability. In Chapter 5, the physical origins of apparent height are interpreted from a geometrical point of view. The analysis considers the finite area of interaction between the tip and the surface and the tip-sample-surface forces rather than the tip-surface forces alone. Simulations are used to predict that even for very small forces and in the non-contact mode, where compression cannot occur, the apparent height decreases with decreasing normalized feature size. The predictions match our results and are general for any AFM technique.

In Chapter 6, we discuss the dynamic character of the effective curvature of the tip and its relationship to plastic deformation and the energy dissipated per atom. A method to achieve the mechanical stability of the tip is also provided and the consequences for reliable data interpretation and future mechanical and chemical mapping discussed. Chapter 6 ends by presenting the results of this work in a compact form as a division of the interaction of a nano-mechanical forced oscillator in ambient conditions; Type I, II and III systems. This division is not arbitrary, has been defined in relation to the dynamics of the oscillator and depends on whether the strength of the restoring force is large relative to the attractive component of the force (type I systems) or not (type II systems). The use, advantages, disadvantages and limitations of each system in ambient conditions are discussed. The conclusions are given in Chapter 7, and the future of imaging heterogeneous samples by dAFM is discussed.

1.2 Introduction to the AFM

1.2.1 AFM overview

The AFM is part of the Scanning Probe Microscope (SPM) family[12] and is a high resolution surface profiling microscope. Its versatility allows the AFM to image and manipulate nanoscale features with high precision, making it one of the main instruments in nanotechnology for surface characterization.[1,13-16] Recent advances in the field are allowing researchers to investigate[17] and identify[18-19] the chemical structure of single molecules. In dynamic imaging modes (dAFM), the excitation of higher harmonics[20-21] and the relationship between the fundamental frequency and higher modes hold promise[20,22-24] for the determination and simultaneous acquisition of mechanical and chemical maps at nanometre length scales.

The AFM is based on a micro-cantilever with a sharp probe at its end which is brought into close proximity with the surface to either characterize it and/or manipulate it. As the tip senses the surface forces, these begin to control the behaviour of the cantilever. In the dynamic mode, the non-linear character of the surface forces implies that understanding and controlling the dynamics of the cantilever when interacting with the surface can be challenging, but need to be very well understood to extract most information about the sample

The use of the AFM in biology was recognized almost as soon as it was invented.[13-14,25-26] The precise control of the xyz-position in AFM is possible thanks to the high sensitivity of the dimensions of piezoelectric materials to applied voltages.[1,12] These are responsible for controlled x, y and z motion and are capable of sub-angstrom precision.[25] In the most common set-up, a laser beam is focused on the end of the cantilever and the deflection is detected by a split photodiode (Fig. 1.1). The signal is then processed by the control system and used as feedback to act on the z-piezo actuator. An important difference between the AFM and the Scanning Tunnelling Microscope (STM) is that the AFM can image both electrical insulators and conductors. This is an important advantage in biological applications where conductivity is rare.[12,14] Furthermore, the AFM can be operated in all environments, including air and liquid[27-28], allowing biomolecules and biological samples to remain hydrated and often active.[13-14,25,29] The operating temperatures also offer a large range of possibilities since these can vary from room temperature to liquid-nitrogen and even lower temperatures.[14,17]

There are several modes of operation, which can be classified as quasi-static, i.e. DC and dynamic, i.e. AC modes while the instrument can also be operated in the whole range of environmental conditions such as ultra high vacuum, ambient and liquid. In the DC modes the deflection of the cantilever is static and several types of information such as topography and friction contrast can be obtained.

Dynamic or AC AFM[30-32], where the cantilever is vibrated so that the tip intermittently interacts with the surface in the normal plane, has been essential for the progression of biological imaging since these methods eliminate damaging shear forces that arise in contact mode.[14,28,32-33]

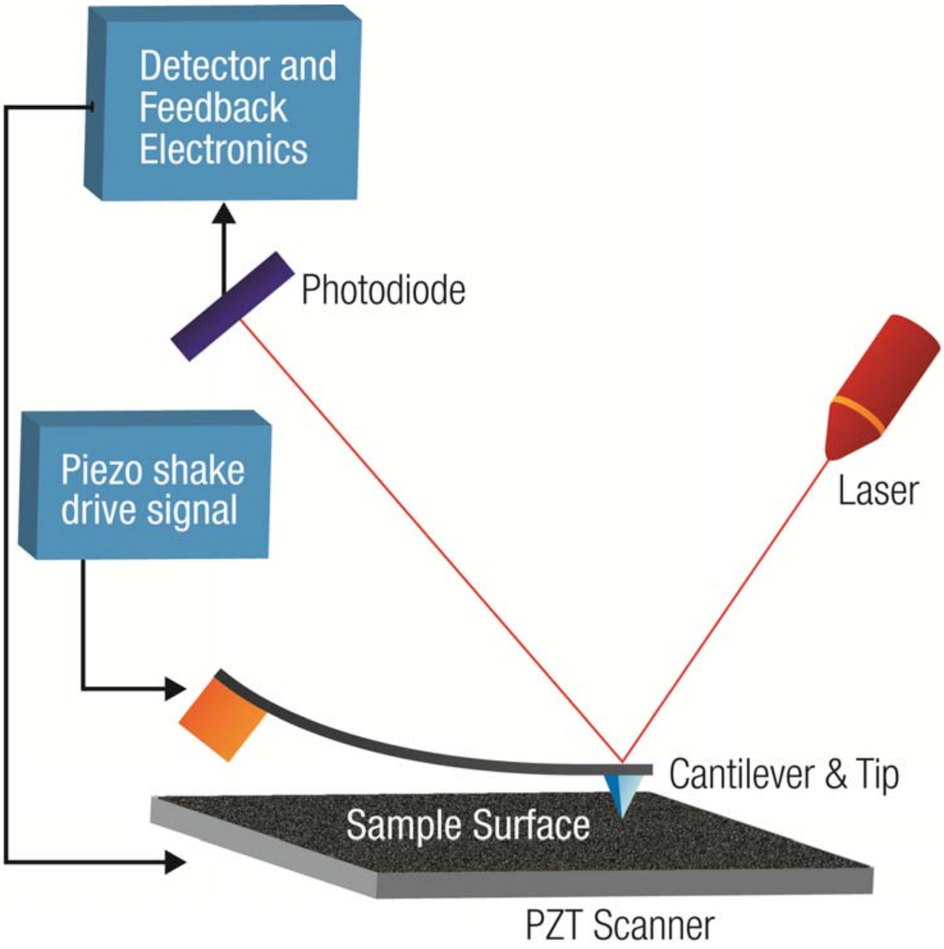

Figure 1. 1

Scheme of the set-up of an AFM. A laser beam is focused onto a reflective cantilever and the reflected signal is focused onto a photodiode. The signal is then processed by the control system and a feedback mechanism is used to maintain a constant deflection, oscillation amplitude, frequency shift and/or phase shift. The position in the x, y and z directions is typically controlled by a piezoelectric transducer (PZT scanner in the figure). The excitation of the cantilever is typically controlled by another piezo actuator (piezo shake drive signal in the figure). This actuator provides the drive amplitude by shaking the cantilever in a given prescribed way, typically a sine in d AFM, in a similar way to what a tuning fork would do. A wave then propagates up and down the cantilever and produces the typical effect of resonance. Examples of resonant systems can be found in standard vibrations and waves text books.[34] Figure adapted from Stark and Heckl.[35]

Two major dAFM methods exist in the AFM community. The two branches are a historical result of the development of AFM where ultra high vacuum and ambient or liquid imaging developed as two separate disciplines.[1,36] Typically, vacuum imaging was performed with a Frequency Modulation (FM) feedback system[30] whereas an Amplitude Modulation (AM) was preferred feedback for liquid[28] and ambient imaging.[31-32] This division was not arbitrary since in vacuum the Quality factor (Q) of the cantilever is orders of magnitude larger than in ambient or liquid imaging.[1,30] Thus AM would be too slow in vacuum whereas FM would lose sensitivity with small values of Q in ambient and liquid. Nevertheless, advances in the technique are allowing FM AFM to make the transition from high resolution vacuum to ambient and liquid imaging where good results have been obtained[37]. Still, it is in vacuum where FM AFM excels.[15,17,19]

1.2.2 DC modes

The Contact Mode of operation (CM AFM) was the first mode of AFM and was invented in 1986.[12] In CM, the tip is driven against the surface until the cantilever deflection becomes positive as a consequence of the repulsive forces. A user defined set-point is input into the controller to attempt to hold the deflection constant. As the tip raster scans the surface in the xy-plane, the feedback mechanism detects the topography of the surface in the vertical or z-axis as variations in deflection set-point.

Topography will increase/decrease the cantilever deflection. The error signal due to finite time feedback response can also be used to get information about the sample.[14] Attractive CM AFM imaging is challenging due to the snap into contact force that occurs as the tip gets close to the surface.[15] Since the force gradient is negative and typically monotonically decreases until a maximum of negative force is reached, the restoring force of the cantilever cannot withstand the attraction. This imposes a limitation on CM AFM where imaging in the close proximity with small forces is hindered by the snap into contact.[15,32] Thus, CM AFM is a repulsive mode of operation. Another limitation of CM AFM relates to the shear or frictional forces. Since the tip is in constant contact with the sample in the repulsive region, xy-motion can easily damage soft matter in CM AFM.[14] In Lateral or Friction AFM[14,25], the cantilever is operated in the same way as in CM AFM but the lateral deflection of the cantilever is monitored instead. As the friction between the tip and the sample increases, so does the lateral deflection.

1.2.3 AC modes

AC or dynamic modes have been part of the AFM family since the very beginning of AFM.[31] In principle, the shift in phase, frequency and/or amplitude of oscillation due to the interaction can be used as feedback mechanisms to track the topography of the surface. There are, however, two main dAFM methods, FM AFM, also known as non-contact (nc) AFM[1,30], and AM AFM, also known as Tapping Mode (TM) AFM.[32] These terminologies can lead to serious misunderstandings about AFM operation and interpretation, which in part arise from the historical development of the instrument and divergence of the field into two sub-communities.

FM AFM was typically driven in the attractive regime where mechanical contact would not occur[30,38] and AM AFM was believed to be driven mainly by repulsive forces[32,39] where the tip would intermittently contact the surface in the repulsive region. Nevertheless experimental and theoretical studies[40-43] later acknowledged the implications of the attractive force components in AM AFM. These advances in the understanding of the dynamics soon allowed soft matter to be imaged with high resolution in the attractive regime in AM AFM.[44] Attractive imaging here refers to the time average value of the force per cycle, but nevertheless, the instrument can also be operated in the nc mode in AM AFM by sufficiently decreasing the drive amplitude and/or driving above resonance.[41,45] Additionally, repulsive nc or FM AFM has also been shown to be possible.[1] Thus, all the advances in the field, since have made the initial terminology of TM and nc modes confusing or at the least, inconvenient. For this reason, in this work, reference to the feedback system is made directly as FM or AM and the mode of operation in terms of force regimes is exclusively reserved to refer to force regimes.

In AM, phase contrast can be simultaneously acquired together with topography. While phase contrast imaging has long been regarded as a method that can deliver other than topographical information about the sample,[33,46-48] its use as a chemical mapping method has been hampered by the difficulties of interpreting it and obtaining meaningful quantitative data.[49-50] In this respect, it is still to be shown whether the energy dissipated in the tip-sample interaction, which makes up the energy dissipation maps, can be deconvoluted to discriminate from where different sources of contrast arise. Still, in a significant contribution García et al.[50] showed that the derivative of the energy dissipated per cycle with separation provides information on whether the source is long range or short range hysteric or viscoelastic. That is, it is the sign of the rate of change of the phase with separation that has information about dissipative processes.

The study of the excitation of higher harmonics and higher flexural modes has also been explored for several years now.[1,5,21,23,35,51-54] The cantilever is a three dimensional object and displays flexural or normal modes. The modes of an oscillating system consist of patterns of sinusoidal motion where all parts of the system oscillate with the same frequency. Flexural modes can but do not have to coincide with higher harmonics and, in particular, the flexural modes of a cantilever do not coincide with the higher harmonics.[55-56] For example, the higher modes do coincide with the higher harmonics in a classic vibrating string system.[34] Higher harmonics might be more sensitive to variations in the elastic modulus of the sample[35], thus advances in this direction are promising in terms of imaging and sensing material properties in the nanoscale.[53] Other forms of dAFM are more recent, such as torsional AFM[54] where the end of the cantilever is slightly modified and torsional harmonics are excited when the tip intermittently interacts with the sample. The analysis of this torsional excitation is said to provide quantitative information about material properties with nanoscale spatial resolution.[54] Overall, the AFM has become one of the main tools for surface characterization[12,15-16,57-58] and recent publications of major advances imply that the relevance of the AFM in science will carry on in the future. For example recent advances in conventional techniques such as FM AFM are allowing researchers to identify the chemical structure of single molecules[17,19] and crystals[18] with sub-nanometer resolution[59] while advances in the speed of data acquisition in liquid AM AFM are allowing visualisation of rapid biomolecular interactions.[29]

1.3 The molecular structure of DNA

It has taken over 100 years to discover the biological importance of deoxyribonucleic acid – DNA since it was first isolated in 1869 by Friedrich Miescher.[60] In fact, initially, DNA was assumed to be a simple repetition of four nucleic acids or bases and proteins were believed to carry the genetic code. This was principally due to the fact that proteins are very complex in comparison to DNA and perform most of the functions in living things. It was already known at that time that proteins are controllers of biochemical reactions, they are structural elements, catalysts, control signals and act as motors in the cells. In turn, it is the three dimensional configuration of proteins that give them their chemical properties and functionalities. Additionally, it is the linear sequence of the twenty types of amino-acids that are encoded by the universal genetic code, that gives proteins their three dimensional configuration. Thus, compared to DNA, proteins are structurally much more complex. The main question then was to find the molecule that coded for proteins and this question was the central part of twentieth century research in molecular biology. That the information of the genetic code was found in genes and that genes were found in chromosomes was already known in the beginning of the twentieth century.[60] Furthermore, in the chromosomes, and in terms of weight, there is much more protein than there is DNA. Nevertheless, experimentation carried out in the 40s[61] and more conclusively in the early 50s[62] showed that DNA was the molecule coding for the genetic code.

Since the chemical structure in proteins was responsible for its functionality, a race to discover the chemical structure of DNA started immediately after these experiments. It was thought that the key for the replication mechanism of DNA would be found by knowing its chemical structure. A key step in this direction was made when Chargaff's rules of base composition were discovered.[60,63] These state that there are always the same amounts of adenine as thymine and guanine as cytosine residues. Later on, Watson and Crick's proposal of the double helix structure set a landmark in the study of the molecule.[64] Chargaff's rules and the intuition for 1) the hydrogen bonding associations of the bases and 2) that DNA is in the form of a double helix, allowed them to visualise and construct the model of the DNA structure that was revealed in 1953. The discovery of the helicity of the structure was derived from X-ray crystallographic data by Rosalind Franklin. It is now known that DNA is a molecule that exists in all cellular life forms and that it carries hereditary and genetic information. Nevertheless, even today, the exact mechanisms of transmission of genetic information are still not fully understood[60,65-66] and research into structural and molecular mechanisms is still ongoing.[29,65,67-68]

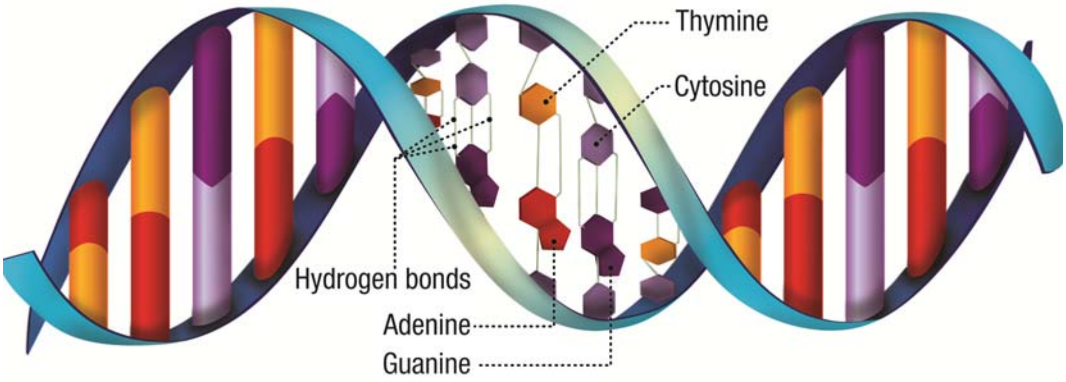

Figure 1. 2

Schematic example of a deoxyribonucleic acid or double-stranded DNA molecule. This is an example of a nucleic acid where the helical structure and base pairing can be observed. Adapted from Voet and Voet.[60]

There are two types of naturally occurring nucleic acids which are found in all living cells and many viruses; *deoxyribonucleic acid* (DNA) and *ribonucleic acid* (RNA).[60,69] There are also artificial nucleic acids such as *peptide nucleic acids* (PNA) and *locked nucleic acids* (LNA); the difference from the natural occurring (DNA and RNA) is that changes are made to the backbone of the molecule.[70]

DNA is a large polymer that consists of repeated elements or nucleotides linked into two chains or strands. These entwine around each other in a right handed manner forming the well known double helix (Fig. 1.2). In its primary structure, these elements consist of a sugar, phosphate and one of the four bases – adenine, guanine, thymine and cytosine; the first two are purine bases (double ringed) and the latter, pyrimidines (single ringed). The bases in DNA are bound to the 1' position of the sugar. Nucleotides bind to each other via phosphodiester bonds that connect the 3'-hydroxyl group of one sugar to the 5'- phosphate group of the next. The distance between these groups is 0.34 nm (Fig. 1.3).[60,66,69] An example of the chemical structure of a nucleotide is given below in Fig. 1.4.

The secondary structure or helix of DNA consists of the two single strands that are linked by a process called annealing.[60,69] For this reason, double-stranded DNA is also known as a DNA duplex or double stranded DNA (dsDNA). Pairing of the bases takes place through hydrogen bonding of the base sequences when complementary sequences combine (Figs. 1.2 and 1.5). Adenine bonds with thymine via two hydrogen bonds and guanine with cytosine via three. In the case of RNA, however, Thymine (T) is replaced by Uracil.[60] When the sequences between two single stranded DNA molecules pair up in a way consistent with the above scheme, annealing occurs and double stranded DNA is obtained (Fig. 1.5).[60,69] The ability of molecular recognition and self assembly of DNA is based on such pairing.[60,64,69] The two strands are antiparallel and the bases are perpendicular to the helix axis. The interior of this structure contains the hydrophobic bases that are bound to the hydrophilic sugar-phosphate backbone exterior.[66]

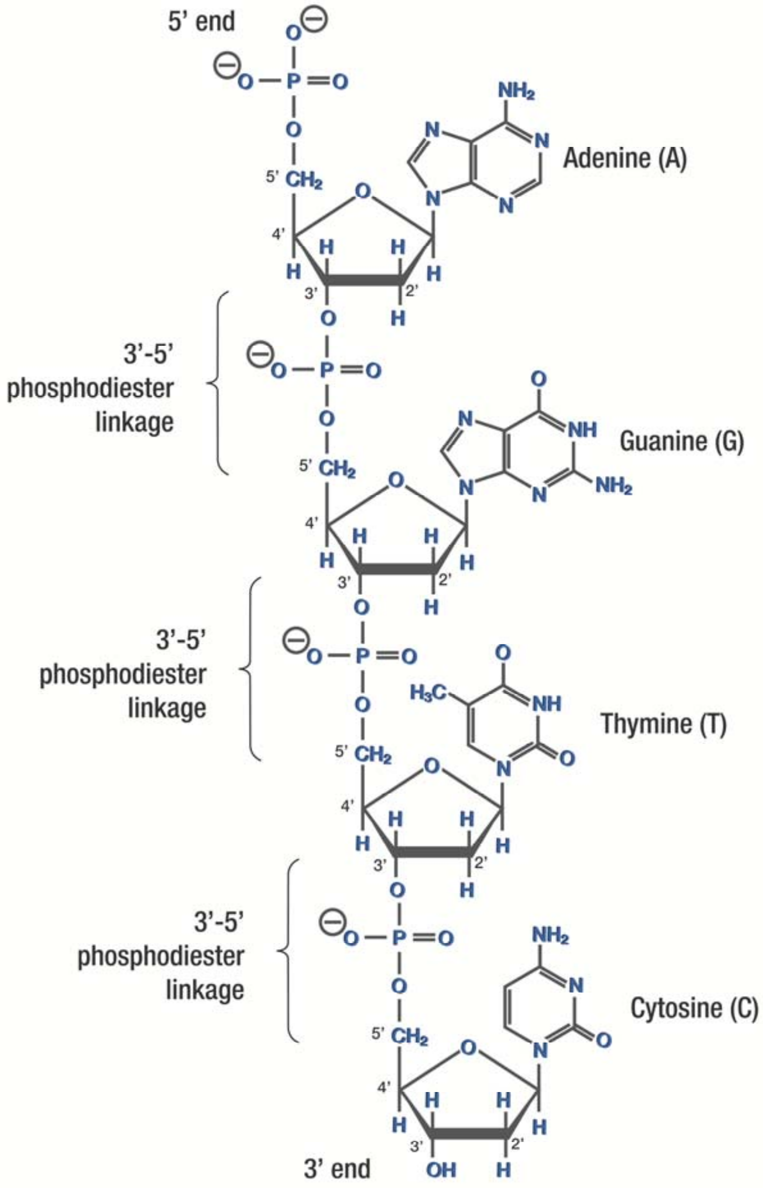

Figure 1. 3

Scheme of the binding between nucleotides via phosphodiester bonds where the 3' and 5' ends are shown. The exposed negatively charged backbone of the molecule is illustrated by the negative signs next to the Oxygen atoms in the phosphate groups. Adapted from Voet and Voet.[60]

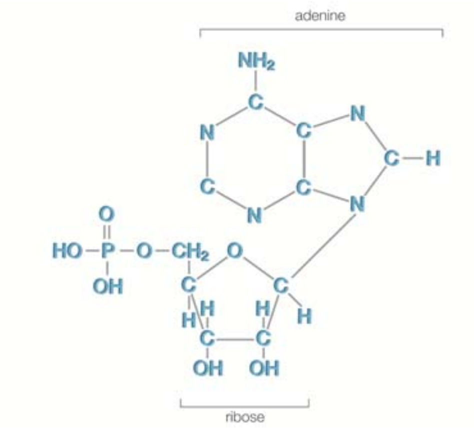

Figure 1. 4

Schematic chemistry of Adenosine monophosphate or AMP; an example of a nucleotide. The AMP nucleotide groups are; a sugar ribose, a phosphate group and an adenine base. Adapted from Voet and Voet.[60]

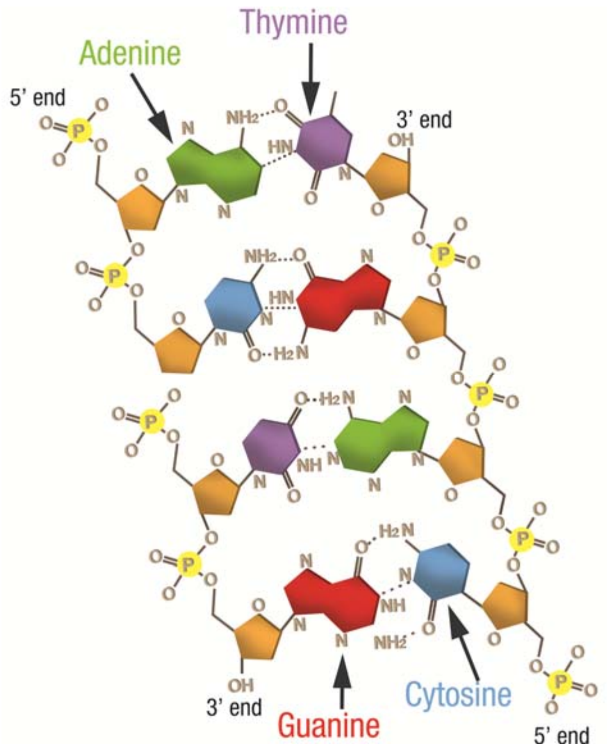

Figure 1. 5

Schematic showing the molecular pairing of two single stranded DNA molecules via hydrogen bonds (T-A and G-C bases). This is the model as described by Watson-Crick and gives rise to a double stranded molecule with strands of opposite polarity. Adapted from Brooker et al.[71]

Three of the main characteristics of DNA and nucleic acids in general are:

- Their high molecular recognition leading to high specificity via the unique base pairing interactions between complementary bases
- The distinct mechanical properties of both single and double stranded DNA.
- Their electrostatic properties that are partly due to their negatively charged backbone composed by phosphate groups.[60,69]

As in the case of proteins, these properties arise from both the characteristic molecular composition and spatial conformation of the molecules.

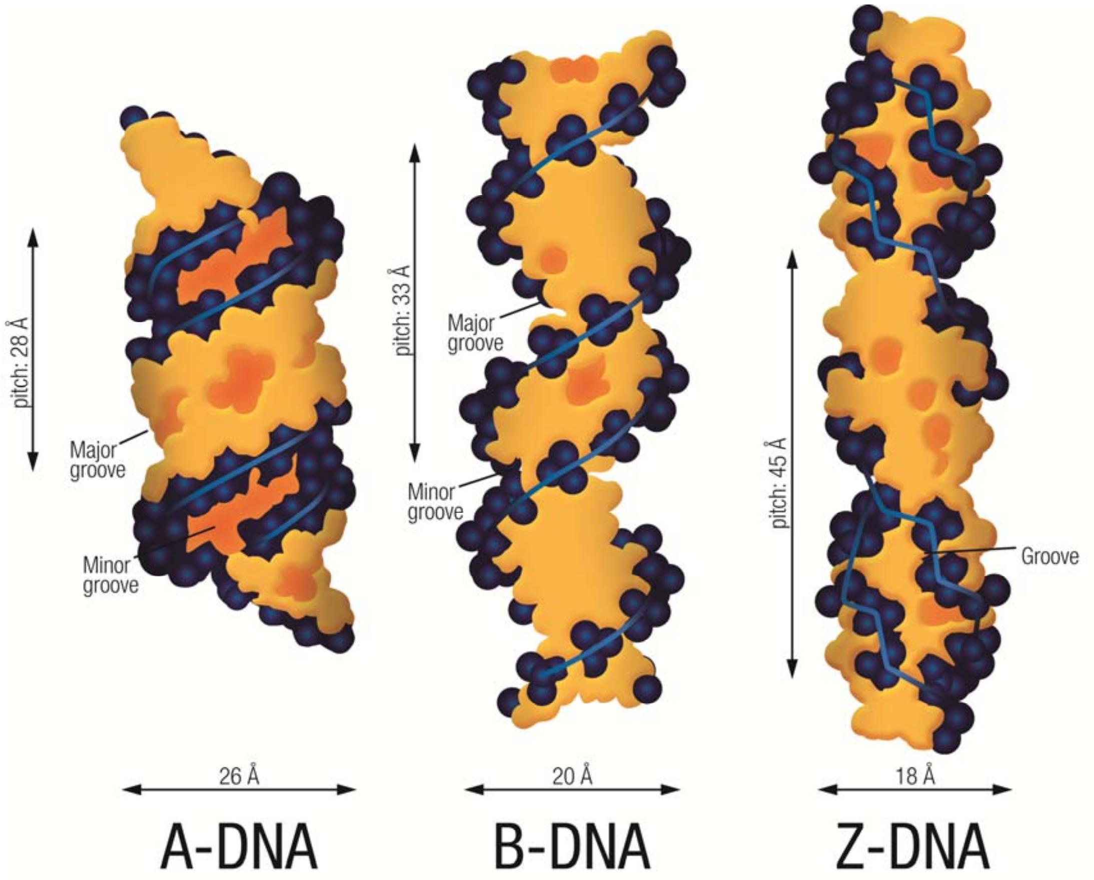

Figure 1. 6

Schematics of the conformations that dsDNA may adopt. The three structures are helical and their respective diameters, base pairs per helical turn and groove's structures are well known. See text for details. Adapted from Voet and Voet.[60]

The structure of DNA adopts a helical conformation that is normally divided into three biologically active families; A, B and Z (Fig. 1.6). The Watson-Crick model is based on B-DNA which is considered to be the ideal DNA structure and is the most abundant form found *in vivo*. From X-ray crystallography, it is found that this conformation is assumed when the relative humidity is 92% and the counterion present is an alkali metal. The B-DNA X-ray pattern is very similar to that of the DNA in intact sperm heads, and for that reason it is considered to be the native form of DNA.[60] The distance between base pairs is averaged to 3.3 Å.[64] Nevertheless, further analysis using X-ray diffraction of single crystals, has shown that this distance is dependent on local sequence variations and varies between 3.41 Å and 3.56 Å.[66]

In the B-form, the helix turns in a right handed fashion – one helical turn is completed almost every 10.5 bp/turn and the diameter is 2 nm.[60,64] The helical axis is slightly curved or writhed - this curvature is now understood to be an important feature for its biological functions.[66] The bases tilt at an angle of 6° and so are not completely perpendicular. In fact they appear to demonstrate a twist similar to that of the blades of a propeller as the two bases do not lie on the same plane. The spaces between the strands, called grooves are unequal due to the fact that the top and bottom edge of each pair are distinct from each other and the asymmetry of the deoxyribose residues. The major groove is wide and shallow and the minor groove narrow and deep (Fig. 1.6).

The A-conformation for DNA (A-DNA) has been identified at a relative humidity of 75%. It forms a wider and flatter version of B-DNA and it also has a right-handed helical turn (Fig. 1.6). A-DNA type structure is most common among double stranded RNA, or RNA/DNA hybrids and certain DNA sequences such as long chains of purines.[60] Its characteristic diameter is about 2.6 nm with 11 base pairs (bp) per helical turn and a pitch of 28 Å which results in an axial hole with a diameter of 6 Å. The base pairs are tilted at an angle of 20º with respect to the axis. Its major groove is deep and its minor one very shallow. A-DNA has only been observed *in vivo* in gram-positive bacteria while they form resistant though dormant cell types. These are called spores when they are under environmental stress and the process is known as sporulation. Small acid-soluble spore proteins (SASPs) are found in these spores in a high proportion (20%). B-DNA is induced to assume the A form in vitro by some of these SASPs.[60]

Under certain conditions and special sequences of bases, DNA may adopt the Z-form. This has been shown through X-ray crystallography in 1979 by Andrew Wang et al.[72] The most surprising feature of Z-DNA is that the helices are left handed. Wang and Rich proposed the name Z-DNA due to the characteristic zigzag pattern the sugar-phosphate backbone forms. It has a pitch of 45 Å and a diameter of 18 Å and 12 bp per helical turn.[60,69,72] Z-DNA does not have a major groove but forms one deep and narrow groove instead (Fig. 1.6). The successive base pairs are found to have alternating conformations and they are flipped at 180º relative to the ones in B-DNA. Thus, Z-DNA is considered to be a helix of dinucleotide pairs.[60,66] At the point where B-DNA transforms into Z-DNA, two B-Z junctions form where two base pairs of adenine and thymine are extruded. This disruption causes a right handed DNA to change to a left handed and vice versa. It is also possible that these junctions are sites for DNA modification.[65]

The existence of Z-DNA in nature has been a controversial issue. Nevertheless, some evidence suggests that it does exist *in vivo* in eukaryotes and prokaryotes.[65-66] It is has been suggested that Z-DNA is very unstable compared to B-DNA as it only appears briefly during transcription and then disappears. During this time its role is believed to be that of torsional strain relief while supercoiling takes place.[65,67] Some characteristics of these 3 conformations are given in Table 1.[60,66]

	B	**A**	**Z**
Direction of helix	Right handed	Right handed	Left handed
Diameter	20 Å	26 Å	18 Å
Base pairs per turn	10.5	11	12
Base tilt to the helix axis	6°	20°	7°
Major groove	Wide and deep	Narrow and deep	none
Minor groove	Narrow and deep	Wide and shallow	Narrow and deep
Phosphate group line	Smooth curve	Smooth curve	Zigzag pattern
Pitch	3.3 nm	2.8 nm	4.5 nm

Table 1.

Comparison of structural features of A, B and Z-DNA. Adapted from Bates and Maxwell and Voet.[60,66]

Chapter 2

2. Imaging single biomolecules with the AFM

2.1 Historical overview of dynamic AFM

2.1.1 From ambient to vacuum and liquid dAFM

The separation of the two main modes of dAFM, i.e. FM and AM, partly came about from the way in which the equation of motion of a perturbed driven harmonic oscillator with damping was initially[30-31] used as a force slope detector. This was the first description of a dAFM.[1,31] A Lorentzian response was assumed for both the unperturbed and the perturbed oscillator (Fig. 2.1). In short, the tip-sample force F_{ts} is added to the equation of a point mass on a spring (2.1) and a linearization is carried out.

$$m\frac{d^2z}{dt^2}+\frac{m\omega_0}{Q}\frac{dz}{dt}+kz=F_{ts}+F_0\cos\omega t \tag{2.1}$$

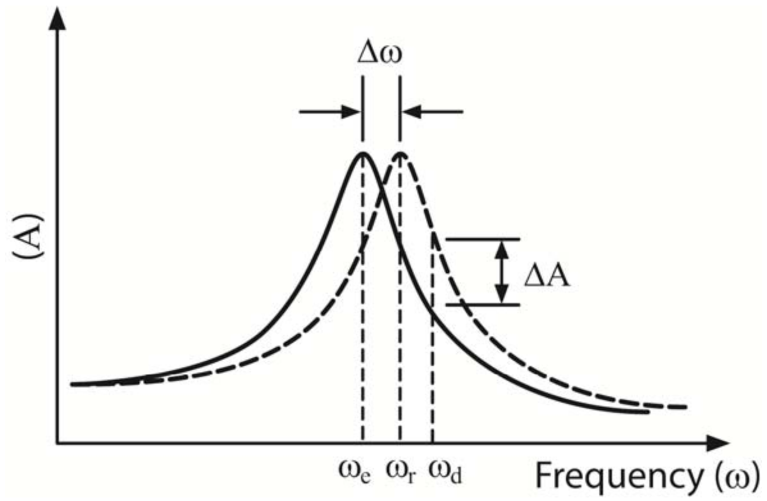

Figure 2. 1

Harmonic approximation. Scheme of the expected response of a forced harmonic oscillator with damping, where a small perturbation is caused by the tip-sample force F_{ts}. Here F_{ts} shifts the free resonant frequency ω_r of the oscillator to ω_e and this shifts the oscillation amplitude for a given drive frequency ω_d. Adapted from Garcia and Perez.[1]

In (2.1) F_{ts} is seen as the perturbation to the driven harmonic oscillator. When the tip is far from the surface ($A<<z_c$) this force does not affect the dynamics and typical simple harmonic motion[34] follows (Fig. 2.1). Then as the tip-sample distance decreases and the oscillation amplitude A approaches the separation ($A\sim z_c$), F_{ts} starts affecting the oscillation amplitude and the slope of the force gradient can be calculated as

$$\left(\frac{\partial F_{ts}}{\partial z}=k_{ts}\right)_{Z_{const}} \tag{2.2}$$

Thus, this method allows for a simple linearization of (2.1) where k_{ts} adds to the linear term on the left hand side. F_{ts} can be recovered by direct integration as

$$F_{ts} \approx \left(\frac{\partial F_{ts}}{\partial z} \Delta z_c \right)_{Z_{const}} \qquad \text{or} \qquad F_{ts} \approx k_{ts} \Delta z_c \tag{2.3}$$

Additionally, and importantly, the value of z_c can be held constant, i.e. constant separation z_{const}, and topography can be tracked. Thus, since ΔA (Fig. 2.1) can be directly and experimentally measured with the detection system (Fig. 1.1) only k_{ts} needs to be recovered with the use of a model. For the linear model, this is done by adding to the system an effective stiffness $k_{eff}=k-k_{ts}$ that gives

$$m\frac{d^2z}{dt^2} + \frac{m\omega_0}{Q}\frac{dz}{dt} + k_{eff}z = F_0 \cos \omega t \tag{2.4}$$

The above equation is simply the equation of motion of the free cantilever with the addition of the linearized perturbation due to F_{ts}; the effective stiffness is modified. The sign of the slope of the force defines whether the cantilever stiffens (repulsive force and/or positive slope) or becomes more compliant (attractive force and/or negative slope) as it interacts with the surface. In practice, perturbations occur once the tip is engaged on the surface by simply raster scanning it (i.e. during imaging). As the tip changes position, a new resonance curve follows. Nevertheless, the steady state is not reached at once and transients initially dominate (the transient decay and transient beat). [1] Since transients increase with increasing Q factor [34,73], AM and/or slope detection is unsuitable in environments such as UHV where Q can reach values of tens of thousands rather than hundreds typical of ambient and liquid imaging respectively. Thus, bandwidth is a limitation in terms of increasing sensitivity thorough increased Q in AM. In fact, Q affects the system's response to variations in its parameters in general.

The strength of this initial approach was that the analytic theory of driven harmonic oscillators could be used. The effective resonant frequency in the linearized approach gives (2.5).

$$\omega_e = \left[\omega_0^2 - \frac{k_{ts}}{m^*}\right]^{1/2} \tag{2.5}$$

In summary, a change in $\partial F_{ts} / \partial z$ produces a variation in resonant frequency $\Delta\omega = \omega_r - \omega_e$. This variation shifts the Lorentzian curve to the left for attractive forces, i.e. reducing the effective stiffness, and to the right for repulsive forces, i.e. increasing the effective stiffness. This effective resonance or shift in frequency is both interpreted and can be calculated by measuring ΔA directly (Fig. 2.1) to obtain ω_e. Then, since m^* in (2.5) is known ($m^* = k/(\omega_r)^2$), k_{ts} is recovered by Δz_c. These variations in A and ω further provide a mechanism for feedback signal in amplitude, i.e. ΔA, implying that the separation can be held constant and equal to z_{const} by monitoring A. The possibility of modulating the amplitude was introduced as soon as dAFM was implemented[31] but was later re-introduced consistently as AM or TM AFM.[32]

Very small amplitudes (i.e. A_0<1-5 nm) were being used with the initial set-up.[1,32] Additionally, the fact that the first detectable force gradient could be used to monitor a change in A, i.e. ΔA, implied that the long range van der Waals forces were responsible for the amplitude, phase and frequency shifts. Hence, the technique received the name non-contact or attractive AFM[30-31,36,38] and was first used to detect the slope of the tip-sample force, $\partial F_{ts} / \partial z$. As it turns out, there were two main problems with this initial set up.

1) First it would only allow for small amplitudes to be used (A_0<1-5 nm)[1,31-32] and these would imply that the tip could sometimes be trapped by the attractive capillary and van der Waals adhesion forces.[27,32,36]

2) Second, the sensitivity of the system was highly dependant on the Q of the system, i.e. the steeper the curve the higher the sensitivity. This implied that to increase sensitivity the Q factor had to be increased.[30,38]

In part, these two issues led to FM and AM becoming two separate disciplines. Both problems were solved by the FM community by moving to vacuum or UHV.[30] In vacuum the sensitivity of the slope in the resonant curve and/or Q increases. Increasing Q was not plausible for AM due to the increasing transients of the system as discussed above, whereas, in FM, high values of Q directly translated into higher sensitivity without hindering the bandwidth or speed.[1,30] In FM, this took care of the second problem above. Moving to vacuum also minimized problems of adhesion by simply getting rid of the capillary interaction.

In ambient conditions, the AM community introduced larger amplitudes (i.e. $1<A_0<100$ nm) as a solution to tip trapping;[32] larger amplitudes involve larger energies stored in the cantilever motion. This was the beginning of TM AFM and allowed a larger number of biomolecular and other soft samples to be imaged with high resolution.[13-14] The principle behind AM and topographic reconstruction is that a one to one relationship between amplitude reduction and separation typically exists (i.e. $\Delta A/\Delta z_c \rightarrow 1$).[41]

Additionally, while the move to liquid imaging was first carried out in the CM of operation[27], the use of lower Qs in liquid was used as an advantage in AM AFM by allowing rapid modulation.[28] In liquid AM imaging, the response in amplitude is fast, cantilever trapping is reduced (that is, the capillary force is avoided [36] and the van der Waals adhesion force reduced[27,36]) and imaging is carried out under physiologically environmental conditions.

A final note on harmonic approximations is appropriate. Briefly, it has been shown that harmonic approximations are only valid for $A \rightarrow 0$[74] or, in other words, when the force is a linear function of distance; this only occurs when the amplitude is zero or close to zero. Thus, the harmonic approximation is known as the small amplitude approximation and gives

$$\Delta f(z_c) = \frac{f_0}{2k} k_{ts}(z_c) \qquad \text{where it is assumed that } k_{ts} << k \tag{2.6}$$

The above approximation is used in FM AFM when using very small amplitudes and relatively stiff cantilevers and has proved successful even in more recent studies.[75] For larger amplitudes, there is the known large amplitude approximation[76] where the cantilever is assumed to be a weakly perturbed oscillator. Here, any loss in amplitude due to dissipation is compensated by the feedback system by keeping the oscillation amplitude constant. This allows one to use the reduced equation of motion where only the conservative forces are accounted for and simulations can be efficiently carried out.[1,74] This reduction also has the advantage that the Hamilton-Jacobi formalism can be used to find analytical approximations[76] from which a stability criterion expression can be deduced.[15,76] The validity of weakly perturbed oscillators in FM AFM has been shown by numerically solving the equation of motion[77-78], including the conservative case[74], and comparing it with the perturbation approach. Such justification shows why perturbed oscillators give accurate values for F_{ts} from the frequency shift and can be used to map the topography. The main outcome is that in FM AFM from conservative considerations analytical approaches using perturbation theory provide quantitative information. The implications are further discussed in the FM control section below.

2.1.2 AM and FM AFM

2.1.2.1 Force regimes, control of interactions and bandwidth

The major differences between nc and TM AFM are now obsolete. The first major difference was the range of oscillation amplitudes used in one and the other.[32,38] This would result in TM involving the tip undergoing motion through a non-linear potential during each cycle where attractive and repulsive interactions would occur as opposed to nc mode AFM. The second major difference was thought to be the highly defined and controlled interaction force in nc AFM as compared to TM AFM.[38] Nevertheless, as stated in section 1.2.3, small oscillation amplitudes are not exclusive of FM AFM experiments and nc can be achieved with AM AFM.[41] That is, true nc AM is possible and can lead to high resolution images of single biomolecules.[44] More generally, AM can be used to switch between nc, attractive and repulsive imaging.[41,79] In terms of the difference in the control of tip-sample forces, the above argument can also be used to show that in AM the force regime can be tuned, highly defined and controlled. For example, driving at the free resonant frequency and by decreasing A_0 to very small values (i.e. A_0<2-5 nm) the force is exclusively attractive and non-contact. Increasing A_0 to intermediate to high values (i.e. 10<A_0<50 nm) typically leads to attractive imaging where intermittent contact might occur. Further increasing A_0 leads to intermittent contact imaging. Of course, the range of parameters for which these regimes occur are not exclusively controlled by A_0 and the cantilever-sample stiffness, surface energy, tip radius and others contribute to the overall dynamics. Nevertheless, the above pattern, i.e. increasing A_0 and the sequence in which regimes are reached, is general.[79] Experimental examples of this behaviour are given in Chapter 3 with the help of Figs. 3.4 and 3.11.

Similar patterns should lead to imaging in the different regimes in FM. This is not surprising since there is a unique equation of motion for a given physical phenomenon such as a tip vibrating in the proximity of a surface.[80] Thus, the intrinsic physical characteristics of the tip-sample interaction in dAFM do not depend on the feedback mechanism. For example, bi-stability was first observed and reported when operating a Scanning Tunnelling Microscope (STM) and vibrating it over a surface.[81] The main outcome in this initial study was the observation that if during its oscillation, the tip experiences an attractive and repulsive interactions, bi-stability could result. The possibility to control whether imaging occurs in the attractive or the repulsive regime by driving above or below resonance respectively and the terminology of high and low amplitude states was also reported there. Thus, this initial work emphasised the generality of tip-sample interactions for a tip vibrating over a surface. Nevertheless, FM AFM has an advantage over AM AFM in that reliable quantitative information about the force in the interaction is possible thanks to the analytical expressions provided by perturbation theory. Moreover, the way in which the surface is approached in FM is different to AM since the free oscillation amplitude A_0 is typically varied in FM as the interaction forces start affecting the dynamics. This is discussed in more detail below under the sections AM and FM AFM control.

In summary, while the general routine above described to reach each regime in AM AFM could also be used in FM AFM, it is typically used only in AM AFM while the frequency shift is used in FM AFM instead to get the actual value of the force.

In terms of sensitivity, it has been shown from the beginning that the minimum frequency shifts that can be recorded in slope detectors are given by[31]

$$\delta(\Delta f) = \delta(f - f_0) = \sqrt{\frac{f_0 k_B T B}{4\pi k Q < A^2 >}} \tag{2.7}$$

where k_B is Boltzmann's constant, T is the temperature in degrees Kelvin, B is a measure of the scanning speed and an approximate measure of the number of pixels per second and $<A^2>$ is the mean square amplitude of oscillation. In AM AFM, B and Q are related since increasing Q leads to increasing values of B. Thus, (2.7) imposes limitations on the minimal δ (Δf) that can be detected. Moreover, increasing Q leads to larger values of B which result in slow AM responses since here B=f(Q). For example, typical scans of 10 nm by 10 nm recording a square image of 256 by 256 pixels implies a bandwidth of $B \approx 10^3$ Hz or pixels per second. This implies scanning at 40 nm/s which is a typical scan speed; increasing Q would increase sensitivity to ΔA but slow B in AM AFM or slope detector methods. For example, increasing Q from ambient (Q~10^2) to UHV values (i.e. Q~10^4) would slow B to B~1Hz; this implies each pixel would take times in the order of seconds to be obtained in slope detector methods.[1]

In FM the minimum detectable frequency shift is given by

$$\delta(\Delta f) = \delta(f - f_0) = \sqrt{\frac{f_0 k_B T B}{\pi k Q A^2}} \qquad (2.8)$$

The similarity between (2.7) and (2.8) is evident, however, since in FM B≠f(Q), Q can be increased without affecting the bandwidth in (2.8). Moreover, improvements in electronics in FM lead to ever increasing bandwidth with more sensitive frequency shift detectors.[82] For example, with the initial set-up[30] $\delta(\Delta f)$~0.01 Hz for f_0=50k Hz and B=75 Hz. More sophisticated electronics offer $\delta(\Delta f)$~0.005 Hz and B=500 Hz.[1]

2.1.2.2 AM control

Most of the work in this thesis relates to AM AFM and all the experimental data has been acquired in ambient AM AFM. Only the basics of the feedback system and the way in which the tip initially approaches the sample are discussed in this section, whereas more detailed information of AM AFM theory is given in Chapter 3.

In AM AFM, the free amplitude of the cantilever A_0 is first set in air by choosing an appropriate drive force F_D and drive frequency ω. At this point, the separation z_c is large relative to the free amplitude (z_c>>A_0). Then the engaging process consists of decreasing the separation z_c until the oscillation amplitude A starts to decay until it reaches the set-point amplitude A_{sp}. Typically, the A_{sp} is first overshot and the feedback system increases and/or decreases z_c until the steady state is reached. In order to follow the topography, the surface is then raster scanned in the xy-plane. Any topography will induce a variation in A to which a transient response will follow. The feedback system will then increase or decrease the z_c position in order to re-establish the prescribed value of A_{sp}. This produces further transients which can be partially controlled by the user with the integral and proportional gains. These transients impose the known limitations in the AM feedback system in terms of bandwidth. That is, the response of the system depends on the decay time τ, which is often described in terms of Q. It is in fact convenient to use harmonic oscillation standard theory and define τ as[34,73]

$$\tau = \frac{Q}{\omega_0} \tag{2.9}$$

where this is the standard Q for the free cantilever for which forced harmonic motion with linear damping applies. Then τ is the time for the energy stored in the cantilever to decrease by a factor of e due this linear damping; i.e. if the forced term does not act. In AM AFM, the time for the system to reach the steady state, i.e. for the transients to die out, can then be given in terms of τ as $C\tau$. In practical terms, the larger Q, the larger $C\tau$. Under liquid, where τ is small, $C\tau$ is small enough to allow rapid AM AFM where even fast AFM is possible. This technology has been recently used to provide visual evidence of molecular behaviour of myosin V walking in actin tracks.[29] In ambient AM AFM, τ is larger than in liquid but still sufficiently small to perform well across a wide variety of samples. Nevertheless, in UHV the values of τ and/or Cτ are so large that AM AFM is not practical since times of the order of seconds are required for the steady state to be reached.

2.1.2.3 FM control

In FM, the dynamics of the cantilever are those of a self-driven oscillator. In FM the driving force and frequency are typically not constant while scanning and are varied to follow the topography instead. More thoroughly, the source of contrast in FM is the resonant frequency shift. For example, for planar structures, small oscillation amplitudes can be used together with constant separations (i.e. the z-piezo or height is not used) to record shifts in frequency. Here the oscillation amplitude also varies with topography. This approach has recently led to resolving the chemical structure of a pentacene molecule in UHV[17] among others.[19] This mode of operation is a consequence of the evolution of FM AFM where oscillation and or frequency shifts might or might not be constant depending on the experiment. Nevertheless, the interpretation of contrast under non-constant oscillation amplitude is challenging due to the dependency of the frequency shift on both cantilever-sample separation and oscillation amplitude.

In the initial and most common mode of FM AFM operation, the amplification of the oscillation amplitude is achieved by means of a feedback loop that always drives the cantilever at its true resonant frequency while maintaining the oscillation amplitude constant. That is, as the sample is raster scanned, a shift in the resonant frequency follows (Δf). Then, the z-piezo tracks the sample keeping this shift constant by increasing or decreasing the cantilever separation accordingly. In this approach, topography images are maps of constant resonant frequency.[1]

The increase in sensitivity in FM led to atomic resolution of planar structures in UHV four years after the first description of FM AFM. The first samples to be atomically resolved were Silicon[83-84] and Indium Phosphide.[85] This high resolution was initially achieved with the use of relatively large oscillation amplitudes (A~30 nm) and stiff cantilevers (k~40 N/m).

A possible explanation for these results can be found by looking at (2.6) and noting that the sensitivity to the frequency shift increases with oscillation amplitude. Additionally, high resolution of IgG antibodies in AM AFM was achieved in a similar way by Thomson in 2005[86-87] by using relatively large values of A_0 and A_{sp}/A_0. Nevertheless, since these initial breakthroughs, small amplitudes have taken over in terms of high resolution imaging.[15,17,37] This is partly due to the increase in frequency shift[1] at smaller separations.

The equation of motion in FM is almost identical to the equation of motion used to understand AM AFM, with the only difference being that the driving force F_D can now vary in amplitude and frequency. When the cantilever is to be excited at its true resonant frequency throughout, the phase of the signal is shifted by the feedback system in order to excite at resonance and keeping the oscillation amplitude constant (i.e. a constant phase shift of 90 degrees between the driving force and the oscillation amplitude of the cantilever).

As stated, comparison between perturbation theory and simulations of the full equation of motion have been used to show that the non-linear potential, where attractive and repulsive forces may be felt by the tip during a whole oscillation cycle, is responsible for non-monotonic variations in frequency shift with separation.[78] Further important conclusions that follow from such comparisons are that perturbation models, where analytical expressions can be found, provide good models to the real phenomenon.[1,74,77] Furthermore, the conservative approach, as discussed in the sections above, is validated in this way in the constant amplitude FM AFM method since it shows that Δf is relatively independent of dissipation effects. Thus, the perturbation scheme first proposed by Giessibl[76] and/or similar approaches can be used to calculate Δf under these circumstances and feedback set-ups where, in general, Δf=f (k, f_0, A, F_{ts}). Further advances have been made in this direction by separating the contributions on Δf from the cantilever parameters and F_{ts}.[76,88]

In the constant drive amplitude FM AFM mode, the FM AFM equation of motion becomes identical to the equation of motion in AM AFM where the driving force is purely harmonic. This implies that the AM AFM theory fully applies. Still, several analytical studies have been carried out to interpret this FM AFM mode[1,89-90] (i.e. perturbation and variational principles). Since FM AFM is based on the true resonant frequency, the implication of the coexistence of several oscillation states has led to an ambiguity in the definition of resonant frequency in this case. Some have defined the true resonant frequency as that belonging to the lower amplitude branch or L-state but further emphasised the phenomenon of the reduction in A relative to A_0 in this state.[91] Briefly, F_D has to be increased relative to the free driving force to reach the set-point in amplitude (i.e. A). These and other difficulties involved in this approach are a consequence of the use of linear terminology and theory such as that of perturbation theory. Moreover, this provides further evidence of the true character of the non-linear phenomenon that the interaction of the tip with the surface represents and exemplifies that it cannot be fully understood or even described by linear approximations, perturbation theory and/or the respective terminology.

Nevertheless, since the constant drive amplitude mode represents a simplification of the varying excitation mode, it should be expected for the constant drive amplitude mode to also match the perturbation theory predictions closely. This follows from the evidence provided by the numerical integration of the full FM AFM model, its agreement with perturbation theory and the observed experimental stability in otherwise (predicted) unstable parameter regions. Thus, taking the above discussion into account, the conclusion is that FM might be able to influence the basins of attraction and make the system stable where AM cannot.[1] In summary, while the phenomenon of a tip interacting with a surface is general for any feedback mode, experimental outcomes might vary due to the additions to the equation of motion by the feedback system.[77] Hence the differences between AM and FM imaging can now be reduced to

1) the sensitivity[1] of the cantilever response to variations in oscillation amplitude and frequency respectively,
2) the dependencies and requirements of each feedback method on the environment or damping, i.e. high or relatively high damping in AM and low damping in FM and
3) the way in which the cantilever is driven.

In FM it is possible to control the oscillation amplitude by increasing/decreasing the drive force. In this way, the energy dissipated in the tip-sample interaction per cycle is compensated with the drive force and the motion can be treated as a conservative system. The variations in the drive force are interpreted as dissipation maps. In AM

AFM the requirement to drive at a constant amplitude results in a complex interplay of energy dissipation, separation and force affecting the amplitude reduction.

2.2 Imaging biomolecules in ambient AM AFM

2.2.1 Biomolecular imaging in AFM

Historically, AM AFM has been the main AFM technique applied to biological systems since its invention.[1,25] The first image of single DNA molecules with a Scanning Probe Microscope (SPM) were obtained by Binnig et al.[92] in 1984 with an STM before the AFM was invented.[14] Since that time, the AFM has been used widely to study biomolecular samples[12,14]. Since the AFM does not require a conducting support surface for the molecules, the interaction of molecules like DNA and proteins to the support can be tuned and thereby strengthened to avoid molecular motion under the AFM tip.[14,93] Thus, with the appearance of AFM, the competition to image soft matter was fierce in the community[26] and the advent of liquid imaging was seen as a key advance for biological applications.[27-28]

The difficulties involved with interpretation and reproducibility in AFM and SPM are discussed everywhere in the literature and are obvious from the development of the field. For example, some stated that despite stability issues, single nucleotides could be resolved in the early days.[14] On the other hand, by looking at the images now, it is apparent that large amounts of noise in the background typically impede sufficient clarity. Other images were soon published where the right-handed helix of double-stranded DNA were thought to be clearly resolved with the STM at a resolution that appeared close to atomic.[94] Soon after, questions were raised about the validity of these data after images of the underlying support surface of graphite (HOPG) gave similar apparently helical structures of the correct dimensions at the interfaces of the layered material (i.e. steps).[95] STM could not regularly retain atomic scale resolution on biological molecular adsorbates, such as DNA, due to tip induced molecular movement and the intrinsic tunnelling mechanism where the current flows through a surrounding sheath of water.[96-97] More evidence of the difficulties of interpreting the tip-sample interaction and sources of contrast in AFM are provided by the fact that while the contrast in phase imaging has long been recognized as the energy dissipated per cycle[48,98], little advance in terms of the separation in interactions has been made since.[49-50] From this, it follows that care needs to be taken when interpreting data and/or the validity of a given sample preparation method and/or AFM operation mode to achieve high resolution of biomolecules reproducibly.

Since the first imaging of single DNA molecules by AFM [14,99] there have been a handful of studies that have reported resolution approaching that of the double-helix.[14,100-102] Nevertheless, these techniques typically involve UHV imaging[101], require special surface treatment[100,103] and the use of very sharp tips[102] (R<2-3 nm) or a combination of these. Moreover, future AFM advances require not only enough resolution to resolve the secondary structure sporadically, but rather, consistently and reproducibly. It follows that some groups overestimate sample preparation and/or methods and underestimate the importance of the cantilever dynamics, while others underestimate sample preparation and/or methods and overestimate cantilever dynamics. As usual, it should be expected that a contribution from both approaches will lead to optimised results. For example, resolving the pitch of the DNA helix has proved difficult even when using sharp probes like carbon nanotube modified tips[104], but little relevance was given to the understanding of the dynamics in this work, and most relevance was given to the modified surface and/or tip. In this thesis, a combination of tip sharpness and cantilever dynamics is shown to greatly enhance reproducibility. In particular, Chapter 4 shows that maximizing resolution would be impossible even with the use of ultra sharp-tips (R<5 nm) in air in the nc regime, attractive and/or the standard repulsive regime. A new method is presented there that has the advantage of providing high resolution, low wear and small forces.

2.2.2 Hydration and substrate in ambient AFM

In AFM, samples, such as biomolecules, must usually be supported on a substrate. Typical substrates are Muscovite mica, glass and Silicon Oxide.[14] For example, glass can be used to image large biological samples such as cells. In biomolecular imaging, the support surface of choice is typically mica. Mica displays an atomically flat surface over large distances (microns to millimetres)[105] on which molecules can be easily detected by the AFM tip.[13-14,106-107] This is due to the perfect basal cleavage of mica and is a consequence of its atomic arrangement (Fig. 2.2). Nevertheless, this choice was not immediately obvious and it took some experimentation to find appropriate conditions and the use of counterions for optimum binding.[107-108]

Additionally, the perfect atomic flatness of mica is typically disturbed by the presence of potassium carbonate crystallites and other salts on its surface.[18,105] Another advantage in using mica as a substrate is that its chemical structure is well known. This is important in AFM experiments since, as molecules are deposited onto the surface, these interact with it through electromagnetic forces.[109] These forces form a complex interplay between physisorption and chemisorption processes depending on the chemical structure of the deposited molecule and the chemical structure and thermodynamic state of the surface. Physisorption, represents weak interaction process where the adsorbates and surfaces interact via mutually induced dipole moments. The forces are fundamentally electromagnetic in nature and represent the long range van der Waals force.[8,109] Chemisorption, represents the ionic and covalent interactions between the adsorbates and surfaces.[8,60]

The perfect chemical structure of Muscovite mica is shown in Fig. 2.2. The word perfect is used here implying that on cleavage, impurities will also be present on the surface whereas no imperfections are shown here.[18,110] The figure shows how cleavage typically occurs via the layer of potassium ions on top of an oxygen network. These are the weakest bonds in Muscovite mica and therefore the most likely to break when peeled. The oxygen network provides a slight negative charge on its surface. Nevertheless, on cleavage, half the Potassium ions remain on each surface on average.[111]

The availability of hydroxyl (-OH) groups positioned slightly below the surface is typically quoted[106] to act as the obvious group for surface binding between biomolecules and mica. The spacing between the surface and the hydroxyl groups in mica is of approximately 0.5 nm below the surface. It is also believed that the Potassium ions bridge between hydroxyl groups in adjacent layers. Nevertheless, the bond to the OH groups is dubious since these already bind to the Al atoms (Fig. 2.2) and are, in any case, too far away from the surface. Thus, there is a shielding effect by the SiO_2 layer between the OH and the K^+ layers. There are several other issues involving the -OH groups in relation to the hypothesis of biomolecules binding to mica. For example, it is known that when the Oxygen atom of an Hydroxyl group is bound to a larger molecule, the Hydroxyl group can act as a functional group and as such, it is responsible for certain characteristic chemical reactions.[112-114] This might have partly induced the above hypothesis. Furthermore, the outermost surface is composed of only Oxygen atoms (12 per Potassium counting top and bottom layers) and not by OH groups.

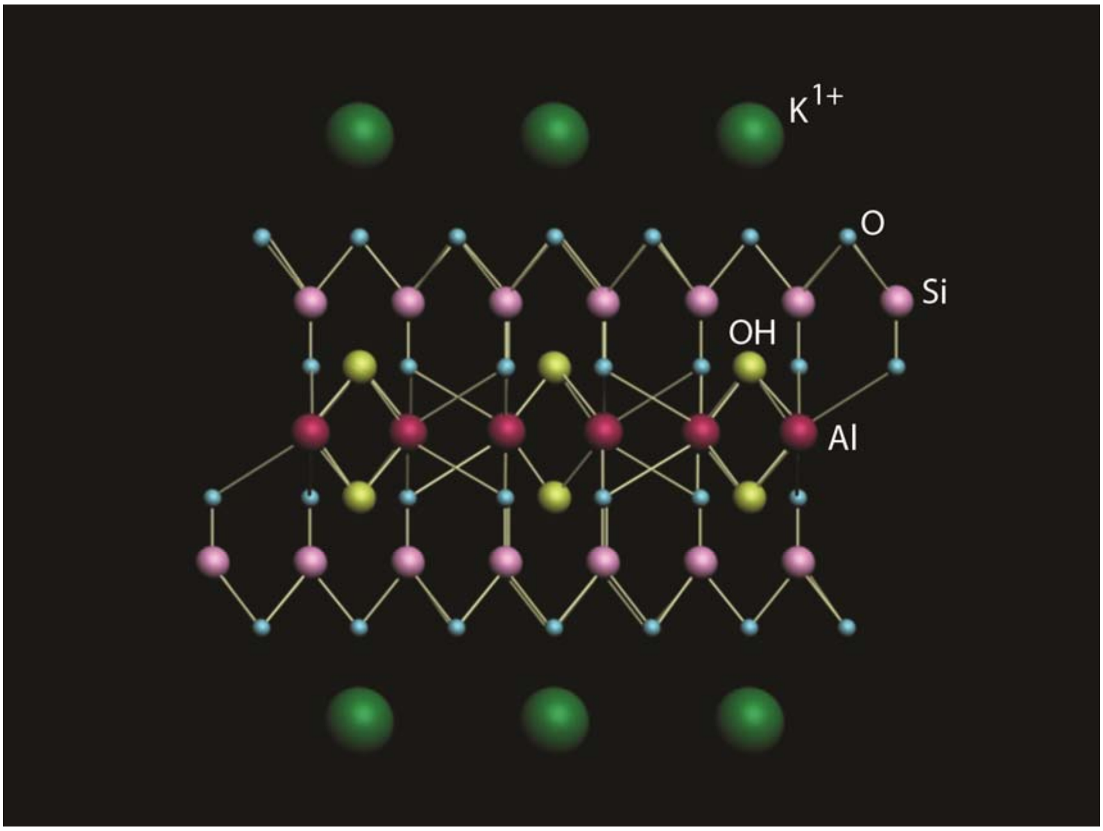

Figure 2. 2

Diagram of the crystal structure of Muscovite mica. Adapted from Richardson[111] See text for details.

As stated, after peeling, half of the K^+ ions are removed from each surface on average and the Oxygen network is exposed underneath. The exposed Oxygen atoms on the surface and water molecules in the liquid state form dynamic hydrogen bonds with each other. Other polar molecules or ions can also bind to the surface depending on the strength of the ions, the thermal energy and whether in liquid or solid state. In particular, the presence of surface ions and salt formation is a characteristic of mica surfaces in ambient conditions.[18,110,115] If there were no salt, polar molecules and/or water (i.e. RH=0%) the surplus charge left on the surface oxygen atoms after removal of half the K+ ions, would most likely redistribute onto the tetrahedral layer of SiO_2. Thus, overall, this is a complex situation where several reactions can occur. Still, from the chemical structure of mica (Fig. 2.2) something can be said in terms of local charge. Before cleavage, each Potassium ion has 12 oxygen atoms weakly binding to it and those have a -1/12 charge each in order to balance the positive charge of the ion atom. Thus, the ions make 12 bonds with the 12 oxygen atoms surrounding each one of them. Nevertheless, these bonds should not be regarded as truly ionic. Thus, on cleavage, the surface is left with each oxygen atom having 1/12 of surplus negative charge together with half the number of potassium atoms.

This makes the exposed surface hydrophilic. The hydrophilicity of mica implies that, even in ambient conditions, there is sufficient humidity, that a thin, nanometre thick water layer is present on the surface[115] that maintains the biomolecules in a hydrated state.[87,116] The above discussion shows that the mechanism for the binding between biomolecules and the surface of mica is not straight forward but occurs through non-covalent interactions such as van der Waals and other electrostatic or ionic interactions. In fact, the use of cations or counterions to pre-treat the mica surface before deposition is common.[106-107,117] Briefly, molecules are typically deposited from a buffer solution through incubation on the mica surface, before rinsing and drying with water.[109,117] But molecular strain[117] and the binding strength highly depends on counterion treatment.[107,109] Typical cations for biomolecular binding to mica are Ni^{2+} and Mg^{2+}.[14] Recalling from the above discussion the role of the OH groups in mica, some believe that covalent binding is stronger with Ni^{2+} because its size is small and it more readily fits into the hole just above the OH groups.[106] Nevertheless, from the above, it is more likely that the Ni^{2+} cations displace and bind to K^+ sites. A scheme of how Ni^{2+} cations could occupy the top of the surface sometimes displacing the K^+ cations is shown in Fig. 2.3. The scheme shows the former perfectly sitting in the sites of the latter, nevertheless, mobility and irregularities should be expected for the reasons above described. Empirical evidence shows that pre-treating the mica surface with cations does improve molecular binding.[107-108] With this surface distribution, and recalling that DNA presents a negative backbone due to the phosphate groups linked by ester bonds, polar molecules such as DNA would readily anchor to the other side of the Ni^{2+} cations. The general argument is that the position of the cations on the mica surface is thermodynamically and/or enthalpically favourable due to the surplus charge of the exposed oxygen atoms as above discussed. However, in the presence of polar molecules, such as water molecules, the strength in the binding should be appreciably decreased due to screening effects. This would allow biomolecules adsorbed to the surface to either release strain energy through conformational changes and/or freely move on it. There are several arguments supporting this interpretation.

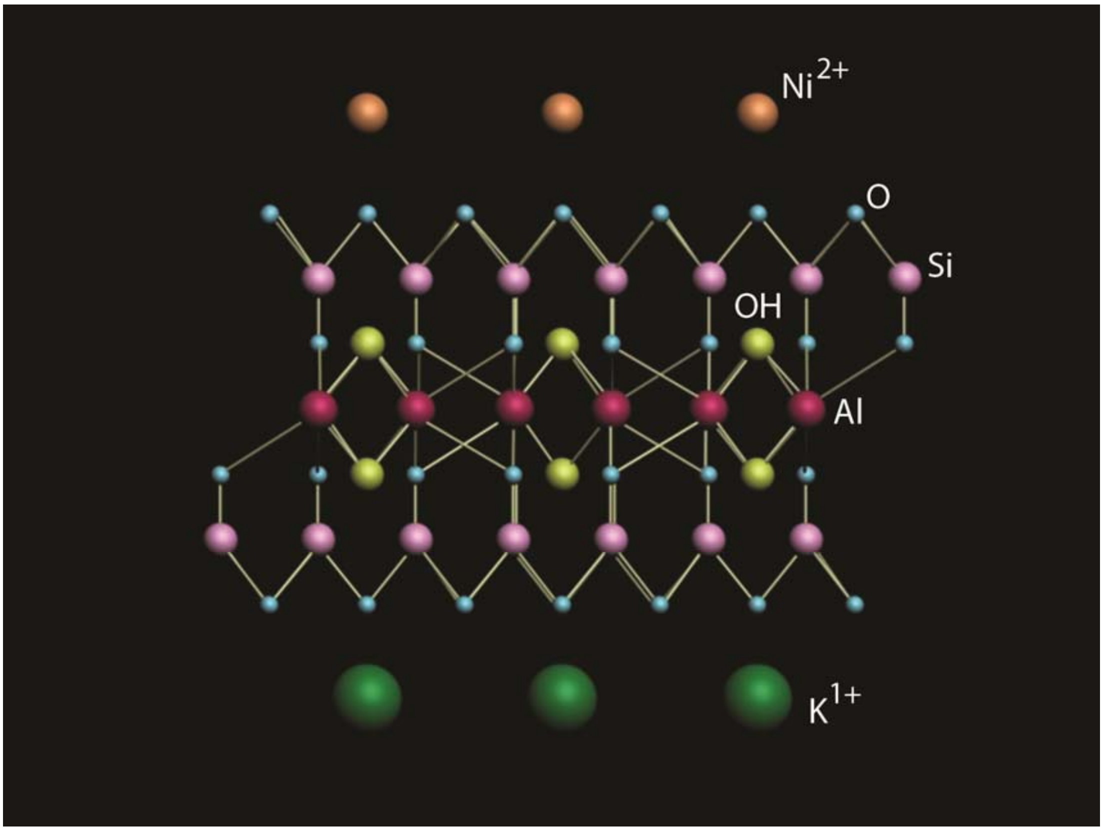

Figure 2. 3

Diagram of the crystal structure of Muscovite mica after being pre-treated with Ni^{2+} cations. In this scheme, the distribution shows only Ni^{2+} cations but, as discussed in the main text, some K^+ cations and salts should also be present. Furthermore the XII site of K^+ should not be expected to be an equilibrium site for Ni^{2+} cations, thus, some position asymmetry and mobility should be expected. Adapted from Richardson[111]

First, conformational changes on DNA molecules have been recently reported at very high humidity.[117] Second, Thomson achieved high resolution images of IgG antibodies by sufficiently decreasing the relative humidity which might have helped more readily immobilise the molecules.[87] Moreover, by sufficiently increasingly the relative humidity, linear dsDNA molecules can be induced to move with the AFM tip (data not shown).

Finally, the above binding mechanisms represent relatively weak interaction between the molecules and the surface. This implies that dynamic AFM methods are essential (unless working in a very dry environment). In conclusion, dAFM, and in particular, AM AFM is the ideal choice for biomolecular imaging[1,28] since frictional forces are minimized[32-33] and molecules remain hydrated.[27,117]

2.2 Summary

Reliably and reproducibly resolving the secondary structure of isolated biomolecules in near-native conformations and without averaging is a crucial step for understanding the heterogeneity of biomolecular structure in complex systems. This would expand the possibilities of AFM to more in depth studies of replication, transcription, translation and DNA-protein interactions that are not possible at the moment.[10,13-14,25,57,102] Thus, these results would affect fields such as molecular recognition, gene expression, structural molecular biology and bionanotechnology.[59] Finally, it should be emphasised that one of the main advantages of the AFM compared to other high resolution techniques such as Electron Microscopy (EM), STM, Nuclear Magnetic Resonance (NMR) and Crystallography is that processes and/or molecular structure and molecular interactions can be studied at the single molecule level under biocompatible conditions. That is, the AFM allows the heterogeneity of biological structure and function to be probed at the single molecule level without the need of crystallizing, submitting the samples to high energy probing and/or introducing contrast agents which might compromise structure.

Chapter 3

3. Fundamentals of cantilever dynamics

3.1 Cantilever models

3.1.1 The point mass model and ambient dAFM

It is clear from the nature of the tip-surface potential that the addition of the tip-sample interaction to the equation of motion introduces the appearance of non-linear effects in the dynamics of the cantilever. Since the cantilever-tip ensemble forms the system that vibrates over the surface, a thorough understanding of the full phenomenon of a cantilever-tip vibrating over a surface involves solving the equation of motion of such a three dimensional object. Still, a simple model consisting of a point mass on a spring (2.1) or (3.1) has been shown to reproduce with considerable accuracy some of the main phenomena in dAFM[41-42,45,118]; equation (2.1) is rewritten here as (3.1) for convenience since it is the equation relevant for this section. More thoroughly, it has been shown that in ambient conditions where the Quality factor is high, Q>100, the fundamental frequency carries most of the information [5,21,48] and (3.1) is a good approximation to the phenomenon.

A major disadvantage of working with the full non-linear equation is the difficulty of solving it analytically and, thus, the necessity to ultimately resulting to numerical integration.[1]

$$m\frac{d^2z}{dt^2}+\frac{m\omega_0}{Q}\frac{dz}{dt}+kz=F_{ts}+F_0\cos\omega t \qquad (3.1)$$

The equation of motion in (3.1) includes the effective mass of the cantilever $m=k/(\omega_0)^2$, the string constant of the cantilever k, the natural angular frequency ω_0, the *Q* factor and the drive force $F_0\cos\omega t$. The theory of AM AFM as predicted by (3.1) is described in the next sections.

3.1.2 Continuous models

Continuous models are relevant when the higher modes of the cantilever are excited and significantly contribute to the overall dynamics.[1,35,53] This is the case when using compliant cantilevers, relatively large drive amplitudes[5] or working in liquid.[119-120] Compliant cantilevers imply that higher modes and harmonics require less energy to be excited whereas higher drive amplitudes imply larger forces in the interaction that more readily excite harmonics and/or higher modes.[5,21,35] Moreover, in liquid the *Q* factor is significantly reduced compared to ambient and UHV and can take values of 10 or less. Thus, it is primarily in liquid that the excitation of higher harmonics and the contributions of higher modes need to be considered.[121]

This approach in liquid has recently been used to extract compositional mapping.[24] Furthermore, compliant cantilevers have typically been used when imaging under liquid, i.e. k<0.1-1 N/m[13,24,28], whereas less compliant cantilevers, k~2 N/m, are currently being used in ambient conditions to study harmonic and second mode excitation.[22,52] These are sometimes known as force modulation levers and are used in pulsed force modes.

The equation of motion of a cantilever beam from the Timoshenko beam theory[35,52] (3.2) can be used as an approximation of the continuous phenomenon as a one dimensional object. This equation has a long history in the theory of elasticity[55] and takes into account rotational inertia; note the use of the moment of inertia *I* in the equation. The equation accounts for lateral loads, rotational inertia and shear strain; the Euler-Bernoulli beam equation is a simplified form which does not take shear strain into account, thus b_1 is zero in (3.2) in this simplified equation; b_0 is the viscous term accounting for the motion in the medium.

$$EI\frac{\delta^4}{\delta x^4}\left[v(x,t)+b_1\frac{\delta v(x,t)}{\delta t}\right]+m(x)\frac{\delta^2 v(x,t)}{\delta t^2}+b_0 m(x)\frac{\partial v(x,t)}{\partial t}=F(x,t) \qquad (3.2)$$

The effects of shear strain are contained in (3.1) in the viscous term. The tip-sample forces are accounted for by the term *F(x,t)*, which expresses the force per unit length acting on it.[1] Finally, *E* is the elastic modulus of the beam, *v(x,t)* expresses the deflection at any given point *x* of the beam at time *t* and m is the mass per unit length of the beam. Eqn. (3.2) is typically used to study the relevance of higher modes.[1,5,35] With all, and even though the equation is already relatively complex, the tip is still assumed to be a massless and dimensionless object.

3.2 Tip-surface forces

3.2.1 The origin of intermolecular forces

The forces acting between the tip and the sample (F_{ts}) are those of interest to AFM whereas the forces damping the oscillation of the cantilever due to the viscosity of the medium (second term in (3.1) and terms b_0 in (3.2)) or viscosity of the cantilever (term b_1 in (3.2)) are background forces which do not provide information about the sample. Thus, here, forces mean tip-sample forces unless otherwise stated.

In AFM all forces are fundamentally electromagnetic in nature.[1] Nevertheless, differentiating between them is possible in terms of distance dependencies. This allows separating the effects of each force on the basis of the distance in which they become relevant. Thus, F_{ts} is in fact a convolution of several forces.[1,8,122] The most relevant interactions in AFM are the long range and attractive van der Waals, the Pauli exclusion, electrostatic and ionic attraction and repulsion, the capillary forces (in ambient conditions) and those of adhesion.[1] While other forces might be present, these are typically set-up dependent. For example, hydrodynamic and other forces are relevant only when imaging in fluid.[36,120-121,123] A compromise is typically made between complexity and computational time where intermediate approaches with realistic long and short range expressions are normally preferred.[41,124] The conservative long and short range forces that have been used in this work are presented below.

3.2.2 Long range interactions

While other forces might or might not be present and/or significantly contribute to F_{ts}, the van der Waals (vdW) are ever present in all environments and thus, always adds a significant contribution.[1-2,8] The resultant of the van der Waals can be represented in AFM as a volume integral of the atomic intermolecular forces as first derived by Hamaker.[2] Moreover the simplified equation (3.3) for small separations ($d<<R$) is typically used.[41,45,118]

$$F_{ts}(z_c, z) = -\frac{HR}{6d^2} \tag{3.3}$$

where, from Fig.3.1 it is clear that

$$d = z_c + z \tag{3.4}$$

Here, H is the Hamaker constant, R the radius of the tip modelled as a sphere, z_c the rest tip-surface separation, z the instantaneous tip position and d the instantaneous tip-surface distance (Fig.3.1).

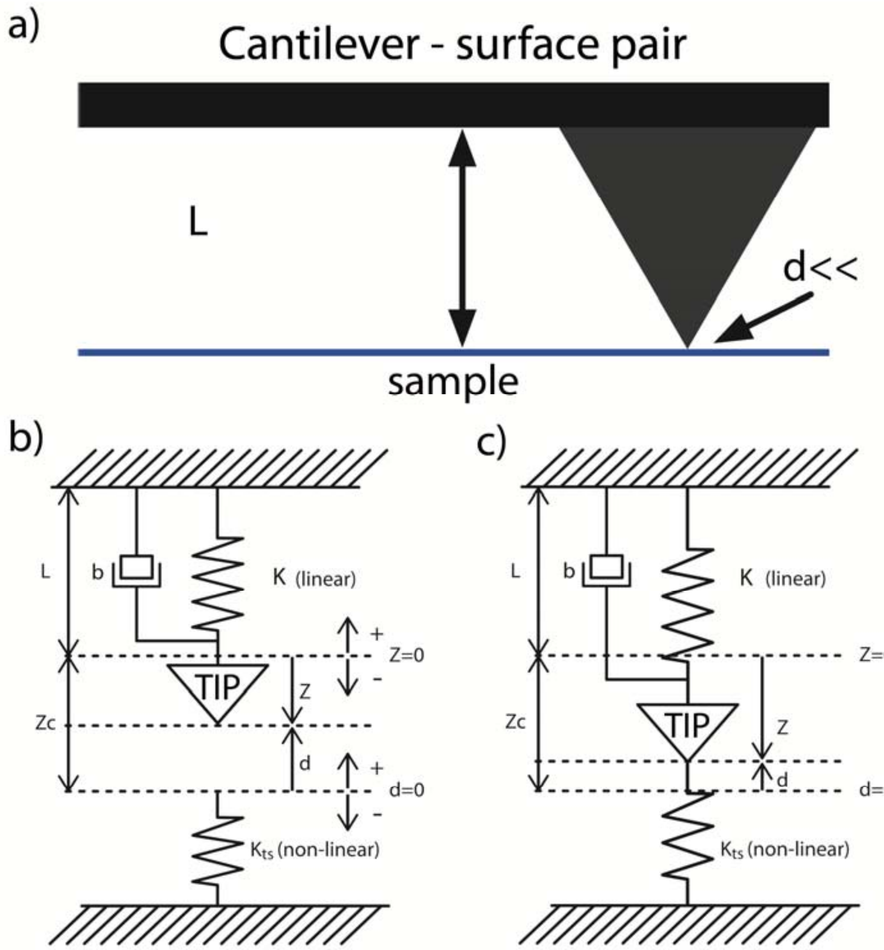

Figure 3. 1

a) Scheme of an AFM cantilever in the proximity of a surface. *L* is the equilibrium separation for the unperturbed cantilever and it is much larger (*L*~1-10μm) than typical tip-sample distances (*d*~1-10-100nm) when the tip is interacting with the surface. Thus, this parameter, i.e. *L*, is typically not used in AFM theory and the more physically significant concept of tip-surface equilibrium separation for the unperturbed cantilever z_c is used instead. The scheme of the tip and the cantilever modelled as a point mass on a spring are shown in b) and c). In a) the tip is not interacting elastically with the surface and $d>>a_0$; a_0 is an intermolecular distance below which contact is assumed to take place. Here *k* is the stiffness of the cantilever and it is typically a highly linear term, $z=0$ coincides for the equilibrium position of the tip for the unperturbed cantilever, *z* is the instantaneous position of the tip measured from $z=0$, $d= z_c+z$, $d=0$ is the reference position of the surface and k_{ts} conceptually implies some elastic interaction with the surface which might or might not occur before mechanical contact. This last term is typically a strong non-linear component. Inelastic tip-sample interactions might also occur but these have not been included in the scheme. In c) a scheme of the tip elastically interacting with the surface is shown. The viscosity with coefficient *b* in the schemes in b) and c) is typically modelled as a linear viscosity due to the damping or the cantilever and not the surface. This term is the physical origin of the (unperturbed) quality factor *Q* in dynamic AFM. This value of *Q* is an important experimental parameter and can easily be obtained experimentally.

3.2.3 Short range interactions

The short range repulsive interactions arise, from a fundamental point of view, as a consequence of the Pauli exclusion principle.[1,8] Nevertheless, in AFM the modelling of the repulsion between the tip and the surface typically considers the elastic deformation of the shapes of the interacting surfaces, which come from continuum elasticity theories instead of more fundamental laws. Two of the most common models are the Derjaguin approximation, or the Derjaguin-Muller-Toporov[125] (DMT) model and the Johnson-Kendall-Roberts[126] (JKR) model. These have been shown to be limiting cases[127] of the phenomenon where, in the transition regime, the Maugis–Dugdale[128] (MD) theory applies.

Most of the work in this thesis has been carried out using the DMT model, which applies when relatively small curvatures and intermediately compliant to stiff samples are used. More thoroughly, a dimensionless parameter λ (3.5) is defined[127-128] where the DMT model applies when $\lambda<0.1$ and the JKR model applies when $\lambda>5$. Intermediate values correspond to the transition or MD regime.

$$\lambda = 2\sigma_0 \left(\frac{R}{\pi E^2 \gamma} \right)^{1/3} \tag{3.5}$$

The above can also be written in terms of the equilibrium separation of the surfaces z_{eq} where, if a typical separation in the range of 0.3-0.5 nm[129] is taken, λ can be easily calculated (3.6).

$$\lambda = \left(\frac{R\gamma^2}{E^2 z_{eq}^3} \right)^{1/3} \tag{3.6}$$

There are several reasons that have led to the use of DMT model and the sphere infinite surface force for the long range forces (3.3). First, relatively sharp tips have been used (i.e. R<20-30 nm). In particular, ultra-sharp tips (R<5 nm) are required for high resolution imaging and these are obviously preferred (see Chapter 4). Mica's effective elastic modulus in the direction normal to the cleavage plane is slightly higher than 10 GPa.[130] These values of R and E imply a low value of λ according to (3.6). Moreover, it has been found (see Chapters 4-6) that using the DMT model, and provided the water layer on the surface and the capillary force is also accounted for, the predictions closely match the experimental results. Furthermore, implementing the MD and/or the JKR models is tedious since the relationships between indentation, contact area and force are implicit and greatly increase the computational time in simulations.[128,131-132] Thus, in the contact region the force is taken as

$$F_{ts}(DMT,d) = F_{ts,a}(a_0) + \frac{4}{3}E^* \sqrt{R(a_0 - d)^3} \qquad d < a_0 \tag{3.7}$$

where the first term on the right is the adhesion force and the last term is the repulsive force as predicted by the DMT theory. Furthermore, a_0 is an intermolecular distance used to avoid divergence[41] and implies that contact occurs at a cantilever surface separation a_0. A value of 0.165 nm can be taken for this constant.[8]

3.3 Fundamentals of AM AFM

3.3.1 Overview

The dynamics of the oscillating micro-cantilever for AM AFM operating in air are well understood theoretically but the experimental outcomes are still emerging.[44-45,79,87,133-136] Furthermore, there are parameter regions, such as small oscillation amplitudes (i.e. A_{sp}<1 nm), which are particularly challenging due to viscoelasticity and capillary interactions for which new and useful phenomena can appear (see Chapters 4 and 6). In the sub-sections below, the predictions of the point mass model (3.1), where the London dispersion and the contact forces as described by (3.3) and (3.7) respectively have been accounted for, are discussed and used to interpret experimental outcomes except otherwise stated. This is a conservative model where inelastic interactions are not implemented. Nevertheless, section 3.3 shows that this model can be used as a pre-requisite to understand energy dissipation. The energy dissipated in the tip-sample interaction is discussed there.

The conservative potential already predicts the appearance of the two common oscillation states in dAFM.[80] These are typically termed the L and H-states standing for Low and High amplitude branch respectively. The physical significance of the coexistence of these two states of oscillation is that for a given tip-surface separation z_c one or the other might be reached depending on both operational parameters and cantilever-surface properties.[79] In this thesis another previously unreported state, i.e. the A-state, is discussed.[137] This is a state which more readily appears, but not exclusively, when there are water interactions. An example of the coexistence of the three states and their relationship with the tip-surface potential is given in Fig. 3.2

below. From the figure, it is clear that the A-state has the least amplitude for a given separation, the H-state the most amplitude and the L-state falls in between. The A-state typically involves only attractive interactions whereas the L and, mostly, the H-state might involve intermittent contact. Thus, the net force per cycle is attractive in the A-state and, in the L and H-states might or might not be net attractive. Typically however, the L-state coincides with an attractive force regime, i.e. the force is net attractive in this state, whereas the H-state coincides with a repulsive force regime, i.e. the force is net repulsive in this state. The details of the L and H-states are given in this chapter whereas the details of the A-state are given in Chapter 6.

Overall, the motion of the cantilever might depend on the environment, the electronic feedback, the mechanical, chemical and geometrical properties of the cantilever-tip in use and the sample under study and, finally, on the operational parameters of the AFM.[1,35,42] Arguably, the aim of AM AFM imaging is to deconvolve the above contributions to the cantilever dynamics in order to obtain information about the sample. AM AFM has already proved to be a powerful tool for sample characterization allowing high resolution images of important biological systems.[1,13-14,25,28,44,86] In this section, double-stranded DNA on mica is used as a model biomolecular system to investigate the connection between standard AM AFM theory and experiment. Demonstration that the switching between the two cantilever oscillation states is stochastic in nature is confirmed, and can be induced by topographical anomalies on the surface. Accessing one of the two standard and known attractors, i.e. the L and H-states, depends on the tip-sample separation history used to achieve the imaging conditions. This section further shows that provided the tip is stable and well characterized the behaviour is reproducible.

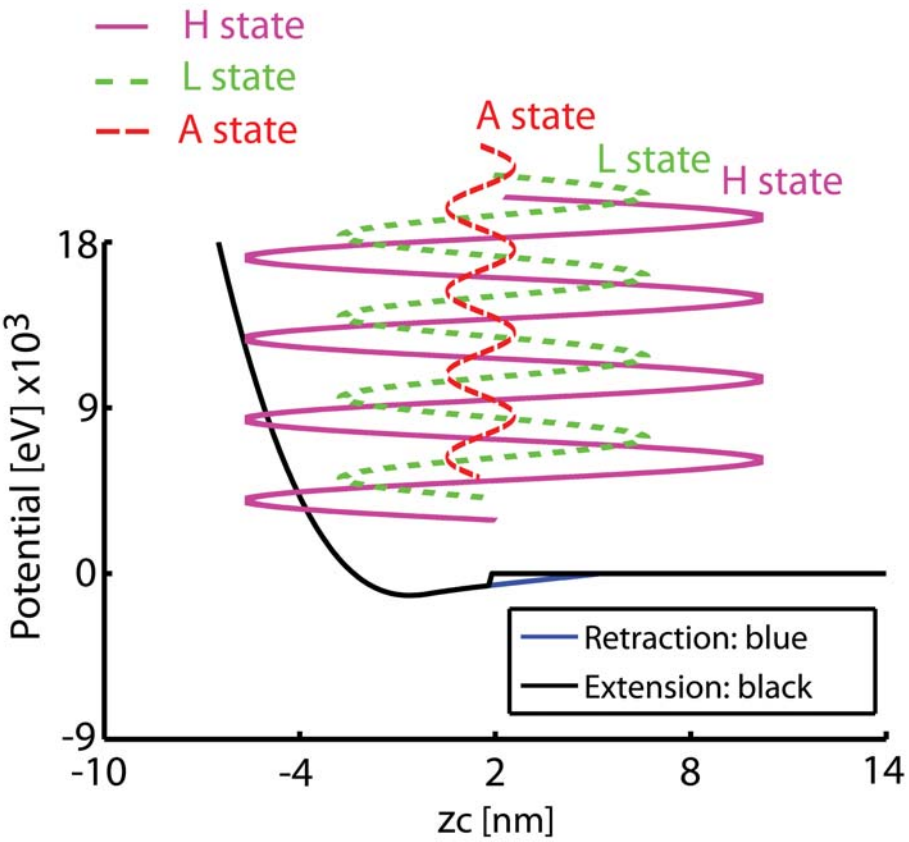

Figure 3.2

Scheme of the tip-surface potential where the vertical axis expresses the energy of the interaction in eV and the horizontal axis expresses the tip-sample separation z_c. The black continuous line in the potential represents the extension of the tip and the continuous blue line the retraction for which some hysteresis is observed. This hysteresis is a consequence of adding the capillary tip-surface force. The scheme has been obtained for a tip of 20 nm in radius, a water layer of h=0.6 nm and an effective, an effective elastic modulus of E^*=10 GPa and a surface energy of 20 mJ. The actual separation here is z_c=2nm implying that any z amplitude larger than 2nm is already mechanically contacting the surface. At this separation, the three possible oscillation states are represented. The H-state is represented with a continuous purple line, the L-state with a dashed green line and the A-state with a dashed red line. Here it is easy to observe that while the A-state is purely attractive in the sense that the amplitude of oscillation is much smaller than the separation z_c, the L and H-states might be net attractive or net repulsive. That is, while intermittent contact with the surface might or might not occur during an oscillation in the L and H-states, the attractive and repulsive regimes are defined by the net force per cycle.

The L-state has been explored in detail and we note that at low to intermediate values of free amplitude, noise free imaging is achieved. Nevertheless, emergence of background noise occurs in certain regions of parameter space regardless of whether the two cantilever oscillation states, i.e. the L and H-states, co-exist. This is later shown (Chapter 6) to relate to the A-state. The outcomes shown here are general since the tips used are mechanically stable and well characterised. Thus, this section demonstrates that a thorough and systematic experimental approach in conjunction with standard modelling gives insight into the mechanisms behind image contrast formation in AM AFM in air. The fundamental theory of phase contrast in ambient AM AFM is also discussed. Finally, the relevance of peak forces in the tip-sample interaction that appear when switching between oscillation states is discussed. The peak forces involved in smooth transitions between force regimes are shown to be several times smaller than those involved in step-like transitions characteristic of bi-stable regions.

3.3.2 Simulation methods

The model has been implemented using Matlab[138] and in the C programming language. A standard Runge Kutta algorithm of the fourth order has been used to solve the equation numerically. The results using both methods are almost identical, however, the C program is orders of magnitude faster. In C everything has been written manually including the numerical algorithms; fourth and eighth order standard Runge Kutta algorithm. Thus, out of all presented data in this thesis, only the phase space projections (Chapter 4 Fig. 4.3) have been obtained using the C program. No problems of divergence have resulted from this approach in Matlab nor C as opposed to the problems experienced elsewhere.[118] In their work, the researchers state that a problem of divergence results when forces like the capillary force abruptly add to the equation of motion. Thus, these used a smoothing function for the interval where no necessity for this kind of procedure has been found.

Amplitude-Phase-Distance (APD) curves are useful in collecting data that provides information about the relationship between amplitude A, the tip-surface separation (z_c) and the phase ϕ. In these, z_c is initially set large enough as for the cantilever to be unperturbed $z_c>>A_0$; this is typically done automatically by the software. Then a triggering is set; this triggering is a minimum value of amplitude A to be reached in the curves. For example, for A_0=30 nm a triggering of A=2 nm means that the separation z_c in the curves will be reduced to the value for which A reaches 2 nm but no less. Thus, practically, first $z_c>>A_0$ *or* $z_c/A_0>>$ 1. Then z_c is slowly reduced while monitoring the amplitude A and the phase ϕ. When the triggering amplitude A is reached, the separation is set to increase again. Several examples of APDs are given in this and the following examples (i.e. Figs. 3.12 c and d and 3.15 d and e). These APDs have been used since the beginning to understand AM AFM[33] and variations may include force-distance curves (in the dynamic mode), contact time-distance curves, etc. Some examples of several of these curves can be found in the literature.[1,33]

While some[118] have solved the equation of motion and obtained APDs by first setting a given z_c distance and initial conditions and waiting for the steady state response to then record both phase and amplitude, here the simulations have been run in an analogous way to the experimental situation. First, a given zc distance has been set (approximately 50% larger than the value of the free amplitude A_0 used in the given simulation). Then the separation has been continuously varied with a speed $\dot{z}_c$ while monitoring the amplitude, phase and average force. Experimental APD curves are normally taken at 1-10Hz ramp rate which for an initial zc distance of 100 nm translates into $\dot{z}_c$ speeds of 0.2 to 2 nm/ms respectively. Here, in the simulations, speeds of $\dot{z}_c \leq 2$ nm/ms have been used and these have reproduced the experimental behaviour remarkably well.[79]

3.3.3 Phase contrast

While topography can be routinely characterized and sensible numerical data can be easily obtained, acquiring numerical data about the mechanical and chemical properties of the samples during the scanning process remains challenging.[23,49-50,54] AFM phase imaging is one of the widely used methods to map chemistry, offers high resolution, and is known to be capable of providing contrast other than just topographical.[1,42,48,50] Nevertheless, its interpretation is not straight forward.[50]

In 1998, J. Cleveland et al.[48] found an analytic expression relating the power $<P_{dis}>$ or energy $<E_{dis}>$ dissipated in the tip-sample interaction per cycle to several parameters (k, ω_0, Q, A_D). Here A_D is the drive amplitude measured in units of length and to be distinguished from the drive amplitude F_D of the equation of motion which is given in Newton units. Nevertheless, since A_D is not easily found experimentally, the relation $A_0=QA_D$ when $\omega=\omega_0$ is typically used. This relationship allows writing the expression with experimental parameters (k, ω_0, Q, A_0) that are easy to quantify; more general expression for A_D at any given ω can also be found (data not shown). The resonant frequency and the natural frequency are related by[34]

$$\omega_r = \omega_0 (1 - \frac{1}{2Q^2})^{1/2} \tag{3.8}$$

where it is clear that for large enough values of Q, i.e. as it is the case in air or UHV, that $\omega_r \approx \omega_0$. Thus, $\omega_r = \omega_0$ might be used in these conditions. The expression for $<E_{dis}>$ was found by noting that, in the steady state and assuming a harmonic response and linear *background* dissipation, the energy entering the cantilever per cycle $<E_D>$ has to equal the energy dissipated per cycle to the background or medium $<E_m>$, plus the energy dissipated in the tip-sample interaction $<E_{dis}>$. The expression is

$$< E_{dis} >_{CYCLE} = \frac{\pi k A_0 A_{sp}}{Q}[\sin(\phi) - \frac{A_{sp}}{A_0}] \qquad \omega = \omega_0 \tag{3.9}$$

Importantly, any background damping such as air damping and the viscosity involved in the internal beam damping is not included in the expression $<E_{dis}>$. That is, only the energy dissipated in a small volume in the tip-sample junction is accounted for by $<E_{dis}>$ and it does not impose any restriction on the character of the tip-sample force. Nevertheless, since a harmonic response is assumed to derive it, when the excitation of higher harmonics in the interaction is relevant, this expression cannot be used reliably. Thus, (3.9) can be safely used in air but typically not in liquid for softer cantilevers where harmonics need to be accounted for.[139] In the rest of this section, conservative interactions are first discussed, then, the relationship between phase shift and force regimes follows and inelastic interactions are discussed at the end.

In AM AFM imaging, A_{sp} is kept constant while scanning. Taking this into account and looking at (3.9) it is easy to observe that the first term inside the brackets, the sine of the phase, is dissipative while, the second term, A_{sp}/A_0, is conservative. It should be noted that in this expression the Garcia and San Paulo's convention[41] is to be used. The response of the free cantilever at resonance is set to 90 degrees. This is in agreement with standard commercial AFM software where the negative sign due to the lag of the response is inverted relative to standard harmonic motion theory.[34] As lagging increases, the phase value tends towards 180 degrees whereas decreasing lagging tends to 0 degrees.

$$\sin(\Phi) = \frac{A_{sp}}{A} + \frac{Q < E_{dis} >_{CYCLE}}{\pi k A A_{sp}} \tag{3.10}$$

Writing (3.9) in the equivalent form (3.10) has heuristic significance. First note that if no dissipation in the tip-sample interaction occurs, i.e. $<E_{dis}>=0$, two solutions are possible (Fig. 3.3). This follows from the symmetry of the sine function and implies

$$\sin(\phi) - \frac{A_{sp}}{A} = 0 \Rightarrow \Phi = \sin^{-1}(\frac{A_{sp}}{A}) \tag{3.11}$$

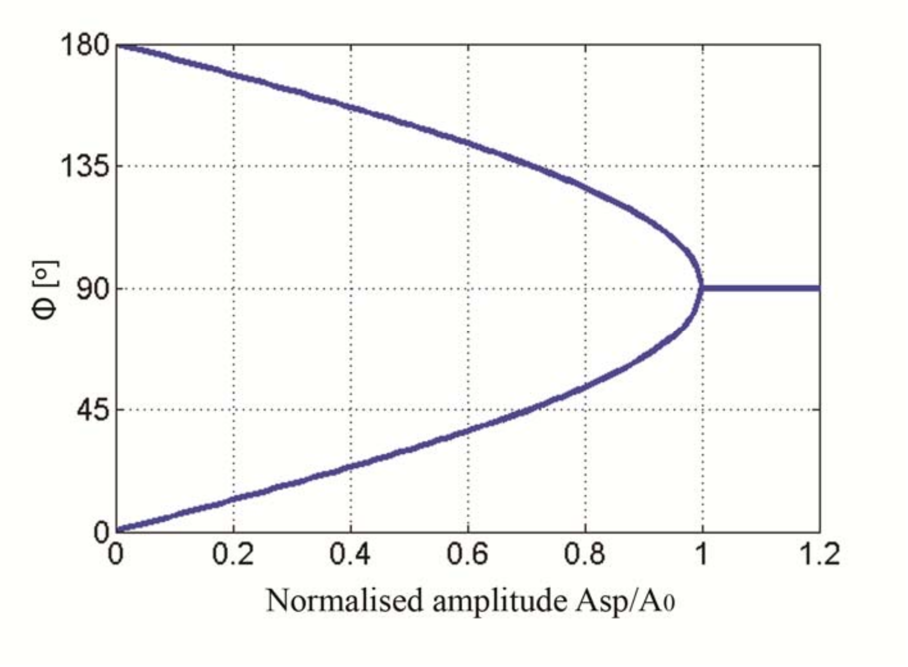

Figure 3. 3

Behaviour of the phase shift ϕ according to (3.9). Two branches appear due to the fact that the sine function is symmetric about 90 degrees. Each branch corresponds to one of the two states, L (top, i.e. 90 to 180 degrees) and H (bottom, i.e. 90 to 0 degrees). Thus, if only elastic interactions are present, the phase shifts monotonously decreases (H-state) or increases (L-state) as the cantilever approaches the surface.

The symmetry of (3.11) shown in Fig. 3.3 has significance beyond energy dissipation. In particular, it can be shown[41] that the solutions correspond to the two steady states that can be reached in dAFM, i.e. the Low and High amplitude branches.

This is discussed in detail in the next section. Nevertheless, here and for the purpose of discussing the figure, it is noted that the branch tending to 0 degrees is identified with the repulsive force regime, whereas the branch tending to 180 degrees is identified with the attractive force regime. This phase shift convention relating the force regimes with phase shifts only applies for negligible cantilever mean deflections, oscillations with small contact times or when the tip-sample force affects the dynamics only at the point of closest proximity, i.e. when A_{sp}/A_0 is relatively large. The above assumptions lead to (3.12) from which the attractive-repulsive force convention through the monitoring of phase shifts is derived.[1,140] Note that the cosine of the angle in (3.12) depends not only on the magnitude of the average force but also on its sign. A word of caution is appropriate here since (3.12) is typically overestimated in dAFM in terms of its ability to predict the sign of the force; the above assumptions are sometimes disregarded or underestimated.

$$\cos\phi \approx 2\frac{<F_{ts}>}{F_0} \tag{3.12}$$

Next, an example of the practical use of (3.12) to differentiate between the attractive and the repulsive regimes is given in Fig. 3.3. First, at resonance and for the free cantilever, i.e. before engaging, the phase lag ϕ between the driving force A_D (black dashed line) and the oscillation amplitude A_0 (red dashed line) is of 90 degrees. In the figure, this initial phase is termed ϕ_1 for clarity. Then, as the cantilever is approached to the surface and the amplitude decays to A_{sp}, the phase varies. In the case shown in the figure, the lag increases to ϕ_2. Recalling that phase shifts above (i.e. numerically higher) and below (i.e. numerically lower) that of the free phase are characteristic of the attractive and the repulsive force regime respectively, the shift in Fig. 3.4 implies that the attractive regime has been reached; $\phi_2>\phi_1$ or $\phi_2>90^o$.

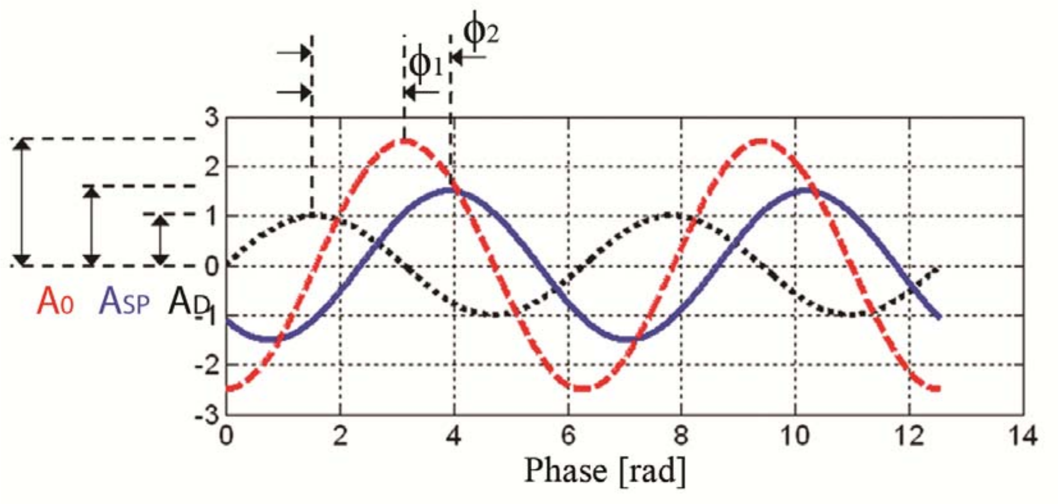

Figure 3. 4

Scheme of the relative phase shifts of the common signals used in AM AFM. The signal of the cantilever when interacting with the sample is the amplitude set-point A_{sp} (continuous blue line) and it is shown to lag the drive amplitude A_D (dotted black line) by an angle Φ (the phase shift). The latter is used in AM AFM to obtain phase contrast images. In the scheme, the amplitude set-point lags the free amplitude, thus the cantilever is in the attractive force regime in this case and the initial phase shift prior to engaging is $\phi=\phi_1=90$ degrees. On engaging $\phi=\phi_2>90$ degrees. Note that both the free amplitude and the amplitude-set point signal cannot actually coexist at a given time since this is the physical amplitude of the end of the cantilever for the free cantilever (A_0) and for the cantilever when interacting with the surface (A_{sp}) respectively. Thus, measurements are always relative.

Finally, the consequences of $\sin(\phi) > A_{sp} / A_0$ in (3.9) and (3.10) are that energy is being dissipated in the tip-sample interaction, i.e. $\langle E_{dis} \rangle > 0$. Furthermore, note that if energy is being dissipated, and for (3.9) to have physical significance, the greater than sign is a necessary condition. Otherwise negative energy dissipation would be predicted. The allowed values of energy dissipated per cycle are those lying within the two branches of the sine function in Fig. 3.3 and, in particular, the largest allowed values are those for which $\phi=90^{\circ}$ or where $\sin(\phi)=1$, i.e. the x-axis in the figure. Thus, from (3.9) phase images can be readily interpreted as energy dissipation maps.

Nevertheless, the limited response of the feedback system implies that care should be taken. For example, for a perfect feedback response the amplitude set-point should be constant ($A_{sp}/A_0=ct.$) and elastic interactions should not contribute to phase contrast. Then any phase contrast would be related to differences in the energy dissipated in tip-sample interactions only. Nevertheless, in practice, the feedback response is finite, implying that phase contrast is a convolution of differences in the energy dissipated in the tip-sample interaction ϕ_{dis} and variations in amplitude set-point ϕ_{error} (i.e. the error signal). Mathematically, the absolute phase shift can be written as the sum of both phase shifts, that is $\phi=\phi_{dis}+\phi_{error.}$; some algorithms to deconvolute these contributions have been developed.[141]

As stated, the above interpretation is particularly relevant in ambient or UHV where a sinusoidal response is a good approximation to the phenomenon. The interpretation of phase imaging in liquid environments is even more challenging and thus, it has taken more time to be theoretically investigated.[142] As a final note, it should be emphasized that few advances have been made in terms of deconvoluting energy dissipation maps in terms of different interactions[49-50] and even less in terms of interpreting these as chemical mappings. This is partly a consequence of the difficulties of finding analytical expressions. Nevertheless, these difficulties could maybe be surmounted in the future with the use of sufficient experimental data and provided the tip is well characterized. This is further discussed in Chapter 6.

3.3.4 Force regimes and bi-stability

3.3.4.1 Overview

Here, a systematic approach to imaging using dsDNA on mica as a test sample is presented. The main characteristics of AM AFM in air are discussed in terms of operational parameters. Oscillation states and force regimes are thoroughly defined below. The theoretical relationships are tested and contrasted with experimental results and it is shown how the cantilever dynamics, in particular bi-stability and force regimes, can be controlled by varying the operational parameters. A good choice of operational parameters optimises phase contrast[42,49], the apparent height and width of the system under investigation[44,80,135] and minimises noise-like artefacts.[45,80] At the end, noise patterns are shown to be found even in regions of parameter space where the H-state is highly inhibited. Thus, noise might or might not be due to constant switching between states.[79] Noise patterns in the L-state, where the H-state is strongly inhibited are further discussed in Chapter 6 and described in terms of the appearance of a third state, the A-state.

Since the main predictions obtained by solving (2.1), or (3.1), numerically are discussed[1,41,79,136], they are summarised and defined here for clarity as follows

1) the average force per cycle might be either net attractive or net repulsive and follows phase shifts above and below 90° respectively. These are the so-called attractive and repulsive regimes and make reference to average forces per cycle only.

2) Monitoring the phase shift is a reliable method to predict average forces as long as the amplitude set-point is not too low (i.e. *Asp/A*<0.2) and/or the energy dissipated in the tip-sample interaction is relatively small compared to the stored energy.

3) There might be either one or two physically stable amplitudes for a given cantilever-sample equilibrium position z_c. When two solutions co-exist these are termed the L and H-state, where the L-state corresponds to the cantilever vibrating at a position higher above the sample. These solutions can be written analytically as shown in (3.13), where z_0 is the mean deflection and can be generally ignored.

$$z_{H/L}(z_C,t) = z_0(z) + A_{SP\,H/L}\cos(\omega t - \phi_{H/L}) \tag{3.13}$$

4) Experimentally, the differences between single and double branched regions can be found by monitoring the behaviour of the amplitude and phase shift as the cantilever transitions from the attractive to the repulsive regime (90°); smooth transitions correspond to single branched regions whereas step-like transitions correspond to double solutions (L and H).

5) The phase shift monotonously increases (decreases) in the L (in the H) state with decreasing separations z_c. In single branched regions, the phase shift also monotonously decreases in the repulsive regime with decreasing z_c. If the phase shift does not behave as stated above, it can be deduced that relatively high energies are dissipated in the tip-sample junction.

6) The critical (A_c) or minimum value of free amplitude (A_0) required to transition from the attractive to the repulsive regime at resonance depends on cantilever and sample properties (see Fig. 3.7 below).

7) The L-state can lead to non-contact imaging as long as the free amplitude is low enough [41,133] and is generally more prevalent above resonance[45] and/or with the use of compliant cantilevers.[42] A good rule of thumb to image in true non-contact, is to use a free amplitude smaller than $0.5A_c$ while imaging at or above resonance. It can also be shown that the occurrence of bi-stability is strongly dependent on drive frequency and free amplitude.[79] The experimental implications of the theory above are discussed below in the following sub-sections.

The bi-stable behaviour of an oscillating micro-cantilever near a solid surface was first proposed by Gleyzes et al.[81] and later investigated by several groups.[43,80,143-146] Since the beginning [81], the hysteresis experimentally observed in amplitude and phase distance (APD) curves was linked to a distortion in the resonant curve caused by the proximity of the surface and later described as differences in the required perturbations to reach one state or the other during extension (approaching the sample) and retraction (retracting from the sample).[80,145] Another issue related to the prediction and interpretation of data in AFM involves the stability of the tip. In particular, mechanical and chemical tip stability is a crucial parameter in AM AFM, and in general any form of AFM, since its geometry and chemistry are significantly responsible for resolution, contrast and dynamics.[15,57,79] Here, tip stability makes reference, in a broad and general way, to the effective curvature of the tip irrespective of possible asperities that might or might not be present. For example, if, initially, and prior to being used, a tip has an effective curvature of 10 nm and this curvature is maintained throughout the experiments, the tip is said to be stable for the experimental operational parameters used in the given experiment. If, on the other hand, the tip radius varies in radius from scan to scan, then the tip is said to be unstable. Later, in Chapter 6, it is shown that provided the maximum pressure per tap in the contact does not increase beyond 0.8-0.9 GPa the tip is stable. The pressure depends on tip radius, cantilever and sample stiffness and the operational parameters used in the experiment.

The focus in Chapter 6 is the free amplitude. There it is shown that provided the free amplitude A_0 is increased smoothly (i.e. in small steps scan after scan) the tip radius typically grows smoothly and reaches a value for which imaging is stable (typically in the order of R~20-30 nm for standard values of free amplitude like A_0<60-70 nm). As an example, in Fig. 3.5 Scanning Electron Microscopy (SEM) images of cantilevers with k~40 N/m are shown (Fig. 3.5). APD curves on a mica surface were obtained at resonance for these cantilevers prior to SEM imaging. Initially, the three cantilevers displayed Type I APD curves (Fig. 3.6a); cantilever-surface pairs displaying Type I APD curves are termed Type I systems for short. In Chapter 6 it is shown that, in ambient conditions, cantilever-surface pairs displaying Type I APD curves correspond to ultra sharp tips (i.e. R<5 nm) provided the elastic modulus of the surface E is large enough, i.e. E>100 MPa. Type I APD curves are shown in Fig. 3.6a below. These display the SASS and N regions but not the A-state. Not all ultra-sharp tips however display Type I APD curves since, if the spring constant is too low , i.e. k<2-10 N/m, Type II (Fig. 3.6b and c) or III (Fig. 3.6d) APD curves are displayed instead even under the ultra-sharp tip conditions. Nevertheless, if k is sufficiently large (i.e. standard cantilevers with k~40N/m) only ultra sharp tips display Type I APD curves.

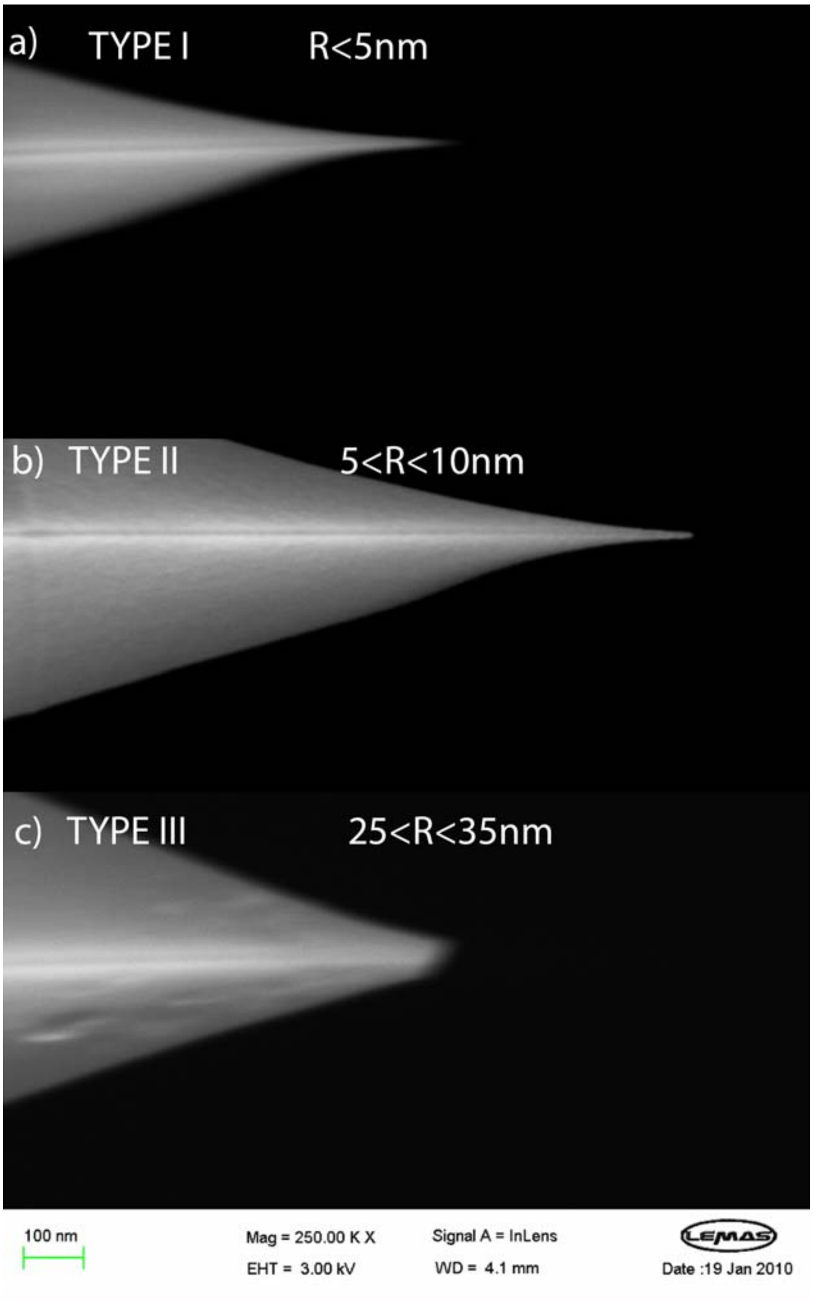

Figure 3. 5

SEM images of the end of three different cantilevers which initially produced Type I APD curves. After submitting a) the first tip to small values of A_0 smaller than 10 nm only it still produced Type I APD curves and, in accordance, the measured SEM radius is smaller than 5nm. b) The second tip was submitted values of A_0 as large as 20nm and then produced Type II APD curves. The SEM image shows a tip radius of approximately 5nm. Finally, the c) last tip produced Type III APD curves after submitting it to A_0 values as large as 60 nm. All these measurements were performed on a mica surface silicon nitride cantilever with spring constants of 40 N/m.

Type III APD curves (Fig. 3.6d) are characteristic of either a larger tip radius, i.e. R>20-30 nm, relatively compliant cantilevers, i.e. k<2-10 N/m, or a combination of both. These require larger values of free amplitude to reach the H-state (compare Type I and III curves in Fig. 3.6a and d). Furthermore, Type III systems display the A-state and it is persistent even with relatively larger values of A_0, i.e. A_0>20-30 nm. Type II APD curves (Fig. 3.6b and c) are displayed by transition cantilever-surface and have characteristics of both. Again, this discussion applies provided E>100 MPa. Practically, for k~40 N/m and sufficiently stiff surfaces, i.e. Mica[130], Type I systems imply R<5 nm, Type II systems imply 5<R<20-30 nm and Type III imply R>20-30 nm. For example, after being submitted to intermediate values of free amplitudes of oscillation, i.e. 5<A_0<20 nm, the second cantilever starting displaying Type II APD curves (Fig. 3.6b and c) and, accordingly, SEM scans showed that R~5-10 nm (Fig. 3.5b). Physically, this implies that while initially the tip in was ultra-sharp, i.e. R<5 nm, subsequently submitting it to these larger values of free amplitude involved tip broadening due to high pressures. This is in accordance with the literature.[147]

The third tip (Fig. 3.5c) was submitted to even larger values of free amplitude scanning, i.e. A_0~60 nm, resulting in even further broadening for what initially was an ultra-sharp tip, i.e. a tip displaying Type I APD curves. After these scans the tip displayed Type III APD curves in accordance with the SEM images taken after the scans (Fig. 3.5c). More detail on Type I, II and III curves and their relationship to the tip radius is given in Chapter 6.

Tip instability more often than not makes systematic investigations of contrast in the different AM AFM imaging modes impossible when the tip is sharp (i.e. R<20 nm). This is mainly due to the difficulties of reproducibility caused by the strong non-linear dynamics of the cantilever interacting with the sample, experimental calibration[42], the simplifications of standard models[45] and, more significantly[79,148], the stability of the tip during repetitive scanning.[149] In particular, relatively stiff cantilevers (k>10-30 N/m) with high aspect ratio tips cannot be used to obtain sequences of scans in the intermittent contact mode with sufficient reproducibility. Thus, the tips in this section have been characterised with a Scanning Electron Microscope (SEM) and only those in the range 20<R<30 nm (see Fig. 3.5c) have been used for imaging. A method used to stabilise them in situ is presented below. Tips submitted to this method of stabilization allow systematic scanning with free amplitudes of $1<A_0<60$ nm[79,147] and the whole range of set-points below, at and above resonance in both ambient conditions and even under very high relative humidity conditions (RH>80%).[79]

Thus, prior to starting a systematic investigation, all tips have been submitted to 1-2 hours of scanning by following a simple technique as follows.[79,147] First, the engaging process has been carried out with a free amplitude below 10 nm (i.e. A_0=6 nm) while scanning at resonance and with set-points of 70-80% (i.e. A_{sp}/A_0=0.70-0.80). Then the free amplitude is systematically increased by 5-10 nm every five to ten minutes while keeping the set-point fixed at 70-80%. The increment in free amplitude is performed by disengaging the tip every time and returning the cantilever to the required free amplitude. A maximum free amplitude of 60-70 nm has been used and these have never been exceeded in subsequent scans while performing such systematic investigations. After submitting the tips to these preliminary scans they smoothly and gradually broaden and reach values in the range of R=20-30 nm (Fig. 3.5c). This allowed acquisition of data reproducibly while keeping the resolution comparable to previously published data.[1,79,134,148] The experimental findings support the theoretical descriptions.

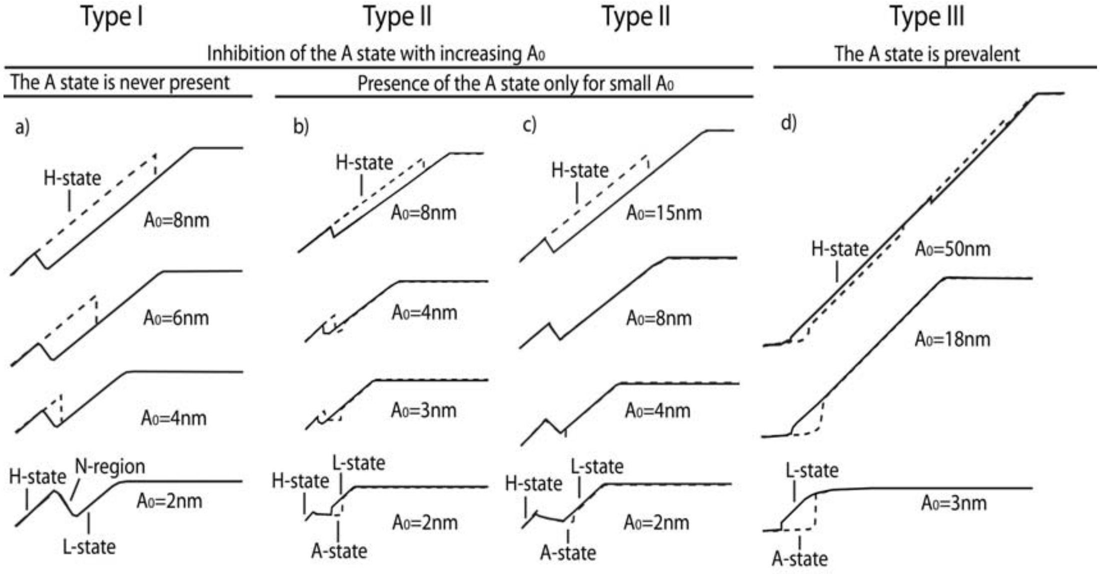

Figure 3. 6

Experimental AD curves obtained on a mica surface at resonance with k~40 N/m. Type a) I, b) II and c) III curves are shown. The y-axis is the amplitude in nm and the z-axis the z_c separation. Nevertheless since it is the shape of the curves with increasing free amplitude which allows differentiation of curves, only the shape and the free amplitude corresponding to each curve is shown. From bottom to top the free amplitude has been increased discretely to allow observation of the several characteristics of the type of curve. The A, L and H-states are pointed for each type. Notice that the A-state is only prevalent with increasing free amplitude for Type III curves.

3.3.4.2 Force regimes and operational and cantilever-sample parameters

The significance of A_c has been defined above, as the critical or minimum value of free amplitude required to observe a transition to the repulsive regime. Furthermore, the A_c value is measured as the free amplitude of oscillation for a given drive amplitude. This transition obviously depends on the cantilever-sample characteristics but also on the operational parameters. This permits controlling force regimes by appropriately choosing a set of operational parameters.

In Fig. 3.7 simulations have been carried out to show that A_c increases with increasing tip radii R, normalised drive frequency β, decreasing elastic modulus of the sample E and cantilever's stiffness k. It is worth mentioning that while the dynamics might depend on the value of relative humidity, cantilever spring constant, surface energy and elastic modulus of the sample, once the tip is stable the results presented here are general and only an offset in A_c has to be applied to account for all these. In this respect, while the surface energy of mica is highly dependent on relative humidity [105,110,115], it can be shown that the transitions between force regimes follow the pattern discussed in this section for a wide range of values of relative humidity (data not shown). Thus, these data (Fig. 3.7) can be used to predict A_c depending upon a given experimental set-up.[79]

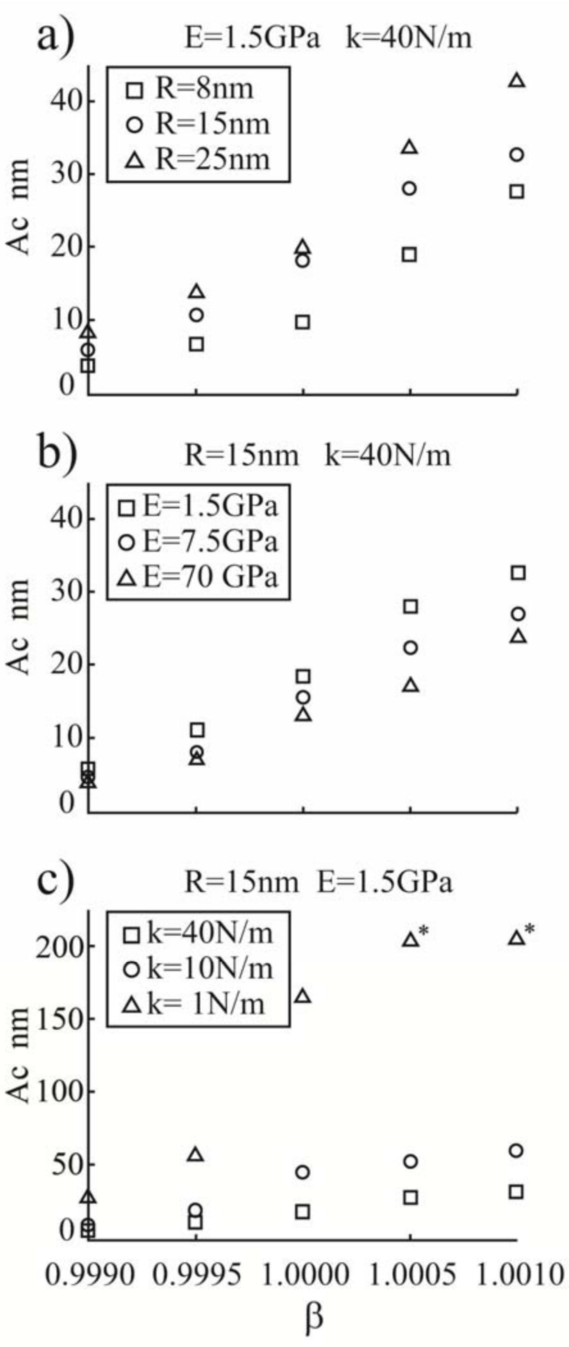

* these values are off scale at>400nm

Figure 3. 7

Simulations. Dependence of critical amplitude A_c to reach the repulsive regime as a function of normalised drive frequency β during Z-piezo extension. The relationship is shown for a) tip radius R, b) elastic modulus of the sample E and c) spring constant k of the cantilever. In a), it is observed that A_c varies with R if E and k are kept constant. Similar relationships are shown in b) and c) by varying E and k instead. The values of the parameters used in the simulations were; f_0=300 kHz, E_t=70 GPa (elastic modulus of the tip), ν=0.3 (Poisson's coefficient), H =7.1x10^{-20} J, γ=35 mJ/m^2 (surface energy) and Q=500.

3.3.4.3 The resonance curve of a tip vibrating near a surface

In Fig. 3.8, the critical value of free amplitude A_c to reach the repulsive regime has been plotted in the vertical axis against the normalised drive frequency $\beta=f/f_0$ in the horizontal axis. This is an experimental resonance curve obtained on a freshly cleaved mica surface. Fig. 3.8a shows the curve with the tip off the surface and Fig. 3.8b shows the evolution of the curve for decreasing cantilever-sample separations z_c of 23, 18, 13, 8 and 3 nm respectively. Below resonance, a single branch exists for all separations, while two branches co-exist at and above resonance. Regions exist, where the phase-shift lies below 90 degrees (repulsive regime: red filled markers) and above 90 degrees (attractive regime: blue unfilled markers). From Fig. 3.7 it can be concluded that the ability to reach the repulsive regime at intermediate values of free amplitude (A_r=24 nm) can be attributed to the combination of a stiff cantilever (k~40 N/m), a relatively stiff sample (mica) and an intermediate to small tip radius (R<20 nm). Here, the free amplitude is termed A_r instead of A_0 implying that the drive amplitude was not changed at any value of drive frequency. Also note that this tip radius is not stable; hence, the shape of the curve such as that in Fig. 3.8 could have changed if a second set of data had been obtained. The fact that only a single branch exists below resonance, in this case, implies that the critical value of free amplitude for which the two states no longer co-exist has been already been surpassed (i.e. A_c<24 nm).[150] Double-branched regions for smaller A_0 below resonance could be observed for this system (data not shown).

3.3.4.4 Bistability and perturbation theory

A standard method to describe the dynamics of non-linear systems is through phase space diagrams.[151] Some have already used these diagrams to understand the dynamics of the cantilever in AM AFM (and dynamic AFM in general). In short, if one sets a given cantilever-sample separation (z_c) to the equation of motion and systematically varies the initial position and velocity in the differential equation, it is possible to construct (or map) a phase space diagram (or projection), where some initial conditions lead to the L-state while others lead to the H-state, by recording the state the cantilever reaches for each set of initial conditions in the steady state.[1,80,145] The set of initial conditions leading to a-state are called the basin of attraction of the state. An example is shown later in Chapter 4 in Fig. 4.3. The strength of each basin of attraction or state (i.e. L and H-state) can be quantified as the ratio of initial conditions that lead to one or the other state respectively. One state is stronger or more stable according to this ratio (i.e. the more initial conditions leading to one state the more stable the state).

Since the equation of motion is deterministic (i.e.. a given set of initial conditions leads to a given state only), the implication during imaging is that once a state (L or H) is reached in the steady state, a switch between states will not be observed in the scan (or APD) unless a perturbation in amplitude is observed (i.e. equivalent to setting new initial conditions in the equation). Also, since topographic features are common sources of perturbations and generate transients due to feedback limitations, switching between states can often be observed if the phase space projection (see Fig. 4.3 for an example) is evenly or close to evenly distributed under those conditions (Figs. 3.9 - 3.10).[1,79-80,145]

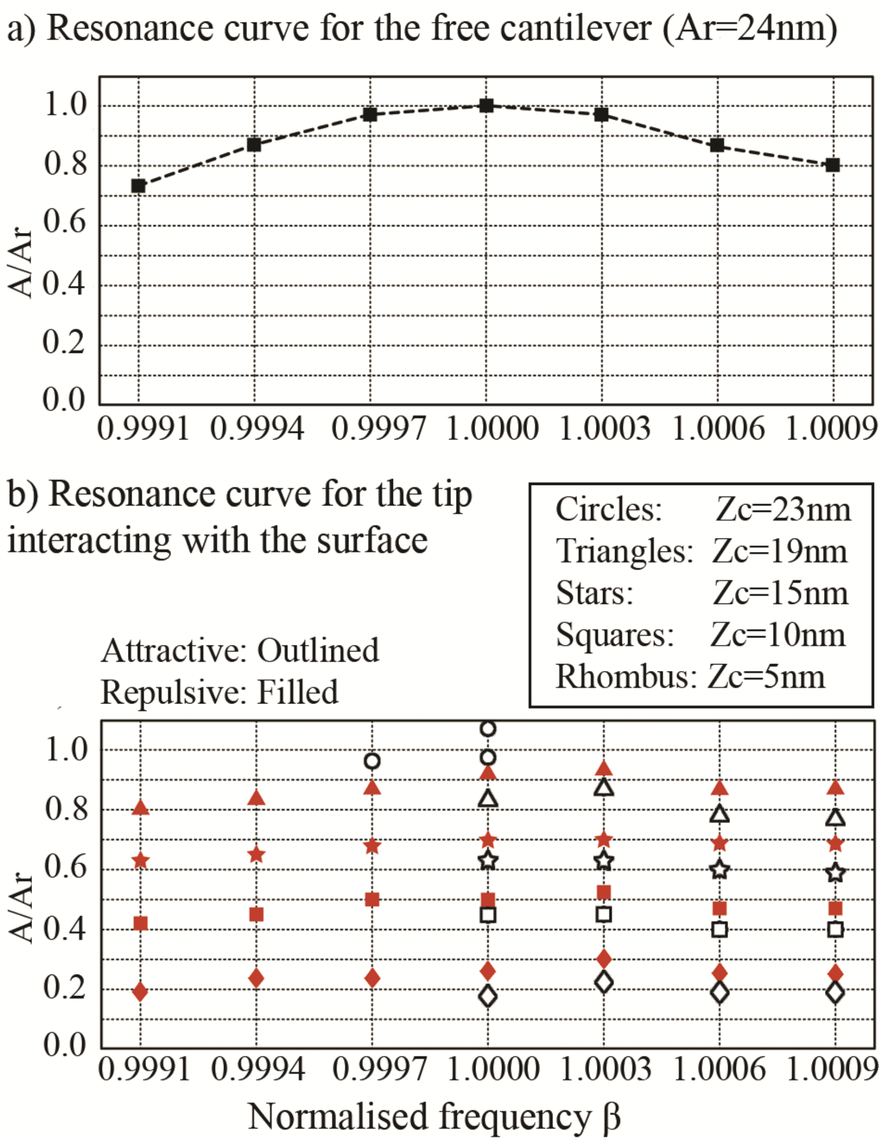

Figure. 3.8

a) Experimental resonance curve in air (free cantilever) for a resonant frequency of 320.64 kHz (k=40 N/m). The black squares correspond to the discrete values of frequency for which the amplitude has been recorded. b) Reconstructed experimental resonance curve near a mica surface for the same cantilever showing the normalised amplitude at different average cantilever-sample separations z_c.. The free amplitude at resonance A_r (24 nm) has been used as the normalising amplitude at all points. The lower amplitude branch (L-state) is observed to correspond to the attractive regime (blue, unfilled markers) whereas the higher amplitude branch (H-state) corresponds to the repulsive regime (red, filled markers). There is one exception for z_c =23nm at resonance when both the H and the L-state fall in the attractive regime. The curves were obtained on freshly cleaved mica at 35% relative humidity (RH).[79]

In summary, a switch between oscillation states has to be caused by a perturbation, otherwise each state is stable and deterministic and no switch should occur. The phase space projection indicates which, if any, of the two states dominates for a set of operational parameters and it is very sensitive to even small variations. Fig. 3.9 shows a particular scan of double-stranded (ds) DNA on mica, for which the L-state dominates the phase space projection. This can be deduced from the fact that the obstacles on the surface are seen to often lead to a transient switch into the H-state, but a switch rapidly occurs back to the L-state. The fast switch-back is an indication of the overall domination of the L-state. Examples of sustained switching are shown later. These occur when the phase space projection is more evenly distributed.

3.3.4.5 Stochastic character of the switch between states

The switch between oscillation branches is stochastic, i.e. for a given set of operational parameters there is a certain probability of a switch from one state to the other. Again, this likelihood is related to the phase space projection and the error in the amplitude during scanning caused by perturbations. Thus, in practice, several scans might be required in order to observe a switch.[79,136] An example is shown in Fig. 3.10 for which the same area has been imaged several times with the same operational parameters while driving slightly above resonance.

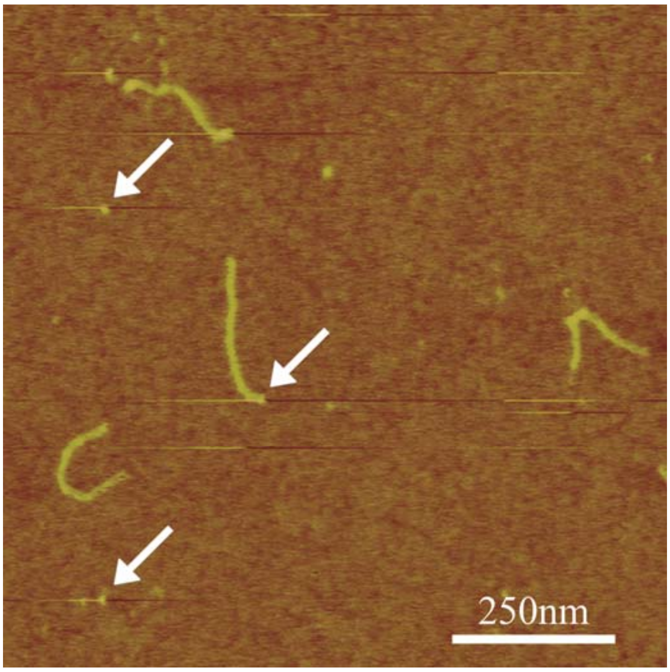

Figure 3. 9

Transient switching between states caused by topographical perturbations. Topography (z-piezo) image of 800 bp fragments of DNA on mica where the scanning parameters correspond to a region of bi-stability. Obstacles on the surface (indicated by arrows) cause transient switching from one state to the other and back. The scan speed here is 2μm/s. The scan speed can influence the switching or transient switching between regimes since switching is caused by perturbations in amplitude and these are increased with increasing speed.

In the first scan (Fig. 3.10a), a switch from the L to the H-state is observed with the slow scan direction from bottom to top. After obtaining several scans without changing the operational parameters, a whole scan of the area has been acquired stably both in the H (Fig 3.10b) and the L (Fig 3.10c) state respectively. Similar behaviour was observed at resonance (β=1.0000) for the same free amplitude (data not shown). Nevertheless, as stated, while switching is often stochastic, topographical anomalies on the surface can cause systematic switching from one state to another, even when the operational parameters and environmental conditions may be different.[79] In the majority of cases, if high values of A_{sp}/A_0 are used, the L-state dominates. This has been common practice for imaging soft biomolecules.[42,44,87,133,135] Then, decreasing the amplitude set-point induces a shift in phase space projection favouring the H-state. If the tip has not changed during the process then it is fully reversible. Significantly, and perhaps counter-intuitively, further reducing the amplitude set-point can result in the L-state regaining strength when the cantilever oscillation is highly damped. This behaviour has been theoretically described in the literature in detail,[150] nevertheless, here the behaviour has been verified experimentally.

An experimental example is shown in Fig. 3.11. It is worth noting that step-like switching at intermediate separations (Fig. 3.11c and d) shows that two states still co-existed with these parameters. The stochastic character of the switch is more prevalent at intermediate (Fig. 3.11c-d) and low (Fig. 3.11e-f) set-points. First, the L-state is seen to fully dominate the scan (Fig. 3.11a-b). The nominal apparent height of the DNA is 0.36 nm (L-state), 0.24 nm (H-state) and 0.28 nm (L-state) for Figs. 3.11a, c and e respectively. Thus, the L-state gives higher apparent heights for DNA than the H-state. However, by decreasing the set-point amplitude, the apparent height in the L-state is also reduced (compare Figs. 3.11a and 3.11e). This might be a consequence of larger average attractive forces inducing intermittent contact, that result in the L-state as the cantilever-sample separation is decreased.[41] In general, this a common behaviour, where the apparent height is reduced with reducing amplitude set-point when imaging in the L-state.[79] Another example is given later.

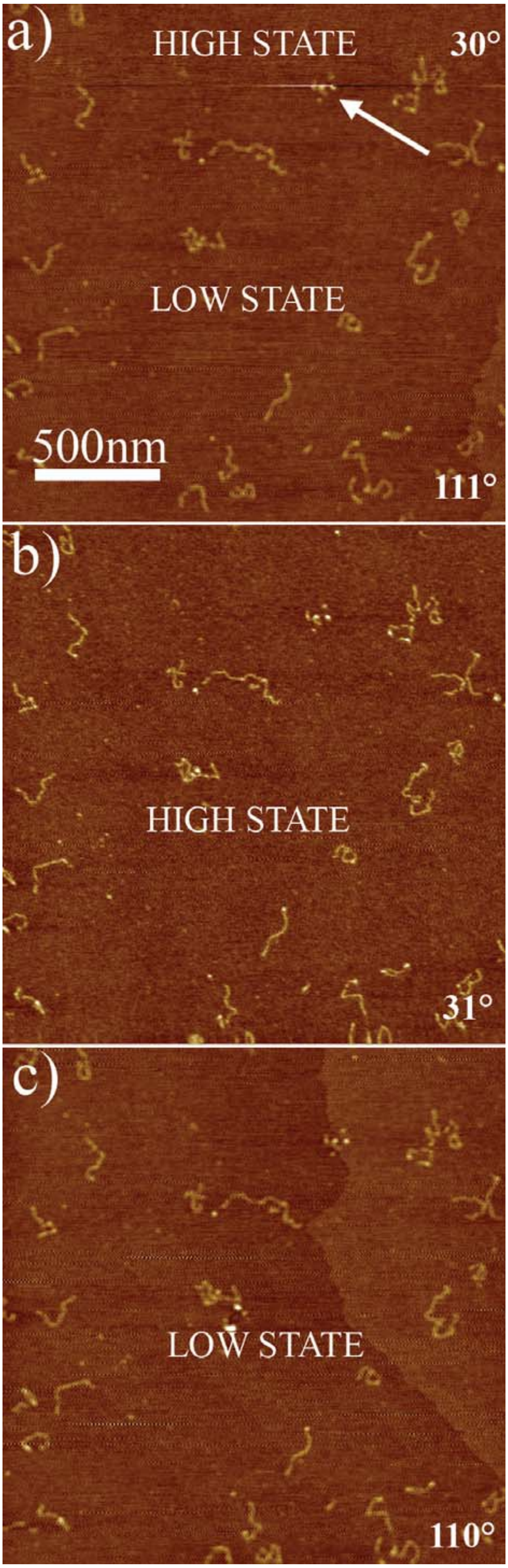
a)
HIGH STATE
30°
LOW STATE
500nm
111°
b)
HIGH STATE
31°
c)
LOW STATE
110°

Figure 3. 10

Selected images from a sequence of height images (Z-piezo) showing the stochastic nature of switching over long time-scales. a) Here, a switch from the L to the H-state is observed. The stochastic character of the switch is then demonstrated by simply leaving the system scanning and observing that in later scans both b) the H and c) the L-state have fully dominated a whole scan. The scans in b) and c) were obtained 15 minutes and 25 minutes after that in (a), respectively. (f_0=332.4 kHz, k=40 N/m, Q factor= 650, A~25 nm, A_{sp}/A=0.20 and β=1.0005).

3.3.4.6 History dependent image contrast generation

The switch between states can also depend on the history of the system, for example, on the way in which the target operational parameters, such as amplitude set-point and drive frequency, are reached. Round and Miles[134] have investigated shifts between the attractive and the repulsive regime as a function of drive frequency. Fig. 3.12 shows how the history of changing the amplitude set-point can affect which state is accessed at a given z_c. For a thorough theoretical description of this effect, one can refer to the literature.[1,80,145] In Fig. 3.12a, the amplitude set-point (A_{sp}/A_0=0.90) has been reached by direct reduction after engaging with A_0=30 nm. For the scan in Fig. 3.12b, the amplitude set-point has been decreased until a switch to the H-state has occurred and then subsequently increased back to 0.90 while staying in the H-state. The hysteric path followed can be seen by means of the APD curves shown in Figs. 3.12c and d. The interpretation is that, in this case, the probability of reaching each state is different during extension and retraction, i.e. for A_{sp}/A_0=0.80-0.90 the L-state dominates during extension whereas the H-state dominates during retraction. In physical terms this probability is explained by the perturbation in amplitude required to switch between states.[80]

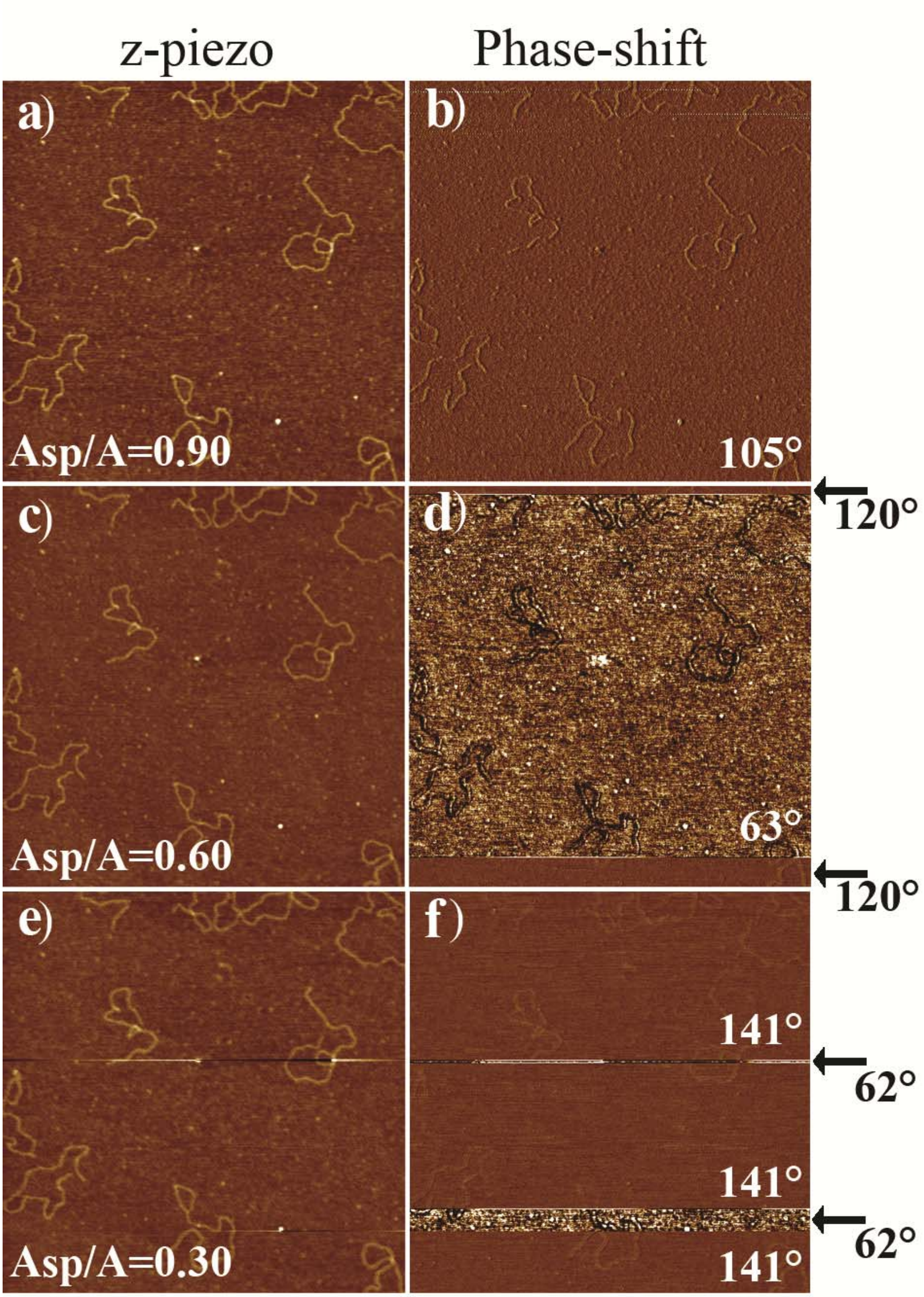

Figure 3. 11

Re-appearance of the L-state at low amplitude set-points. a), c) and e) Topography (Z piezo) and b), d) and f) phase images of the same area at decreasing set-points. Changes in phase space projection are observed as the amplitude set-point is decreased from a-b) 0.85 to c-d) 0.60 and e-f) 0.33. Scan size: 2 μm. (f_0=325.0 kHz, β=1.0000, k=40 N/m, Q factor=600, A=22 nm and relative humidity (RH) =10 %).

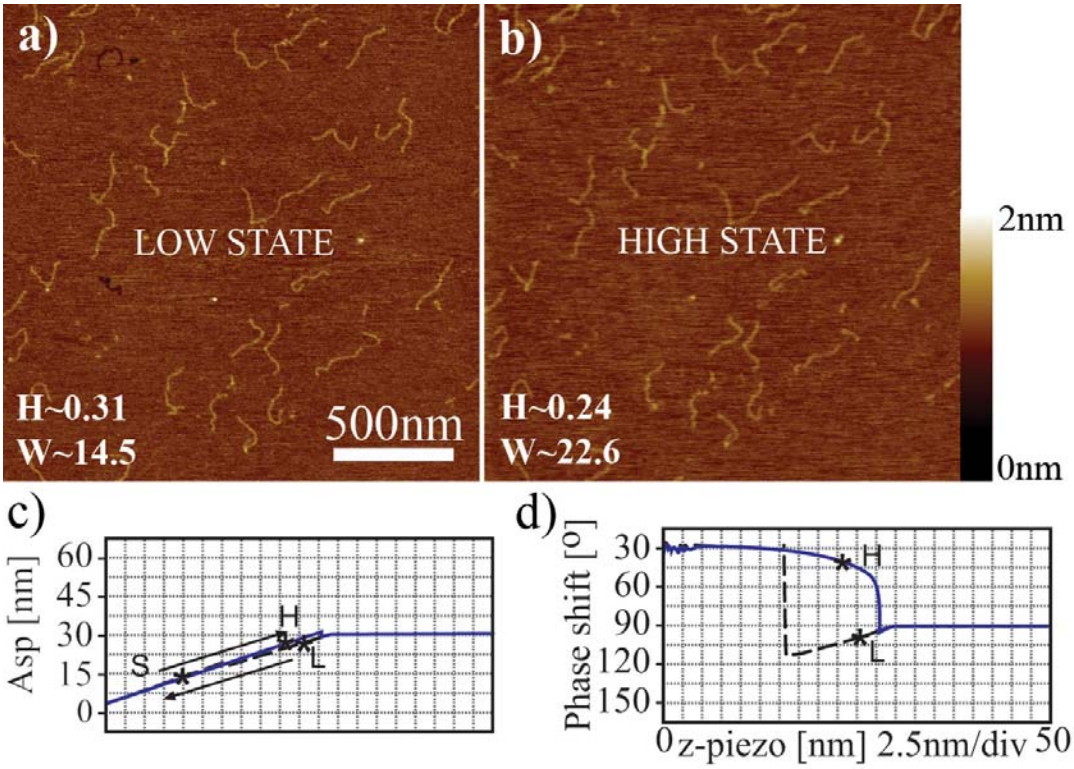

Figure 3. 12

Influence of cantilever history on image contrast. a) Topographic (Z piezo) image obtained in the L-state for a free amplitude of 30 nm while driving above resonance (β=1.0005) and for a normalised amplitude set-point of A_{sp}/A_0=0.90. b) The same area imaged in the H-state by reaching the amplitude set-point during retraction rather than extension. c) Amplitude and d) phase distance curves describing the path followed to reach the L-state in a) and the H-state in b). The intermediate point for which the H-state was reached during extension (A_{sp}~15 nm) is labelled with an S, standing for switch. The dashed lines correspond to z-piezo extension and the continuous lines to retraction. (A_0=30 nm, f_0=315.0 kHz, β=1.0005, k=40 N/m and Q factor= 500).

Interestingly, the background noise in each image is different and can also be explained by the coexistence of the two states and their relative strength quantified via the phase space projection; the noise is interpreted as a greater instability of the H-state for the given set of operational parameters. Nevertheless, a more fundamental or physical interpretation relates this noise with high mean cantilever deflections in the H-state above resonance for large free amplitudes and high set-points as predicted by performing numerical simulations above resonance (data not shown). For this particular set-up, the small probability of reaching the H-state for these operational parameters by simply engaging and directly decreasing the amplitude set-point to A_{sp}/A_0=0.90 has been verified by obtaining ten consecutive scans (data not shown); the L-state dominated for these ten scans.

3.3.4.7 Controlling the interaction in AM AFM

In Fig. 3.13, the operational parameters have been systematically varied in the L-state in order to monitor how image contrast is influenced by the cantilever dynamics. This is an example of L-state imaging for which the H-state is highly inhibited. The inhibition of the H-state for the values of free amplitude used in Fig. 3.13 (i.e A_0~10 nm) can be experimentally verified by finding A_c for the whole range of frequencies. This represents one of the uses of A_c as described in the introduction. In the case of Fig. 3.13, A_c>20 nm for the whole range of frequencies used (data not shown). For example, in Fig. 3.14 a switch to H-state is seen to occur for this system for A_0=22 nm below resonance. The interpretation of Fig. 3.13 follows.

All images in Fig. 3.13 have been obtained in the L-state and attractive regime with phase shift Φ>90° and a free amplitude of A=10 nm. The L-state is typically used to image soft matter[44] (i.e. proteins and DNA) where deformation and contact forces are typically not present. Nevertheless, high levels of background noise can be a problem in these cases. Moreover, in the repulsive regime, the noise arising from the cantilever dynamics can be brought below the intrinsic instrument and environmental noise floor by sufficiently increasing the free amplitude, decreasing the amplitude set-point and driving at or below resonance (see Fig. 3.13). Thus, the effects of noise in the L-state are discussed here. For example, Fig. 3.13 shows that there are certain choices of A_{sp} and f for a given A_0 where background noise is apparent (i.e. Figs. 3.13a-c, 3.10e, 7h). In the L-state, large values of mean cantilever deflection z_0 typically follow the patterns of noise.[79] These patterns are also reproduced in simulations (data not shown). The fundamental source of noise is related to the appearance of the A-state and is discussed in Chapter 6. Thus, only a qualitative description of noise patterns as experimentally observed is given next. The first image (Fig. 3.13a) has been obtained below resonance (β=0.9995) with a high value of normalised amplitude set-point and some noise can be observed in the background. Then the amplitude set-point is decreased (Fig. 3.13b), and, as the noise persists, the amplitude set-point is further decreased (Fig. 3.13c) to relatively low values. Still, the noise remains. This is an example of high levels of noise for the whole range of A_{sp} in the L-state and it typically occurs for relatively low values of A_0. Then, the drive frequency is increased to resonance, where the image is almost noise-free at high A_{sp}/A_0 values (Fig. 3.13d). Further reducing the amplitude set-point at resonance (Figs. 3.13e and f) only increases the noise in this case. This is an example of monotonous increase in noise with reducing A_{sp}.

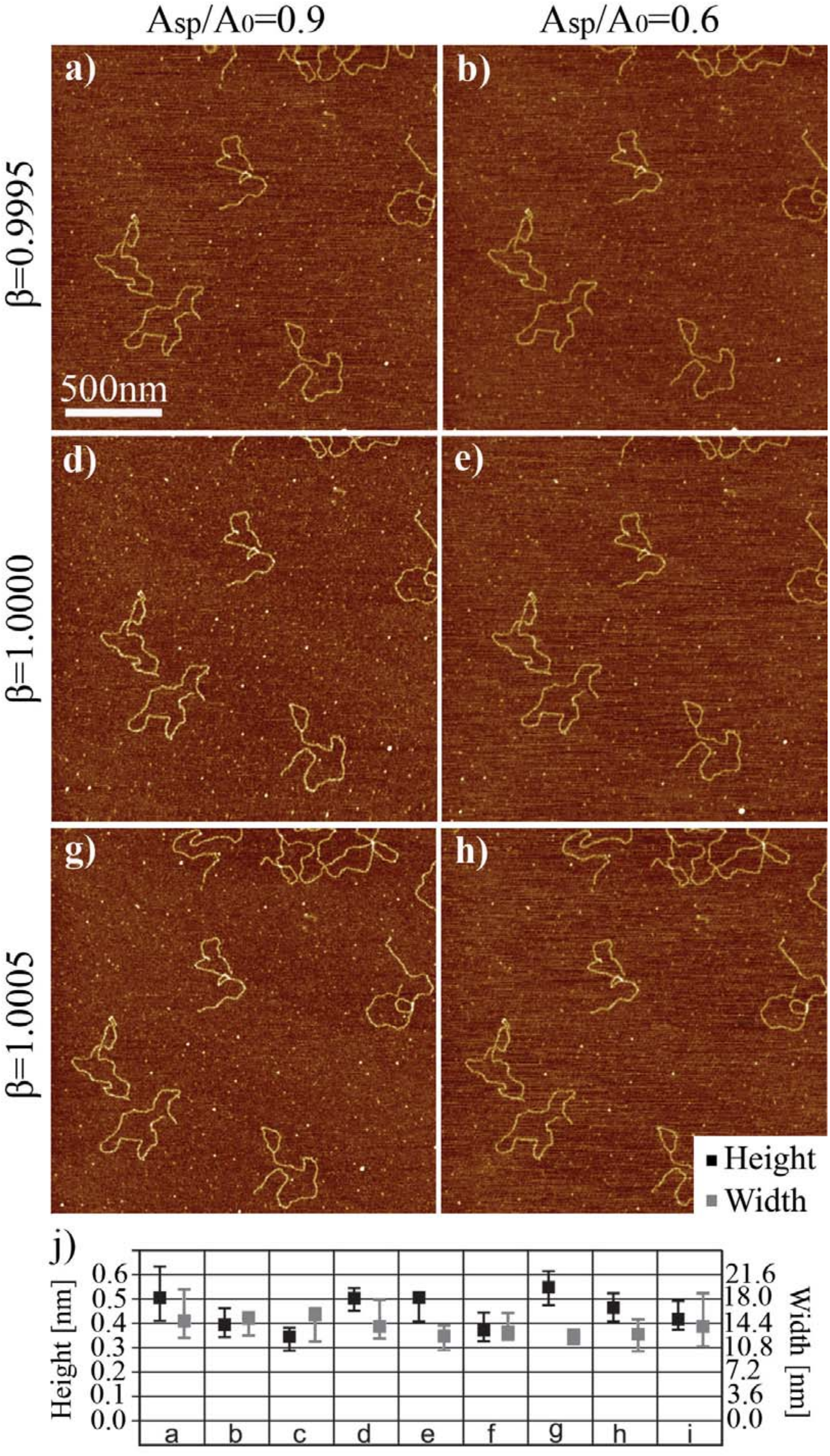
Asp/A0=0.9
Asp/A0=0.6
β=0.9995
β=1.0000
β=1.0005
a)
b)
d)
e)
g)
h)
500nm
▪ Height
▪ Width
j)
Height [nm]
0.6
0.5
0.4
0.3
0.2
0.1
0.0
a
b
c
d
e
f
g
h
i
21.6
18.0
14.4
10.8
7.2
3.6
0.0
Width [nm]

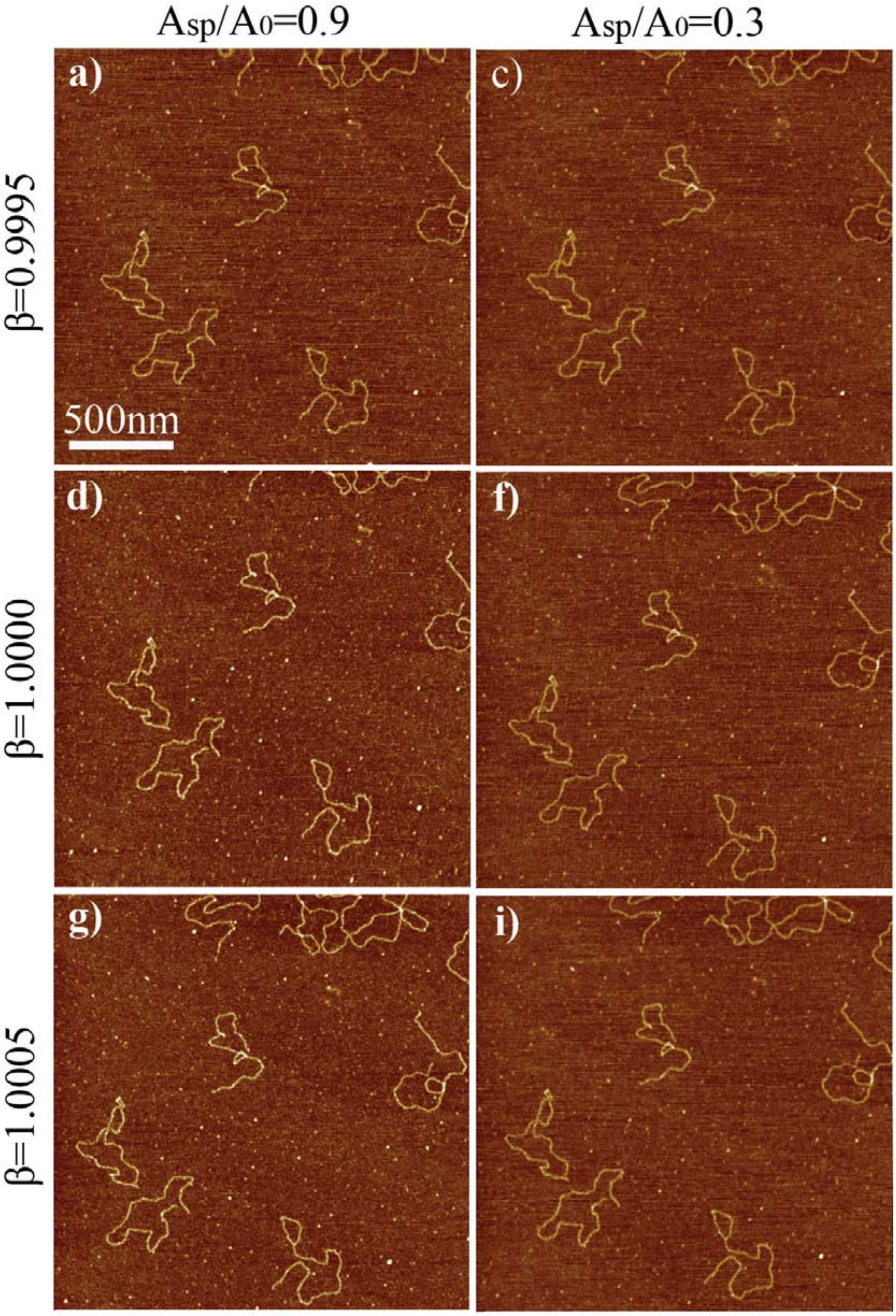
Asp/A0=0.9
Asp/A0=0.3
β=0.9995
β=1.0000
β=1.0005
a)
c)
d)
f)
g)
i)
500nm

Figure 3. 13

Presence of noise while imaging in the L-state and attractive force regime. a) to i) Sequence of topographic images where noise features are seen to vary as the drive frequency (rows) and the set-point amplitude (columns) are systematically varied. The behaviour above resonance (g, *h* and i) is counterintuitive as decreasing the amplitude set-point to intermediate values (A_{sp}/A_0=0.6) increases the noise whereas further decreasing it improves the clarity of the image. j) DNA height and width relationships for the sequence; points are average values with minimum and maximum values delimiting the error bars. For better comparison while still allowing relatively large figures to be displayed, first (a, b, d, e, g and h) the behaviour at the larger (A_{sp}/A_0=0.9) and intermediate (A_{sp}/A_0=0.6) set-points and then (a, c, d, f, g and i) the behaviour at the larger (A_{sp}/A_0=0.9) and smaller set-points are shown (A_0~10 nm, f_0= 325.0 kHz, k~40 N/m, *Q* factor~500 and RH=55%). Scan size: 2 x 2 µm.

Finally, driving above resonance also produces good results at high values of amplitude set-point (Fig. 3.13g), then the noise increases as the amplitude set-point is decreased (Fig. 3.13h). Significantly, further decreasing the set-point amplitude (Fig. 3.13i) produces a counter-intuitive result; the noise slightly decreases as compared to the intermediate set-point (compare 3.13h with 3.13i).[79] This is an example of the case where a maximum in noise is observed before reaching close to zero amplitude values. In fact, this shape is similar to that of the energy dissipated in the tip sample interaction with decreasing separation z_c.[48-49] These three cases are general in the L-state and are discussed theoretically as the appearance of the A-state in Chapter 6. In particular, these noise patterns are correlated with the basins of attraction of the system where, the appearance of A-state, which is insensitive to z_c separations, follows the same noise patterns.[137]

In summary, and from an experimental point of view, for the case shown in Fig. 3.13, an experienced user would set the operational parameters to those shown in Fig. 3.13d or Fig. 3.13g since these minimise noise features. Some groups have reported[5,21] that for small z_c both the dynamic response and signal formation could be highly affected by higher harmonics, and, more readily by those close to higher eigenmodes. In particular, Stark, reported complications to the dynamics of the cantilever for relatively small tip-sample separations z_c due to the highly anharmonic behaviour of the cantilever in these situations leading to chaos.[136] Noise patterns have also been discussed in terms of stability criterions[15,76], in terms of the ratio of the stored energy in the cantilever and the energy dissipated in the tip-sample interaction and/or in terms of the gradient of the force being larger than the spring constant of the cantilever at the distance of closest approach.[15] However, the results of Fig. 3.13 show that there is not a linear relationship between decreasing A_{sp} and the levels of noise. More thoroughly, in Chapter 6, a pattern for which the noise is minimum for very small values of A_{sp} (and or z_c) is discussed. Finally, it should be noted that an inadequate choice of gains also tends to lead to an increase of background noise. This is well known in AFM in general.[86-87,109,152] Nevertheless, here, no choice of gains would make the noise disappear (data not shown). The values of apparent height and width for the scans are given in Fig. 3.13j. Briefly, the apparent height decreases with decreasing A_{sp} and the apparent width is practically independent of A_{sp}, i.e. there is a plateau. The plateau in apparent width in the L-state is predicted by a model described in Chapter 4. The reduction of apparent height in the L-state for these values of R, i.e. R>20 nm, are described in Chapter 5 and shown to be related to the geometry of the interaction and the effective area of interaction.

An example of how to optimise background noise, lateral resolution and apparent height by varying A_0 is shown in Fig. 3.14. The behaviour is shown only below resonance but it is found to be general for typical drive frequencies close to resonance.[79] Reducing A_0 to very small values (i.e. A_0<2 nm) results in severe noise for all drive frequencies for this particular cantilever-sample system (data not shown). In our experience there is always a limit in the minimum free amplitude required to obtain noise-free scans and the value typically varies from 1 nm to a few nm depending on the set-up. The physical interpretation of this phenomenon is that the basins of attraction, and particularly in systems defined as Type III such as the one used to obtain Figs. 3.13 – 3.14 (see Chapter 6), are almost completely dominated by the A-state for these very small values of A_0. This imposes a limitation in dAFM to image with very small values of A_0.

Increasing A_0 in Fig. 3.14 (i.e. 3 nm<A_0<10 nm) generally leads to noise-free scans (Fig. 3.14a, A_0=4 nm) at large values of A_{sp}/A_0 (see discussion of Fig. 3.13). This also correlates with the inhibition of the A-state with increasing A_0 and A_{sp}/A_0. Further increasing A_0 (i.e. 10 nm< A_0<40 nm) leads to a region of strong bi-stability where switching between states might lead to severe noise (Fig. 3.14b, A_0=10 nm). Finally, increasing A_0 to relatively high values (i.e. A_0>40-50 nm) leads to a noise-free region below, at and above resonance. This type of noise has been previously reported[80,135] but can be generally decreased by fine tuning of either A_0 or A_{sp}/A_0. Thus, this type of noise is not related to the A-state but to the standard L and H-states. In fact, the A-state is more prevalent for small values of Asp. The fact that this region is bi-stable (Figs. 3.14c and d) has been verified[79] by acquiring multiple APD curves for these values of A_0 (data not shown). For example, it is found that by increasing A_0 (Fig. 3.14c, A_0=22 nm, A_{sp}/A_0=0.9) and decreasing A_{sp} (Fig. 3.14d, A_{sp}/A_0=0.6) the H-state can reached stably and immediately, producing a noisy images in the L-state and noise-free images in the H-state. In the region of bistability and while imaging in the H-state, the apparent width is typically minimum and resolution maximised. This is a consequence of intermittently contacting the sample and decreasing the effective area of interaction. The theoretical description is given in Chapter 4. Finally, increasing A to relatively high values (i.e. A_0>40-50 nm) leads to a noise-free region below, at and above resonance. In this case, a single branch exists at and below resonance (Fig. 3.14e, A_0=50 nm). Imaging in these conditions corresponds to standard tapping mode and has the advantage of avoiding the noise related to switching between states since a single branch exists there.[79,136] Nevertheless, typically, the apparent height is reduced and the apparent width increases compared to the above, more complex conditions where the L and H-states co-exist (Fig. 3.14f). Moreover, for these values of free amplitude (A_0>50 nm) and set-up conditions the H-state is typically reached at once even above resonance and for relatively high values of normalised set point (i.e. A_0=50, A_{sp}/ A_0<0.9 and β>1). These results are general and could potentially be transferred to other imaging scenarios provided variations in cantilever-sample characteristics (Fig. 3.7) are accounted for. Significantly, also note that even though the average force dramatically scales with A_0[41], the apparent height for A_0=4 nm is similar to that obtained for A_0=10 nm. This is also a general result since a dramatic increase in apparent height by reducing A_0 has been never been observed in this study. The physical interpretation of this phenomenon is discussed in Chapter 5.

As a further model system, experiments with DNA-protein systems on mica substrates have also been carried where similar results have been obtained.[153] This implies that the stability of the operation mode (i.e. L-state (non-contact), L-state (attractive-intermittent contact), H-state (repulsive) and single branched imaging) highly depends on the substrate of choice when imaging isolated and small (i.e. nanoscale) single molecules. This could be due to the ratio of surface area covered by the substrate as opposed to that covered by the given molecules. Nevertheless, even when increasing the density of DNA molecules on the surface (data not shown) the results provided in this section hold. In particular, for a layer of DNA on mica (i.e. 10-30 molecules per μm^2) the value of A_c (according to Fig. 7) could double but the stability of force regimes and operation modes and the ability to control them with operational parameters remains consistent with the results presented here.[79]

3.3.5 Continuous and discontinuous force transitions: peak forces

3.3.5.1 Overview

In this section the differences between force regimes and oscillation states are discussed in detail.[122] The relevance of this discussion is that even though it is typical in the literature[44,134] to use such terminology interchangeably, the differences are, sometimes, dramatic.[59] For example, a major difference is the magnitude of the transient and peak forces during transitions. All of this is discussed below. Some of the definitions are repetitive and are used here for clarity, although they have already been discussed in previous section.

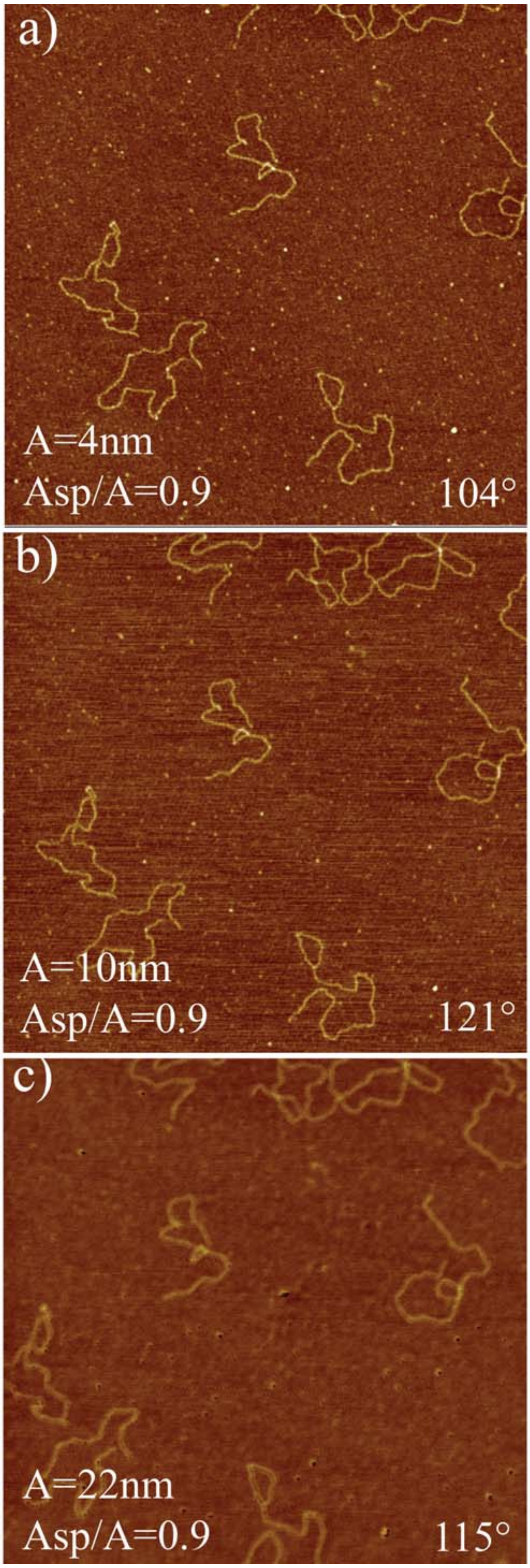
a)
A=4nm
Asp/A=0.9
104°
b)
A=10nm
Asp/A=0.9
121°
c)
A=22nm
Asp/A=0.9
115°

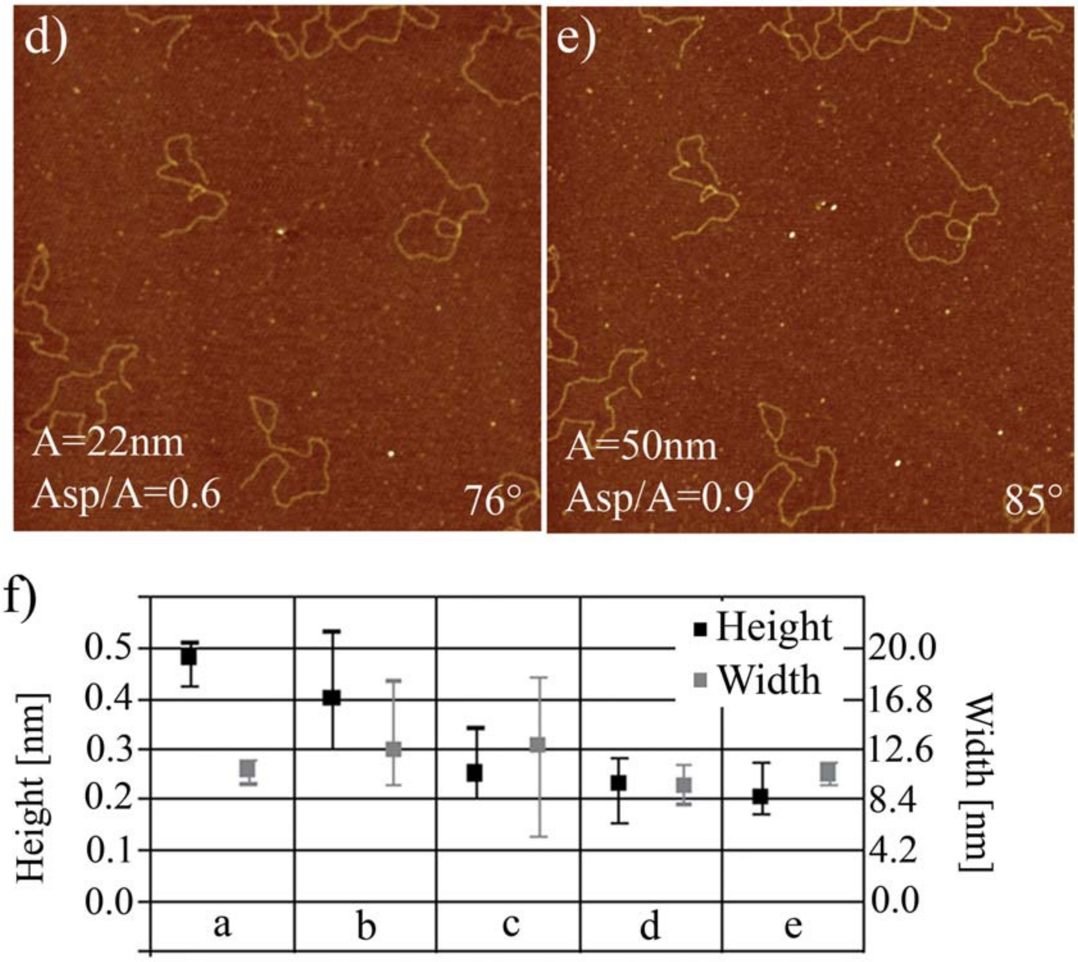

Figure 3. 14

a) to e) Sequence of topography (Z piezo) scans where cantilever free amplitude, is gradually increased from 4 nm to 50 nm respectively. The value of A_0 and relative set-point used in each scan is shown in the bottom left corner of each image. The average-phase shift is shown in the bottom right corner indicating whether in the attractive or the repulsive regime. The apparent molecular heights and widths are shown in f) in black and grey respectively. (f_0= 325.0 kHz, β=0.9995, k~40 N/m, Q factor~500 and RH=55%, Scan size: 2 x 2 µm).

It has already been discussed that when two solutions exist, these are termed the High (H) and Low (L) state respectively and correspond to two different cantilever amplitude branches for a given equilibrium tip-sample distance (z_c). In addition, a net attractive and a net repulsive average force per cycle define what are commonly termed the attractive and the repulsive force regimes[41] and, with some exceptions[1], these correspond to the L and the H-state when they exist (Figs. 3.2 – 3.3). Nevertheless, the attractive and the repulsive force regimes can also be defined when a single branch exists (see Fig. 3.14e), thus, a transition between force regimes might or might not involve a switch between amplitude branches.[41] In fact, there are several fundamental differences between force transitions and state transitions from a physical point of view. First, a force transition has to be defined whereas the existence of states is a fundamental property of the system. For example, initially, force transitions were defined as purely non-contact to intermittent contact force per cycle whereas the net attractive to net repulsive force transition is now more commonly used. On the other hand, the dynamics of the cantilever dictate whether there is one, two or more physically available oscillation states and this is an inherent characteristic of the system that can be explained mathematically as a multiple solution (double for bi-stability) to the differential equation governing the motion (see equation (3.13)).

Additionally, it turns out that for a microcantilever vibrating near a surface and for the typical parameters used in dynamic AFM the transition between states has to be discrete[41,80,145] (i.e. step-like changes in amplitude and phase have to occur) and it is stochastic in nature[79,145] (e.g. the transition might be caused by any noise resulting in an error or perturbation in amplitude). In fact, the latter convention (e.g. force transitions as transitions from net attractive to net repulsive forces per cycle) has become more common, partly because it allows 1) distinguishing between the L and the H-state when these exist and 2) these can be experimentally monitored by recording the phase shift.[41-42,48,98] However, while phase shifts always follow the net force in this way *by definition*, large energy dissipation in the tip sample junction might impede distinguishing between the L and the H-states with the phase convention. This is because even though these might still co-exist when severe dissipation takes place; both might lie either in the repulsive or in the attractive regime. However, even in these situations, APDs curves may still be used to differentiate between oscillation states by monitoring the phase shift. Additionally, the emphasis on the above remark, i.e. *by definition*, is necessary here since, strictly speaking, the actual average force might not follow the phase shift as in the convention.[1,122] For example, for small values of set point (i.e. $A_{sp}/A_0 << 1$), the average force might be negative and the phase shift might lie below 90 degrees. This agrees with equation (3.12) above and the assumption made to derive it. Nevertheless, in the absence of inelastic interactions and when the two states are present, the L and H-states always follow the phase convention. This last statement agrees with equation (3.11) and is described in Fig. 3.3.

In summary, when phase shifts are used to differentiate between force regimes this should be done with the understanding that this is strictly a convention. That is, the phase convention typically, but not always, provides actual information about the real sign of the average force per cycle.[122] This last point is very important when dealing with ultra small set-points which is the topic of Chapter 4. Furthermore, the phase convention is used throughout as otherwise stated. Next a demonstration of differences between step-like and smooth transitions from the attractive to the repulsive regime is provided. At the end of this section a discussion about the magnitude of forces involved in the two different types of transitions is given.

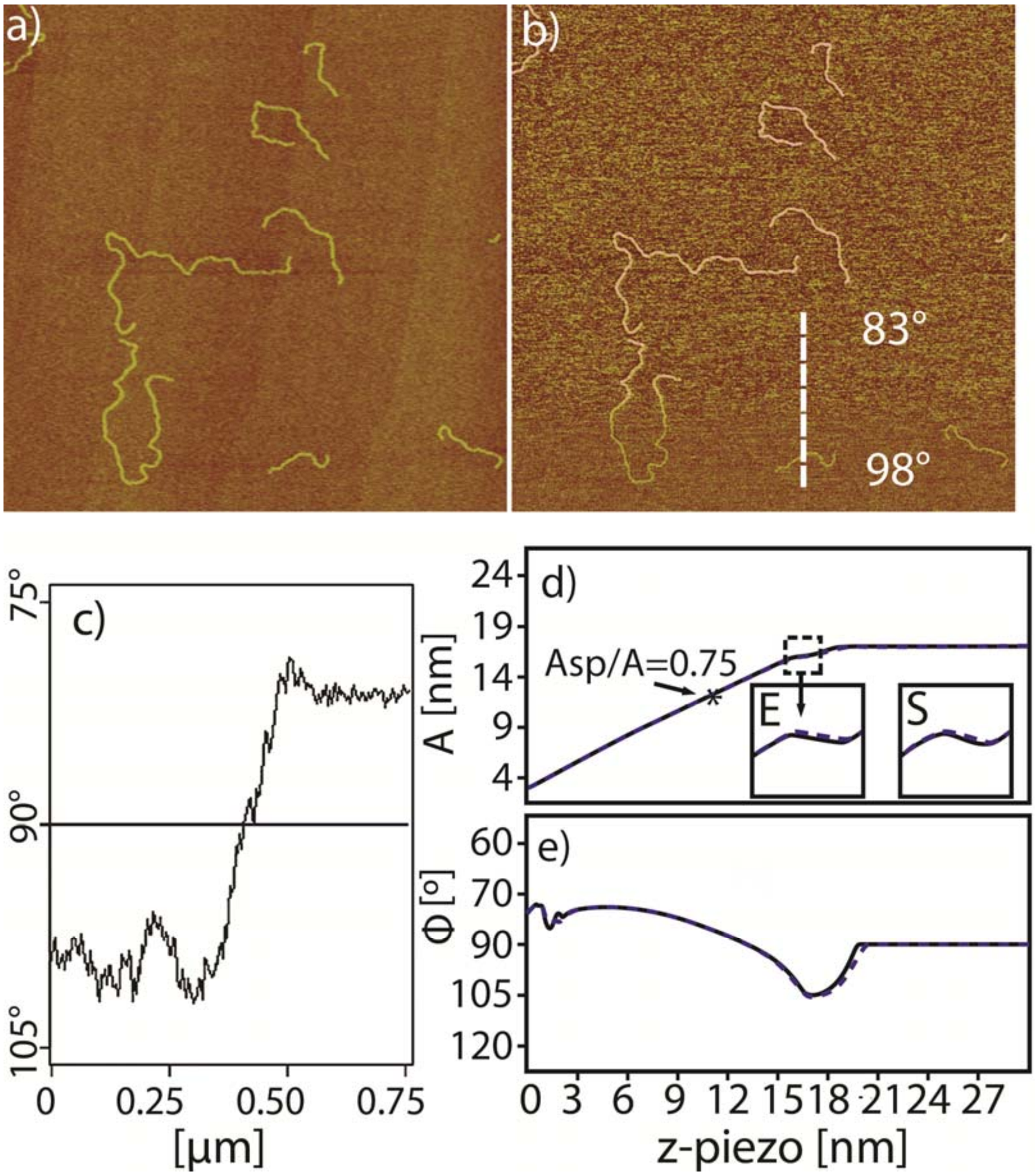

Figure 3. 15

An experimental smooth transition between force regimes occurring where a single branch or oscillation state exists. Thus, no switch between states can occur, but a transition between force regimes is still possible through the single branch. a) Topography and b) phase contrast of dsDNA molecules on mica where a smooth transition from the attractive to the repulsive regime is observed. c) Line-section of the phase image as indicated by the dashed line in b. Corresponding d) amplitude and e) phase distance curves. Insets in (d) show the smooth transition observed experimentally (E) and by simulation (S). The continuous (dashed) line stands for extension (retraction). Slow scan axis upwards. (Experimental Parameters: A_0=17 nm, A_{sp}/A_0=0.75, k=40 N/m, Q=550, f_0=318 kHz and f=f_0).[122]

3.3.5.2 Continuous transitions

Here, the two most common scenarios in AM AFM are considered; 1) regions where a single branch exists (Fig. 3.15) and) and 2) regions where bi-stability is present and the amplitude set-point (and/or free amplitude and/or drive frequency) has to be adjusted to avoid and/or control bistability (Fig. 3.16). A switch between states involves a small perturbation in A and a step-like shift in Φ and z_c. This follows from the discussion on phase space diagrams and the non-linear analysis of the system given in section 3.3.4.4. However, it can be experimentally verified that cases exist where neither the topographic (Fig. 3.15a) nor the phase contrast (Fig. 3.15b) images show a discrete step as the phase shifts from $\Phi > 90^\circ$ (bottom of the scan) to $\Phi < 90^\circ$ (top of the scan). Amplitude (Fig. 3.15d) and phase (Fig. 3.15e) distance curves readily allow experimental verification that, in this case, the transition is smooth. Note that a smooth transition in phase, occurs both on z-piezo extension and retraction, with no signs of hysteresis. A region with negative slope can be observed in the amplitude curve (Fig. 3.15d) in the region close to where the phase crosses 90° indicative of a single branched region as previously reported for APDs.[1,41,154] This negative slope is smooth and deterministic and does not imply the onset of intermittent contact from purely non-contact nor is it due to adhesion. This can be shown with simulations and the use of the point mass model and the DMT and van der Waals forces as described in section 3.1 and 3.2 respectively.[79] The model shows instead that this negative slope always coincides with a smooth increase in the repulsive net force (and decrease in phase shift) with decreasing z_c. Nevertheless intermittent contact already occurs before this negative slope starts (i.e. for higher values of z_c). This negative slope region might, however, cause instabilities and/or artefacts when using an AFM with an amplitude feedback.[1,154] Nevertheless, in the single branch region the cantilever can, in principle, be driven from the repulsive to attractive force regime (irrespective of the sign of the slope in amplitude), for example with z-piezo modulation. Hence, the behaviour here is drastically different from the situation when two oscillation branches exist where no form of feedback could control a switch between states. Note that, here, controlling a switch between states means controlling the cantilever when a switch occurs. This is different from choosing an appropriate set of operational parameters for which one or the other state is highly stable; this type of control has been shown in the previous section (Fig. 3.14).

A line-section (Fig. 3.15c) of the phase image across the transition region (dashed line in Fig. 3.15b) shows that the transition takes place for a distance of approximately 250 nm (~ 40 sec) in the slow scan direction. When bi-stability is not present, then a single branch or state exists and a shift in phase for a constant set of operational parameters and cantilever properties is always associated with a change in energy dissipated in the tip-sample interaction[48]; this indicates a change in either the local environment or the properties of the sample[42,48,98,118] as discussed in detail in section 3.3.3. Also, as discussed in section 2.2.2, at intermediate values of relative humidity, the surface of mica is extremely active and the height of the water layer and the concentration of salts and other impurities might rapidly vary.[18,155] Thus, since the image in Fig. 3.15 has been taken at 60%RH, it is reasonable to think that such activity has been the trigger of the smooth phase shift.[122]

3.3.5.3 Discontinuous transitions

Here an experimental example of a transition from the H to the L-state for small set-point ratios (e.g. $A_{sp}/A_0<0.3$) is discussed. In this case, a step-like discontinuity is observed both in the topographic (Fig. 3.16a) and the phase contrast (Fig. 3.16b) images. The discontinuity can also be observed in the corresponding APD curves (Fig. 3.16e and f). This is a characteristic transition between states, except for the fact that both the L and the H-state occur when the phase is greater than 90°. Fig. 3.16e is significant for three reasons;

1) First it shows that this is a Type III APD system since, even for this relatively large value of A_0=56 nm, the A-state can be observed (note the zoomed view of the end of the curve labelled *E* for experimental). Thus a relatively large value for *R* can be deduced (see also the discussion below).

2) Second, it shows that for the smaller values of normalised set-point here discussed, i.e. $A_{sp}/A_0=0.18<<1$, the L and the H-state coexist. Note the two amplitude branches there. Thus a switch between states can be expected.

3) Third, the second zoomed view marked with an S represents the same region as the other zoomed view but this is a simulated APD curve obtained with the conservative potential described in the beginning of Chapter 3. Since the A-state is also observed there, even though it has zero amplitude in this case (see the zoomed view in Fig. 3.13e), this implies that the A-state is not exclusive of non-conservative potentials or hydrated environments, at least for zero-amplitude solutions.

Further information about this system is provided by the phase response as shown in the Amplitude Phase (AP) curve in Fig. 3.16e. There, comparing the Amplitude Distance (AD) curve (Fig. 3.16e) with the AP curve Fig. 3.16e one first observes that while on extension (continuous black lines) the H-state prevails, on retraction (dashed blue lines) the A and then the L-states are first reached before the H-state. The comparison between the two is important because, while by convention, the attractive (repulsive) regime is that for which values of phase are larger (smaller) than 90 degrees, both solutions produce a phase lag larger than 90 degrees in this case (note that markers for L and H where L stands for L-state and H for H-state). That is, both the L and H-states have phase lags larger than 90 degrees implying that both lie in the attractive regime, by convention (see the details of this convention in Chapter 3.3), in this case. Thus, this is an example where severe inelastic interactions disturb the shape of the perfect elastic response in phase for the L and H-states in Fig. 3.3.[41,48,98] However, since a switch between states still occurs, this is a transition between states but not a transition between force regimes. Thus, that a switch between states has occurred can be established by comparing the average phase shift in the scans (Fig. 3.16b) with the behaviour in amplitude and phase in the APD curves (Figure 3.16f and g); markers (H and L) are placed in the phase curve (Figure 3.16f) for the set-point used in the scan (Figures 3.16a-b).

Note that both the AD and the AP curves are required to understand this phenomenon since the phase on its own is not enough criterion to establish transition between states but force regimes only. There is considerable loss of contrast in the L-state, both in topography and phase. We have consistently had the same outcome for over 50 probes and the situation for which the L-state can only be physically reached with small set-points (A_{sp}/A_0<0.3) occurred only when using relatively high free amplitudes (A_0>40-50 nm). This situation generally coincides with higher instabilities and loss of contrast in the L-state compared to the H-state (see Fig. 3.16) and the requirement of high critical (minimum) free amplitudes (A_0>30-35 nm) to reach the H-state at resonance even with stiff cantilevers (k>20 N/m). The above indicates that a large tip radius *R* might be required to experimentally observe such behaviour.[42,118] This has been confirmed by imaging the AFM tips with an SEM (i.e. Fig. 3.5) and, in all cases (provided k is sufficiently high), this behaviour (Fig. 3.16) was displayed only for *R*>20-30 nm, i.e. Type III systems. Furthermore, energy dissipation calculations (3.9) show that more energy is dissipated per cycle in the H-state (ΔE_{ts}~500 eV) than in the L-state (ΔE_{ts}~50 eV). This phenomenon occurs even when allowing for large errors in the parameters involved in the calculation (i.e. ±20% in Q, ±20 N/m in k and ±30° in φ). This dramatic difference in energy dissipation between states can also be qualitative deduced by looking at the dramatic difference in phase contrast in the L and H-states (note the scales; Δ1° in the L-state and Δ30° in the H-state in Fig. 3.16b). Hence arguments similar to those used to derive the stability criteria for energy[15] (3.16) cannot be used to interpret this common and highly reproducible phenomenon. It is also unlikely that more energy is dissipated into higher harmonics in the L-state than in the H-state since, typically, harmonics are more readily excited in the repulsive regime and/or for larger sample indentations.[5,21,23]

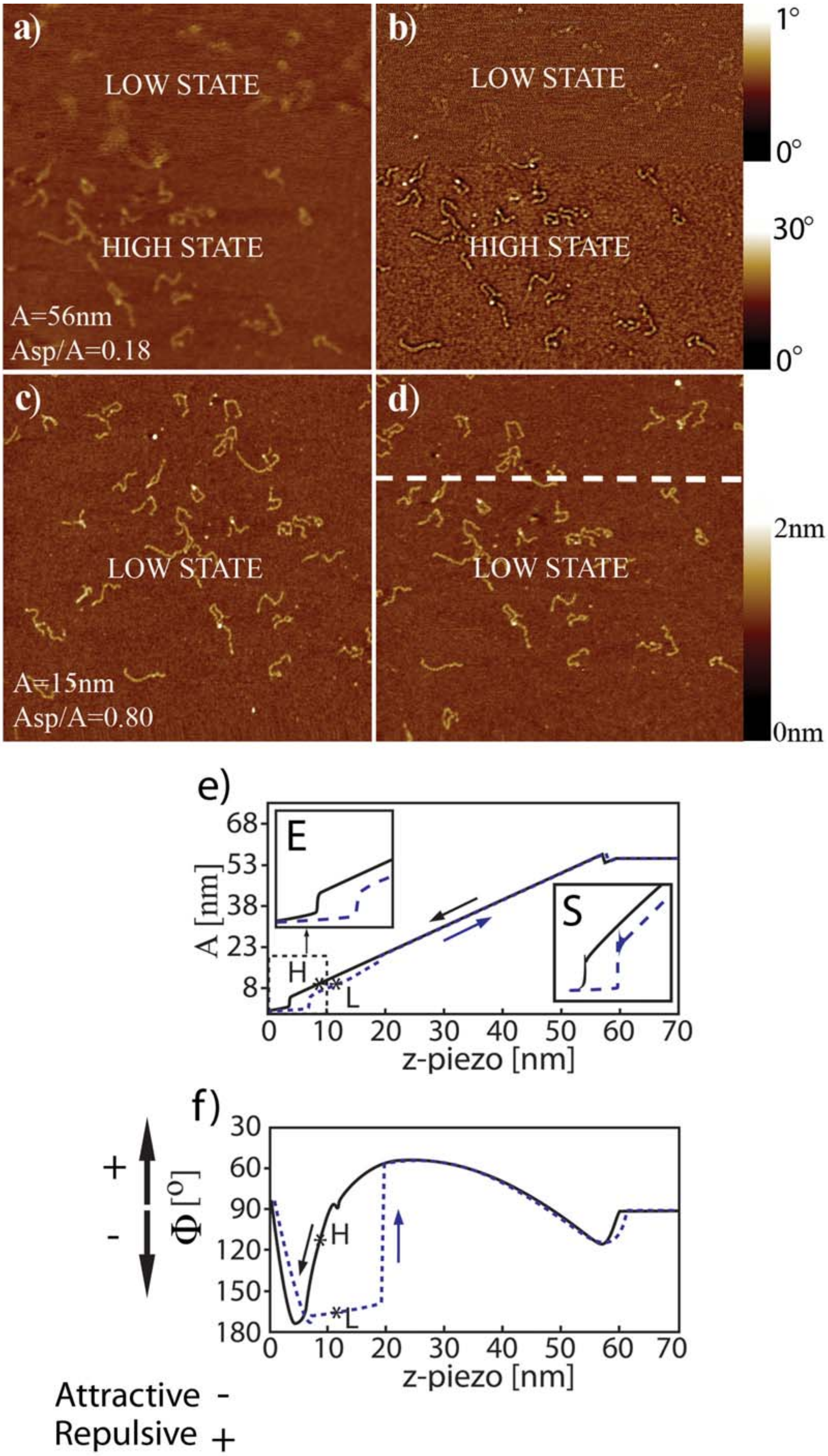
a)
LOW STATE
HIGH STATE
A=56nm
Asp/A=0.18
b)
LOW STATE
HIGH STATE
1°
0°
30°
0°
c)
LOW STATE
A=15nm
Asp/A=0.80
d)
LOW STATE
2nm
0nm
e)
E
S
H
L
A [nm]
68
53
38
23
8
0
10
20
30
40
50
60
70
z-piezo [nm]
f)
+
-
Φ [°]
30
60
90
120
150
180
H
L
z-piezo [nm]
Attractive -
Repulsive +

Figure 3. 16

An experimental discontinuous transition at high A_0 and low A_{sp}/A_0. a) Topography and b) phase contrast where a switch from the H to the L-state occurs. Topographic scans in the L-state with small free amplitudes (A_0) taken both c) before and d) after the scans shown in a-b). The dashed line separates the regions scanned in the L and H-state in the top images respectively. Corresponding e) amplitude and f) phase distance curves are shown in extension (continuous line) and retraction (dashed line) with a free amplitude of A_0=56 nm at resonance. Insets in e) show snap-to-contact and adhesion hysteresis for experiment (E) and simulation (S). The "zero" for z-piezo is chosen arbitrarily in the APD curves. (Experimental Parameters: a-b) A_0=56 nm, A_{sp}/A_0=0.18, k=40 N/m, Q=650 and f_0=332 kHz and f=332 kHz; c-d) A_0=15 nm, A_{sp}/A_0=0.80 and k=40 N/m).[122]

It could also be argued that as the effective resonant frequency shifts to higher frequencies with increasing free amplitude[150] and, usually, decreasing set-point, noise should be observed for these choice of operational parameters (i.e. relatively high free amplitudes and low set-points). Nevertheless, as discussed in section 2.1.2.3 the effective resonant frequency has a single value for a set of operational parameters (except set-point), separation (z_c) and cantilever-sample properties [150], hence the same (or less) noise should be observed in the L-state in these cases. This follows from the fact that for a given set- point (as in Fig. 3.16 or any scan in AM AFM) the cantilever vibrates higher above the sample (larger z_c) in the L-state (implying lower resonant frequencies there) than in the H-state; this (larger z_c) has been theoretically shown to lead to lower effective resonant frequencies, i.e. there are two values of resonant frequency and in the L-state the resonant frequency is lower.[150]

In Chapter 6, APD curves like those shown in Figs. 3.16e-f are defined as Type III curves. The A-state is particularly prevalent for even relatively large values of set-point for this Type III curves. Hence the noise observed in Figs. 3.16a-b can be readily interpreted as a consequence of the existence of the A-state where this can trap the tip onto the surface, or more thoroughly, the water layers on the surface.[137] The A-state is little or no sensitive to separation z_c. Thus, an AFM operated in the AM AFM mode cannot properly track the surface since sensitive to separation is a prerequisite of AM AFM. This argument further agrees with the values of R required to strengthen the A-state and get Type III systems (i.e. R>20-30 nm).

$$\frac{k}{2}(Asp)^2 \geq \Delta E_{ts}\frac{Q}{2\pi} \tag{3.14}$$

The area shown in Figs. 3.16a-b was also imaged in the L-state with relatively small free amplitudes (A_0=15 nm) before (Fig. 3.16c) and after (Fig. 3.16d) performing these high free amplitude scans. The dashed line in Fig. 3.16d divides the scan between the area imaged in the L-state in Figs. 3.16a-b (bottom) and the H-state (top). No significant loss of contrast is observed between top and bottom in Fig. 3.16d or between the scan taken before and after high free amplitude imaging (cf. Figs. 3.16c and d). These results are general in our experiments, such that when R>20-30 nm and, consequently, the dynamics are similar to those observed in Fig. 3.16e-f (i.e. Type III systems), no tip or sample damaged could be observed. These results can be interpreted as the tip having achieved mechanical and chemical stability. The physical interpretation for this stability is discussed in Chapter 6.[148]

Finally, Figs. 3.16c-d are also demonstration of how by simply reducing the free amplitude to low or intermediate values (typically $2<A_0<15$ nm according to experiments), L-state imaging with relatively low noise levels can occur even when using Type III systems.

The interpretation is also provided by the behaviour of the basins of attraction for the A-state with decreasing A_0 and perturbation theory (Chapter 6). Similar experiments have been performed below and above resonance where some trends for these mechanically stable tips have been found (Type III systems). Note that the system (or set-up) used to obtain s. 3.13 – 3.14 is also of the Type III, or, more thoroughly, of the Type II evolving into III (see Chapter 6).[137] This is also consistent with the noise patterns discussed in Fig. 3.13. The discussion below is relevant to Type III systems.

First, the noise can be reduced in the L-state for relatively small free amplitudes by keeping the set-point relatively high and while driving close enough to resonance (see Figs. 3.13d and g and Figs. 3.16c-d). Then for relatively high values of free amplitude (A_0>40-50 nm) repulsive imaging is generally observed to reduce noise at and/or below resonance (Fig. 3.14e). This reduction in noise can be observed via single branched regions as in Fig. 3.14e or via the H-state with intermediate set-points (i.e. Fig. 3.14d).[122]

3.3.5.4 Peak forces

An amplitude curve has been obtained by setting appropriate parameters to the equation of motion and the cantilever-sample parameters[122] to reproduce the APD curves in Fig. 3.16. As an example, Fig. 3.17 shows the mean tip-sample forces occurring and the amplitude (Fig. 3.17c) and phase (Fig. 3.17d) at high set-points. For very small separations ($z_c/A_0<0.03$) the tip adheres onto the surface where the mean deflection is approximately 1 nm. For higher separations ($0.03<z_c/A_0<0.23$), the L-state dominates on retraction. This is the same behaviour as that shown in Fig. 3.16 and it is also typical of Type III systems (see Chapter 6). Significantly, there is still a considerable amount of negative deflection in the L-state (approximately 1 Å), while the average force remains negative and relatively high (2-3 nN). For the same range of separations, the deflection is smaller in the H-state (Fig. 17a, extension), i.e. the H-state exists with the cantilever closer on average to the unperturbed equilibrium position. This larger mean deflection in the L-state is a consequence of adhesion and tip-sample proximity and a source of noise in situations such as that described in Fig. 3.16. Here the restoring force on the cantilever is pulling it back towards the H-state with mean forces of the order of nano-Newtons. Furthermore, the adhesive force gains strength against the restoring force in the L-state for a given set-point as the free amplitude increases.[122] Nevertheless, the tip-sample proximity cannot be the only source of noise since the cantilever is always closer, on average, to the surface in the H-state (see discussion above regarding the stability criterion). As discussed, the source of noise is the A-state which, for a given set-point, can gain strength with increasing free amplitude.[137]

For the parameters in the simulations (Fig. 3.17), a single branch with respective smooth transitions on both extension and retraction (amplitude, force and phase) and a region with negative slope in amplitude could only be observed experimentally for $A_0>150$ nm. Nevertheless, these large values of A_0 are experimentally unsuitable with $k>40$ N/m for imaging soft matter.[148] In terms of the average and peak forces, in the single branch case and for A_0=190 nm, the peak repulsive (average) forces are 30 nN or less (zero) with a slight dependence on $\dot{z}_c$. When A_0<150 nm and bi-stability exists then these forces can be as high as 400-600 nN (40-50 nN) and are independent of $\dot{z}_c$ (Fig. 3.17). These numbers imply forces of at least an order of magnitude larger when discontinuous transitions occur.

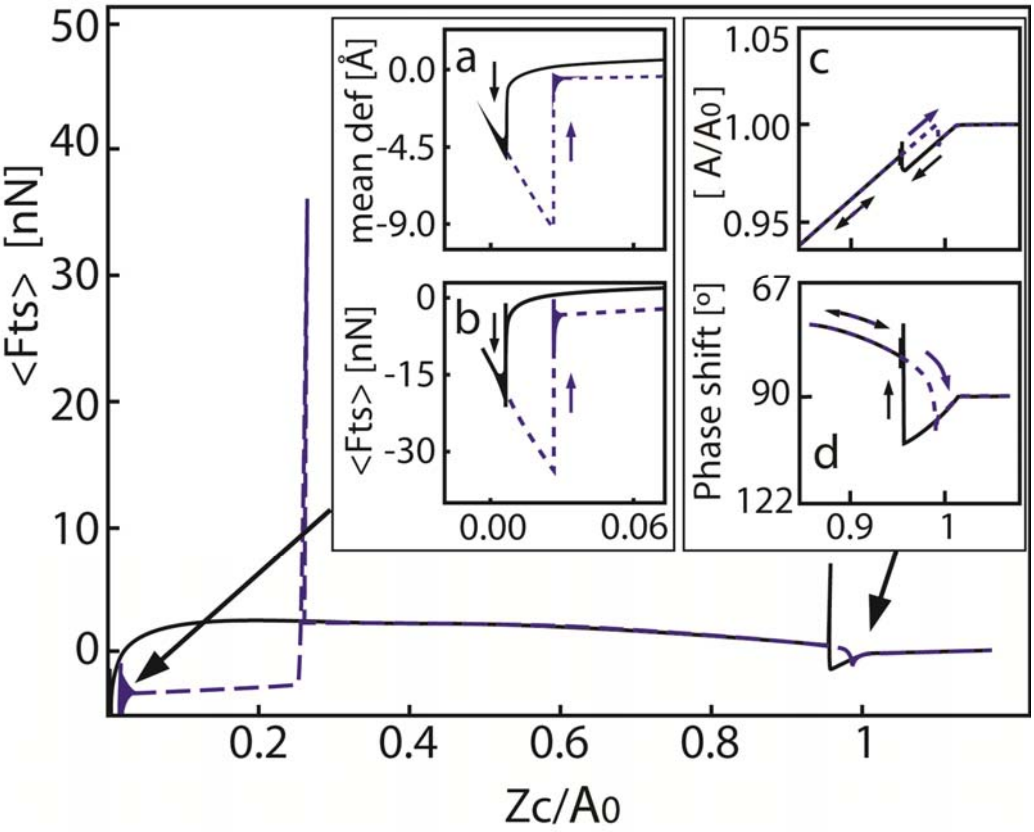

Figure 3. 17

Simulated average tip-sample forces during approach-retract curve, where the cantilever first switches discontinuously to the H-state on extension (continuous black line) and gets trapped onto the surface. On retraction (dashed blue line) it starts trapped in the L-state, then switches to the H-state discontinuously resulting in high transient forces and it finally smoothly returns to the L-state once the H-state ends. Zoomed views of a) mean deflection and b) average force at small separations and c) normalised amplitude and d) phase shift at large separations. Parameters: A_0=63 nm, k=40 N/m, f_0=300 kHz, f=300 kHz, E_t=120 GPa, ν =0.3, H =2x10^{-19} J, γ (surface energy)=100 mJ/m^2, R=30 nm, Q=500 and z_c=73 nm. Note that these are predicted values for H and γ for mica at 40% relative humidity.[115]

Simulations of single branched regions at resonance with free amplitudes as low as 25 nm can be obtained by reducing γ, H and R to 30 mJ/m^2, 6x10^{-20} J and 10 nm respectively. Note that these parameters are those which control the strength of the attractive force component. In this case, smooth transitions (with intermediate free amplitudes, i.e. A_0=25 nm) induce peak repulsive (average) forces which are no higher than 5 nN (zero nN); the average force in a smooth force transition has to be zero by definition. Significantly, for A_0=8 nm these can be as high as 30 nN (2.5 nN); here values in parenthesis refer to average forces. These large differences in applied forces imply that step-like discontinuities should be avoided, even when slowly approaching the surface, to prevent tip and sample damage when transitioning into the repulsive force regime. According to experimental results, this is particularly significant when the tip is sharp[148]; this is due to the high pressures involved when using sharp tips and the energy dissipated per atom.[148] Furthermore, a large tip radius is stable even if using large free amplitudes (see Fig. 3.5c) to achieve L to H transitions even though peak forces can reach several hundred nN whereas sharper tips (e.g. R<20 nm) degrade under these circumstances even when small free amplitudes are used.[122,148] Note for example the outcome of the discontinuous transition in Fig. 3.17 (R>20 nm) and compare it with the consequences of a discontinuous transition when using a sharper tip R<5 nm in Fig. 3.18.[59]

3.3.5.5 The relevance of smooth an discontinuous transitions

The differences between smooth and discontinuous transitions have been thoroughly investigated and discussed. These results provide insight into carefully controlling peak and average forces to preserve both AFM tips and soft samples, such as biomolecules bound to stiff surfaces.

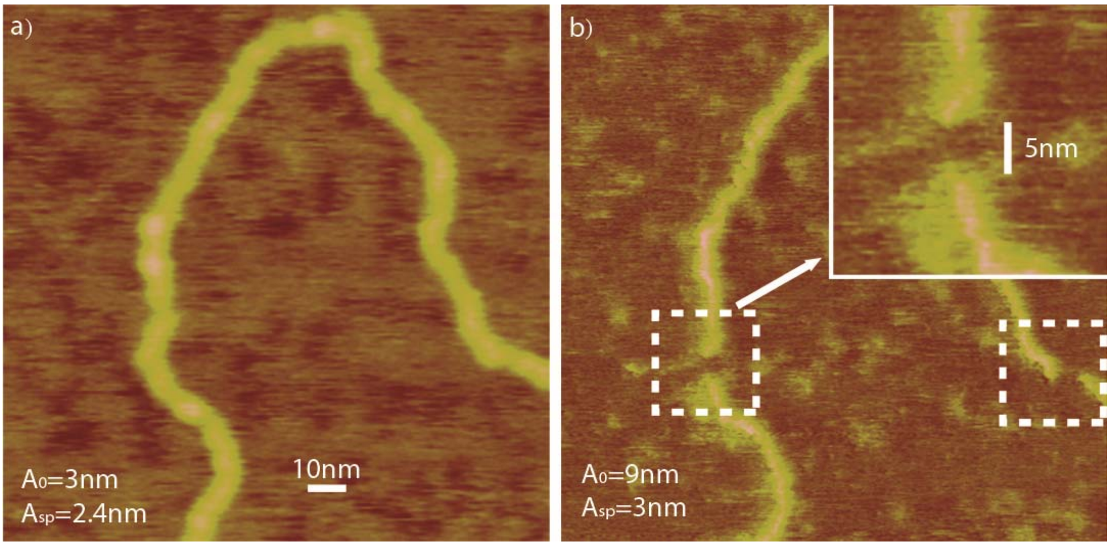

Figure 3. 18

Standard AM AFM imaging of DNA with a sharp tip (*R*<5 nm). Topographic images of a DNA molecule in a) the non-contact mode of operation (A_0=3 nm A_{sp}=2.4 nm) and b) in the intermittent contact mode through the H-state (i.e. tapping). The DNA widths at mid-height, are ~12 and ~4.5 nm respectively. For b) A_0=9 nm was first set for the free cantilever and then the set-point was reduced to A_{sp}=3 nm as it is common practice in AM AFM. A switch to the H-state rapidly followed. The large transient forces induced by a switch from the L to the H-state, plus the inherent high pressures induced in tapping mode, and in particular the H-state when *R*<< [122], have caused localized and severe sample damage for approximately 15 scan lines (~5 nm) in the slow scan axis. The experimental parameters are f_0=315 kHz, f=315 kHz, k~40 N/m, *Q* factor=600 and *R*<5 nm.

Nevertheless, while smooth transitions are preferred because the induced transients are more than an order of magnitude smaller[122], larger values of free amplitude are also required to turn the system into single branched.[150] These larger values of free amplitude invariably imply that more energy is stored in the cantilever while interacting with the sample[148] and, since in the steady state, forces scale with free amplitude[41,79], large forces result as compared to small free amplitude imaging.[59] Furthermore, large amplitude imaging in the repulsive regime typically induces tip-sample wear even with the steady state values of forces, particularly when the tip is ultra sharp.[59,148] On the other hand, it is clear from Fig. 3.18 that intermittent contact, or at least tip-sample proximity, is required to obtain high resolution. Thus, it would seem that the conditions for high resolution, i.e. tip-sample proximity and small free amplitudes (and/or drive forces to use FM AFM terminology) are contradictory concepts. Nevertheless, a phenomenon described in Chapter 4 shows that even with ultra-small oscillation amplitudes and free and/or drive amplitudes, tip-sample proximity is possible.[59] Thus, this phenomenon satisfies both conditions. A model to obtain quantitative data about the effective area of interaction as a function of tip radius in the dynamics mode is also presented in Chapter 4.

3.3.6 Summary

An experimental approach for the systematic acquisition and interpretation of images in AM AFM has been presented using DNA on mica as a model system. The approach has allowed direct interpretation of the experimental data by using the theoretical predictions obtained with the point mass model. The differences between force regimes and oscillation states have been emphasised and the high sensitivity of noise and phase space projection to slight changes in operational parameters has been demonstrated. Furthermore, the likelihood of switching and the presence of noise has been experimentally correlated to the phase space projection and a given cantilever trajectory and/or high mean cantilever deflections. This has been shown under conditions where bistability (i.e. the coexistence of the L and the H-states) is present. The presence of noise in other circumstances, i.e. when the H-state is highly inhibited and/or for small free amplitude imaging, has also been discussed experimentally. The source of noise in these circumstances has been identified with the appearance of a third previously unreported state, i.e. the A-state: the amplitude in this state is insensitive to cantilever-sample separation and, thus, it is not suitable for feedback. The A-state is also related to large values of negative mean cantilever defection as recently reported.[79] The A-state is described in detail in Chapter 6.

From the above results, it is proposed that divergence in height measurements of isolated biomolecules adsorbed on hard surfaces in AM AFM are significantly related to the high sensitivity of the dynamics of the cantilever and cantilever-sample separations to variations in the AFM operational parameters even in the non-contact mode. The apparent width[59,148] and height[156] are modelled in Chapters 4 and 5 respectively and support these conclusions.

Finally, the advantages and drawbacks of the standard imaging procedure involving driving below resonance with relatively high amplitudes (i.e. tapping mode with intermittent tip-sample contact) have been discussed and compared with the advantages and drawbacks of imaging both at and above resonance with relatively small and intermediate free amplitudes.

The thorough and systematic approach taken here, particularly on the experimental side, should allow microscopists using AM AFM to more carefully choose operational parameters for a given imaging application.[79] Since this systematic analysis has been performed with a mechanically stable tip[79,148] (i.e. a Type III system as discussed in Chapter 6), the results lead to reproducible measurements and allow direct comparisons between experiments, advancing data interpretation and instrument development of AM AFM for biomolecular and other systems. Deeper understanding of the mechanisms of image contrast formation has the potential to lead to reproducibly higher resolution and robust data comparison between the different imaging modes and new methods for compositional mapping of surfaces by AM AFM.

Chapter 4

4. Surface proximity and resolution

4.1 Overview

Deformability and topography impose great challenges for resolution on soft matter with the atomic force microscope.[13,15,57] High resolution requires tip-sharpness, proximity and small forces[15,59] but the cantilever dynamics do not always allow satisfaction of all three[59,79] as discussed in Chapter 3. The accepted dogma, discussed in Chapter 2, is that small drive amplitudes lead to either tip trapping or non-contact mode imaging, where proximity is inhibited.[150,154] Contrary to this, the main finding presented in this chapter shows that, in ambient conditions, water layers allow the AFM tip to be brought within several angstroms of the surface using a small amplitude small set-point (SASS) mode[59] with high stability. Thus, the conditions of high resolution imaging are satisfied in the region close to the surface, i.e. z_c~0.1-0.3 nm, where SASS operates.

The key to observing the SASS region in simulations is to add an effective tip-sample distance d^* and the capillary force to the equation of motion. Here, d^* is the distance between the tip and the surface minus the height of the water layers or $d^*=d-2h$. The two makes reference to the fact that there is water layer of height h on the surface of the tip and another on the surface of the substrate. The results of implementing this model are presented below only for ultra-sharp tips (*R*<5 nm). The outcomes for other ranges of *R* (i.e. 5 nm<*R*<30-40 nm) are discussed in Chapter 6. A model to obtain the effective area of interaction in the dynamic mode is also presented[59]. This model has recently been used to estimate the energy dissipated per nm or atom in the dynamic mode[148]; this is discussed in detail in Chapter 6.

The results presented in this section have further implications in terms of the foundations and development of dAFM since they involve small oscillation amplitudes and take into account the effects of capillary interactions (see Chapter 2). For example, the stability criterion (3.14)[15,76] has been used to establish that either large oscillation amplitudes, stiff cantilevers or both are required to avoid tip-trapping and/or to minimize background noise due to tip trapping. Nevertheless, SASS is shown to lead to high resolution, small tip-sample wear and low background noise with ultra-small oscillation amplitudes and with the use of cantilevers of standard stiffness.[59] More significantly, modelling and experimentation shows that stability does not monotonically decrease with decreasing oscillation amplitude provided the SASS region exists.

4.2 SASS and monostability

4.2.1 Model: water effects and the area of interaction

The tip-surface interaction is modelled with the use of the point mass model (3.1) and the long range (3.3) and contact forces (3.7). This is the model described in Chapter 3. Furthermore, in order to reproduce the experimental phenomenon involving the SASS and N regions, the effective distance d^* between water layers on tip and sample and the capillary force F_{CAP} are also added to the tip-sample force. The full model is described in detail in Appendix A.

Furthermore, the interaction between the probe (i.e. tip) and the surface or sample occurs relatively locally but not as if between two mathematical points or delta functions.[59] This results in an effective area of interaction, which, in the dynamic mode, can be termed $<S>$ and it is not straight-forward to define.[59,148] The effect of $<S>$ is to give an apparent width to surface features which is twice the radius $<r>$of $<S>$ plus the real width of the feature or sample. Thus, in the case of a spherical sample the apparent width is $2(<r>+R_2)$ where R_2 is the radius of the spherical sample (see Appendix A). A model to obtain a numerical value of $<S>$ is described next.

The effective area for the vdW force is given by (4.1) (derived in Appendix A). This area is valid for the static case only. In particular, the static effective area of interaction for the vdW forces accounting for 90% of the energy of interaction (note the index 0.90 has been used here). The equation is derived by assuming that the interaction is taking place between an infinitely long, end-on cylinder of radius r (surface) and a sphere of radius R (tip). The reference energy is that for an infinite surface and it is used to normalise the energy of interaction (Appendix A). Then to account for 90% of the vdW energy of interaction, r is chosen so that the energy of interaction between the cylinder and the tip is 90% that of the infinite surface and the tip. Note that the effects of the capillary F_{CAP}, F_{DMT}, or any other, forces can be also accounted for. For example the Kelvin equation has been used here to obtain the radius of interaction due to F_{CAP}. The radius due to the contact forces has also been accounted for (Appendix A).

With the expression for the static area of interaction of a given force, (26) and (27) can be used to finally obtain <*S*> in the dynamic mode (28). The index i stands for the iteration parameter or instantaneous value in the simulations.[59] The final value <*S*> Eqn. (28) is the effective area of interaction per cycle for a given equilibrium cantilever-surface separation z_c.[59,148]

$$S_{vdW}(d,R) = \pi(8.9R^{1/4}d^{4/5} + 0.6R)^2 \tag{4.1}$$

$$< S_{vdW} >= \frac{1}{< F_{vdW} >}\sum_{i=1}^{i=n} Area_{vdW,i}F_{vdW,i} \tag{4.2}$$

where

$$< F_{vdW} >= \sum_{i=1}^{i=n} \left|F_{vdW,i}\right| \tag{4.3}$$

and similarly for the DMT and capillary forces.

Finally

$$<S>=\frac{<S_{vdW}><F_{vdW}>+<A_{DMT}><F_{DMT}>+<A_{CAP}><F_{CAP}>}{<F_{vdW}>+<F_{DMT}>+<F_{CAP}>}$$

(4.4)

and the effective radius is simply

$$<r>=\sqrt{<S>/\pi} \quad (4.5)$$

4.2.2 SASS mode

The phenomenon which makes SASS possible is shown in Fig. 4.1a; this is an experimental AD curve taken on a muscovite mica surface at 40%RH. For large equilibrium cantilever-surface separations (A_0/z_c<<1) the oscillation amplitude remains constant (A/A_0~1). As the cantilever approaches the surface (dashed lines) there is an outer region of positive (OP) slope, then a region of negative slope (N) follows, after which a local maximum in A is observed, and finally an inner region of positive slope (IP) occurs. No hysteresis is observed (continuous lines: retraction). In the OP region, the mode of oscillation is typically termed L-state of oscillation and generally leads to non-contact (nc) imaging for these small values of A_0.[41,80] The IP region corresponds to the H-state of oscillation where the tip is closer to the sample. The trajectory followed is always the same (OP, N and then IP) and is deterministic. This is a general characteristic of a sharp tip using small values of A_0 ($A_0 \leq$2-3 nm) in ambient conditions. Deterministic here implies that out of any number of APD curves the same trajectory always follows. This behaviour is opposed that obtained in dAFM when the L and H-states coexist since the behaviour is stochastic then. That is, while a switch might occur for a given APD curve, it might not occur in the next even though the same operational parameters might be used for the two curves. The stochastic phenomena has been extensively discussed in Chapter 3.3.4. In Fig. 4.1b, the corresponding mean deflection of the cantilever is shown indicating that at no value of amplitude is the tip in continuous contact with the surface. The existence of the N region is of significant experimental relevance for two principle reasons:

1) Firstly, it implies that the surface can be reached smoothly without step-like transitions in force and amplitude.[122] The relevance of smooth transitions has been discussed in Chapter 3 (Figs. 3.12 – 3.15).
2) Secondly, the tip can get closer to the sample than it would otherwise through the L-state; i.e. the cantilever is led onto the H-state via this N region.

In summary, tip-sample proximity is achieved through the H-state (IP-region) with very small values of free (A_0) and/or drive (F_D) force[59]. An example of the difference in resolution due to this increased proximity is shown in Figs. 4.1c and d respectively, where a dsDNA molecule on a mica surface has been imaged in the OP (L-state and nc-mode) and the IP (SASS mode) regions. The double helix of the DNA molecules can only be resolved using the latter, the conformation is consistent with the B-form (helical pitch: 3.3 nm) and the right-handed pitch is observed (compare with Fig. 1.6). A further example of nc versus SASS mode is shown in Figs. 4.1e-h and in Fig. 4.1i another SASS mode example is given.

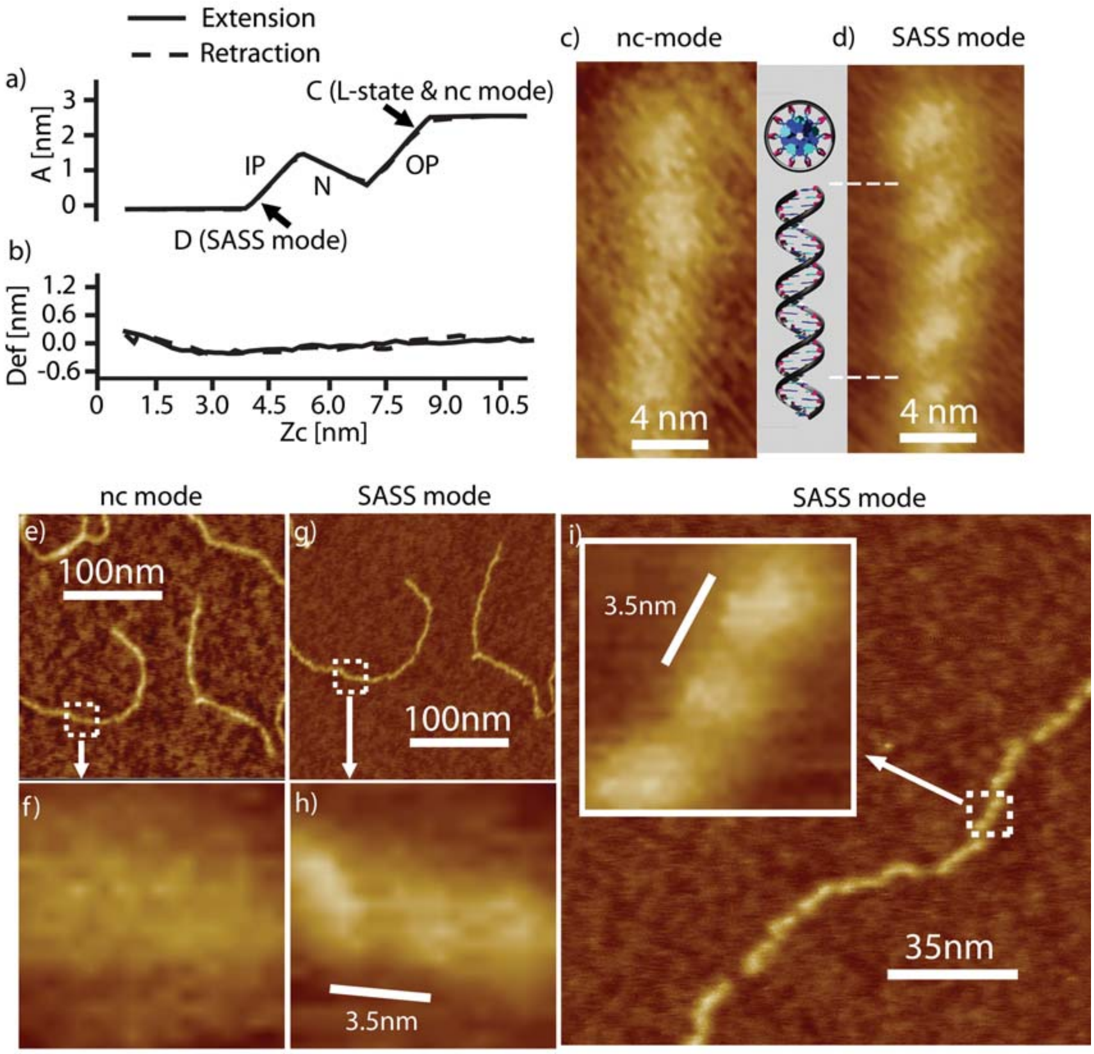

Figure 4. 1

Experimental a) amplitude distance AD curve and b) corresponding mean deflection where the OP (L-state and nc mode), the N and IP (H-state SASS region) regions can be observed in the AD curve. Here OP stands for outer positive and refers to the outer amplitude branch with a positive slope. Similarly IP stands for inner positive and refers to the inner amplitude branch with a positive slope. The N stands for negative and refers to the amplitude branch with negative slope. The markers point at the values of amplitude used to obtain c) and d) respectively. It is in the SASS region d) where maximum resolution is obtained and where periodicity is observed in the DNA molecule. The molecular model of 30 bp B-form DNA is rendered at the same magnification. Another example is shown where e-f) the nc mode is compared to g-h) the SASS mode. The experimental parameters are: f_0=312 kHz, f=f_0, k~40 N/m, Q=550, RH=40%, R<5 nm, A_0=2.5 nm and A_{sp}=2.2 and 0.1 nm for nc and SASS mode respectively. The scan speed was 0.6 μm/s.

Thus SASS is a mode of operation that works in the H-state past the local maxima in A.[59,137] Nevertheless there are two main differences between this region and the standard H-state reported and discussed in Chapter 3. First, in the standard H-state, the two stable oscillation states (L and H) coexist. This leads to intrinsic noise due to the finite probability of switching dynamics (Figs. 3.6, 3.8 – 3.9).[79-80,145] By contrast, the SASS region is monostable and no tip trapping can occur. Second, in order to reach the standard H-state, A_0 and/or F_D need to be significantly increased, meaning that small forces are not possible. This holds irrespective of the cantilever drive frequency and has been shown in Chapter 3 (Figs. 3.11 and 3.13).[137] The small forces involved in SASS, as compared to the standard H-state, can be experimentally verified by observing that, in the standard H-sate, and when using an ultra-sharp tip, the tip and/or sample get damaged immediately (Figs. 3.15 and 4.2), as opposed to SASS where imaging can be carried out for hours with high resolution and no tip wear.[59] Because of these physical differences, it is preferred to refer to the former IP region as the SASS region and to the latter IP region as the standard H-state (Fig. 4.3a). Thus, this is the terminology employed from now onwards in the discussion. The engaging method in SASS is described next.

In standard AM AFM methods, the amplitude A_0, or the magnitude of the driving force F_0 (I.2), is generally first set for the free cantilever and then A_{sp} is slowly decreased once the tip is engaged. Unfortunately, in this way, it is not possible to avoid the high interaction regions $A_{sp}/A_0>0.2\text{-}0.3$ observed in the force simulations.[1,147-148] Also note that, in FM AFM (Chapter 2), F_0 is typically varied as tip-sample forces start affecting the dynamics of the lever. Discontinuous force transitions[122] (Chapter 3) also typically occur which dramatically increase the force

(Fig. 3.15). The standard way in which to reach the repulsive regime further consists in using relatively large values of A_0[79] (Chapter 3). Thus, this method of approach results in an increase in pressure with increasing A_0 which induces tip broadening and an increase in $<S>$, especially for high set-point values.[148] On the other hand, the maximum in pressure is avoided in the SASS method of engaging thanks to both the SASS and the N regions. An example is given next by describing Fig. 4.2. First a very small free amplitude (A_0<2-3 nm) is set for the free cantilever. Then, safe engaging follows by slowly reducing A_{sp} down to small amplitudes (i.e. A_{sp}=1.7 nm). At this point the L-state and nc mode is reached (Fig. 4.2a). Then, the set-point is further reduced (i.e. A_{sp}=0.15 nm) and, if the SASS region exists, it is reached smoothly through the N region. That is, once A_{sp}=0.15 nm, the tip is generally safe from damage. Note that the velocity of approach while engaging has to be minimized to not blunt the tip even with these very small free amplitudes.[122] Finally the driving force can sometimes be increased to several nm to enable the tip to more readily track the sample; note the parameters in Fig. 4.1d and g. This is because enough energy needs to enter the cantilever per cycle in order to stabilize the motion. This phenomenon can be used as a verification of the stability criterion[15] (3.14). For example A_{sp}=0.1 nm and A_0<1 nm might result in severe noise whereas A_{sp}=0.1 nm and A_0=1.5 nm might result in low noise and ultra high resolution.[59] These small values of free amplitude (A_0<3-5 nm) would be the preferred for small tip-sample forces. Nevertheless, in Fig 4.2b A_0 has been increased to emphasize the differences between Tapping Mode (TM) and SASS. Furthermore, when larger free amplitudes are required to minimize noise, the resolution is not maximum. For example, compare Fig. 4.1 where SASS is shown in operation with A_0<3-5 nm with Fig. 4.2b where SASS is used with A_0~3 nm. In summary, the SASS engaging method avoids hard tapping regions (i.e. A_{sp}>0.1-0.5 nm) and large transients so that the SASS region shown in the APD in Fig. 4.1a can be safely reached. An example of the effects of the transients in force when reaching the H-state in the typical engaging approach is shown in Fig. 3.15. There a DNA molecule is cut at the point where the H-state has been reach via a step-like switch from the L-state. The standard engaging approach is also shown in Fig. 4.2g-i to allow for direct comparison between the standard repulsive and the SASS method.

A further advantage of this engaging method is that it allows careful tuning of the tip-surface forces. This outcome is not self evident but it can be shown with simulations (data not shown) that once the tip is engaged in the SASS region (i.e. A_{sp}~0.1 nm), the average (and peak) force per cycle can be made to smoothly and monotonically increase from close to zero to any given value by increasing the driving force (i.e. A_0 or F_0). Furthermore, this is both possible and practical since the driving force can be very finely tuned with an AFM thanks to the precision in control of the z-piezo motion via piezoelectric actuators. In comparison with standard AM AFM, it is worth noting that while the set-point can also be finely tuned in standard TM, even small changes in set-point can induce large differences in force[1,122] (Fig. 3.15) (Chapter 3).

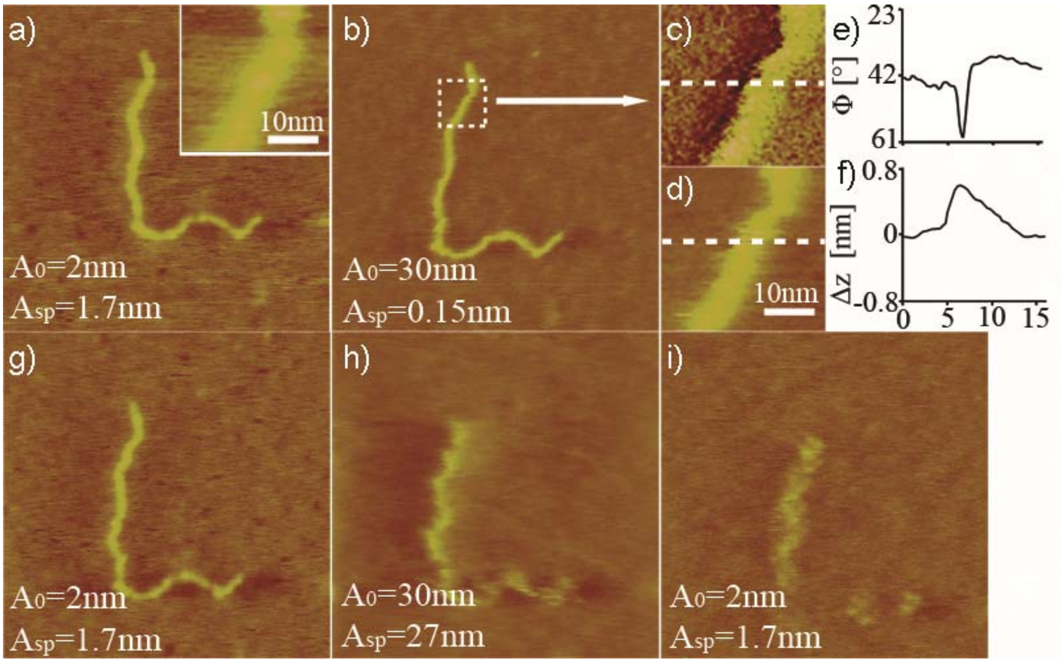

Figure 4. 2

Sequence of topographic scans that experimentally demonstrate that A_{sp}/A_0<<1 is light tapping as compared to larger values of A_{sp} and that the SASS approach of engaging is less damaging for the tip. a) Image obtained in the nc mode by using a small value of A_0 and a large value of A_{sp}/A_0 (i.e. A_0=2 nm A_{sp}/A_0=0.85). Here the N and SASS regions could be observed in an APD curve (data not shown). b) Then A_{sp} has been smoothly decreased to 0.15 nm. This ensures that increasing the free amplitude at this point will not produce a sudden or step-like transition to the H-state since the cantilever is already oscillating in the SASS region and, hence, the system is monostable. c-d) Zoomed views of the phase and topography respectively. e-f) Respective cross sections demonstrating the resolution of this method even for such (relatively) high free amplitudes. The width at mid-height is approximately 7 nm. g) Another nc mode image was taken to ensure that neither tip nor sample had been damaged (A_0=2 nm and A_{sp}/A_0=0.85). h) Standard tapping mode image obtained with a high set-point and in the standard (see text) engaging method (A_0=30 nm and A_{sp}/A_0=0.90). i) Another nc image (A_0=2 nm and A_{sp}/A_0=0.85) taken immediately after h) showing that the sample (and likely also the tip) has undergone severe plastic deformation.[148] The SASS method could not be used any longer with this tip after performing standard tapping mode, presumably due to tip damage.[148] Other surrounding molecules have been imaged with similar parameters (i.e. A_0=2 nm and A_{sp}/A_0=0.85) to guarantee that the deformation of the molecule was not an artefact (data not shown).[157]

Finally, experiments such as those shown in Fig. 4.2 can be used to demonstrate how cantilever-sample systems where the N and SASS regions appear (Type I systems defined in Chapter 6) turn into Type III systems at once after engaging in the standard TM method. This is further evidence of the high forces induced in standard TM as opposed to the SASS mode, since, as discussed in Chapter 6, for a cantilever-sample system, only changes in *R* can lead to a system changing from Type I to Type III. Thus, this division for cantilever-sample systems has the advantage of allowing one to monitor the size of the tip radius at once and in situ.

The monostability of the system in SASS can be verified with simulations and the use of phase space diagrams as shown in Fig. 4.3. Here the capillary force and the effective distance introduced by the water layers in the tip and sample junction d^* have been taken into account. With these additions to the equation of motion (see Appendix A) the region of negative slope in amplitude (N) is observed and the experimental ADs are fully reproduced as shown in Fig. 4.3a. In the left column, the limit cycles are shown for z_c=0.5 nm, z_c=1.5 nm and z_c=2.5 nm (Figs. 4.3b, d and f). For z_c=0.5 nm (Fig. 4.3b) there is a unique limit cycle and it is typically reached after just over 0.003 s of simulation for any set of initial conditions (z_0, $\dot{z}_0$, t_0). The shape of the limit cycle in three dimensions (z, $\dot{z}$, t), with time being the third dimension, is a helix (data not shown). In two dimensions (z, $\dot{z}$), the limit cycle is an ellipse with eccentricity close to zero and forms a closed loop in accordance with the requirement of periodic motions.[151,158] The corresponding basins of attraction for t_0=0 are shown in Fig. 4.3c. Here the set of (z_0, $\dot{z}_0$, t_0=0) leads to a single attractor, which, accordingly, leaves a black square (SASS region): monostability. The Poincaré section (z, $\dot{z}$) for t_0=0 is shown with a cross. When z_c is increased to 1.5 nm (Figs.

4.3d-e), two limit cycles are observed corresponding to the N-region (grey) and the H-state (white) respectively. Further increasing z_c to 2.5 nm (Figs. 4.3f-g) results in the standard L and H-states as limit cycles. For each limit cycle there is an ellipse (left column in Fig. 4.3). The amplitude in the L-state increases from absolute minima to local maxima via the N region and with decreasing z_c, where it finally overlaps with the H-state. From Fig. 4.3, four major advantages to imaging in the region where the attractors converge, i.e. the SASS region, can be stated. First, the average and peak tip-surface forces are minimized relative to standard tapping mode. This is due to the cantilever vibrating only angstroms above the surface without the requirement of high values of A_0 which lead to larger tip-surface forces.[41,122] From this, markedly reduced tip-sample wear also follows[59,148]. Second, the proximity to the surface minimizes the radius $<r>$of the effective area $<S>$ of interaction in the SASS region. This is shown with the use of a simulation in Fig. 4.4a for <r>. There, $<r>$forms plateaus in the standard L and H-states. In the N region, $<r>$monotonically decreases while as z_c decreases, $<r>$increases in the H-state. Finally $<r>$monotonically decreases in the SASS region and reaches a minimum there. Third, the system is monostable in the SASS region, guaranteeing that tip-trapping and or switching between states cannot occur. Fourth, small drifts in the resonance curve are unlikely to affect the operation of the instrument in the SASS mode because the set-point ratio is much smaller than one (A_{sp}/A_0<<1). In particular, the combination of reduced tip and sample wear and drift in the resonance not influencing the operation, hundreds of consecutive high resolution images can be obtained in SASS. This can be done with the same tip and sample without having to change the operational parameters for continuous imaging over 24 hours or more.[59]

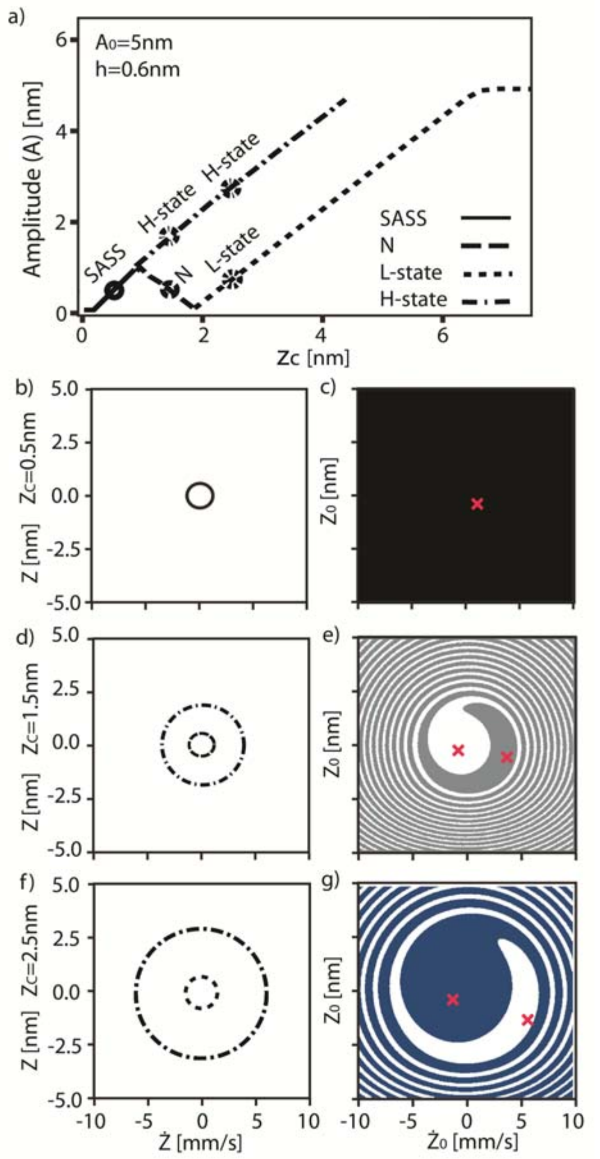

Figure 4. 3

Simulations. a) Simulated AD curve, where the L and H-states and the N and SASS regions are reproduced. The markers indicate discrete values for which the limit cycles and basins of attraction have been calculated. A switch between two states can take place wherever there are two solutions for a given z_c. In the left column b-d), the limit cycles $(z, \dot{z})$ for z_c= 0.5, 1.5 and 2.5 nm are shown. The vertical axis is the instantaneous tip position, z and the horizontal axis is the instantaneous tip velocity, $\dot{z}$ in the steady states. When there are two ellipses, two limit cycles co-exist. In the right column c), e), g), the respective basins of attraction (z_0, $\dot{z}_0$, t_0=0) are shown. These are coloured in black (SASS), grey (N region), blue (L-state) and white (H-state). The Poincaré sections are marked with red crosses. The parameters are: f=f_0=312 kHz, k=40 N/m, R=2.5 nm, Q=500, γ=40 mJ, E=10 GPa[130], E_t=120 GPa, h=0.6 nm and A_0=5 nm. 400x400 initial conditions have been used to obtain the basins of attraction on the right.

An experimental example of the relevance of the separation, A_{sp}, and the step in resolution as the cantilever is brought close to the surface through and past the N region is shown in Fig. 4.4 and 4.5.

The sequence in Fig. 4.5 has been obtained with a similar set-up as that used for Fig. 4.1. For the largest values of amplitude set-point (Figs. 4.5b-e), the L-state in the nc mode is reached and the lateral resolution is similar throughout. This matches the predicted plateau in $<r>$in Fig. 4.4. Then a dramatic change in resolution is observed when the set-point is lowered to 0.1 nm (Figs. 4.5f-i); this is the SASS region imaging mode. Provided the N and SASS regions exist, these images are readily obtainable with SASS imaging and require no averaging. Attempts to image with small values of A_{sp} when the N and SASS regions are not observed lead to severe noise.[59]

When the SASS and N regions are not observed the systems are Type III. Thus, the increase in noise when the SASS and N regions are not present is in accordance with the results described in Chapter 3 for Type III systems[122] and relate to the standard problem of tip trapping as described in the literature and Chapter 2.[15,32,36] The physical phenomenon of tip trapping relates to the A-state in these cases. This is shown in Chapter 6.[137]

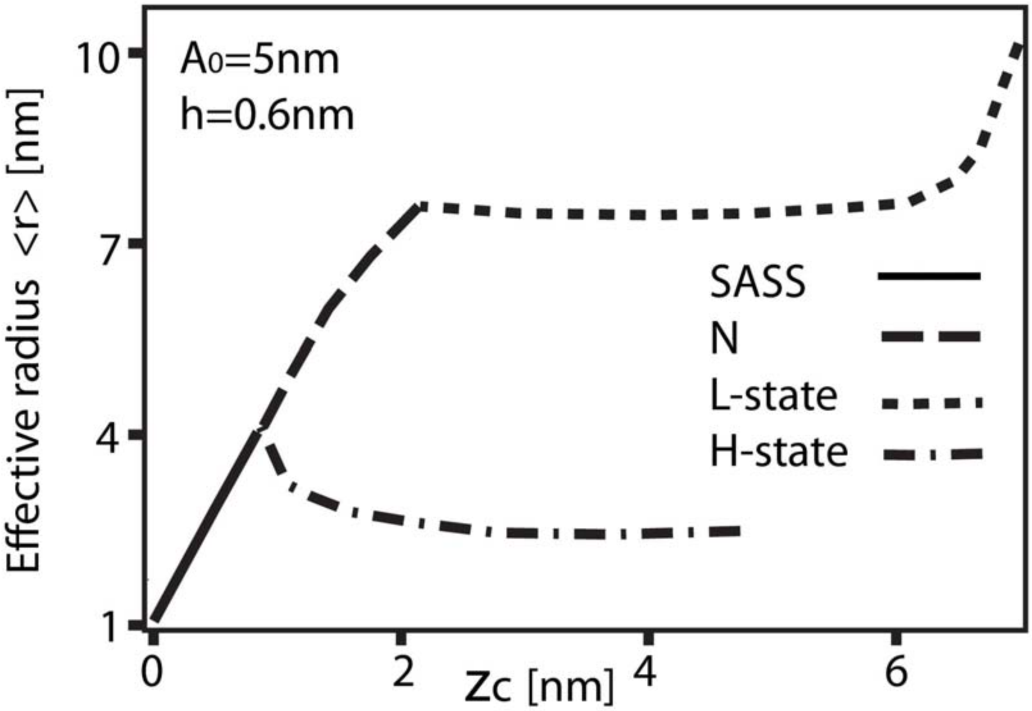

Figure 4.4

The radius <*r*> of the effective area of interaction <*S*> calculated by square rooting the expression <*S*>/π obtained for the same parameters as those used in Fig. 4.3. The radius <*r*>decreases monotonically in the SASS region (continuous black line) and reaches an absolute minimum there. The H-state (dashed dotted line) shows a pattern where <r> slightly increases before the SASS region starts. In the L-state (short dashes) <r> shows a plateau whereas in the N region (large dashed) <r> monotonically decreases. Nevertheless the N region is not satisfactory for the standard AM AFM operation mode since the amplitude increases there with decreasing separation, i.e. it has negative slope).

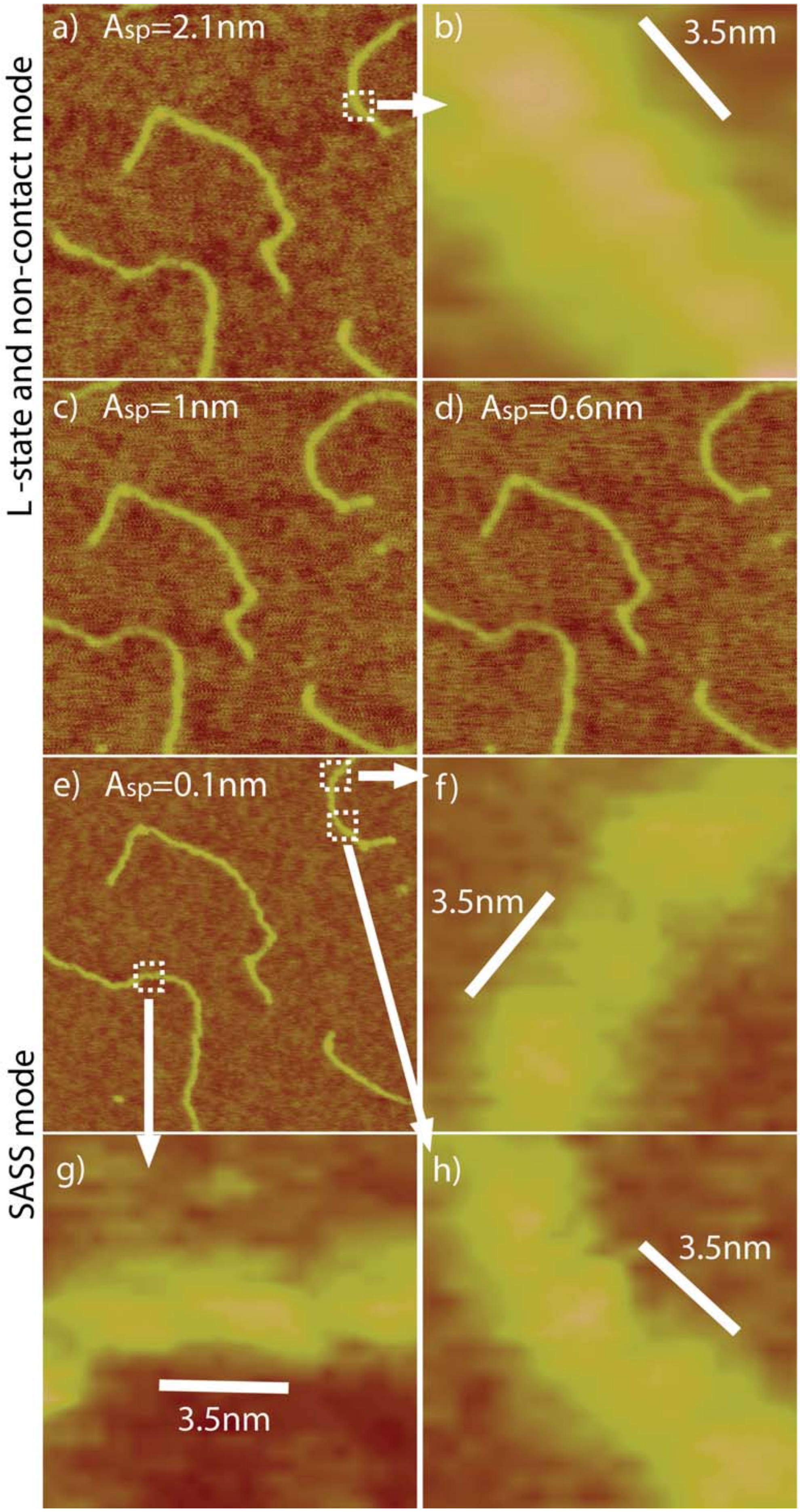
L -state and non-contact mode
SASS mode
a) Asp=2.1nm
b)
3.5nm
c) Asp=1nm
d) Asp=0.6nm
e) Asp=0.1nm
f)
3.5nm
g)
3.5nm
h)
3.5nm

Figure 4. 5

a-h) Sequence of topographic images of dsDNA on mica for which A_{sp} has been systematically decreased from 2.1 nm to 0.1 nm. b) and f-h) are software zooms. The step change in stability and resolution is observed in the SASS region where periodicity is observed at all angles of the molecules relative to the fast scan direction (horizontal). The apparent widths at half-height are ~8 nm for b-e) (nc mode) and <4.5 nm for f-i) (SASS mode). The experimental parameters are f_0=331 kHz, f= f_0, k~40 N/m, Q=550 and A_0=2.5 nm. Scan size of b), d), e) and f) 300 nm by 300 nm.

4.3. Summary

The appearance of a single attractor at just several angstroms of tip-surface separation is the key physical phenomenon for future developments in high resolution ambient AFM due to the high stability of the system and the reduced area of interaction there. This phenomenon leads to SASS mode[59] and it is a requirement for tip-surface proximity and stability with small drive amplitudes and forces in ambient dAFM.

Thus, the discovery of SASS region paves the way for advances in high resolution dynamic AFM in hydrating ambient conditions. It allows reliable and repeatable imaging of the double helix of individual DNA molecules showing right-handed helicity in B-form. Furthermore, SASS increases resolution while preventing the high wear of standard tapping mode. For all these advantages, it is expected that SASS will become the standard imaging method for high resolution dAFM in ambient conditions.

Chapter 5

5. True and apparent height in AFM

5.1 Overview

The field of Nanotechnology is defined through the dimensions of the nanoscale objects that make up new materials and devices.[10] More thoroughly, phenomena occurring in the range of 1 to 100 nm, where the properties of matter vary from those displayed by atoms or macro-objects, provided the initial motivation and drive towards the development of the field of Nanotechnology.[3-4,69,159] The size of the objects can give rise to distinct physical and chemical properties relative to either single atoms or bulk matter. When the size of a material enters the nanoscale (<100 nm) dramatic changes in its physico-chemical properties typically occur. Size is a key parameter determining characteristics, where materials might exhibit novel and/or significantly improved physical, chemical, biological, electrical, optical, catalytic, magnetic and vibrational properties, phenomena and/or processes.[10,69,159] Instruments that accurately measure dimensions of nano-objects are, therefore, key enablers of the field.[3,10] The atomic force microscope (AFM) is a high-resolution surface profiler capable of producing 3D topographical maps and is versatile, able to measure all range of surfaces in vacuum, ambient or liquid environments.

The measured height of nanoscale features, however, is almost always smaller than the true value. Many reasons for this anomaly have been put forward, including, sample deformation and/or dehydration, differences in local charge distribution and salt deposits.[1,116,160-161] While such phenomena can contribute to this effect, this section describes that the real height of nano-objects cannot be obtained directly: a result arising as a consequence of the local probe-sample geometry. Once the size of a feature becomes smaller than the effective area of interaction between the AFM tip and sample, the height is compromised. This general result is the major contributor to loss of height and can amount to up to ~90% for nanoscale features.

5.2. Modelling and results

5.2.1 Introduction

Typical measurements of nanoscale features with an AFM give an apparent height that is almost always lower than their known true height[1,86-87,116,160], even when feedback gains are optimized. In particular, the apparent height of dsDNA as measured in AFM can be anything from 10 to 90%[79,100,104,116,134] of its true height even after careful calibration of the instrument. The nominal true diameter of B-form dsDNA should be 2 nm[64] according to X-ray measurements.[162] Some have reported that changes in elastic modulus of the sample and/or the attractive component of the force[160] can produce variations in the cantilever-surface separation (z_c) leading to loss of true height[42,86] (and references therein). Others have concluded that contamination or salt deposits around molecules on typical support surfaces for molecules, such as mica[115], and/or dehydration could be partly responsible for height reduction.[116] Generally, it has been commonplace to attribute height loss to sample deformation[116,163-164] and/or high forces[1,22,160-161,163-164], whenever they are observed. In this chapter, the finite size of the surface feature (i.e. the sample) and the tip radius R are shown to be intrinsically responsible for the loss of true height in all types of AFM. This is a direct consequence of the fact that the force arise from an effective area of interaction $<S>$ (Chapter 4 and Appendix A) which is larger than a single point directly under the tip. Demonstration of this fundamental limit is carried out using AM AFM, but the approach has the potential to be generalized to include all forms of probe microscopy for which $<S>$ is finite. Comparison of AM AFM experimental data on single isolated DNA and protein molecules with a model which includes the tip-sample interaction area, leads to quantification of intrinsic height loss in the different imaging modes (non-contact (NC) and intermittent contact (IC)). Note that IC here makes reference to both the standard H-state and/or standard TM (Chapter 3). Both dsDNA (1074 bp) and Immunoglobulin G (IgG) antibodies[109] samples are used here as model systems. These systems have been chosen as a model system because of being compliant, small and biologically relevant.

Furthermore, for simplicity and since emphasis is placed on the concepts discussed rather than on specific details, here some experimental and simulation parameters always take the same numerical values throughout. These are ζ =[k, Q, E, Et, ν, R_2, driving frequency (f_0)] with ζ=[40 N/m, ~500, ~10 GPa[130], 120 GPa, 0.3, 1 nm, ~300 kHz] throughout. All experiments in this chapter have been conducted at resonance except otherwise stated.

The term deformation, termed δ, in this thesis is borrowed from contact mechanics theory[165] and refers to the compression, typically expressed in nm, of a sphere-sphere pair or a sphere-surface pair. Mathematically there is deformation, i.e. $\delta>0$, whenever the tip-surface or tip-sample distance d is smaller than a_0. Here a_0 is an intermolecular distance and physically implies that interpenetration cannot occur and generally takes the value of 0.165nm or something in that order.[8] In some of the simulations in this chapter a viscoelastic component has been added to the equation of motion to account for viscosity when deformation occurs. A simple Voigt model has been used here, as sometimes done in the literature[50], where the equation is

$$F_\eta = -\eta\left(R^*\delta\right)^{1/2}\dot{z} \tag{5.1}$$

where F_η refers to the viscous force when deformation occurs, i.e. $\delta>0$, η is the viscous coefficient, R^* is the tip radius R when the interaction is between a sphere, i.e. the tip, and a surface, and $R^*=(RR_2)/(R+R_2)$ when the interaction occurs between the tip of radius R and a sphere of radius R_2. Finally, δ is the deformation as defined above and $\dot{z}$ is the instantaneous tip velocity. This is standard terminology.[8] The minus sign implies that this force opposes the motion.

5.2.2 The origin of apparent height

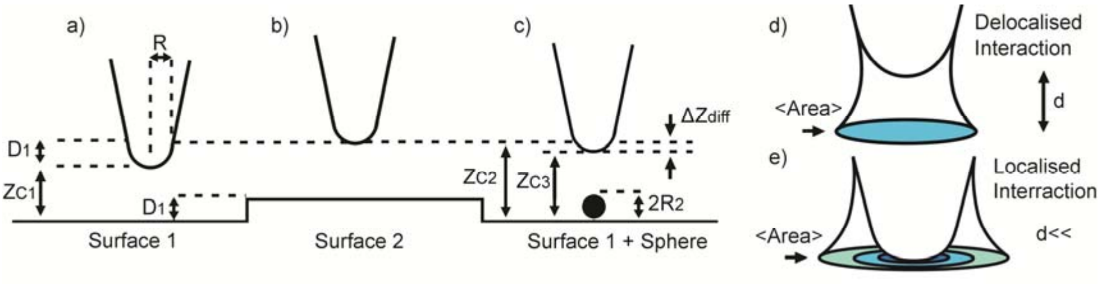

Figure 5. 1

Schematic of the interaction between the tip, an infinite surface and a finite sample feature. a) Scheme of the interaction between a tip and a flat surface (surface 1). The equilibrium cantilever-surface separation (z_c) is defined as z_{c1} *b*) When the tip is over a second surface (surface 2) of height D_1, the z-piezo actuator increases z_c to z_{c2}. The displacement z_{c2}-z_{c1} is termed the apparent height of the surface step. c) When encountering a sphere of height $2R_2$ the z-piezo varies z_c to z_{c3}. d-e) Scheme of the interaction area between the end of the AFM tip and a surface at large and close distances, respectively. The force is not localized at a single point but acts over a finite area <*S*>, with a radial profile.

The origins of apparent height in AFM can be understood qualitatively by observing that, when topography occurs, the tip-sample forces occurring are fundamentally different from the forces occurring when the tip interacts with an infinite and flat surface. This situation arises from the localised change in the geometry coupled with the distance dependencies of all the forces involved. For example, in Fig. 5.1a, initially, the surface forces originate from the interaction between the tip radius, *R* and an infinite surface (surface 1); then a given z_{c1} follows. Over a second surface 2 with the same properties as surface 1 with a true height of D_1, (relative to the level surface 1), z_c is now z_{c2} (Fig. 5.1b). Since the surface properties and local geometry between surface 1 and 2 has not changed, the cantilever dynamics remain the same over both surfaces and it follows that z_{c2}-z_{c1}=D_1, so the true topography of the step is measured. Note that if the properties of surface 1 and 2 were different then the true height would not be measured. Now, let us assume that the tip encounters a small feature such as a sphere of radius R_2 on surface 1 with the same material properties as surfaces 1 and 2 (Fig. 1c). In this case the tip-surface forces include not those from the tip-surface 1 interaction alone but those from tip-surface 1 interaction and the tip-sample interaction. The surface feature or sample here is a sphere of radius R_2. Thus, the true height of the sample is $2R_2$. In practice, this is particularly relevant when $<S>$ is bigger than $2R_2$, the diameter or size of the nanoscale feature. In order to obtain the true height of the sphere, the separation should now be $z_{c3}= z_{c1}+2R_2$ and if $2R_2=D_1$, $z_{c3}=z_{c2}$ would be required. This would only happen if the force for the tip-surface-sphere system was *coincidently* equivalent to that between the tip and the infinite surface 2. In practice a difference $\Delta z_{\mathrm{diff}}= z_{c2}-z_{c3}$ occurs and $z_{c3}-z_{c1}$ is the apparent height. It is significant that we do not refer here to changes in the magnitudes of the forces due to the chemical or material properties of the sample, but to changes based purely on geometry. A comparison of the effects of a hypothetical point-like area of interaction (Figs. 5.2a-b), are made to the experimental or real effects for a dsDNA molecule on a mica surface (Figs. 5.2c-d). A tip of finite size means the height profiles broaden and become lower in the experimental case. In essence, the height information is spread out across the width of the interaction area. The full width-height integral that occurs when the tip moves in say the slow scan axis, or x-axis as in Fig. 5.1a-c, has not been conducted here. As an example however, consider Fig, 5.1c. Physically, the apparent height should start to increase as soon as the tip starts sensing the force due to the surface feature at a distance <*r*>from the surface. This distance is that for which the surface feature first enters the effective area of interaction <*S*>. The relationship is <r>=<*S*>/pi as in Chapter 4. Then the maximum apparent height would occur when the tip is exactly over the surface feature. Finally, the apparent height would start to decrease as the tip moves further in the x direction and would become zero when the surface feature is completely outside <*S*>.

The reason why the full width-height integral has not been carried out here is that the equations of deformation when the tip and the surface feature, a sphere of radius R_2 in this case, interact in other than the vertically symmetrical case, i.e. when the tip is just on top of the sphere, are cumbersome. Thus, only the simple case for the maximum apparent height have been worked out.

5.2.2 Model and results

The fact that the interaction occurs in a finite area of interaction <*S*> where the tip-sample force adds to the tip-surface force can be demonstrated with the use of the point mass model and the conservative vdW and DMT forces (Chapter 2) and the addition of the tip-sample forces (30-32). Note that the sample here is modelled as a sphere of radius R_2. The “surface” and the “sample” are defined here to be specifically distinguished: the sample is any nanoscale feature on the surface.[156]

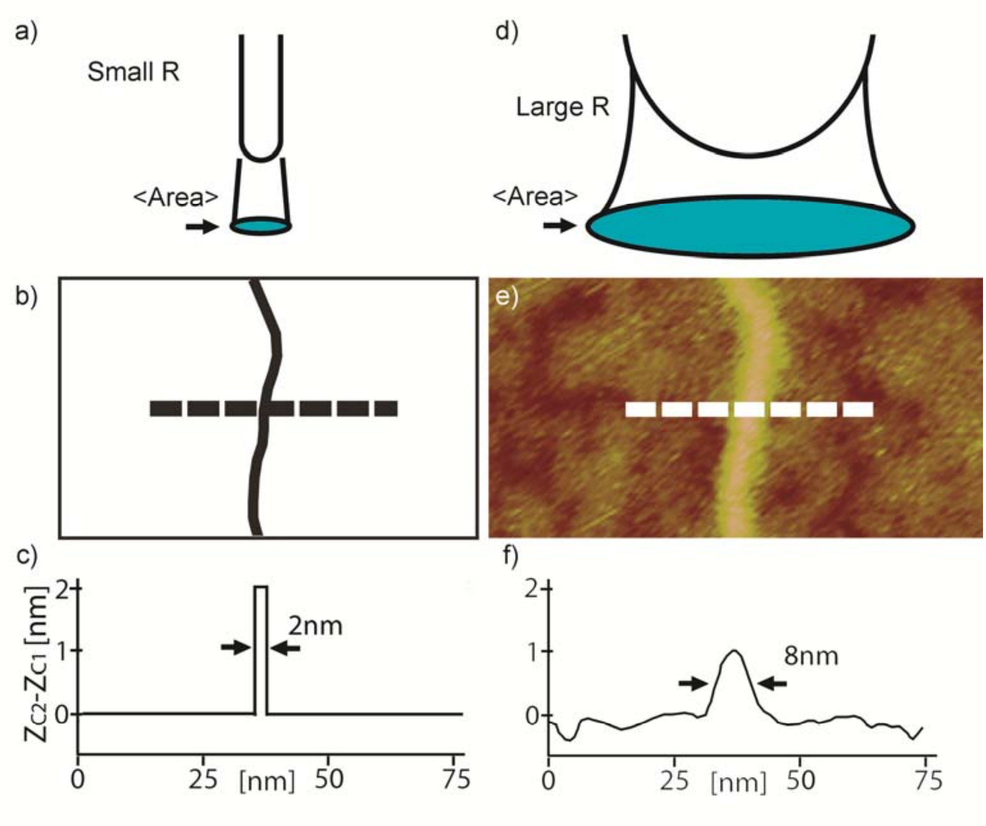

Figure 5. 2

Scheme of a hypothetical point area versus experimental outcomes where the area is finite. a) Scheme of the small <*S*> (blue) with a hypothetical delta-function tip on a perfectly flat surface. b) Hypothetical topographic scan of a dsDNA molecule with such a tip and surface. c) Scheme of the perfect height profile (dashed line) achieved with this hypothetical set-up. d) Scheme of the larger <*S*> (blue) resulting from a typical AFM tip (e.g. $5<R<30$ nm). e) Topographic scan of a dsDNA molecule on mica with a standard tip in AM AFM in air. f) Experimental height profile (dashed line). The apparent height is approximately 1 nm or half its true height and it appears lower and broader. Breaks in the layer of surface contamination allow the apparent height of the DNA to be measured relative to the mica surface. The surface layer, which contains salts and water and appears as troughs and valleys, accounts for approximately 0.2 nm. Experimental parameters: (e) A_0=3 nm and A_{sp}/A_0=0.9.

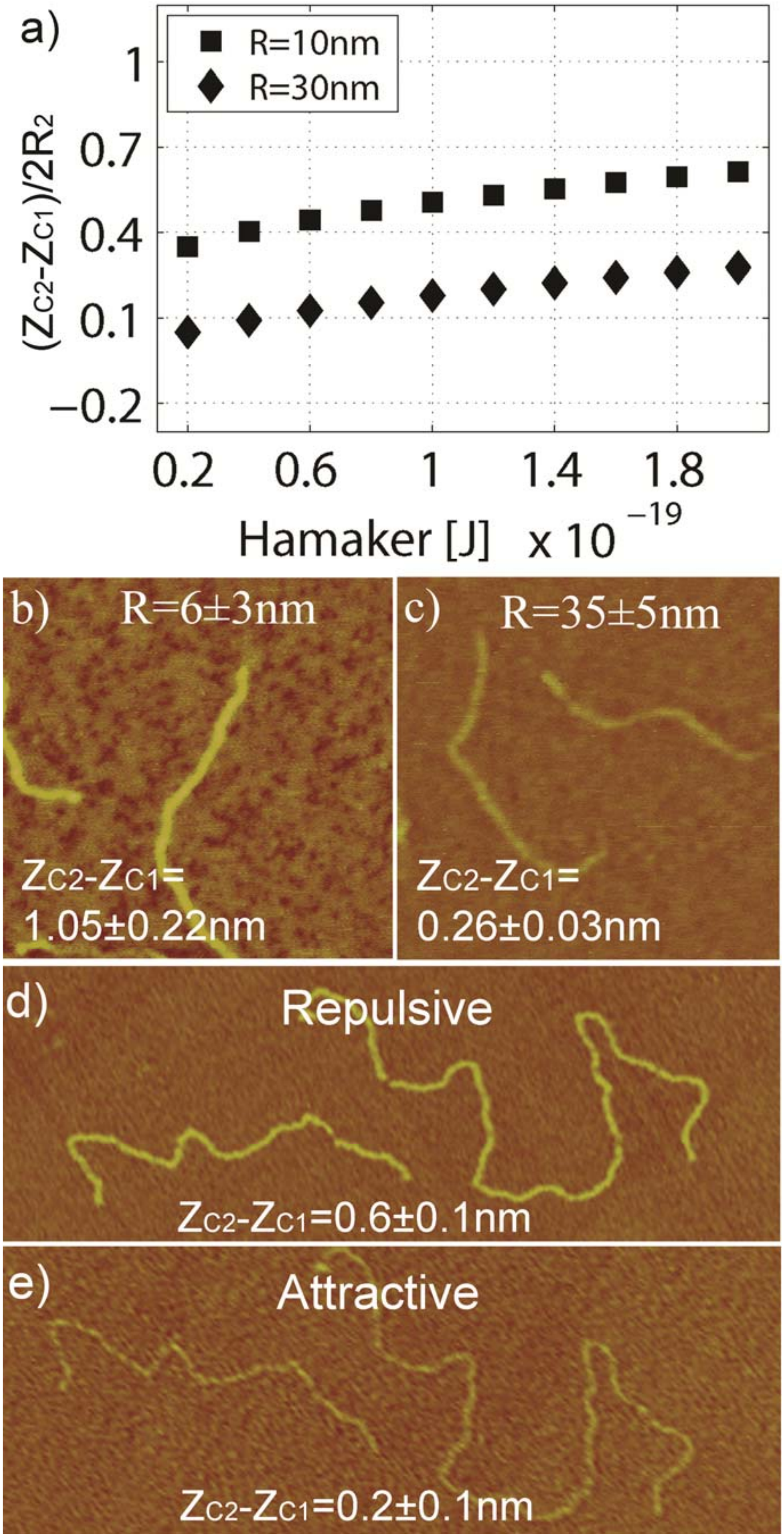
a)
R=10nm
R=30nm
$(Z_{C2}-Z_{C1})/2R_2$
1
0.7
0.4
0.1
−0.2
0.2
0.6
1
1.4
1.8
Hamaker [J] x 10^{-19}
b) R=6±3nm
$Z_{C2}-Z_{C1}$=
1.05±0.22nm
c) R=35±5nm
$Z_{C2}-Z_{C1}$=
0.26±0.03nm
d) Repulsive
$Z_{C2}-Z_{C1}$=0.6±0.1nm
e) Attractive
$Z_{C2}-Z_{C1}$=0.2±0.1nm

Figure 5. 3

Model versus predictions of apparent height. a) Model predictions obtained for the normalized apparent height $(z_{c2}\text{-}z_{c1})/2R_2$ as a function of H_s. H_s is the Hamaker of the tip-sample interaction pair as opposed to H which is the Hamaker of the tip-surface pair. The vertical axis here corresponds to different values of H_s and the vertical axis to the normalised height obtained through simulations. R_2 is the radius of a sphere, which here it is the sample. Thus, $2R_2$ is the true height of the sample in this case. The normalized apparent height $(z_{c2}\text{-}z_{c1})/2R_2$ increases with R_2 and decreases with R where R is the tip radius. Significantly, $(z_{c2}\text{-}z_{c1})/2R_2$ can be smaller than 0.1 or 10% even though all the data has been obtained in the nc mode where no deformation can occur. In b) and c) experimental topographic images of dsDNA molecules on mica show the relationship between R and $(z_{c2}\text{-}z_{c1})/2R_2$. Since the samples here are dsDNA molecules we take the true height of DNA to be $2R_2$=2 nm which is the true dsDNA nominal height (see Chapter 1). As in the simulations $(z_{c2}\text{-}z_{c1})/2R_2$ increases with decreasing R. In d) and e) a single molecule has been imaged in the repulsive and the attractive regimes and the higher value of $(z_{c2}\text{-}z_{c1})/2R_2$ has been obtained in the former. Simulation parameters: A_0=1 nm, A_{sp}/A_0=0.95, E_s=0.2 GPa, γ=50 mJ/m^2 (surface energy of the surface) and $H=10\times10^{-20}$ J (Hamaker of the tip-surface pair). Experimental parameters: b-c) A_0=4 nm and A_{sp}/A_0=0.9; d) A_0=20 nm and A_{sp}/A_0=0.9; e) A_0=2 nm and A_{sp}/A_0=0.9.

For the tip-surface scenario we have,

$$F_{ts} = -\frac{RH}{6d^2} \quad d>a_0 \quad \text{and} \quad F_{ts}(DMT,d) = -\frac{RH}{6a_0^{\,2}} + \frac{4}{3}E^*\sqrt{R(a_0-d)^3} \quad d< a_0$$

(5.2)

whereas for the tip-sphere-surface we have,

$$F(d) = -\frac{HR}{6d^2} - \frac{H_S R^*}{6d^{*2}} \qquad R^* = \frac{RR_2}{R+R_2} \qquad d^* > a_0$$

(5.3)

and

$$F_{ts}(DMT,d) = -\frac{HR}{6d^2} - \frac{H_S R^*}{6a_0^{\,2}} + \frac{4}{3}E_S^*\sqrt{R^*(a_0-d^*)^3} \quad d^* < a_0$$

(5.4)

The distance d is the instantaneous tip-surface distance in the absence of a "sample" (2.1) whereas for the tip-sample forces (5.3-4) the parameter d^* is to be used. This is the effective distance between the tip and the "sample". From this model, several conclusions follow:

1) In the non-contact (nc) mode of operation, where mechanical contact never occurs, the interpretation of height reduction as tip-sample-deformation can be ignored by definition, yet still $(z_{c2}-z_{c1})/2R_2<1$ (Fig. 5.3a). Thus, other interpretations for height reduction need to be found.

2) A dependency on R is observed (Fig. 5.3a) that agrees with experimental observations (Figs. 5.3b-c).

3) The interpretation of increasing height $(z_{c2}-z_{c1})$ with decreasing forces is also ruled out since, it can be shown both experimentally (Figs. 5.3d-e) and with simulations (Fig. 5.4) that $z_{c2}-z_{c1}$ can increase with increasing force or free amplitude A_0.

4) Simulations show that the apparent height might increase with decreasing elastic modulus of the sample (E_s)(Fig. 5.4a).

5) The model predicts that height reversal might occur when the attractive regime is reached on the surface and the repulsive regime is reached on the molecules (Fig. 5.4a). Furthermore, the size of the nanoscale feature directly affects the transition between regimes and is a consequence of the geometry dependency of the forces with the repulsive regime more readily reached with decreasing sample size (data not shown).[156] An experimental example of height reversal is shown in Figs. 5.4b-d. Subsequent scanning with lower values of A_0 allows attractive imaging on both the surface and the antibodies. Importantly, molecular damage is not observed when height reversal occurs (Fig. 5.4b) or in the attractive regime (Figs. 5.4d-e).

6) In the repulsive mode of operation, and according to simulations (Fig. 5.4f), the value of z_{c2}-z_{c1} might actually increase relative to the attractive regime. This can be observed experimentally (Figs. 5.3d-e and Figs. 5.4g-n).

7) Significantly and reiterating, height loss and deformation δ do not follow directly follow from each other, that is $\delta/2R_2 \neq (z_{c2}-z_{c1})/2R_2$). This can be easily verified with the aid of simulations[156] (data not shown).

From this, it follows that sample deformation cannot be deduced from the observation that decreasing height occurs with variations of operational parameters and/or sample preparation. This is significant because it had become standard procedure in the literature and it is false.[44,54,79-80,116,135,160-161,163]

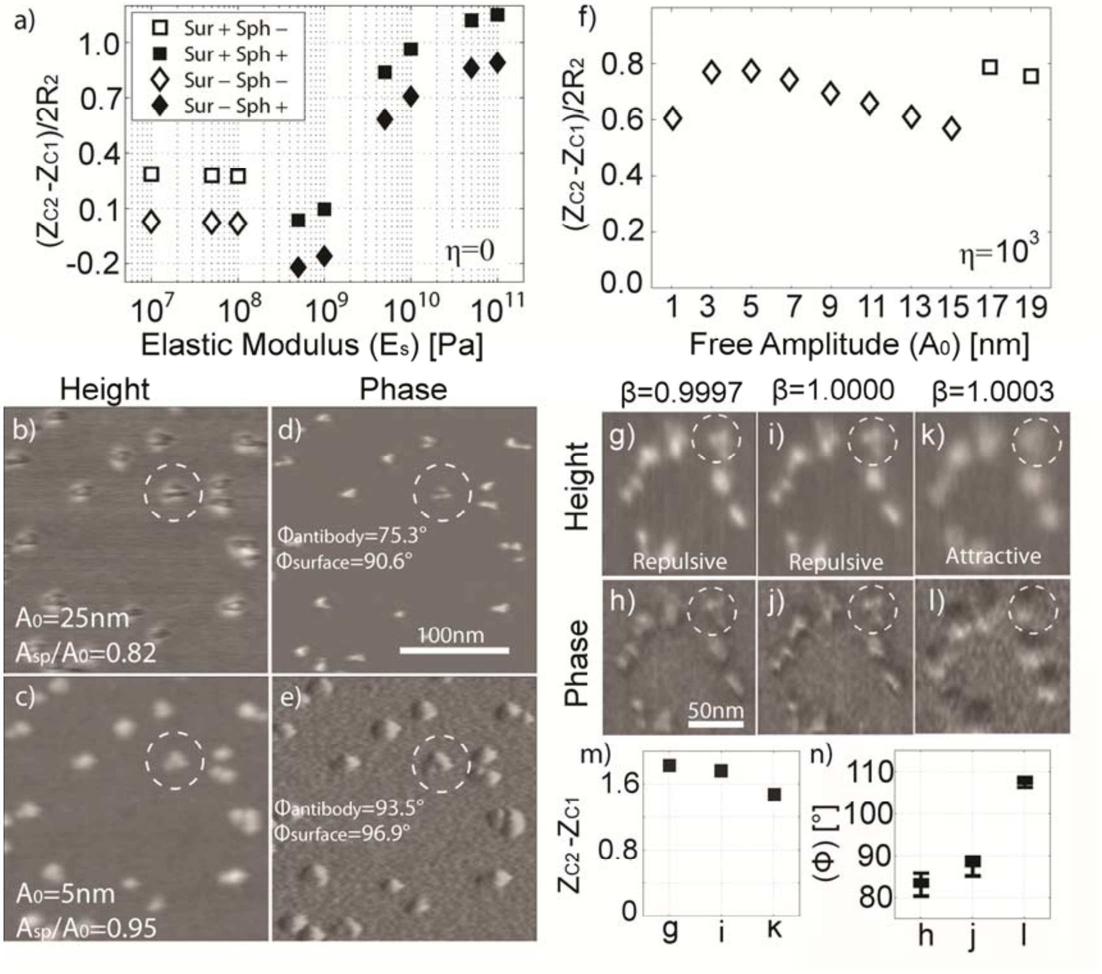

Figure 5. 4

The effects of the elastic modulus and the free amplitude on apparent height. a) Simulations of the tip-surface and tip-surface-sample interaction. Normalized apparent height $(z_{c2}\text{-}z_{c1})/2R_2$ versus E_s. Note that apparent height $(z_{c2}\text{-}z_{c1})/2R_2$ might initially decrease with increasing E_s. The attractive and repulsive regimes might be reached only on either the surface or the sample. The outcomes of the four possibilities are shown with squares and rhombuses where Sur and Sph stand for surface and sphere respectively. The minus and plus signs refer to the attractive and the repulsive regime. b) Topography and c), phase contrast of IgG antibodies on mica where height reversal is observed. The attractive regime is stably reached on the surface whereas the repulsive regime is immediately reached where any topographical sample feature occurs (e.g. the antibodies). (f) Simulations of the tip-surface and tip-surface-sample interaction. An extra viscoelastic component η has been added to the contact region where deformation occurs. Normalized apparent height $(z_{c2}\text{-}z_{c1})/2R_2$ versus A_0 for A_{sp}/A_0=0.88. The attractive regime is reached both on the surface and the sphere for the lower values of A_0 and $(z_{c2}\text{-}z_{c1})/2R_2$ initially increases and then decreases with A_0. For larger values of A_0, the repulsive regime is reached on the surface only and $(z_{c2}\text{-}z_{c1})/2R_2$ increases. (g-l) Topography and phase images of IgG antibodies with different normalized driving frequencies (β=f/f$_r$) and constant A_0 and A_{sp}. Here $(z_{c2}\text{-}z_{c1})/2R_2$ increases in the repulsive regime. The respective values for m) height and n) phase for the circled antibody are shown to allow comparison between apparent height and force regime. Recall that the attractive force regime is that for which the phase is larger than 90 degrees whereas the repulsive regime is that for which the phase is less than 90 degrees. Simulation parameters: (a) A_0=12 nm, A_{sp}/A_0=0.70, E=1 GPa, γ=50 mJ/m^2 and H=10×10^{-20} J; (f) A_{sp}/A_0=0.88, E=10 GPa, E_s=0.1 GPa η=1000 and the rest as above. Experimental parameters: (b-e) as detailed in the figures; (g-l) A_0=24 nm and A_{sp}/A_0=0.7. The size of g) to l) is 100nm by 100nm.

5.3. Summary

It has been shown that the geometry of the tip-surface-sample interaction area can induce deviations in the apparent relative to true height of up to 90% (Fig. 5.3). A physical interpretation has been given for this phenomenon where the intrinsic resolution limit in the atomic force microscope causes height information to be spread-out laterally across the tip-sample interaction area. This results in loss of height for features of nanoscale lateral dimensions. Furthermore, this interpretation brings AFM into analogy with other forms of microscopy where there is an intrinsic resolution limit. For example in optical and electron microscopy, the wavelength is an intrinsic parameter limiting resolution and for AFM it is the effective area of interaction.[166]

Since phenomena occurring in the nanoscale, where the properties of matter vary from those displayed by atoms or macro-objects, are largely dependent on the dimensions of the features, accuracy of measurements is paramount and allow quantitative comparison between samples. In this respect, the results presented in this Chapter are relevant to all fields of research using the AFM to characterize the dimensions of nanoscale samples. The results have further shown that the effects of the size of the sample here described are significantly relevant in the nc mode of operation where very small and attractive forces are typically employed. Since this is a common mode of operation when imaging soft matter and for preserving the sharpness of the tip (see Chapters 3 and 4), special care should be taken in these experiments to interpret data.

Predicted heights from this model (and future adaptations for other situations) could be compared with experimental data and used to deduce the real height values. This will enable decoupling of intrinsic height loss from other sources allowing local mechanical properties of molecules and surfaces to be more rigorously defined at the nanoscale. Quantification of the intrinsic height loss, as demonstrated here, will now allow accurate mechanical and chemical mapping of surfaces at the highest possible spatial resolution

Chapter 6

6. The tip radius and stability

6.1 Energy dissipation in a dynamic nanoscale contact

6.1.1 Overview

An advantage of AM AFM is that data from the phase shift and the z-piezo displacement can be simultaneously acquired to produce topographical and phase contrast images respectively.[13,33,47] The mechanism causing phase contrast has been discussed in Chapter 3 in detail and shown to relate to the energy dissipated in the tip-sample interaction. The promise of phase contrast to provide quantitative information about the chemical and/or material properties of the sample has also been discussed. Nevertheless, for any technique involving chemical and/or material properties mapping, the stability of the tip is crucial since the data strongly depends on the state of the tip at a given time.

The difficulties of accounting for a variable size of the tip while scanning are clearly stated everywhere in the literature.[42,118,167-168] Typically, some ignore the instantaneous curvature of the tip in their experiments[42,118], even if indicating its relevance, while others simply use the nominal value as provided by the manufacturers.[50] With these simplified approaches only the magnitude of the tip-sample force can typically [22,161] be used to predict and/or account for tip and sample elastic and plastic deformation.[27,33,36,161,163] One can see however, that on their own, they cannot account for the divergences in measurements and/or sample deformation of soft matter typically reported in the literature.[44,86,134,163]

In this chapter, a method to characterize and stabilize the tip in situ and use this knowledge to interpret and predict elastic and plastic deformation of soft matter from a more fundamental mechanism, namely, the energy dissipated per atom and a limit in pressure in nanoscale interactions, is described. This is achieved by using the model to calculate $<S>$ described in Chapter 4. Then the energy dissipated in $<S>$ is calculated in terms of eV dissipated per nm^2 and/or atom.[148]

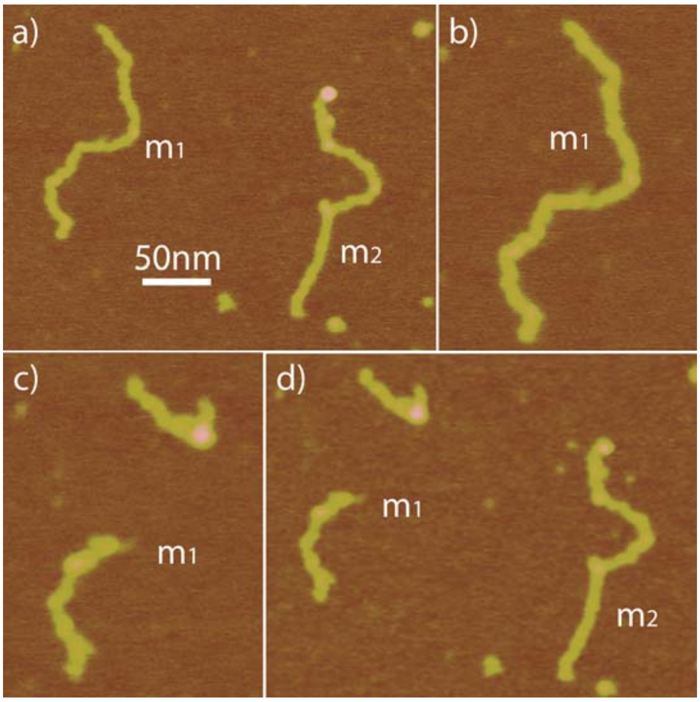

Figure 6. 1

a, b) Topography images (Z-piezo) of two dsDNA molecules imaged in the nc mode. Molecule (m_1) has then been cut by scanning in the repulsive regime and has folded up. c, d) This outcome is verified with subsequent scans of both molecules in the nc mode. Experimental parameters: $f=f_0$=302 kHz, k=40 N/m, R<10 nm, Q=500. All the images shown have been taken with A_{sp}/A_0=0.9 and A_0=3 nm. The scan sizes of a) and d) are 400 nm by 380 nm whereas b) and c) are zoomed views.

6.1.2 The tip radius as a dynamic variable

First, note that, from the expression to calculate the energy dissipated per cycle (6.1), no dependency on AFM tip radius, *R* or <*S*> can be deduced. This equation is the same as (3.9) but it is reproduced here for clarity.

$$< E_{dis} >_{CYCLE} = \frac{\pi k A_0 A_{sp}}{Q}[\sin(\phi) - \frac{A_{sp}}{A_0}] \qquad \omega=\omega_0 \qquad (6.1)$$

Nevertheless, the importance of *R* and <*S*> when interpreting energy dissipation can be demonstrated with a highly reproducible experiment as described next (Figs. 6.1 – 6.2). The topography of two DNA molecules (m_1 and m_2) on a mica surface is shown in Fig. 6.1a. The images have been obtained in the non-contact (nc) mode using a standard but relatively sharp tip (*R*<10 nm, Olympus AC160TS). Then m_1 has been centred (Fig. 6.1(b)) and cut using a nanoscission technique by temporarily driving the tip into the repulsive regime. The nanomanipulation event takes place for 10 scan lines in the slow scan axis (scan rate 2Hz) with A_0=12 nm and A_{sp}/A_0=0.4. The dissection of molecule, m_1, shows that imaging in the repulsive regime can result in molecular damage (Figs. 6.1(c)-(d)). From (6.1), $<E_{dis}>$ =18 eV is found. Eighteen eV are then responsible for plastic deformation and scission of the dsDNA molecule. Moreover, in similar experiments molecules have been completely wiped from the surface in this way.[148]

The relationship between plastic deformation and tip sharpness however, is not demonstrated with this type of experiment and, more thoroughly, the mechanism though which plastic deformation occurs cannot be reduced to the regime of operation. This is due to the fact that <S>, <E_{dis}>, the pressure in the contact P_m and R might greatly differ from system to system and, in particular, F_{ts} might be large but P_m might be small due to a large value of <S>.[148] For example Round and Miles[134] conducted experiments with dsDNA similar to those conducted by San Paulo and Garcia with antibodies and concluded that DNA could not be permanently deformed in the repulsive regime. Nevertheless, the simple experiment shown in Fig. 6.1 argues otherwise. Also, Thomson imaged antibodies with considerably high resolution in the repulsive regime with no sign of plastic deformation.[86-87]

An experimental example of the relevance of <S> and R is shown in Fig. 6.2 where a nearby molecule to those in Fig. 6.1 has been imaged systematically by discretely increasing the value of A_0 and keeping A_{sp}/A_0 constant with the same tip as in Fig. 6.1. The minimum A_0 inducing severe observable plastic deformation has been reached at approximately A_0~110-130 nm (Figs. 6.2(h)-(j), light grey) but critical deformation could only be observed above A_0>120-130 nm (c.f. Figs. 6.2(i) and 2(j), dark grey). The average energy dissipated per cycle <E_{dis}> has been calculated for every value of A_0 in the sequence (Fig. 6.3(a)). For comparison, the average energies per cycle dissipated to the medium <E_{med}> and the mean energy stored in the cantilever <E_c> are also shown; <E_c> $=\frac{1}{2}kA_{sp}^2$ and <E_{med}>$=\pi\frac{k}{Q}A_{sp}^2$ assuming viscous damping. The three energy variables grow exponentially with A_0 and rapidly reach hundreds and thousands of eV. Significantly, tips submitted to these imaging sequences can later be used to scan biomolecules such as DNA and antibodies with relatively high values of A_0, i.e. A_0<60-70 nm, and any given set-point without inducing molecular plastic deformation.[148]

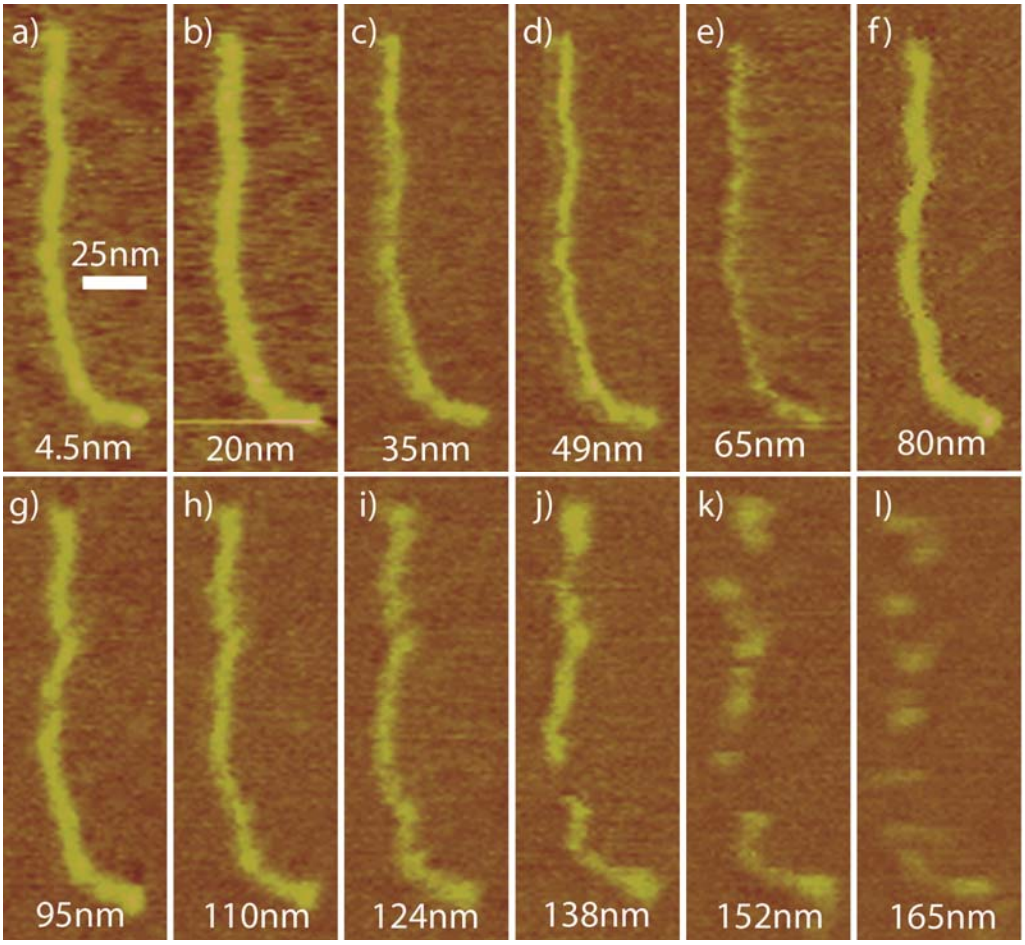

Figure 6. 2

Topographic sequence of dsDNA molecules on a mica surface with the same cantilever-sample system as that shown in Fig. 1. The value of A_0 has been systematically increased from a) 4.5 nm to (l) 165 nm while keeping A_{sp}/A_0=0.80. The molecules submitted to the sequence have been labelled m_3 to m_7.[148] For easy comparison only a zoomed view of m_4 is shown. The values of A_0 are shown at the bottom of each panel. The scan size is 240 nm by 80 nm and it is a zoomed view of the original 1 µm by 1 µm scan.[147]

Thus, it is clear in these experiments that R and $<S>$ have to increase with A_0. It is important to realize, however, that failure to increase A_0 smoothly and systematically typically results in the tip mechanically fracturing in an uncontrolled fashion.[122,148]

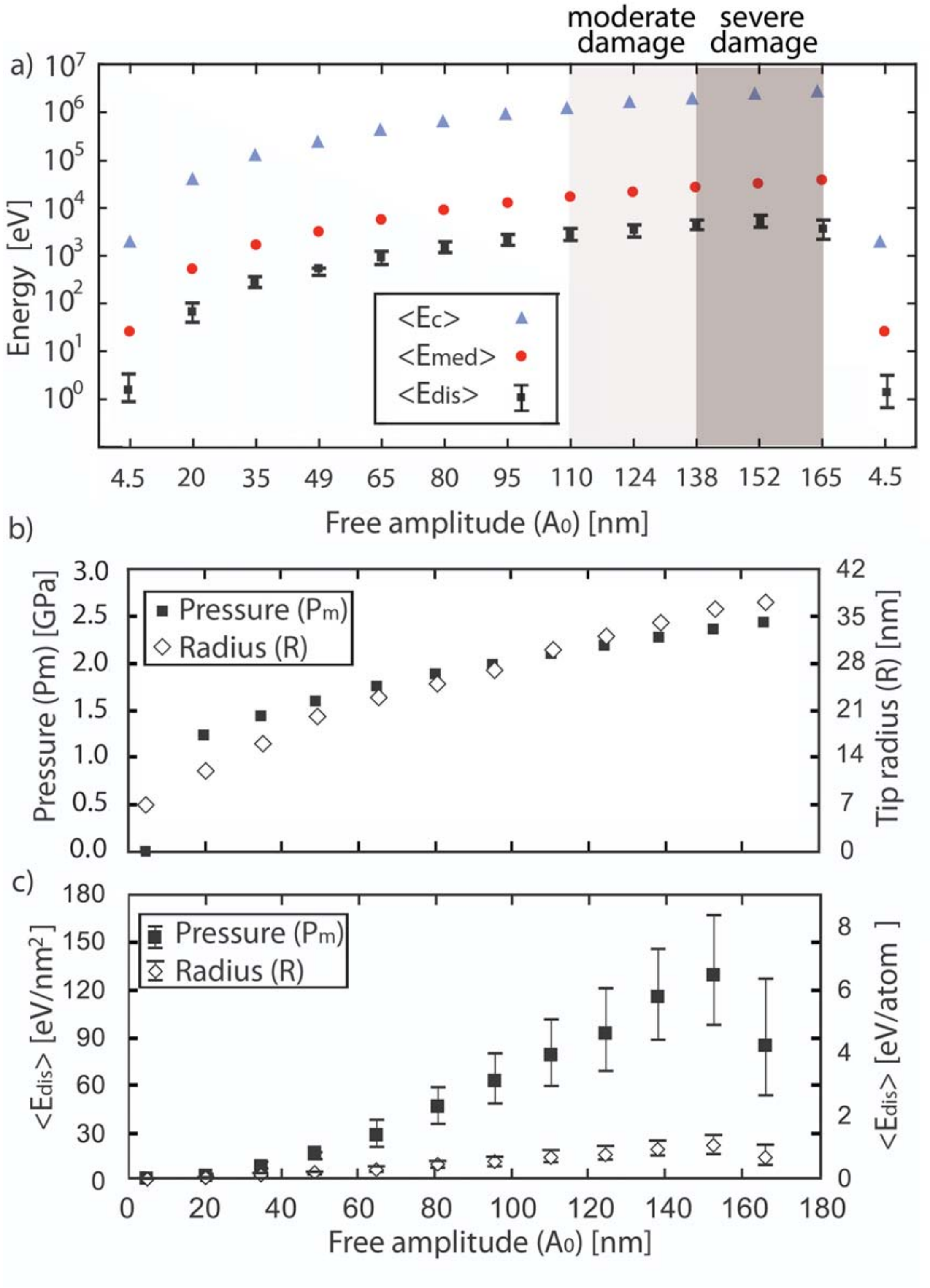

Figure 6. 3

a) Experimental values of <E$_{dis}$> (black squares), <E$_{med}$ > (red circles) and <E$_c$> (blue triangles) for the sequence in Fig. 2 and calculated from (6.1). The values of A_0 are also shown and errors of ±12%, ±10% and ±5% have been allowed for k, Q and ϕ respectively. The error bars for <E$_{med}$> and <E$_c$>, almost coincide with the average values in this logarithmic scale, thus they have not been shown for clarity. b) Predictions (simulations) of the increase in P_m with increasing A_0 (filled squares) when the tip radius is set to a constant value (R=7 nm) and predictions of the increase in R (outlined rhombuses) when a limit to the pressure is set (P_m=0.9 GPa). c) Prediction of the eV dissipated per nm^2 and per atom in both cases when inputting the experimental data from a) into the model. The range of free amplitudes for which moderate molecular damage has occurred are coloured with light grey and the those for which severe molecular damage has occurred with dark grey. The parameters are: $f=f_0$=300 kHz, k=40 N/m, Q=500, γ=40 mJ, E=10 GPa, E_t=120 GPa.[148]

Nevertheless, Scanning Electron Microscope (SEM) [79,122] images can be used to show that tips with curvatures in the range of 5 nm become stable when reaching values of R=20-30 nm provided A_0<60-70 nm. These values of R can be shown to correspond to Type III systems even when large values of k are used. For example, an SEM image of a tip submitted to this range of free amplitudes in air, on a mica surface and using k~40N/m is shown in Fig. 3.5c (Chapter 3).

Furthermore, tips that stabilise at R=20-30 nm and display the characteristic APD curves of Type III systems have already been shown[122] (Chapter 3, Fig. 3.16) to involve noise at low values of A_{sp}/A_0 and large values of A_0. This is the characteristic monotonic increase in noise in the L-state for Type III systems. Values of R<5 nm produce Type I systems and Type II systems are observed when 5<R<20-30 nm. This is shown in detail in the next section and verifies that Type III systems are mechanically stable. Note however, that other values of k (i.e. k~2 N/m) involve smaller pressures in the tip-sample interaction and, thus, imply that the tip could stabilize for smaller values of R (i.e. R<20-30 nm) with these free amplitudes (A_0<60-70 nm=A_{0L}).[148] In fact, Type II or III systems are obtained for k~2 N/m even when R~5 nm.[137] The concept of the critical limiting amplitude A_{0L} is defined below and discussed in the last section of this chapter. Still, for the cantilever-sample parameters that concerns this study (Figs. 6.1 - 6.3) and provided that A_0 is smoothly increased in a sequence of scans following the method in Fig. 6.2 and keeping A_0<60-70 nm=A_{0L}, the tip mechanically stabilises at values of R=20-30 nm. Furthermore, this value of A_0 (i.e. A_0<60-70 nm=A_{0L}) is termed a critical value A_{0L} standing for limiting free amplitude.[148] Furthermore, in principle, other values of A_{0L} could be used in these sequences to stabilize the tip at different values. In particular, SEM data can be used to verify that for A_{0L}=20-30 nm stability occurs for R=10-20 nm whereas for A_{0L}=150-200 nm, the radius of the tip stabilises in the range R=30-40 nm (data not shown). Furthermore, these data agrees with our predictions in the simulations below.

In Fig. 6.3b, R has been set to the constant value of 7 nm and A_0 has been gradually increased while keeping A_{sp}/A_0 constant. The figure shows how P_m increases with A_0 (filled squares), with no upper bound, which is physically unrealistic. Alternatively an upper bound on P_m can be set (outlined rhombuses). In Fig. 6.3b, the initial radius is R=7 nm but the maximum pressure is $(P_m)_{\max}$=0.9 GPa while R has been allowed to increase with A_0. The value $(P_m)_{\max}$=0.9 GPa has been obtained from simulations by setting A_{0L}=60-70 nm and R=20-30 nm[79] in the model where P_m~0.8-1 GPa is obtained. The predicted value is also consistent with other values of A_{0L} (data not shown). In Fig. 6.3c, the experimental values of $<E_{dis}>$ in Fig. 6.3a have been introduced in the model. The value of $<S>$ has been calculated according to (28). This allows one to estimate eV/nm^2 and/or eV/atom if 1) the tip radius remains constant (R=7 nm) and the pressure is allowed to increase without upper bound (filled squares) and 2) if the pressure has an upper bound (i.e. P_m=0.9 GPa) and R is allowed to increase (outlined rhombuses) (Fig. 6.3c). A total of 20 atoms per nm^2

have been accounted for in the nanoscale contact implying an average of 10 atoms per nm^2 on each surface.[148] If R is not allowed to increase, several eV/atom are predicted. This situation is physically unrealistic since a covalent bond has a typical value of 2eV.[169] If R is allowed to increase, the number of eV per atom always remains below or close to 1eV. Figs. 6.3b-c can be readily used to interpret elastic and plastic deformation and their relationship with $<S>$, R and A_0 and eV/atom. A limit to the tip broadening phenomenon demonstrated in Fig. 6.3 could be reached for extremely large values of A_0. For example, we have observed that as A_0 is further increased, holes can be punched in the mica surface.[148]

6.1.3 Summary

Demonstration of the tip radius being a dynamic variable has been achieved and quantified. These results have important physical significance: they allow the unambiguous definition of what large values of A_0 (i.e. A_0>100-150 nm) are in dAFM, namely, those for which an otherwise stable tip (i.e. R>20-30 nm) and/or relatively stiff surface (i.e. E>10 GPa[130]) can mechanically fracture.[148] Practically, it is then convenient to use R<20-30 nm and values of A_0 below 100 nm to carry out nanomanipulation experiments with an AFM and/or to obtain mechanical information about the sample by harmonic excitation. More thoroughly, from the above and in order to keep the tip radius stable and in the range of R<20-30 nm, values of A_0<60-70 nm=A_{0L} should be used. Experimentally, the tip should be initially submitted to a sequence similar to that in Fig. 2 with A_{0L}=60-70 nm. Then reliable experimentation with the tip can be performed provided A_0<60-70 nm throughout, guaranteeing mechanical stability.

The energy quantification presented here is fundamental for reliable characterisation of nanoscale processes in dynamic AFM. Importantly, an experimental method has been developed to reliably stabilize the tip radius by smoothly increasing A_0. Quantification of the interaction area between the tip and sample will lead to better mapping of local chemistry and mechanics and shed light on the mechanism of elastic and plastic deformation at the nanoscale.[148] In particular, with the methods developed in this chapter it should be possible to create a profile of the energy dissipated in $<S>$ by taking into account the regions where the pressure, and/or force per unit area in the case of attractive forces is higher.

Finally, it is worth mentioning that while 0.9GPa seems to be the limiting pressure for a silicon nitride tip and, in particular, an Olympus AC160TS cantilever, other limiting values could possibly be obtained for other cantilevers. That is, while the limiting value in pressure possibly depends on tip apex and the material properties, and in particular the yield compressive and yield shear strength and ductility properties, with which the end of the tip is fabricated, the limit in pressure should be independent of the elastic modulus of the surface or sample being imaged. Nevertheless, for a given surface or sample, this limit might never reached with standard cantilevers provided the elastic modulus of the surface is not large enough. This is simply because even though the limiting pressure that the end of the tip could support is a property of the tip itself, the pressure depends on the load, either static, i.e. DC AFM, or dynamic, i.e. dAFM, and this increases, in the dynamic case, with free amplitude (Fig. 6.3b), elastic modulus of the surface or sample and spring constant. This can be readily shown with the model used to obtain Fig. 6.3.[147]

6.2 The A-state: the three stages of a tip in ambient dAFM

6.2.1 Overview

A unified theory of nano-mechanical oscillators in ambient conditions is presented in this section. The appearance of a 3rd attractor, the A-state, associated with the surface water layer is described. The model is that presented in Chapter 4 but here, a larger range of R (R<20-30 nm) and more compliant cantilevers (i.e. k~2 N/m) are also discussed. Both experimental and simulated dAFM data shows that either one, two or three attractors might coexist depending on the amplitude, the attractive interaction component and the restoring force of the oscillator. In one extreme, systems can be either tri-stable (Type III systems) and show a characteristic monotonic increase in the levels of noise with decreasing amplitude. Hence, the L, H and A-states might co-exist. In the other extreme, the system might be mono-stable at small oscillation amplitudes with a maximum in noise before the amplitude reaches zero (Type I and II systems).

The monostability of the system is identified with the SASS region. Type I systems are those where the A-state is not present and are the preferred situations for SASS imaging (Chapter 4). Type I systems are, at most, bistable for a region of the operational parameter space.

6.2.2 Type I, II and III systems

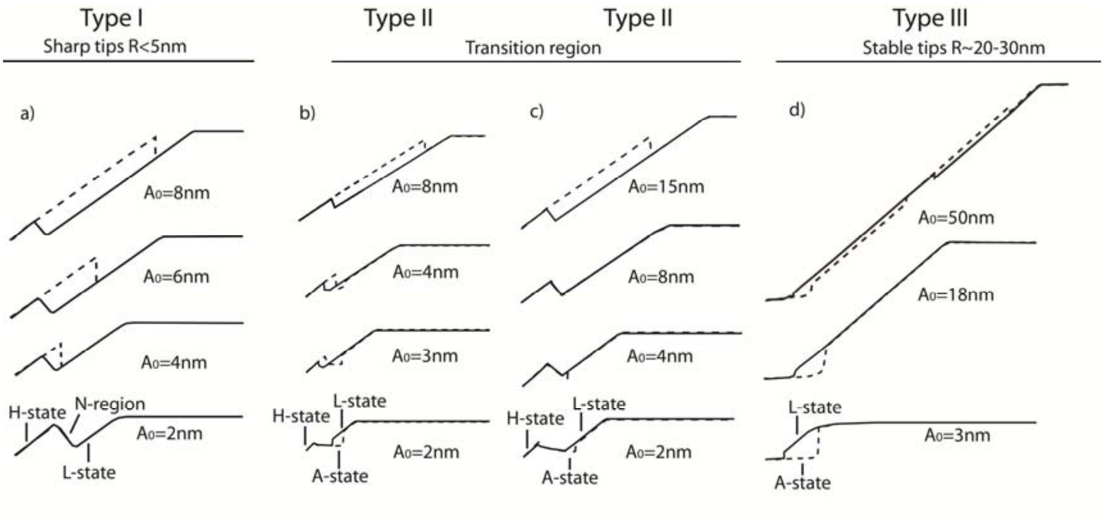

Figure 6. 4

Experimental Amplitude Distance (AD) curves where the behaviour of *A* (vertical axis) as a function of z_c (horizontal axis) is shown. The curves are not to scale and the axes are not shown since it is only A_0 and the shape of the curves that are relevant in this study. A_0 is increased from bottom to top in the columns. For the smaller values of A_0 the A, L and H-states are labelled. The N-region is labelled in a). Approach and retraction are shown with continuous and dashed lines respectively. These are the three types of AD curves that can be observed experimentally where a) Type I and d) Type III are the two extremes and b-c) Type II are transition curves presenting characteristics of both Type I and III. The A-state may a) not exist even for very small values of A_0 (Type I systems), b-c) exist for small values of A_0 only (i.e. A_0<5-10 nm) or d) present zero or positive slope in amplitude and be present for larger values of A_0 (Type III systems). The experimental parameters are: f=f_0~300 kHz, k~40 N/m, Q~500 and relative humidity (RH) 40%[115].

In Fig. 6.4 experimental AD curves on a mica surface are shown. In Fig. 6.4a and for a free amplitude of A_0=2 nm the L-state is first reached on approach, then a negative slope region with local maxima in A follows. There is no hysteresis on retraction for small values of A_0. Nevertheless, as A_0 is increased, the path is L-state, N-region and H-state on approach and H-state, L-state on retraction (Fig. 6.4a). This is a Type I system and has already been discussed in Chapter 4. An example of such a curve has already been shown in Fig. 4.1. Type II systems (Figs. 6.4b-c) differ from Type I because for small values of A_0 the A-state can typically be reached for Type II systems, then three attractors coexist. More thoroughly, it will be shown that the physical phenomenon of tip trapping relates to this third oscillation state, i.e. A-state, with the property that $\Delta A/\Delta z_c \rightarrow 0$.[170] Furthermore, phase space diagrams such as those used in Chapter 4 can be used to demonstrate the existence of the A-state.[137] For Type III systems (Fig. 6.4d), the L-state is initially reached on approach, then the A-state is reached. Nevertheless, the A-state is not a dynamic solution (A~0) for the smallest values of A_0. That is, the A-state traps the tip onto the surface impeding any oscillating motion (see A_0=3 nm Fig. 6.4d). Furthermore, hysteresis is observed in the extension-retraction cycle. This hysteresis allows observation of the characteristic flat amplitude of the A-state. In general, the L and H-states are oscillation solutions here but the H-state is not typically observed experimentally for these small values of A_0 in Type III systems. Thus, practically, the cantilever can only oscillate in the L-state and/or get trapped in the A-state.[137] Nevertheless, the existence of the H-state in these cases can also be shown with the use phase space projections (data not shown)[137] where it can be numerically shown the A-state becomes more prominent with decreasing z_c.[137] For larger values of A_0 the L-state is also reached initially while approaching the surface. Then, for small enough values of A, the A-state is reached and exists as an oscillating solution of the system. On retraction, the A-state controls the motion until, for large enough values of A, the L-state is re-attained. For sufficiently large values of A_0, the H-state is observed (e.g. A_0=50 nm in Fig. 6.4d)).

In Fig. 6.5 the three types of curves have been reproduced in simulations. The APDs on the first row (Figs. 6.5 a, f and k) are experimental curves obtained on a mica surface with a free amplitude of 5 nm. The APDs on the second row are simulated curves. These have been obtained by implementing the model described in Chapter 4 (Appendix A) where the effective distance between water layers and the capillary force are taken into account.[137] Both extension (black continuous lines) and retraction (red dashed lines) are shown. One parameter that has been changed to obtain the three different curves in the simulations has been the tip radius. For the Type I system (Fig. 6.5b) a radius of R=2 nm has been used. For the Type II (Fig, 6.5g) and III (Fig, 6.5l) systems values of R=12 nm and R=3 nm have been used respectively. The second parameter that has been changed for the three types of curves has been the strength of the capillary force. The strength of the capillary force is maximum for the Type I curve (Fig. 6.5b) and is reduced to one third and less than a tenth of its maximum value for the Type II (Fig, 6.5g) and III (Fig, 6.5l) curves respectively. This reduction of the magnitude of the capillary force as the tip radius increases is necessary in order to reproduce the three types of curves in the simulations. If the magnitude is not reduced an artefact is observed for Type III curves where the H-state is stably reached on retraction for these curves (data not shown). Future investigations of this phenomenon should be possible with the help of this model (Appendix A). This is clear from the similarities between experimental and simulated curves and implies that the physical origin of the three different types of behaviour is imbedded in the equation of motion here used.

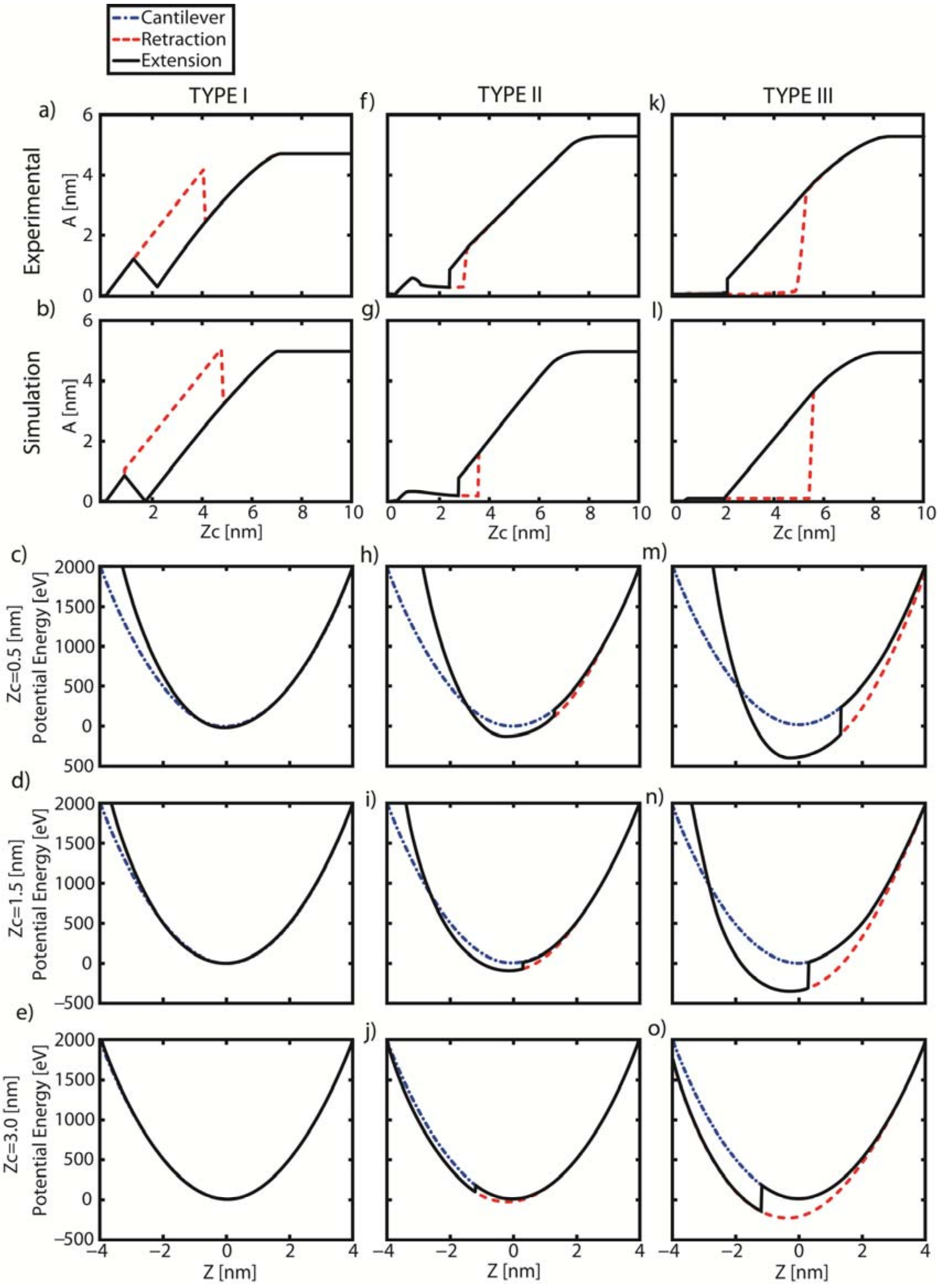

Figure 6. 5

On the top row experimental AD curves for the three types of systems are shown. These have been obtained on a mica surface with tips of different effective curvature. The three types of AD curves are shown experimentally (top row) and with simulations (bottom row) for A_0=5 nm. The behaviour of Type I, II and III are shown in the form of AD curves and with the respective hysteric potentials at different tip-surface separations z_c in the left, middle and right columns respectively. On the row below simulations are shown to reproduce the three different types of behaviour by increasing *R* from left to right. The effective potentials for the cantilever while interacting with the sample are shown on the rows below for the three systems for increasing tip-surface separation. The parameters are: $f=f_0$=300 kHz, k=40 N/m, Q=500, γ=20 mJ (surface energy), γH_20=72 mJ, *E*=10 GPa[130], E_t=120 GPa, *h*=0.6 nm and A_0=5 nm. The value of *R* has been increased from *R*=2 nm to 12 and 30 nm from left to right.

Further insight of the physical origins of the A-state is gained by looking at the effective potential of the cantilever interacting with the surface for the three values of R. Some examples of the behaviour of this effective potential are shown below the APDs in Fig. 6.5 for each type of system. On the first row of potentials (Figs. 6.5c, *h* and m) the effective values are shown in eV for a separation of z_c=0.5 nm. Again extension (black continuous lines) and retraction (red dashed lines) are shown and, in addition, the potential of the cantilever is also shown in blue (blue dash dotted lines). Here the potential energy is defined as the negative of the required work to take the tip from the given position to an infinitely large separation. In the plots the surface is on the left and a zero potential for the force is taken as the reference potential at infinity. The potential energy of the cantilever is defined as zero for *z*=0 (i.e. at the equilibrium position of the free cantilever) as usual. Thus, the horizontal axis (i.e. z) represents the instantaneous position of the tip. The discontinuity observed on extension is due to the onset of the capillary force and, thus, it is controlled by the distance for which the capillary force sets in. The attractive component of the force is seen to dominate and rapidly increase for these small separations with increasing *R* (i.e. from Type I to III); this is the physical origin of the A-state and what causes the tip to be trapped into the water layers. The fact that in the A-state the tip is trapped into the water layers between the tip and the surface can be readily shown with the simulations where the minimum and maximum distances in the A-state can be obtained. However, it can also be deduced from the simulations in Figs. 6.5b, g and l. The way to see this is by noting that the amplitude of oscillation in the A-state (see the above figures) is much smaller than the tip-surface separation and the separation is relatively small. That is $A<<z_c$ implies that contact with the surface does not occur and z_c~nm implies that the tip is already interaction with the water (see the details on the separations for which water interactions occur in Appendix A).

Furthermore, the A-state might or might not be an oscillation state. For example, compare the amplitude in Figs. 6.5f and g where As the separation increases the effects of the attractive force component decrease as expected. An effective well is clearly visible for the Type III systems and this is responsible for the A-state. Thus, it should also be expected that the effects of the A-state would be particularly relevant at small separations. This agrees with everything stated so far regarding the A-state and implies that stability should increase with increasing separation (i.e. oscillation amplitude) even for the larger values of R (i.e. R~20-30 nm). This statement also agrees with the stability criterion (3.14). Nevertheless, simulations and experiment can be used to show (data not shown) that for these very small separations and even for these larger values of R (Type III systems) monostability can result by sufficiently increasing the value of free amplitude. This might explain the fact that in FM AFM stability can be induced by increasing the drive amplitude as opposed to AM AFM where the drive amplitude is kept constant. In fact since the energy that enters the cantilever per cycle is controlled by the drive amplitude, the possibility to control the stability of the cantilever by increasing the drive force could be deduced by looking at the stability criterion expression (3.14). However, from the previous section (Fig. 6.3), it is evident that increasing the free (or equivalently drive) amplitude in order to increase stability is not advised if a sharp tip is to be maintained.

Experimentally, hundreds of AD curves have been produced with a range of spring constants k=2, 10 and 40 N/m and tip radii ($2<R<30$ nm) on mica, silicon and graphite.[137] After analyzing the experimental data, it is concluded that these (Figs. 6.4 and 5) are the three most common types of amplitude behaviour in ambient conditions with uncontaminated tips. When tips are contaminated, the results discussed in this chapter cannot provide information about the nature of the tip-sample interaction and/or the dimensions of the tip radius. These data leads directly to the solution of one of the basic problems of AFM, namely, characterizing tips in situ differentiating between those which are contaminated and those that are not. Briefly, curves might actually differ in terms of where the L, A and the H-states are reached on extension and/or retraction relative to the curves in Figs. 6.4a-d and 6.5 (this is due to the stochastic character of the switch between states[80,145]), but, otherwise, the behaviour is general. Overall, therefore, the approximate location of the A-state, its behaviour and the distinct shape of the curves is general for a nano-mechanical oscillator near a surface in ambient conditions with an uncontaminated tip; a tip is contaminated if an AD curve does not behave as any of the types described in Fig. 6.4 or 6.5.[137] More information on the nature of the contamination might be obtained in future investigations by analyzing the behaviour of the phase since it seems particularly sensitive to contamination (data not shown). A further method to characterise the tip radius in situ that can be used either on its own or in combination with the method described in this section consists of monitoring the minimum value of free amplitude required to reach the repulsive regime.[157] The former has been used on its own in 2009 to monitor very small changes in the wearing and creeping of the tip and the wearing of DNA molecules *in situ*. That this is possible could be deduced from Fig. 3.4. Thus, the combination of these methods makes tip characterisation more robust and, in particular, while distinguishing between Type I, II and III gives idea of the range of R (Fig. 6.4) the latter is sensitive to even small variations in R (i.e. ΔR~1 nm).[157]

It should be noted that simulations (data not shown) also show that as the cantilever stiffness is reduced from 40 to 10 and 2 N/m Type II and III systems become more prevalent even for very sharp tips (i.e. R<2-3 nm). Still, with Type II systems SASS can be performed even if resolution is not maximised (Fig. 6.6). Furthermore, these results might explain why, even with very compliant cantilevers and ultra sharp tips (i.e. k~2 N/m and R<5 nm), resolution does not seem to improve even though these cantilevers might involve forces orders of magnitude smaller than cantilevers with k=40 N/m. Overall, simulations show (data not shown) that there is a relationship between the prevalence of the A-state and the strength of the attractive component of the force relative to the restoring force of the cantilever. This partly explains the sensitivity of the A-state to R since R is always related to the attractive component of the force (i.e. vdWs and capillary forces) in the sense that it scales with it. To sum up, in one extreme, large values of R and very compliant cantilevers imply that very large oscillation amplitudes, and thus free amplitudes, are required to not observe the A-state[137] (these are Type III systems). In the other extreme, ultra-sharp tips and very stiff cantilevers imply that the A-state is never observed even with ultra small oscillation and free amplitudes (Chapter 4). The name A-state has been chosen for this reason; the A stands for attractive since it is the strength of the attractive component of the force relative to the stiffness of the cantilever that leads to the three different types of systems and the appearance of the A-state. Thus, while the sensitivity of the dynamics to the tip radius is very significant, other parameters such as cantilever stiffness and, for example, the elastic modulus of the sample, should not be underestimated. Still, for relatively stiff supporting surfaces such as mica the tip radius seems to be the main parameter leading to the most drastic differences in dynamics as exemplified in the above APDs. The implications of characterising the tips in these distinctive three types and the relationships to imaging and tip sharpness are discussed later.

Note that the practical implications of the above discussion are that stiff cantilevers and ultra-small oscillation amplitudes should provide high resolution. This is in accordance with experimental data[15,57] (Chapter 4). Nevertheless, care should be taken when using stiff cantilevers since large contact forces result even with the smallest oscillation amplitudes. This can be easily shown with simulations (data not shown) and can also be deduced by comparing the numbers in the energy dissipated in the tip-sample interaction in Fig. 6.3, where k=40 N/m, and those in the literature where k=2 N/m.[49] Moreover, it is clear from (6.1) that the energy stored in the cantilever rapidly scales with k.

While the recent trend of some groups for using compliant cantilevers in ambient conditions is clearly related to the fact that higher harmonics are more readily excited[5,49], the above observations might have also prompted this move.

Nevertheless, from the results here presented, it follows that small oscillation and free amplitudes and compliant cantilevers invariably result in domination by the A-state. This makes this combination unsuitable for imaging in agreement with the stability criterion (3.14).

Finally, from the study of the experimental and simulated AD curves and the phase space diagrams[137] several conclusions follow. First, the A-state does not follow the same linear relationship with z_c that the L and H-states do (i.e. $\Delta A/\Delta z_c \sim 1$) but either has negative slope ($\Delta A/\Delta z_c < 0$), zero amplitude ($A=0$) or close to zero slope ($\Delta A/\Delta z_c \rightarrow 0$) and/or a combination of these (see regions labelled as A-state in Fig. 6.4). This explains why the A-state is not suitable for imaging and generates background noise (see Fig. 6.6). Second, for Type I and II systems the L-state does not exist below a critical value of z_c ($z_{critical}$), i.e. only the H-state exists then and the system is monostable (Figs. 6.4a-c).[137] The value of $z_{critical}$ below which the system is monostable can be experimentally observed in the AD curves and typically coincides with a local maxima in A on approach (see regions labelled as H-state in Figs. 6.4a-c). Third, for $z_c > z_{critical}$ the A-state is inhibited with increasing z_c.[137] This is actually a pattern that can be observed from the potentials (Fig. 6.5).

In summary, there are two possibilities from an experimental point of view when A_0 is small. First, for Type II systems the noise should be expected to initially increase with decreasing z_c or A_{sp}. For $z_c \sim z_{critical}$ the noise should be maximized as the A-state inhibits the L and/or H-states (Fig. 6.6a). For values of $z_c < z_{critical}$ the noise should decrease and the resolution generally increase. This pattern is experimentally observed in Figs. 6.6a-c.

The experimental maximum in noise follows from the appearance of the A-state at intermediate values of z_c and/or A_{sp} for a given A_0.[137] The increase in stability and resolution at small proximities, Fig. 6.6c, follows from monostability and increased tip-surface proximity respectively (Fig. 6.4). Type I systems present similar characteristics in terms of resolution but stability is higher than for Type II systems since the A-state is not present and the system is, at worst, bi-stable for intermediate z_c values (Chapter 4). Second, for Type III systems the noise due to the A-state should be prevalent for small oscillation amplitudes (Figs. 6.6d-f) and should increase monotonically with decreasing z_c.[137]

Hence, high resolution is not possible with small oscillation amplitudes with Type III systems both because of lack of stability under these conditions and the unavailability of the tip-sample proximity that Type I and II systems offer through the monostable or SASS region (Chapter 4). It should be further noted that the H-state more readily prevails below resonance for lower values of A_0.[150] Nevertheless, the behaviour described here is general in terms of drive frequency everywhere near resonance, especially for small values of free amplitude. That is, similar behaviour can be found both below and above resonance in terms of the appearance of the A-state and its characteristics[137] (data not shown).

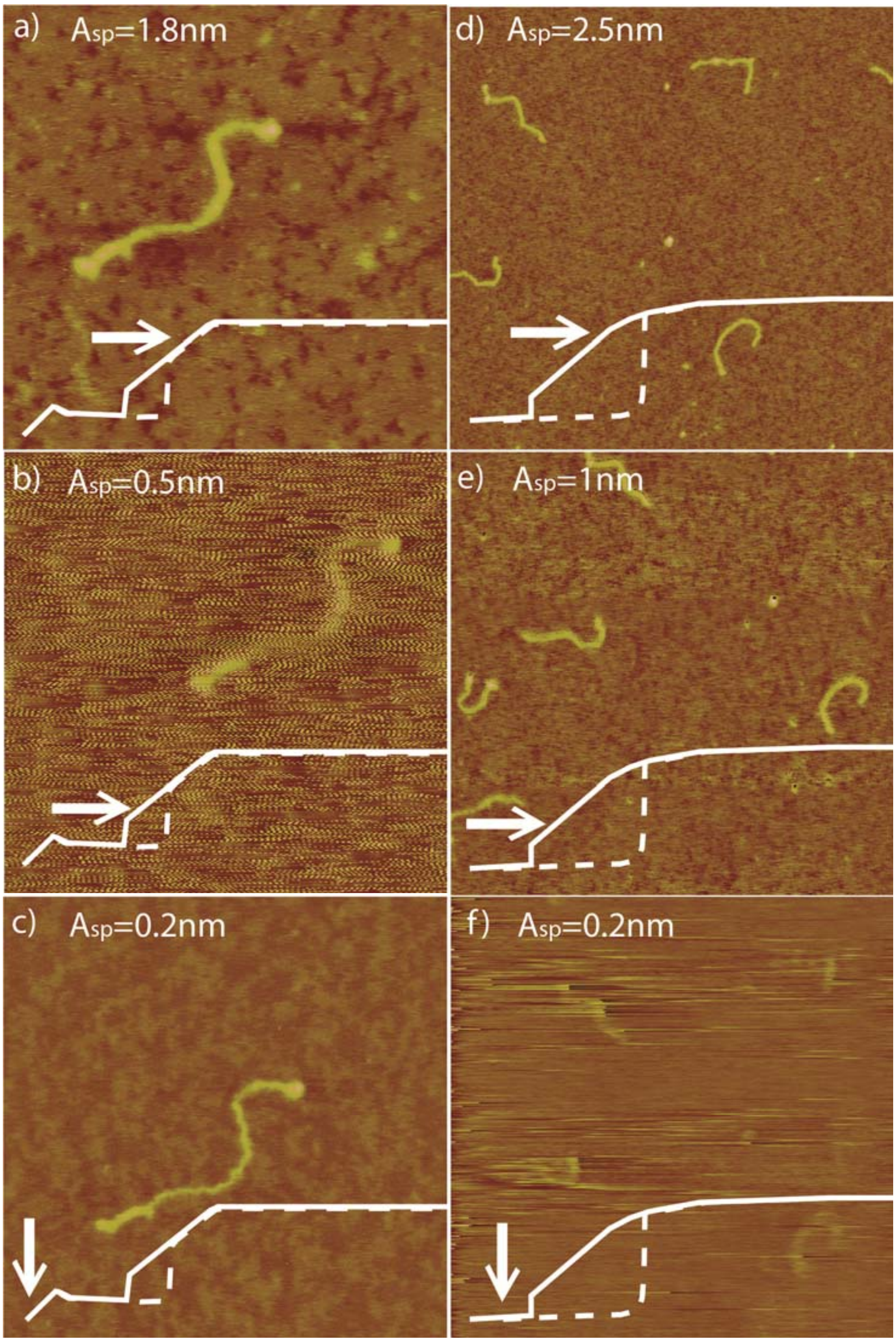

Figure 6. 6

Topography of dsDNA molecules on a mica surface. In the left column A_{sp} has been decreased systematically from (a) 1.8 nm to (b) 0.5 nm and (c) 0.2 nm. The noise pattern shows a maximum at intermediate values of A_{sp} as expected for a Type II system. The experimental parameters are as in Fig. 6.4b where A_0=2 nm. In the right column, the results on another cantilever-sample system are shown; a Type III system. Here the noise monotonically increases with decreasing A_{sp}. The experimental parameters are as in Fig. 6.4d where A_0=3 nm.

6.3 Summary

These results show that only Type I and II systems can provide high resolution and stability with small oscillation amplitudes and forces in ambient conditions. The capillary force[171] and the effective distance d^* between the tip and the sample for a given water film thickness h are the key parameters to be added to the otherwise conservative equation of motion in order to reproduce the experimental phenomenon. The relative appearance of the A-state depends on the strength of the attractive component of the interaction force relative to the restoring force of the cantilever, hence the name A-state. Since the capillary force and the water film effects apply for oscillatory motion with a frequency in the range of hundreds of kHz, these results imply that capillary formation and rupture can occur at timescales on the order of at least microseconds. This follows from the fact that capillary interactions have to be added to the equation of motion in order to reproduce the experimental data. Furthermore, while other studies have not considered small oscillation amplitudes due to concerns of reproducibility[118], these results hold for amplitudes down to zero and effective tip curvatures R of 5 nm or less. This also follows from experimental reproducibility considerations.

Furthermore, a classification of the dynamics of nano-mechanical forced oscillators with small amplitudes in hydrated environments in the presence of surface forces has been provided; three types of systems have been presented depending on the relative prevalence of the A-state. Thus, it is now possible to refer any future measurements in dAFM in ambient conditions to the three types of systems here described. This implies reproducibility and predictability. Where the A-state controls or influences the dynamics, the performance of AM feedback systems is greatly compromised due to its characteristic relationship between oscillation amplitude and separation. Type I and II systems can provide high resolution in ambient dAFM. The validity of the model is justified with experimental outcomes.

Significantly, Type I systems heavily depend on the state of the tip radius at a given time. More thoroughly, ultra-sharp tips typically evolve from Type I systems into Type II and Type III systems with increasing free amplitude. This is consistent with the results of the first section of this chapter. Namely, a cantilever with a k of 40 N/m and an *R* of 5 nm or less submitted to the sequence in Fig. 6.2 will first display an AD curve of the Type I (Fig. 6.4a). Then a Type II curve will follow as the free amplitude is increased. This is the case for amplitudes as small as 5-10 nm provided the tip is sharp (i.e. a tip displaying Type I AD curves). The tip will then broaden until it displays Type III AD curves (Figs. 6.4d). At this point the tip radius will be stable (*R*=20-30 nm) in accordance with the results presented in the first half of the chapter. In fact, the three types of curves in Fig. 6.4 have been obtained with the same tip by submitting to the sequence in Fig. 6.2.

Finally, it is actually possible to go from a one type to another, i.e. Type I to III or II. Nevertheless, the typical outcome of repeated use of a Type I system presenting a sharp tip is that it becomes Type II and eventually Type III where it stabilises. It is possible however, to go from a Type III to a Type II or I system by submitting the end to the tip to extremely high pressures by, for example, suddenly increasing the free amplitude and inducing temporary and extreme high pressures. This has in fact been done in some experiments during the thesis (data not shown). Moreover, while this process constitutes a random way in which shaping a tip, it is easy and be repeated indefinitely. Since the tip radius can be monitored by simply taking an APD curve, one could then repeat the process and wait until obtaining a Type I APD curve. Moreover, the fact that one can go from a Type I APD curve to a Type II and then a III on a given surface and with a given cantilever by simply increasing the value of free amplitude, implies that the type is strongly dependent on tip radius. For example, the three stages shown in Fig. 6.4 have been obtained with the same cantilever and surface in order, i.e. from Type I to II and III. Moreover, even the simulations show this. For example, as stated, the curves in Figs. 6.5b, g and l have been obtained by simply increasing the tip radius from 2 (Type I) to 12 (Type II) and 30nm (Type III).

Chapter 7

7. Conclusions

The findings presented in this thesis have dealt with three of the most controversial issues in AFM, namely small oscillation amplitudes, tip stability and characterisation and the interpretation of apparent height. These have been principally discussed for the case of ambient dAFM. Nevertheless a similar approach to interpret tip wear and stability in UHV and liquid environments could be followed. On the other hand, the subject of small oscillation amplitudes, as discussed in this thesis, and, in particular, the appearance of the A-state and the N and SASS regions, is characteristic of ambient dAFM imaging because of the relationship of these to capillary interactions. Still, it is likely that thorough investigations in which the tip is thoroughly characterised could give rise to the discovery of other relevant phenomena in these environments. Furthermore, the outcomes for apparent height have been shown to be general to all force microscopy (and by extension all scanning probe microscopes). It is the concept of the geometrical character of the force, resulting from the size of the object that gives erroneous measured heights in AFM. Thus, future investigations for liquid and UHV environments can be implemented in models where the force due to the tip-sample forces are added to the tip-surface forces, and should lead to similar results. This is because the concept of apparent height formation as interpreted here relies on the finite area of interaction that is prevalent in any AFM mode of operation.

The concept of effective area of interaction, and, in particular, the way in which the energy dissipated per atom has been calculated, will lead to much improved chemical and/or mechanical properties mapping. In particular, a more accurate distribution or profile of the energy dissipated in the area of interaction could be found by modifying the model and accounting for the differences in force per unit area across the interaction area. Furthermore, these results should be used in future investigations in conjunction with the results regarding tip characterisation that have also been presented in Chapter 6. In this respect, well characterised Type III systems are well suited to investigate chemical and material mapping. The results on tip characterisation and energy dissipation could also be used to investigate the mechanism of elastic and plastic deformation and energy dissipation in the nanoscale. These could provide further information on the mechanisms responsible for energy dissipation and the ways in which this dissipation propagates in small nanoscale volumes as the tip or sample deforms. The results could have applications in molecular physics in general and, in particular, in the fields of tribology and molecular interactions. More thoroughly, in-situ tip characterization should have implications in all branches of AFM where quantitative information is required.

These results have also shown that it would be necessary for an ultra-sharp tip (i.e. R<5 nm) to withstand the interactions involved in mechanical contact, where relatively high pressures (i.e. ~1 GPa) occur, to image in standard AM AFM with high resolution. Nevertheless, these would still involve very large pressures that would likely damage soft matter such as DNA, and, thus, would not be suitable for high resolution imaging of biomolecular systems. In this respect, using specially prepared tips such as nanotube functionalised or diamond coated tips are unlikely candidates for future applications in biomolecular imaging in AM AFM. Nevertheless, these might offer a solution if the N and SASS regions are used, where the forces are minimised and the stiffness of the cantilever does not have to be particularly large for high stability and small oscillation amplitude imaging. Sample mobility might still be a problem in these cases even in ambient conditions, but these could be minimised by further decreasing the forces. This is a technical challenge but not physically impossible and requires that a very sharp tip integrated onto a cantilever with an intermediate spring constant is oscillated with ultra-small oscillation amplitudes, probably in the sub-angstrom range, at very small separations. A compromise would be necessary since the cantilever should be stiff enough to inhibit the A-state while minimising forces for a given oscillation and drive amplitude and separation. Both requirements could be met however by sufficiently decreasing the tip radius since a decreasing tip radius implies that more compliant cantilevers can be used without inducing the appearance of the A-state. Thus, in ambient and liquid environments where the nature of the medium more readily perturbs the dynamics of the cantilever, efforts should be made to detect ultra-small oscillations with high precision and produce ultra sharp and resistant tips. Finally, with these highly sensitive and high resolution instruments, it is likely that continuum models would not match experimental data. The effects of these small dimensions would be particularly relevant in terms of modelling sample deformation, viscoelastic processes and pressure. Thus, these would directly affect the results of the apparent height model and capillary interactions. Nevertheless, the forces in the equation of motion could be replaced by atomistic models where more fundamental phenomena such as coordination chemistry, orbital interactions and quantum effects could be accounted for.

In liquid environments bistability is not typically observed. Nevertheless standard liquid imaging is typically carried out with very compliant cantilevers (k<0.1-1N/m) and very low Q factors (Q<2-10) which are known to dramatically inhibit the H-state. Thus, maybe future investigations with stiffer cantilevers could show that bistability and even the A-state could be observed. Nevertheless, it is unlikely that the A-state in liquid environments will behave similarly to the A-state in ambient conditions. This is because it is addition in the equation of motion of the effective distance between water layers and the capillary adhesion typical of hydrated environments that allow predicting the experimental behaviour and phenomena characteristic of the A-state here presented.

Advances in the aforementioned directions should result in a microscope capable of routinely imaging molecular systems with sub-molecular resolution and simultaneously acquiring chemical and mechanical information. Still, the basic results in this thesis show that conventional ultra-sharp probes with standard stiffness and standard sample preparation together with standard AFM equipment and software allow sub-molecular resolution of dsDNA molecules in the SASS mode. Significantly, the macroscopic expressions for the tip-sample model closely match experimental data implying that the limits of microscopic models are not still reached under these conditions.

Appendix A

A.1. Model

A.1.1. Equation of motion

The dynamics of the cantilever in air in AM AFM have been shown to closely respond to the equation of motion of a forced simple harmonic oscillator Eqn. (A1) with the addition of the tip surface forces F_{ts}.[1,33,41,45,118,145] In particular, when the Q factor is high, as in ambient conditions, and where relatively stiff cantilevers are used, the excitation of harmonics[35,48] and the dynamics of the second mode of oscillation can be ignored[5]. Moreover, in the study of higher harmonics, relatively high values of free amplitude A_0 are typically used[22-23,35]; here, the focus in on small values of A_0 and amplitude set-point A_{sp}.

$$m\frac{d^2z}{dt^2}+\frac{m\omega_0}{Q}\frac{dz}{dt}+kz=F_{ts}+F_0\cos\omega t \qquad \text{(A1)}$$

The equation of motion in (A1) includes the effective mass of the cantilever $m=k/(\omega_0)^2$, the string constant of the cantilever k, the natural angular frequency ω_0, the Q factor and the drive force $F_0\cos\omega t$. Then F_{ts} is the tip-surface or tip-sample force.

A.1.2. Tip-surface forces

For the F_{ts} it is typical[1] in AM AFM to use the non-retarded and zero frequency long range van der Waals (vdW) forces Eqn. (A2) [2] where the force between a sphere of radius R and an infinite and flat surface is used. In order to take into account the water layers in ambient conditions, the tip-surface distance d is replaced by the effective distance d^* (Fig. A1) in the non contact region and when the capillary force does not act as shown in Eqn. (A2). Here $d^*=d-2h$ where h is the height of the water layers on the tip and the surface. The universal nature of the vdW force[8] implies that it prevails in all AFM experiments. For the short range interactions it is common practice to use models from contact mechanics[1] where, in particular, the Derjaguin-Muller-Toporov (DMT) model applies when the surface is not very compliant and/or R is small[1,132,172]; there exists an analytical relationship between the values of these two parameters that can be used to predict in which cases the DMT applies.[1,131-132] This has been discussed in Chapter 2. The use of these two forces in dynamic AFM (dAFM) has led to highly accurate descriptions of the phenomena occurring when the tip vibrates near the surface, such as bi-stability[80,145] and the relationship between average forces and the phase shift.[41,45] Other forces such as magnetic and electrostatic might affect the dynamics of the cantilever but those are typically set-up dependent.[1] Still, there is another force which in ambient conditions has already been shown to affect the tip dynamics[118]; the capillary force. Zitzler et al. reported that the addition of the capillary force only resulted in the inhibition of the H-state (the H-state is discussed in Chapter 3 and the Terminology section) the for a given A_0. AD curves were acquired for range of A_0 both experimentally and by simulations and it was concluded that the minimum required value of A_0 to intermittently contact the surface increased almost linearly with RH. Furthermore, they reported the remarkable property of no particular change in the slope of the AD curves with the addition of this hysteric force. Nevertheless, they used relatively high values of A_0, in particular several times larger than 2-5 nm, and never discussed the phenomena of small oscillation amplitudes $A_{sp}/A_0<0.2$, due to the lack of reproducibility associated with unknown tip shape and quality. According to the simulations and experiments here presented, it is precisely for the range of parameters that they did not consider that the single attractor exists giving rise to the N and SASS regions. It should be noted, however, that Zitzler et al. did not consider the tip-surface effective distance d^* from the water layers on the tip and surface. In particular, adding only the capillary force or only the distance d^* to F_{ts}, does not produce the required results observed in Fig. A1; both the capillary force and d^* have to be taken into account.

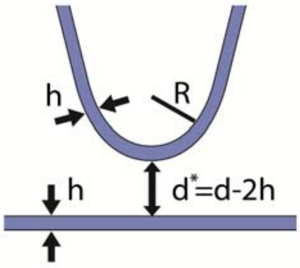

Figure A. 1

Schematic of the geometrical relationships between d, h and d^*. Here d is the tip-surface distance, h is the height of the water layer on the tip and the supporting surface and R is the tip radius.

More thoroughly, the effective distance d^* is a more fundamental phenomenon than the addition of the capillary force in order to reproduce the experimental data. This has been verified by implementing both variations of the model (data not shown). The tip-surface distance (d) dependencies are then as follows

$$F_{ts}(d^*) = -\frac{H_{H_2O}R}{6(d^*)^2} \qquad \text{(A2)}$$

when $d > d_{off}$ and also when $d_{on} < d < d_{off}$ provided the capillary force is not acting.[118] Here *H* is the Hamaker constant. The suffixes on and off make reference to the distance for which the capillary is formed as the tip approaches the surface and the distance when it breaks during retraction respectively. When the capillary is on and provided $d > a_0$ the tip-surface force is

$$F_{ts}(d) = F_a(H^*) + F_{CAP}(d) \qquad \text{(A3)}$$

where[171]

$$F_{CAP}(d) = -\frac{2\pi\gamma_{H_2O}R}{1 + \dfrac{\pi R d^2}{V_{men}}} \qquad \text{(A4)}$$

and

$$F_a(H^*) = -\frac{H^*R}{6a_0^2} \qquad \text{(A5)}$$

Here F_a is the adhesion force, a_0 is an intermolecular distance[41] typically taken to be 0.165 nm[8] and *H* is interpolated when the capillary neck is formed between the tip and the surface

$$H^* = \frac{\Delta H}{(d_{0ff} - a_0)} d + H_S - \frac{\Delta H a_0}{(d_{0ff} - a_0)} \qquad \text{(A6)}$$

where $\Delta H = H_{H_2O} - H_s$ and H_{H_2O} and H_s stand for the Hamaker constant for water and the surface respectively. In this model, the only dissipative mechanism is the hysteresis provided by the capillary (A4) and van der Waals and adhesion (A2 and A4) forces. The influence of the effective van der Waals is an indirect result of the hysteresis between formation and rupture of the capillary bridge. If during one cycle the capillary forms and ruptures, the energy dissipated is dependent only on d_{on}, d_{off} and h; i.e. the geometry of the tip and the height of the water layer *h* respectively. For the contact region, $d < a_0$ and the force is

$$F_{ts}(d) = F_a(H_s) + F_{CAP}(d) + F_{DMT}(d) \qquad \text{(A7)}$$

where[125]

$$F_{DMT}(d) = \frac{4}{3} E^* \sqrt{R(a_0 - d)^3} \qquad \text{(A8)}$$

A.1.3.Model

The capillary force is in fact given by[8,171]

$$F_{CAP}(d) = -\frac{2\pi\gamma_{H_2O}R}{1 + \frac{\pi R d^2}{V_{men}}}\cos\theta \qquad \text{(A9)}$$

The simplification $\cos\theta = 1$ as been used here as in previous studies.[118] Still, in order to reproduce the experimental curves in Figs. 6.4 and 6.5 the capillary force magnitude (A9) has to be inhibited with increasing R. This has been discussed in

Chapter 6. Also note that Zitzler et al used[118] a slightly different[8,171] form of Eqn. (A9). Both Eqn. (A9) and the equation used by Zitzler et al. produce simulations that reproduce the N and SASS regions provided d^* is also used (data not shown). Furthermore $d=a_0$ is taken in Eqn. (A9) when $d<a_0$. The volume of the water meniscus V_{men} is given, from geometrical considerations[118], by

$$V_{men} = 4\pi R h^2 + \frac{4}{3}\pi h^3 + 2\pi a^2 h \qquad \text{(A10)}$$

where a is the DMT contact radius. The expression for a is

$$a = \sqrt{R|\delta|} \qquad \text{for} \qquad d<a_0\,; \qquad \text{otherwise } a=0 \qquad \text{(A11)}$$

Here δ is the tip-surface deformation. Also, for computational purposes

$$\delta = z_c + z + a_0 \qquad \text{when} \quad d<a_0 \qquad \text{otherwise } \delta=0 \qquad \text{(A12)}$$

The conditions for the capillary interaction are[118,171]

$$d_{on} \approx 3h \qquad \text{capillary on} \qquad \text{(A13)}$$

$$d_{off} \approx V_{men}^{1/3} - \frac{1}{5R} V_{men}^{2/3} \qquad \text{capillary off} \qquad \text{(A14)}$$

Note that when $d<a_0$, the capillary force can still increase with increasing δ since V_{men} is a function of a which is a function of d. Physically this implies that as δ increases the volume of water on the tip-sample interface displaced in the deformation adds to the V_{men}, thus increasing the magnitude of F_{CAP}. The relationships between d, h and d^* are shown in Fig. A1.

A.1.4. Simulations versus experimental outcomes

The model has been implemented in two ways; using Matlab[173] and in the C programming language. In C everything has been written manually including the numerical algorithms; fourth and eighth order standard Runge Kutta algorithms. No problems of divergence have resulted from this approach as opposed to the problems discussed elsewhere.[118] A standard Runge Kutta algorithm has also been used when implementing the model in Matlab. The results using both methods were almost identical (data not shown), however the C program was orders of magnitude faster. Thus, the phase space projections for $t_0=0$ were carried out using the program written in C (Fig. 4.3).

In Fig. A2a experimental Amplitude Distance (AD) curves taken on a muscovite mica surface at 40% relative humidity (RH) for small A_0 are shown. AD curves are explained in detail in Chapter 3 and the Terminology section. The experimental ADs can be compared with simulations in Fig. A2b where only the conservative potential has been used ($h=0$). The conservative potential alone does not reproduce the experimental behaviour. In Fig. A2c, the capillary forces and the concept of the effective tip-surface distance d* have been added for h=0.6 nm. This is the full model as described by Eqns. (A1-A8). It is only for this complete model that the N and SASS regions are observed and experimental ADs are reproduced.

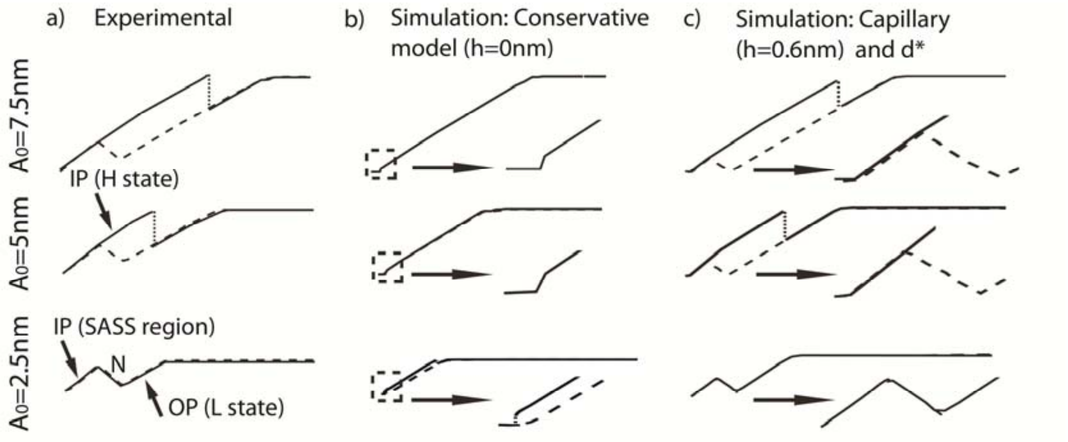

Figure A. 2

a) Experimental AD curves for A_0=2.5, 5 and 7.5 nm. The vertical axis shows A as a function of z_c. The amplitude reduction is approximately linear with decreasing z_c where positive slopes are observed. The experimental parameters are: f_0=312 kHz, $f=f_0$, k~40 N/m, Q=550, RH=40% and R<5 nm. Simulations for the same range of A_0 where b) only the conservative potential has been used and c) the capillary force and d* has been incorporated into the model. As shown, only with the addition of the capillary force and d* can the experimental phenomena be reproduced. The arrows point to zoomed views for smaller values of z_c, i.e. regions near contact. The parameters for the simulations are: **b)** $f=f_0$=312 kHz, k=40 N/m, R=2.5 nm, Q=500, γ=40 mJ (surface energy of the surface), E=10 GPa, E_t=120 GPa; **c)** as above plus h=0.6 nm and γ_{H2O}=72 mJ. For both experiments and simulations, z_c has been reduced from $2A_0$ to 0 nm and then increased back to $2A_0$ nm at a speed of $\dot{z}_c$=0.05 nm/s or less.

A.2 The effective area of interaction

A2.1 The static effective area of interaction

In AFM techniques surfaces are tracked with very sharp probes (i.e. with effective curvatures in the order of several nm) mounted on microcantilevers.[12] The principle is that when the probe is sufficiently close to the surface, it senses forces which either deflect the cantilever (i.e. contact mode CM AFM) or damp the amplitude (amplitude modulation (AM) AFM) and vary the effective resonant frequency (frequency modulation (FM) AFM).[1,13-14,16] In order to understand how all sources of contrast from different force fields affect lateral resolution, one has to come to terms with the fact that the interaction between the probe (i.e. tip) and the surface or sample occurs relatively locally but not as if between two mathematical points or delta functions. Thus, the approach used here is applicable to all kinds of scanning probe microscopes (SPMs) whether they are scanning surfaces which are not completely flat (i.e. atomic terraces, lipid bilayers, mineral crystals etc.) or when they are flat.

In practical terms, the effect can be understood as the tip-sample interaction occurring inside an effective area of radius r, where r can vary depending on local topography and surface properties (i.e. r(x,y,z)). Having this in mind, assume that a tip with effective curvature R is located at a static distance d (i.e. with constant cantilever sample equilibrium separation z_c) from an infinite surface (Fig. A3a).

Then, the total energy (E_n) of interaction between the tip, modelled as a sphere of radius R, and the surface can be determined by integrating across an infinite surface. Nevertheless, it is reasonable to assume that a large fraction or percentage of this interaction occurs in within an infinitely long end-on cylinder of radius P, i.e. the interaction area is the circular end of the cylinder (Fig. A3b). Hence, it will mainly be the interaction from this cylinder (E_p) that will modulate the sensing parameter in any AFM mode. First assume that a sufficiently large percentage is accounted for by this effective area of interaction. Then, assume that a tip is scanning an infinite surface. As the surface is raster scanned, imagine that it encounters a sample sphere of radius R_2. The key concept is that before the tip is in-line with the edge of the sphere, the sphere will fall within this effective area of interaction and will start affecting the sensing parameter, i.e. the amplitude reduction.

Hence the topography will be sensed and reconstructed by the instrumentation as soon as the surface feature lies within this area of interaction. The amplitude reduction will be affected until the tip finds itself on the other side of the sphere and far enough from it for the sample to fall outside the effective interacting area. The measured width of the sphere will be no less than twice the effective radius of interaction (r), where r coincides with P, plus the diameter of the sphere ($D=2R_2$). Mathematically this means that the apparent width in the infinite sample plane will be larger than $2(r+R_2)$. That is $w \geq 2(r+R_2)$, where w is the apparent width of the sphere.

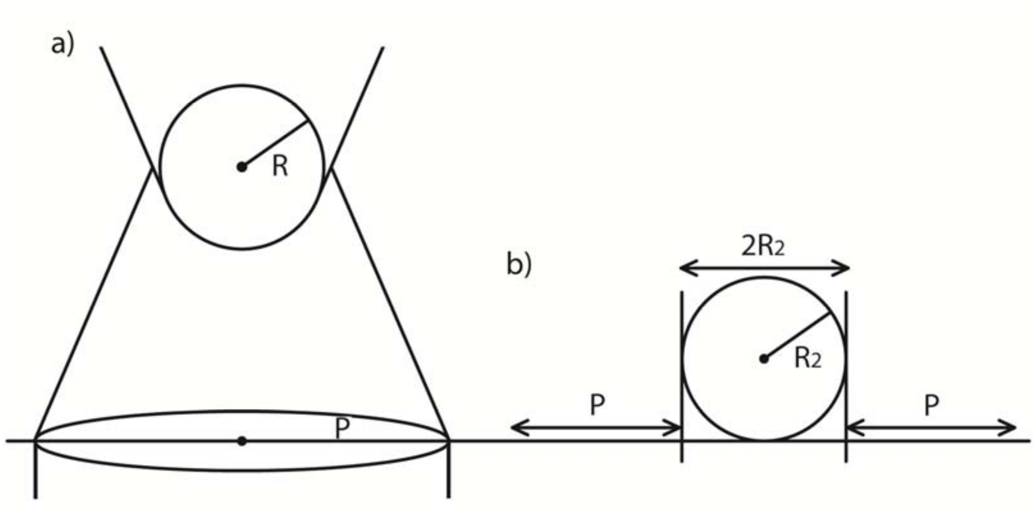

Figure A. 3

a) A tip, modelled as a sphere of radius R, interacting with an infinite surface can be thought of as interacting with an infinitely long cylinder of radius *P* going down from the sample surface (i.e. an end-on cylinder). The effective area of interaction can be defined by comparing the energy of interaction between the sphere of radius *R* and the surface of radius *P* with that of the sphere of radius *R* and an infinite surface. These energies can be termed E_p (energy cylinder) and E_n (energy infinite surface) respectively. Thus, mathematically, the radius *P* can be calculated for any given E_p/E_n. **b)** The apparent width of a sample (sphere) of radius R_2 can be written mathematically as $2(P + R_2)$. This might represent a single macromolecule, i.e. DNA or protein, or a nanoparticle but could also be a surface protrusion on a continuous material.

The effective radius of interaction in the contact region can be obtained by using the DMT model of contact mechanics which is given by Eqn. (A11). For the van der Waals (vdW) forces we use the approach of Hamaker and proceed to calculate the interaction energy for an end on cylinder of radius *P* (effective area of interaction) and a sphere of radius *R*. With this approach we find

$$E_p(d)_{C-S} = -\frac{HR}{6}\int_{z=d}^{z=\infty}\left[\frac{-1}{(\beta+D)^2}+\frac{-1}{\beta^2}+\frac{-1}{R(\beta+D)}+\frac{1}{R\beta}+\frac{1}{(z+D)^2}+\frac{1}{z^2}+\frac{1}{R(z+D)}-\frac{1}{Rz}\right]\delta z$$

(A15)

which is the interaction energy between **an infinitely thick circular section (or cylinder) of radius *P* and a sphere of radius *R* at a distance *d*.** Here z is the vertical axis, $D=2R$ and $\beta=(z^2+P^2)^{1/2}-R$ have been used in order to make the expression more compact.

The first four terms involving β can be integrated numerically giving Eqn. (A16)

$$\zeta(d)_{C-S} = -\frac{HR}{6}\left[\frac{2d+D}{\alpha d}+\frac{1}{R}Ln(\frac{d}{\alpha})\right] \qquad \text{(A16)}$$

$$\psi(d,P)_{C-S} = -\frac{HR}{6}\int_{z=L}^{z=\infty}\left[\frac{-1}{(\beta+D)^2}+\frac{-1}{\beta^2}+\frac{-1}{R(\beta+D)}+\frac{1}{R\beta}\right]\delta z \qquad \text{(A17)}$$

Here $\alpha=d+2R$ and C-S stands for cylinder sphere system. Eqn. (A16) is the same expression as that for a sphere and an infinite surface.[2] This result is meaningful since the last four terms from Eqn. (A15) do not take the radius of the cylinder (P) into account. These other terms, Eqn. (A17), account for the radius of the cylinder. This is emphasised in Eqn. (A17) by writing that the function is a function of both d (the minimum distance between the sphere and the cylinder) and P (the radius of the cylinder). The final equations can be written more compactly by writing

$$\zeta(d)_{C-S} = -\frac{HR}{6}\mathrm{Z}(d)_{C-S} \qquad \text{(A18)}$$

$$\psi(d,P)_{C-S} = -\frac{HR}{6}\Psi(d,P)_{C-S} \qquad \text{(A19)}$$

Then, the total energy of interaction between the sphere and the end-on cylinder can be written as

$$E_p(d,P)_{C-S} = -\frac{HR}{6}\left[\Psi(d,P)_{C-S} + \mathrm{Z}(d)_{C-S}\right] \qquad \text{(A20)}$$

Since Eqn. (A18) coincides with the energy for the sphere-infinite surface, this expression gives the energy E_n, whereas Eqn. (A20) gives E_p. Thus, the ratio that we were seeking (E_p/E_n) is obtained by dividing Eqn. (A20) by (A18). Of course a value of P where $E_p/E_n \rightarrow 1$ would give unrealistic values since the effective area is then the infinite surface. Numerical simulations can be used to show that values in the range $0.8 < E_c/E < 0.95$ are significant enough to account for the effective area of interaction (data not shown). This is because $\partial(E_p / E_n)/\partial P$ falls off rapidly below 0.8-0.9.

It can be further shown that for $E_p/E_n = 0.9$ and where $R < 5$-10 nm, Eqn. (A21) holds for the effective vdW area of interaction.

$$S_{vdW}(d,R) = \pi(8.9R^{1/4}d^{4/5} + 0.6R)^2 \qquad \text{(A21)}$$

Furthermore, the effective area of interaction due to the capillary force is

$$S_{CAP} = \pi\left|\frac{\gamma_{H_2O}V_m}{R_C T Ln(\frac{RH}{RH_s})}\right|^2 \qquad \text{when } F_{CAP} \text{ is on} \qquad \text{(A22)}$$

This last expression is the Kelvin equation[174] where RH/RH_s is the relative water pressure or the relative humidity (RH) where the suffix s stands for saturated, R_c is the universal gas constant, T is the temperature in degrees Kelvin and V_m is the molar volume. For water $V_m \approx 18\times 10^{-6} m^3$.

A2.2 The effective area of interaction in the dynamic mode

In the dynamic mode, care needs to be taken since the time average of the area of interaction would not produce the required results. This is due to the fact the area of interaction becomes meaningful only as the forces affect the dynamics of the cantilever. Since the force is the physically meaningful parameter controlling the dynamics it is reasonable to use an expression such as

$$< S_F > = \frac{1}{\sum_{i=1}^{i=n} |F_i|} \sum_{i=1}^{i=n} A_i |F_i| \qquad \text{(A23)}$$

where <S> is the effective area of interaction per cycle due to a given interaction force F acting in the tip-sample interface. The suffix i implies that the instantaneous value needs to be taken. As the suffix n tends to infinity, or for simulation purposes n>100 where the values converge (data not shown), <S> converges to a single value. Every force acting between the tip and the surface adds to give an instantaneous area of interaction and a given absolute force magnitude at a given distance d during one cycle. A suffix is used to describe the area of interaction that each expression relates to.

Thus, from the above we get

$$< S_{vdW} > = \frac{1}{< F_{vdW} >} \sum_{i=1}^{i=n} A_{vdW,i} \left| F_{vdW,i} \right| \tag{A24}$$

and

$$< F_{vdW} > = \sum_{i=1}^{i=n} \left| F_{vdW,i} \right| \tag{A25}$$

Similar expressions can be used to account for the contact region (DMT force) and the capillary force. Then the effective area <*S*> is

$$< S > = \frac{< S_{vdW} >< F_{vdW} > + < A_{DMT} >< F_{DMT} > + < A_{CAP} >< F_{CAP} >}{< F_{vdW} > + < F_{DMT} > + < F_{CAP} >} \tag{A26}$$

and the effective radius is simply

$$< r > = \sqrt{< S > / \pi} \tag{A27}$$

The effective radius <*r*>has been used to produce Fig. A3 in the simulations. As observed, the simulations match the experimental outcomes (c.f. Fig. A2 with Fig. A3).

Appendix B: Publications resulting from this thesis

1. Santos, S. & Thomson, N. H. *High resolution imaging of Immunoglobulin G (IgG) antibodies and other biomolecules using amplitude modulation atomic force microscopy in air*. (Davide Ricci and Pier Carlo Braga, 2011) Humana Press, *In press*.

2. Santos, S., Barcons, V., Font, J. & Thomson, N. H. (2010) Cantilever dynamics in amplitude modulation AFM: continuous and discontinuous transitions. *J. Phys. D: Appl. Phys.* **43**, 275401-275407.

3. Santos, S., Barcons, V., Font, J. & Thomson, N. H. (2010) Bi-stability of amplitude modulation AFM in air: deterministic and stochastic outcomes for imaging biomolecular systems. *Nanotechnology***21**, 225710-225720

4. Santos, S. & Thomson, N. H. (2011) Energy dissipation in a dynamic nanoscale contact. *Applied Physics Letters* 98, 013101

5. Santos, S., Barcons, V., Christenson, H. K., Font, J. & Thomson, N. H. (2011) True and apparent height of nanoscale features in the atomic force microscope, PLoS ONE, *Submitted*.

6. Santos, S., Billingsley, D. J., Bonass W. A. and Thomson, N. H. The double-helix of single DNA molecules, submitted to Nature (re-submission).

7. Barcons, V., Santos, S, Thomson N. H. and J. Font (2011) Dynamics of nano-mechanical junctions under the influence of adsorbed water layers, Pys. Rev. Letts., *Submitted.*

8. Barcons, V., Santos, S., Bonass, W. A., Font, J. & Thomson, N. H. (2011) Monostability of sharp-tip impact oscillators interacting with surface hydration layers, Euro Physical Letters, *Submitted* (2011).

9. Santos, S., Barcons, V., Font, J. & Thomson, N. H. (2009) Tip creep and single DNA molecule wear in amplitude modulation AFM in air, *Unpublished.*

The last manuscript was presented as the second year report by the candidate but has been held unpublished due to patent considerations by the University of Leeds and Asylum Research Corporation.

References

1 Garcia, R. & Perez, R. Dynamic Atomic Force Microscopy Methods. *Surface Science Reports* **47** 197-301 (2002).

2 Hamaker, H. C. The London – van der Waals attraction between spherical particles. *Physica* **4**, 1058-1072 (1937).

3 Feynman, R., Leighton, R. & Sands, M. *The Feynman lectures on physics*. Second edn, Vol. 1 (Addison Wesley, 2005).

4 Feynman, R. *The pleasure of finding things out*. New edn, (Pinguin Books Ltd, 2001).

5 Rodríguez, T. R. & García, R. Tip motion in amplitude modulation tapping-mode atomic-force microscopy: Comparison between continuous and point-mass models. *Applied Physics Letters* **80**, 1646-1648 (2002).

6 Doster, W., Gutberlet, T., Khodadadi, S., Malkovskiy, A., Kisliuk, A., Sokolov, A. P., Jansson, H., Swenson, J., Nakagawa, H., Kamikubo, H., Kataoka, M., Kealley, C. S., Sokolova, A. V., Kearley, G. J., Kemner, E., Russina, M., Faraone, A., Hamilton, W. A. & Gilbert, E. P. in *Protein-Water Interactions* Vol. 1804 eds W. Doster & T. Gutberlet) 1-242 (Elsevier, 2010).

7 Pakarinen, O. H., Foster, A. S., Paajanen, M., Kalinainen, T., Katainen, J., Makkonen, I., Lahtinen, J. & Nieminen, R. M. Towards an accurate description of the capillary force in nanoparticle-surface interactions. *Modelling and simulation in material science and engineering* **13**, 1175–1186 (2005).

8 Israelachvili, J. *Intermolecular & Surface Forces*. 2 edn, (Academic Press, 1991).

9 Köber, M., Sahagún, E., García-Mochales, P., Briones, F., Luna, M. & Sáenz, J. J. Nanogeometry Matters: Unexpected Decrease of Capillary Adhesion Forces with Increasing Relative Humidity. *Small* **6**, 2725–2730 (2010).

10 Brydson, R. M., Hammond, C., Mowbray, D., Gibbs, M. R. J., Todd, I., Grell, M., Hamley, I. W., Geoghegan, M., Jones, R. A. L. & Leggett, G. J. *Nanoscale Science and Technology*. (Wiley, 2005).

11 Thiel, P. A. & Madey, T. E. The interaction of water with solid surfaces: Fundamental aspects *Surface Science Reports* **7**, 211-385 (1987).

12 Binnig, G., Quate, C. F. & Gerber, C. Atomic Force Microscope. *Physical Review Letters* **56**, 930-933 (1986).

13 Bustamante, C. & Keller, D. Scanning force microscopy in biology. *Physics today* **48**, 33-38 (1995).

14 Hansma, H. G. & Hoh, J. H. Biomolecular Imaging with the Atomic Force Microscope. *Annual Review of Biophysics and Biomolecular Structure* **23**, 115-140 (1994).

15 Giessibl, F. J. Advances in atomic force microscopy *Reviews of Modern Physics* **75**, 949-983 (2003).

16 Quate, C. F. The AFM as a tool for surface imaging. *Surface Science* **299-300**, 980-995 (1994).

17 Gross, L., Mohn, F., Moll, N., Liljeroth, P. & Meyer, G. The Chemical Structure of a Molecule Resolved by Atomic Force Microscopy. *Science* **325**, 1110-1114 (2009).

18 Ostendorf, F., Schmitz, C., Hirth, S., Kühnle, A., Kolodziej, J. J. & Reichling, M. Evidence for Potassium Carbonate Crystallites on Air-Cleaved Mica Surfaces. *Langmuir* **25**, 10764-10767 (2009).

19 Gross, L., Mohn, F., Moll, N., Meyer, G., Ebel, R., Abdel-Mageed, W. M. & Jaspars, M. Organic structure determination using atomic-resolution scanning probe microscopy. *Nature Chemistry* (2010).

20 Turner, R. D., Kirkham, J., Devine, D. & Thomson, N. H. Second harmonic atomic force microscopy of living Staphylococcus aureus bacteria *Applied Physics Letters* **94**, 043901 (2009).

21 Stark, R. W. Spectroscopy of higher harmonics in dynamic atomic force microscopy. *Nanotechnology* **15**, 347-351 (2004).

22 Patil, S., Martinez, N. F., Lozano, J. R. & Garcia, R. Force microscopy imaging of individual protein molecules with sub-pico Newton force sensitivity. *Journal of Molecular Recognition* **20**, 516-523 (2007).

23 Proksch, R. Multi-frequency, repulsive mode amplitude modulated atomic force microscopy. *Applied Physics Letters* **89**, 113121–113123 (2006).

24 Xu, X., Melcher, J., Basak, S., Reifenberger, R. & Raman, A. Compositional contrast of biological materials in liquids using the momentary excitation of higher eigenmodes in dynamic atomic force microscopy. *Physical Review Letters* **102**, 060801-060804 (2009).

25 Alessandrini, A. & Facci, P. AFM: a versatile tool in biophysics. *Measurement Science and Technology* **16**, R65-R92 (2005).

26 Gould, S., Marti, O., Drake, B., Hellemans, L., Bracker, C. E., Hansma, P. K., Keder, N. L., Eddy, M. M. & Stucky, G. D. Molecular resolution images of amino acid crystals with the atomic force microscope. *Nature* **332**, 332 - 334 (1988).

27 Drake, B., Prater, C. B., Weisenhorn, A. L., Gould, S. A., Albrecht, T. R., Quate, C. F., Cannell, D. S., Hansma, H. G. & Hansma, P. K. Imaging crystals, polymers, and processes in water with the atomic force microscope. *Science* **243**, 1586 (1989).

28 Hansma, P. K., Cleveland, J. P., Radmacher, M., Walters, D. A., Hillner, P. E., Bezanilla, M., Fritz, M., Vie, D. & Hansma, H. G. Tapping mode atomic force microscopy in liquids. *Applied Physics Letters* **64**, 1738-1740 (1994).

29 Kodera, N., Yamamoto, D., Ishikawa, R. & Ando, T. Video imaging of walking myosin V by high-speed atomic force microscopy. *Nature* **468**, 72–76 (2010).

30 Albrecht, T. R., Grutter, P., Horne, D. & Rugar, D. Frequency modulation detection using high‐Q cantilevers for enhanced force microscope sensitivity. *Journal of Applied Physics* **69**, 668-673 (1991).

31 Martin, Y., Williams, C. C. & Wickramasinghe, H. K. Atomic force microscope-force mapping and profiling on a sub 100-Å scale. *Journal of Applied Physics* **61**, 4723-4729 (1987).

32 Zhong, Q., Innlss, D., Kjoller, K. & Elings, V. B. Fractured polymer/silica fiber surface studied by tapping mode atomic force microscopy. *Surface Science Letters* **290**, L688-L692 (1993).

33 Tamayo, J. & Garcia, R. Deformation, Contact Time, and Phase Contrast in Tapping Mode Scanning Force Microscopy. *Langmuir* **12**, 4430-4435 (1996).

34 French, A. *Vibrations and Waves*. (Thomas Nelson and sons Ltd, 1981).

35 Stark, R. & Heckl, W. Higher harmonics imaging in tapping-mode atomic-force microscopy *Review of Scientific Instruments* **74**, 5111-5114 (2003).

36 Weisenhorn, A. l., Hansma, P. K., Albrecht, T. R. & Quate, C. F. Forces in atomic force microscopy in air and water. *Applied Physics Letters* **54**, 2651-2653 (1989).

37 Fukuma, T., Kobayashi, K., Matsushige, K. & Yamada, H. True molecular resolution in liquid by frequency modulation atomic force microscopy. *Applied Physics Letters* **86**, 193108–193110 (2005).

38 Anselmetti, D., Luthi, R., Meyert, E., Richmond, T., Dreier, M., Frommer, J. E. & Guntherodt, H.-J. Attractive-mode imaging of biological materials with dynamic force microscopy. *Nanotechnology* **5**, 87-94 (1994).

39 Pérez, R., Štich, I., Payne, M. C. & Terakura, K. Surface-tip interactions in noncontact atomic-force microscopy on reactive surfaces: Si(111). *Physical Review B* **58**, 10835–10849 (1998).

40 Boisgard., R., Michel, D. & Aime, J. P. Hysteresis generated by attractive interaction: oscillating behavior of a vibrating tip-microlever system near a surface. *Surface Science* **401**, 199-205 (1998).

41 Garcia, R. & San Paulo, A. Attractive and repulsive tip-sample interaction regimes in tapping mode atomic force microscopy *Physical Review B* **60**, 4961-4967 (1999).

42 Chen, X., Davies, M. C., Roberts, C. J., Tendler, S. J. B., Williams, P. M. & Burnham, N. A. Optimizing phase imaging via dynamic force curves. *Surface Science* **460**, 292–300 (2000).

43 Anczykowski, B., Krüger, D. & Fuchs, H. Cantilever dynamics in quasinoncontact force microscopy: Spectroscopic aspects. *Physical Review B* **53**, 15485-15488 (1996).

44 San Paulo, A. & Garcia, R. High-Resolution Imaging of Antibodies by Tapping-Mode Atomic Force Microscopy: Attractive and Repulsive Tip-Sample Interaction Regimes. *Biophysical Journal* **78**, 1599–1605 (2000).

45 Stark, R., Schitter, G. & Stemmer, A. Tuning the interactions forces in tapping mode atomic force microscopy *Physical Review B* **68**, 0854011-0854015 (2003).

46 Bar, G., Thomann, Y., Brandsch, R. & Cantow, H. J. Factors Affecting the Height and Phase Images in Tapping Mode Atomic Force Microscopy. Study of Phase-Separated Polymer Blends of Poly(ethene-costyrene) and Poly(2,6-dimethyl-1,4-phenylene oxide). *Langmuir* **13**, 3807-3812 (1997).

47 Tamayo, J. & Garcia, R. Effects of elastic and inelastic interactions on phase contrast images in tapping-mode scanning force microscopy. *Applied Physics Letters* **71**, 2394-2396 (1997).

48 Cleveland, J. P., Anczykowski, B., Schmid, A. E. & Elings, V. B. Energy dissipation in tapping-mode atomic force microscopy. *Applied Physics Letters* **72**, 2613-2615 (1998).

49 Martinez, N. & Garcia, R. Measuring phase shifts and energy dissipation with amplitude modulation atomic force microscopy. *Nanotechnology* **17**, S167-S172 (2006).

50 Garcia, R., Gómez, C. J., Martinez, N. F., Patil, S., Dietz, C. & Magerle, R. Identification of Nanoscale Dissipation Processes by Dynamic Atomic Force Microscopy. *Physical Review Letters* **97**, 016103-016104 (2006).

51 Stark, R. W. & Heckl, W. M. Fourier transformed atomic force microscopy:tapping mode atomic force microscopy beyond the Hookian approximation. *Surface Science* **457**, 219-228 (2000).

52 Rodriguez, T. & Garcia, R. Compositional mapping of surfaces in atomic force microscopy by excitation of the second normal mode of the microcantilever. *Applied Physics Letters* **84**, 449-551 (2004).

53 Sahin, O., Quate, C., Solgaard, O. & Atalar, A. Resonant harmonic response in tapping-mode atomic force microscopy. *Physical Review B* **69**, 165416 (2004).

54 Sahin, O., Magonov, S., Su, C., Quate, C. F. & Solgaard, O. An atomic force microscope tip designed to measure time-varying nanomechanical forces. *Nature Nanotechnology* **2**, 507 - 514 (2007).

55 Gere, J. & Timoshenko, S. *Mechanics of materials*. Fourth edn, (PWS Publishing Company, 1997).

56 Steidel, R. *An introduction to mechanical vibrations*. 3 edn, (John Wiley & Sons, 1989).

57 Gan, Y. Atomic and subnanometer resolution in ambient conditions by atomic force microscopy. *Surface Science Reports* **64**, 99-121 (2009).

58 Voïtchovsky, K., Kuna, J. J., Antoranz Contera, S., Tosatti, E. & Stellacci, F. Direct mapping of the solid–liquid adhesion energy with subnanometre resolution. *Nature Nanotechnology* **5**, 401 - 405 (2010).

59 Santos, S., Billingsley, D. J., Bonass, W. A. & Thomson, N. H. *The double-helix of single DNA molecules*

60 Voet, D. & Voet, J. *Biochemistry*. Second edn, (John Wiley and Sons, 1995).

61 Avery, O. T., MacLeod, C. M. & McCarty, M. Studies on the Chemical Nature of the Substance Inducing Transformation of Pneumococcal Types: Induction of Transformation by a Desoxyribonucleic Acid Fraction Isolated from Pneumococcus Type III. *The Journal of Experimental Medicine* **79**, 137-158 (1944).

62 Hershey, A. D. & Chase, M. Independent Functions of Viral Protein and Nucleic Acid in Growth of Bacteriophage. *The Journal of general physiology* **36**, 39-56 (1952).

63 Chargaff, E., Lipshitz, R. & Green, C. Composition of the deoxypentose nucleic acids of four genera of sea-urchin. *Journal of Biological Chemistry* **195**, 155–160 (1952).

64 Watson, J. D. & Crick, F. H. C. A Structure for Deoxyribose Nucleic Acid *Nature* **171**, 737-738 (1953).

65 Ha, S. C., Lowenhaupt, K., Rich, A., Kim, Y. G. & Kim, K. K. Crystal structure of a junction between B-DNA and Z-DNA reveals two extruded bases. *Nature* **437**, 1183–1186 (2005).

66 Bates, A. D. & Maxwell, A. *DNA Topology*. (Oxford University Press, 2005).

67 Rich, A. & Zhang, S. Timeline: Z-DNA: the long road to biological function. *Nature Reviews Genetics* **4**, 566-572 (2003).

68 Heddle, J. G., Mitelheiser, S., Maxwell, A. & Thomson, N. H. Nucleotide binding to DNA gyrase causes loss of DNA wrap. *Journal of Molecular Biology* **337**, 597-610 (2004).

69 Simmel, F. C. & Dittmer, W. U. DNA nanodevices. *Small* **1**, 284-299 (2005).

70 Mirkin, C. A., Letsinger, R. L., Mucic, R. C. & Storhoff, J. J. A DNA-based method for rationally assembling nanoparticles into macroscopic materials. *Nature* **382**, 607-609 (1996).

71 Brooker, R. J., Widmaier, E. P., Graham, L. E. & Stiling, P. D. *Biology*. (McGraw-Hill Higher Education, 2006).

72 Wang, A. H. J., Quigley, G. J., Kolpak, F. J., Crawford, J. L., van Boom, J. H., van der Marel, G. & Rich, A. Molecular structure of a left-handed double helical DNA fragment at atomic resolution. *Nature* **282**, 680-686 (1979).

73 Pain, H. J. *The physics of vibrations and waves*. 3rd edn, (John Wiley & Sons Limited 1983).

74 Hölscher, H., Schwarz, U. D. & Wiesendanger, R. Calculation of the frequency shift in dynamic force microscopy. *Applied Surface Science* **140**, 344-351 (1999).

75 Choe, H., Hong, M.-H., Seo, Y., Lee, K., Kim, G., Cho, Y., Ihm, J. & Jhe, W. Formation, Manipulation, and Elasticity Measurement of a Nanometric Column of Water Molecules. *Physical Review Letters* **95**, 187801-187804 (2005).

76 Giessibl, F. J. Forces and frequency shifts in atomic-resolution dynamic-force microscopy. *Physical Review B* **56**, 16010–16015 (1997).

77 Gauthier, M., Pérez, R., Arai, T., Tomitori, M. & Tsukada, M. Interplay between Nonlinearity, Scan Speed, Damping, and Electronics in Frequency Modulation Atomic-Force Microscopy. *Physical Review Letters* **89**, 146104 (2002).

78 Gotsmann, B., Seidel, C., Anczykowski, B. & Fuchs, H. Conservative and dissipative tip-sample interaction forces probed with dynamic AFM. *Physical Review B* **60**, 11051-11061 (1999).

79 Santos, S., Barcons, V., Font, J. & Thomson, N. H. Bi-stability of amplitude modulation AFM in air: deterministic and stochastic outcomes for imaging biomolecular systems. *Nanotechnology* **21**, 225710-225720 (2010).

80 Garcia, R. & San Paulo, A. Dynamics of a vibrating tip near or in intermittent contact with a surface. *Physical Review B* **61**, R13381-R13384 (2000).

81 Gleyzes, P., Kuo, P. K. & Boccara, A. C. Bistable behavior of a vibrating tip near a solid surface. *Applied Physics Letters* **58**, 2989-2991 (1991).

82 Loppacher, C., Bammerlin, M., Battiston, F., Guggisberg, M., Müller, D., Hidber, H. R., Lüthi, R., E., M. & Güntherodt, H. J. Fast digital electronics for application in dynamic force microscopy using high-Q cantilevers *Applied Physics A* **66**, S215-S218 (1998).

83 Giessibl, F. J. Atomic Resolution of the Silicon (111)-(7x7) Surface by Atomic Force Microscopy *Science* **267**, 68-71 (1995).

84 Shin-ichiKitamura & Iwatsuki, M. Observation of 7×7 Reconstructed Structure on the Silicon (111) Surface using Ultrahigh Vacuum Noncontact Atomic Force Microscopy. *Japanese Journal of Applied Physics* **34**, L145-L148 (1995).

85 Yasuhiro Sugawara, Ohta, M., Ueyama, H. & Morita, S. Defect Motion on an InP(110) Surface Observed with Noncontact Atomic Force Microscopy. *Science* **270**, 1646-1648 (1995).

86 Thomson, N. H. The substructure of immunoglobulin G resolved to 25 kDA using amplitude modulation in air. *Ultramicroscopy* **105**, 103-110 (2005).

87 Thomson, N. H. Imaging the substructure of antibodies with tapping-mode AFM in air: the importance of a water layer on mica. *Journal of Microscopy* **217**, 193-199 (2005).

88 Giessibl, F. J. & Bielefeldt, H. Physical Interpretation of Frequency-Modulation Atomic Force Microscopy. *Physical Review B* **61**, 9968-9971 (2000).

89 Nony, L., Boisgard, R. & Aime, J. P. Nonlinear dynamical properties of an oscillating tip–cantilever system in the tapping mode. *Journal of Chemical Physics* **111**, 1615-1627 (1999).

90 Aimé, J. P., Boisgard, R., Nony, L. & Couturier, G. Nonlinear Dynamic Behavior of an Oscillating Tip-Microlever System and Contrast at the Atomic Scale. *Physical Review Letters* **82**, 3388-3391 (1999).

91 Sasaki, N. & Tsukada, M. Theory for the effect of the tip–surface interaction potential on atomic resolution in forced vibration system of noncontact AFM *Applied Surface Science* **140**, 339-343 (1999).

92 Binnig, G. & Rohrer, H. *Scanning tunneling microscopy.* 38-46 (The Hague: Eur. Phys. Soc., 1984).

93 Thomson, N. H., Fritz, M., Radmacher, M., Cleveland, J. P., Schmidt, C. F. & Hansma, P. K. Protein tracking and detection of protein motion using atomic force microscopy. *Biophysical Journal* **70**, 2421–2431 (1996).

94 Robert J. Driscoll, Youngquist, G. M. & Baldeschwieler, D. J. Atomic-scale imaging of DNA using scanning tunnelling microscopy. *Nature* **346**, 294-296 (1990).

95 Clemmer, C. & Beebe, T. P. J. Graphite: a mimic for DNA and other biomolecules in scanning tunneling microscope studies. *Science* **251**, 640-642 (1991).

96 Amrein, M., Durr, R., Stasiak, A., Gross, H. & Travaglini, G. Scanning tunneling microscopy of uncoated recA-DNA complexes *Science* **243**, 1708-1711 (1998).

97 Guckenberger, R., Hacker, B., Hartmann, T., Scheybani, T., Wang, Z., Wiegräbe, W. & Baumeister, W. Imaging of uncoated purple membrane by scanning tunneling microscopy. *J. Vac. Sci. Technol. B* **9**, 1227-1230 (1991).

98 Tamayo, J. & Garcia, R. Relationship between phase shift and energy dissipation in tapping-mode scanning force microscopy. *Applied Physics Letters* **73**, 2926-2928 (1998).

99 Hansma, H. G., Weisenhorn, A. L., Gould, S. A. C., Sinsheimer, R. L., Gaub, H. E., Stucky, G. D., Zaremba, C. M. & Hansma, P. K. Progress in sequencing deoxyribonucleic acid with an atomic force microscope. *J. Vac. Sci. Technol. B* **9**, 1227-1230 (1991).

100 Kienbergera, F., Costab, T. L., Zhua, R., Kadad, G., Reithmayere, M., Chtcheglovaa, L., Rankla, C., Pachecof, B. F. A., Thalhammerb, S., Pastushenkoa, V., Hecklb, M. W., Blaase, D. & Hinterdorfer, P. Dynamic force microscopy imaging of plasmid DNA and viral RNA. *Biomaterials* **28** 2403–2411 (2007).

101 Uchihashi, T., Tanigawa, M., Ashino, M., Sugawara, Y., Yokoyama, K., Morita, S. & Ishikawa, M. Identification of B-Form DNA in an Ultrahigh Vacuum by Noncontact-Mode Atomic Force Microscopy. *Langmuir* **16**, 1349-1353 (2000).

102 D. V. Klinov, Neretina, T. V., Prokhorov, V. V., Dobrynina, T. V., Aldarov, K. G. & Demin, V. V. High resolution Atomic Force Microscopy of DNA. *Biochemistry (Moscow)* **74**, 1150-1154 (2009).

103 Maaloum, M. A close encounter with DNA. *European Biophysics Journal* **32**, 585–587 (2003).

104 J. Martinez, Yuzvinsky, T. D., Fennimore, A. M., Zettl, A., Garcia, R. & Bustamante, C. Length control and sharpening of atomic force microscope carbon nanotube tips assisted by an electron beam. *Nanotechnology* **16**, 2493–2496 (2005).

105 Ostendorf, F., Schmitz, C., Hirth, S., Kühnle, A., Kolodziej, J. J. & Reichling, M. How flat is an air-cleaved mica surface? *Nanotechnology* **19**, 305705 (2008).

106 Bezanilla, M., Manne, S., Laney, D. E., Lyubchenko, Y. L. & Hansma, H. G. Adsorption of DNA to Mica, Silylated Mica, and Minerals: Characterization by Atomic Force Microscopy. *Langmuir* **11**, 655–659 (1995).

107 Hansma, H. & Laney, D. DNA binding to mica correlates with cationic radius: assay by atomic force microscopy. *Biophysical Journal* **70**, 1933-1939 (1996).

108 Vesenka, J., Guthold, M., Tang, C. L., Keller, D., Delaine, E. & Bustamante, C. Substrate preparation for reliable imaging of DNA molecules with the scanning force microscope. *Ultramicroscopy* **42-44**, 1243-1249 (1992).

109 Santos, S. & Thomson, N. H. *High resolution imaging of Immunoglobulin G (IgG) antibodies and other biomolecules using amplitude modulation atomic force microscopy in air.* (Humana Press, 2010).

110 Christenson, H. K. & Israelachvili, J. N. Growth of Ionic Crystallites on Exposed Surfaces. *Journal of colloid and interface science* **117**, 576-577 (1987).

111 Richardson, S. M. & Richardson, J. W. Crystal structure of a pink muscoyite from Archer's Post, Kenya: implications for reverse pleochroism in dioctahedral micas. *American Mineralogist* **67**, 69-75 (1982).

112 Adams, G., Ashton, M. R. & Khoshdel, E. Hydroxyl-functionalized dendritic macromolecules in topical cosmetic and personal care compositions. (2003).

113 Overberger, C. G., Salamone, J. C. & Yaroslavsky, S. Cooperative effects in the esterolytic action of synthetic macromolecules containing imidazole and hydroxyl functions. *Journal of American Chemical Society* **89**, 6231–6236 (1967).

114 Medici, A., Fantin, G., Pedrini, P., Gleria, M. & Minto, F. Functionalization of phosphazenes. 1. Synthesis of phosphazene materials containing hydroxyl groups. *Macromolecules* **25**, 2569–2574 (1992).

115 Balmer, T. E., Christenson, H. K., Spencer, N. D. & Heuberger, M. The Effect of Surface Ions on Water Adsorption to Mica. *Langmuir* **24**, 1566-1569 (2008).

116 Moreno-Herrero, F., Colchero, J. & Baro, A. DNA height in atomic force microscopy. *Ultramicroscopy* **96**, 167-174 (2003).

117 Billingsley, D. J., Kirkham, J., Bonass, W. A. & Thomson, N. H. Atomic force microscopy of DNA at high humidity: irreversible conformational switching of supercoiled molecules. *Physical Chemistry Chemical Physics* **12**, 14727-14734 (2010).

118 Zitzler, L., Herminghaus, S. & Mugele, F. Capillary forces in tapping mode atomic force microscopy. *Physical Review B* **66**, 155436-155438 (2002).

119 Xu, X., Melcher, J. & Raman, A. Accurate force spectroscopy in tapping mode atomic force microscopy in liquids. *Physical Review B* **81**, 035407-035414 (2010).

120 Basak, S., Raman, A. & Garimella, S. V. Hydrodynamic loading of microcantilevers vibrating in viscous fluids. *Journal of Applied Physics* **99**, 114906-114915 (2006).

121 Kiracofe, D. & Raman, A. On eigenmodes, stiffness, and sensitivity of atomic force microscope cantilevers in air versus liquids. *Journal of Applied Physics* **107**, 033506-033515 (2010).

122 Santos, S., Barcons, V., Font, J. & Thomson, N. H. Cantilever dynamics in amplitude modulation AFM: continuous and discontinuous transitions. *J. Phys. D: Appl. Phys.* **43**, 275401-275407 (2010).

123 Preiner, J., Tang, J., Pastushenko, V. & Hinterdorfer, P. Higher Harmonic Atomic Force Microscopy: Imaging of Biological Membranes in Liquid. *Physical Review Letters* **99**, 046102-046105 (2007).

124 Sarid, D., Ruskell, T. G., K., W. R. & Chen, D. Driven nonlinear AFM cantilevers: from noncontact to tapping modes of operation. *Journal of Vacuum Science & Technology B* **14**, 864-867 (1996).

125 Derjaguin, B. V., Muller, V. & Toporov, Y. Effect of Contact Deformations on the Adhesion of Particles. *Journal of Colloid and Interface Science* **53**, 314-326 (1975).

126 Johnson, K. L., Kendall, K. & Roberts, A. D. Surface energy and the contact of elastic solids. *Proc. R. Soc. Lond. A* **324**, 301-313 (1971).

127 Tabor, D. Surface forces and surface interactions. *Journal of colloid and interface science* **58**, 2-13 (1976).

128 Maugis, D. Adhesion of spheres: The JKR-DMT transition using a dugdale model *Journal of Colloid and Interface Science* **150**, 243-269 (1992).

129 Ebenstein, D. M. & Wahl, K. J. A comparison of JKR-based methods to analyze quasi-static and dynamic indentation force curves. *Journal of colloid and interface science* **298**, 652–662 (2006).

130 McNeil, L. E. & Grimsditch, M. Elastic moduli of muscovite mica. *Journal of Physics: Condensed Matter* **5**, 1681-1690 (1993).

131 Fischer-Cripps, A. C. *Nanoindentation*. Second edn, (Springer, 2004).

132 Lin, D. C., Dimitriados, K. E. & Horkay, F. *Advances in the mechanical characterization of soft materials by nanoindentation* 1edn, Vol. 5 1- 38 (Transworld Research Network, 2006).

133 Nony, L., Boisgard, R. & Aimé, J. P. DNA Properties Investigated by Dynamic Force Microscopy. *Biomacromolecules* **2**, 827-835 (2001).

134 Round, A. & Miles, M. Exploring the consequences of attractive and repulsive interaction regimes in tapping mode atomic force microscopy of DNA. *Nanotechnology* **15**, S176-183 (2004).

135 Abou-Saleh, R. H., Connell, S. D., Harrand, R., A. Ajjan, R., Mosesson, M. W., Smith, D. A. M., Grant, P. J. & Ariëns, R. A. S. Nanoscale Probing Reveals that Reduced Stiffness of Clots from Fibrinogen Lacking 42 N-Terminal Bβ-Chain Residues Is Due to the Formation of Abnormal Oligomers. *Biophysical Journal* **96**, 2415-2427 (2009).

136 Stark, R. W. Bistability, higher harmonics, and chaos in AFM *Materials Today* **13** (2010).

137 Barcons, V., Santos, S., Thomson, N. H. & Font, J. Dynamics of nano-mechanical junctions under the influence of adsorbed water layers. *Physical Review Letters* **Submitted** (2011).

138 Matlab and Simulink, Release 2010a (The MathWorks, Inc. Natick 2010).

139 Garcia, R., Tamayo, J. & San Paulo, A. Phase contrast and surface energy hysteresis in tapping mode scanning force microsopy. *Surface and Interface Analysis* **27**, 312-316 (1999).

140 Paulo, A. S. & Garcia, R. Tip-surface, amplitude, and energy dissipation in amplitude-modulation (tapping mode) force microscopy. *Physical Review B* **64**, 193411-193414 (2001).

141 Stark, M., Möller, C., Müller, D. J. & Guckenberger, R. From Images to Interactions: High-Resolution Phase Imaging in Tapping-Mode Atomic Force Microscopy *Biophysics Journal* **80**, 3009-3018 (2001).

142 Melcher, J., Carrasco, C., Xu, X., Carrascosa, J. L., Gomez-Herrero, J., de Pablo, P. J. & Raman, A. in *Proceedings of the National Academy of Sciences of the United States of America.* 13655-13660.

143 Aimé, J. P., Boisgard, R., Nony, L. & Couturier, G. Nonlinear Dynamic Behavior of an Oscillating Tip-Microlever System and Contrast at the Atomic Scale. *Physical Review Letters* **82**, 3388-3391 (1998).

144 Wang, L. The role of damping in phase imaging in tapping mode atomic force microscopy. *Surface Science* **429**, 178-185 (1999).

145 Marth, M., Maier, D. & Honerkamp, J. A unifying view on some experimental effects in tapping-mode atomic force microscopy. *Journal of Applied Physics* **85**, 7030-7036 (1999).

146 Whangbo, M. H., Brandsch, R. & Bar, G. Description of phase imaging in tapping mode atomic force microscopy by harmonic approximation. *Surface Science* **411**, L794-L801 (1998).

147 Santos, S. & Thomson, N. H. Energy dissipation in a dynamic nanoscale contact. *Applied Physics Letters* **98**, 013101-013103 (2011).

148 Santos, S. & Thomson, N. H. Energy dissipation in a dynamic nanoscale contact. *Applied Physics Letters* **In Press** (2010).

149 Fang, S. J., Haplepete, S., Chen, W. & Helms, C. R. Analyzing atomic force microscopy images using spectral methods. *Journal of Applied Physics* **82**, 5891-5898 (1997).

150 Paulo, A. S. & Garcia, R. Unifying theory of tapping-mode atomic force microscopy *Physical Review B* **66**, 0414061-0414064 (2002).

151 Thompson, J. M. T. & Stwart, H. B. *Nonlinear Dynamics and Chaos*. (John Wiley and Sons, 1987).

152 Couturier, G., Boisgard, R., Nony, L. & Aimé, J. P. Noncontact atomic force microscopy: Stability criterion and dynamical responses of the shift of frequency and damping signal. *Review of Scientific Instruments* **74**, 2726-2734 (2003).

153 Santos, S. & Thomson, N. H. *High resolution imaging of Immunoglobulin G (IgG) antibodies and other biomolecules using amplitude modulation atomic force microscopy in air*. (Humana Press, 2011).

154 Garcia, R. & San Paulo, A. Amplitude curves and operating regimes in dynamic atomic force microscopy. *Ultramicroscopy* **82**, 79-83 (2000).

155 Christenson, H. K. Adhesion and surface energy of mica in air and water. *Journal of Physical Chemistry* **97**, 12034-12041 (1993).

156 Santos, S., Barcons, V., Christenson, H. K., Thomson, N. H. & Font, J. The intrinsic resolution limit in the atomic force microscope: implications for heights of nano-scale features. *PLoS ONE* **Submitted** (2011).

157 Santos, S., Barcons, V., Font, J. & Thomson, N. H. Tip creep and single DNA molecule wear in amplitude modulation AFM in air. *Unpublished* (2009).

158 Strogatz, S. H. *Nonlinear Dynamics and Chaos: With Applications to Physics, Biology, Chemistry and Engineering (Paperback)*. First edn, (Westview Press, 2001).

159 Zhang, L. & Webster, T. J. Nanotechnology and nanomaterials: Promises for improved tissue regeneration. *Nano Today* **4**, 66-80 (2009).

160 Müller, D. J. & Engel, A. The height of biomolecules measured with the atomic force microscope depends on electrostatic interactions. *Biophysical Journal* **73**, 1633–1644 (1997).

161 Yang, C.-W. & Hwang, I.-S. Soft-contact imaging in liquid with frequency-modulation torsion resonance mode atomic force microscopy. *Nanotechnology* **21**, 065710-065716 (2010).

162 Saenger, W. *Principles of Nucleic Acid Structure*. (Springer, 1984).

163 Yang, C.-W., Hwang, I.-S., Fu Chen, Y., Seng Chang, C. & Ping Tsai, D. Imaging of soft matter with tapping-mode atomic force microscopy and non-contact-mode atomic force microscopy. *Nanotechnology* **18**, 084009 (2007).

164 Müller, D. J., Fotiadis, D., Scheuring, S., Müller, S. A. & Engel, A. Electrostatically Balanced Subnanometer Imaging of Biological Specimens by Atomic Force Microscope. *Biophysical Journal* **76**, 1101-1111 (1999).

165 Fischer-Cripps, A. C. *Introduction to contact mechanics*. Second edn, (Springer, 2007).

166 Oatleya, C. W., Nixona, W. C. & Peasea, R. F. W. Scanning Electron Microscopy. *Advances in Electronics and Electron Physics* **21**, 181-247 (1966).

167 Bloo, M. L., Haitjema, H. & Pril, W. O. Deformation and wear of pyramidal, silicon-nitride AFM tips scanning micrometre-size features in contact mode. *Measurement* **25**, 203-211 (1999).

168 Kopycinska-Mueller, M., Geiss, R. H. & Hurley, D. C. in *Mater. Res. Soc. Symp. Proc.* Vol. 924 Z3.2.1 - Z3.2.6 (Materials Research Society San Francisco, CA, 2006).

169 Grandbois, M., Beyer, M., Rief, M., Clausen-Schaumann, H. & E. Gaub, H. How Strong Is a Covalent Bond? *Science* **283**, 1727 - 1730 (1999).

170 Barcons, V., Santos, S., Thomson, N. H. & Font, J. A third attractor in dynamic AFM: consequences for stability and imaging. *Not published* (2010).

171 Yaminsky, V. V. The hydrophobic force: the constant volume capillary approximation. *Colloids and Surfaces A* **159**, 181–195 (1999).

172 Unertl, W. N. Implications of contact mechanics models for mechanical properties measurements in scanning force microscopy *J. Vac. Sci. Technol.* **17**, 179-1786 (1999).

173 MATLAB R2008a and SIMULINK, T. M., Inc., Natick, Massachusetts, US.

174 Christenson, H. K. Capillary condensation due to the van der Waals attraction in wet slits. *Physical Review Letters* **73**, 1821-1824 (1994).